Formation and dissolution of metastable ferrite above the upper Ae1

A Dissertation

Presented to

the faculty of the School of Engineering and Applied Science

University of Virginia

in partial fulfillment

of the requirements for the degree
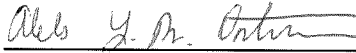
Doctor of Philosophy

by

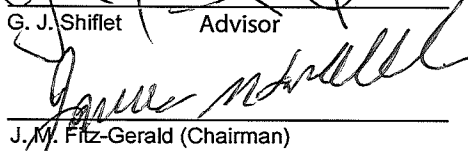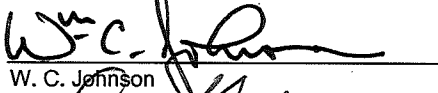Aleks Y. M. Ontman

December

2012

APPROVAL SHEET

The dissertation

is submitted in partial fulfillment of the requirements

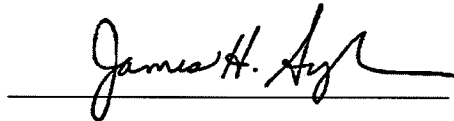for the degree of

Doctor of Philosophy

_____
AUTHOR

The dissertation has been read and approved by the examining committee:

_____
G. J. Shiflet   Advisor

_____
J. M. Fitz-Gerald (Chairman)

_____
R. E. Hackenberg

_____
W. C. Johnson

_____
S. R. Agnew

_____

Accepted for the School of Engineering and Applied Science:

_____
Dean, School of Engineering and Applied Science

December

2012

Acknowledgments

Firstly, I would like to express my unbound gratitude to Professor Gary J. Shiflet for serving as my advisor during my graduate tenure. I consider myself extremely fortunate to be provided with his unending support, encouragement, sound advice, and patience over the years. I especially appreciate the latitude and the degree of independence he afforded me in my various undertakings. It is hard to imagine a better advisor and a mentor.

I am very grateful for the invaluable input provided by the Ph. D. committee: Prof. James M. Fitz-Gerald, Prof. Sean R. Agnew, Prof. William C. Johnson, and Dr. Robert E. Hackenberg of the Los Alamos National Laboratory. It is a privilege to be associated with and learn from such knowledgeable and caring group of individuals. Special thanks to Dr. Hackenberg for taking a personal interest in the project and providing a continuous stream of discussions and ideas.

I am indebted to Diane M. Lutz for her relentless pursuit of perfect metallography, a truly underappreciated skill. Andrew Cheung gets numerous thanks for, amongst others, helping me with the TEM work, diffusing his mechanical acumen while keeping the lab functional, and for all the discussions we had. Former colleagues I would like to acknowledge for their various contributions are Jason Wang, Azusa Furihata, and Eric Lass.

Honorable mention goes to my friends Cecilia Davis, Joshua Copeland, Alex Mironov, and Sonya Maslova for providing me with the much needed balance in the work-balance equation.

I wish to thank my extended family for the constant encouragement and support in all of my endeavors.

Lastly, and most importantly, I wish to thank my mother whose limitless patience I have relentlessly tested ever since I can remember. To her I owe the opportunity to be as ambitious as I wanted and to her I dedicate this dissertation.

Abstract

This work explores kinetic and thermodynamic transformation path characteristics for austenite decomposition above the upper Ae1 temperature – the temperature separating the two (γ + cem) and the three (γ + α + cem) phase fields – in an Fe-0.85C-11.56Mn (wt. %) alloy. The analysis concentrates on the temperature range from 700 to 650 $^{\circ}$C where decomposition includes two reactions, pearlite and cellular, both of which produce non-equilibrium products. The cellular reaction is previously unreported for this alloy. At 660 and 650 $^{\circ}$C, ferrite forms in association with cementite in a pearlite microstructure, however cases of mixed cellular-pearlite colonies are also reported. Although ferrite is not an equilibrium phase, excessive manganese depletion in the austenite caused by cementite formation moves small matrix regions into the (austenite + cementite + ferrite) three-phase field of the phase diagram which explains its formation. As cementite continues to form in the system, the carbon content and its activity in austenite decrease, which ultimately leads to ferrite dissolution because of the two phase's relative carbon chemical potential difference. Long isothermal heat treatments are used to document when and how the system eventually eliminates ferrite and the thermodynamic conditions associated with dissolution.

Quantitative progression of individual constituents (austenite, ferrite, and cementite) is followed at the selected temperatures using optical microscopy/SEM and quantitative energy dispersive (X-ray) spectroscopy employing mostly the SEM but also some TEM, during each evolution time step. Several data analytic techniques (active contours and k-clustering) are introduced to the field of materials science to increase the accuracy, remove any user bias, speed up the existing methods, and compliment data processing and analysis. Volume fraction and manganese content of individual phases over time ranges up to 180 days permit evaluation of the Gibbs free energy as the alloy approaches equilibrium. Additionally, carbon activity in the austenite matrix can be calculated and, in conjunction with manganese data, superimposed on ternary isotherm sections of the phase diagram. Thermodynamic computations utilize quantitative data with thermodynamic modeling software packages (MatCalc and Thermo-Calc) to provide a comprehensive explanation for ferrite formation and ultimate dissolution.

Table of Contents

Table of Contents

List of Figures

List of Figures

6

List of Figures

List of Tables

12

List of Tables

List of Tables

List of Symbols

a_C^{time}	Carbon activity in the austenite matrix at the time specified by the superscript
AC	Active contours, active contouring
Upper Ae1	In ternary Fe-C-M, the upper Ae1 is the temperature above which ferrite is thermodynamically prohibited
α	Ferrite, BCC solid solution phase
cem-c	Cellular cementite
cem-p	Pearlitic cementite
cem-gb	Grain boundary cementite
$D_{element}^{phase}$	Chemical diffusion coefficient of an element, indicated by the subscript, in a phase, indicated by the superscript
EDS	Energy-dispersive (X-ray) spectroscopy
Φ^{phase}	Volume fraction of the phase indicated by the superscript
GAC	Geometric active contour
GB	Grain boundary
γ^{form}	Austenite, FCC solid solution phase, where the form specified austenite type: depleted (d), retrenched (r) or bulk
LE-NP	Local Equilibrium – No Partition
LE-P	Local Equilibrium – Partition
$\lambda_{phase}^{reaction}$	Width of the phase, indicated by the subscript, produced by the reaction (pearlite or cellular), indicated by the superscript
OE	Orthoequilibrium
OM	Optical microscopy
PAC	Parametric active contour
PE	Paraequilibrium
ROI	Region of interest
RMSE	Root mean squared error
SEM	Scanning electron microscope
SNR	Signal to noise ratio

List of Symbols

TEM	Transmission electron microscope
TTT	Time-Temperature-Transformation
$U_{element}$	$\frac{X_{element}}{1-X_C}$, where $X_{element}$ is the mole fraction of the element in the alloy
$U_{element}^{phase}$	U-fraction of the element, indicated by the subscript, in the phase, indicated by the superscript

"To a worm in horseradish, the whole world is horseradish"

Yiddish Proverb

"The question, gentlemen, is not whether it should or shouldn't, but whether it does."

R. F. Mehl

Thesis Overview

The work reported in this dissertation is undertaken to gain a better insight into the initiation and progress of the metastable ferrite growth and evaluate the corrective mechanism utilized by the Fe-C-Mn alloy during its evolution towards thermodynamic equilibrium.

In Chapter 1, thermodynamic and kinetic aspects of the system are systematically developed to introduce the reader to the various nuances associated with Fe-C-Mn system. The concept of local equilibrium and its applicability for calculation of growth rates and some thermodynamic outcomes of phase transformations has permeated the literature of the last 60 years. As such, the starting point of the discussion is the Fe-C binary equilibrium phase diagram and how it is changed by the addition of manganese, a substitutional alloying element. The concepts of local (interphase) equilibrium and isoactivity will be introduced to provide a previously developed theoretical framework for the formation of pearlite above the Ae1. It is introduced as a starting point for the discussion but, experimentally, it proves futile for the current problem. Two austenite decomposition phase transformations, pearlite and cellular (discontinuous), and their variations are introduced as a prelude to the discussion on the kinetic evolution of the system.

Chapter 2 lists techniques used to observe and confirm, when necessary, the evolution of the Fe-0.85C-11.56Mn (wt. %) alloy at various temperature-time conditions. Many of the techniques listed are considered standard in the materials science community and, therefore, only those aspects that deviate from the norm are discussed in greater detail. Application of active contours to metallurgical microstructures, along with k-clustering and artificial neural networks, is part of a series of tools developed specifically to accommodate and accelerate analysis of microstructures in two and three dimensions. The discussion of active contours and k-clustering, which are used extensively in this work, is expanded to demonstrate the viability and usefulness of these techniques in this study. A publication on the application of neural networks to the field of metallurgy is available. [ontman2012] It was developed for this work to assist in completely 'hands- off' three-dimensional reconstruction of microstructures but, in the end, not applied because of a lack of time.

Chapter 3 tabulates the data obtained during the course of this research. Analytically, special attention is paid to the 650 °C and 700 °C temperatures for reasons which will become apparent in the subsequent chapters.

Chapter 4 discusses results from this study using neighborhood thermodynamics to explain experimental observations. This chapter uses MatCalc and Thermo-Calc software packages for thermodynamic modeling of the system and its evolution. While comments and discussion regarding the kinetics and thermodynamics of several microstructures are detailed, the scope of the discussion is focused on the growth and the dissolution of the metastable ferrite.

Finally, Chapter 5 sums up the discussion and provides general conclusions from this work. The relationship between global, neighborhood, and local thermodynamics is of particular interest since it helps explain the observed phenomena.

Chapter 1 – Introduction

1.1 Ternary Phase Equilibria in Fe-C-Mn

In Fe-C-Mn alloys, manganese is a substitutional alloying element with weak carbide forming, but potent carbide and austenite stabilizing characteristics. Similarly, carbon is an interstitial alloying element with austenite stabilizing ability. From a thermodynamic point of view, the effects of manganese and carbon on the Fe-C-Mn phase diagram are well established. In the binary Fe-C alloy, three-phase equilibrium, austenite (γ) + ferrite (α) + cementite (cem), occurs at a single temperature-composition point, the eutectoid point, as shown in Fig. 1.1. The addition of manganese lowers the temperature and opens up the three-phase field which is bounded by upper and lower Ae1 boundaries, Fig. 1.2a. The $\gamma/(\gamma + \alpha)$ phase boundary is also shifted to lower temperatures.[1]
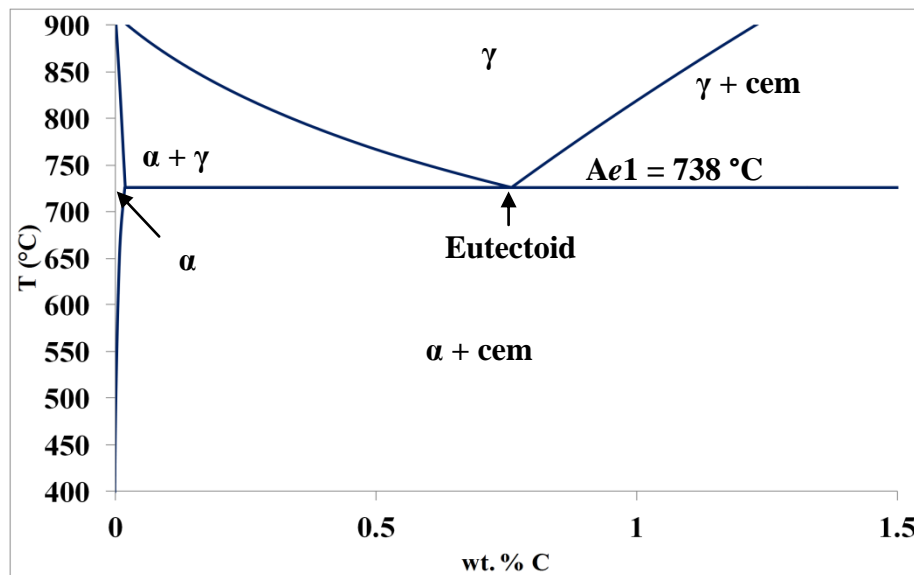
Figure 1.1: Section of the Fe-C phase diagram. The eutectoid point represents ($\gamma + \alpha + $ cem) three-phase equilibrium. Use of graphite or cementite as the reference phase in the construction of the phase diagram will vary the eutectoid temperature between 738 °C and 727 °C respectively.

---

[1] All experiments and calculations are at a constant pressure of 1atm.
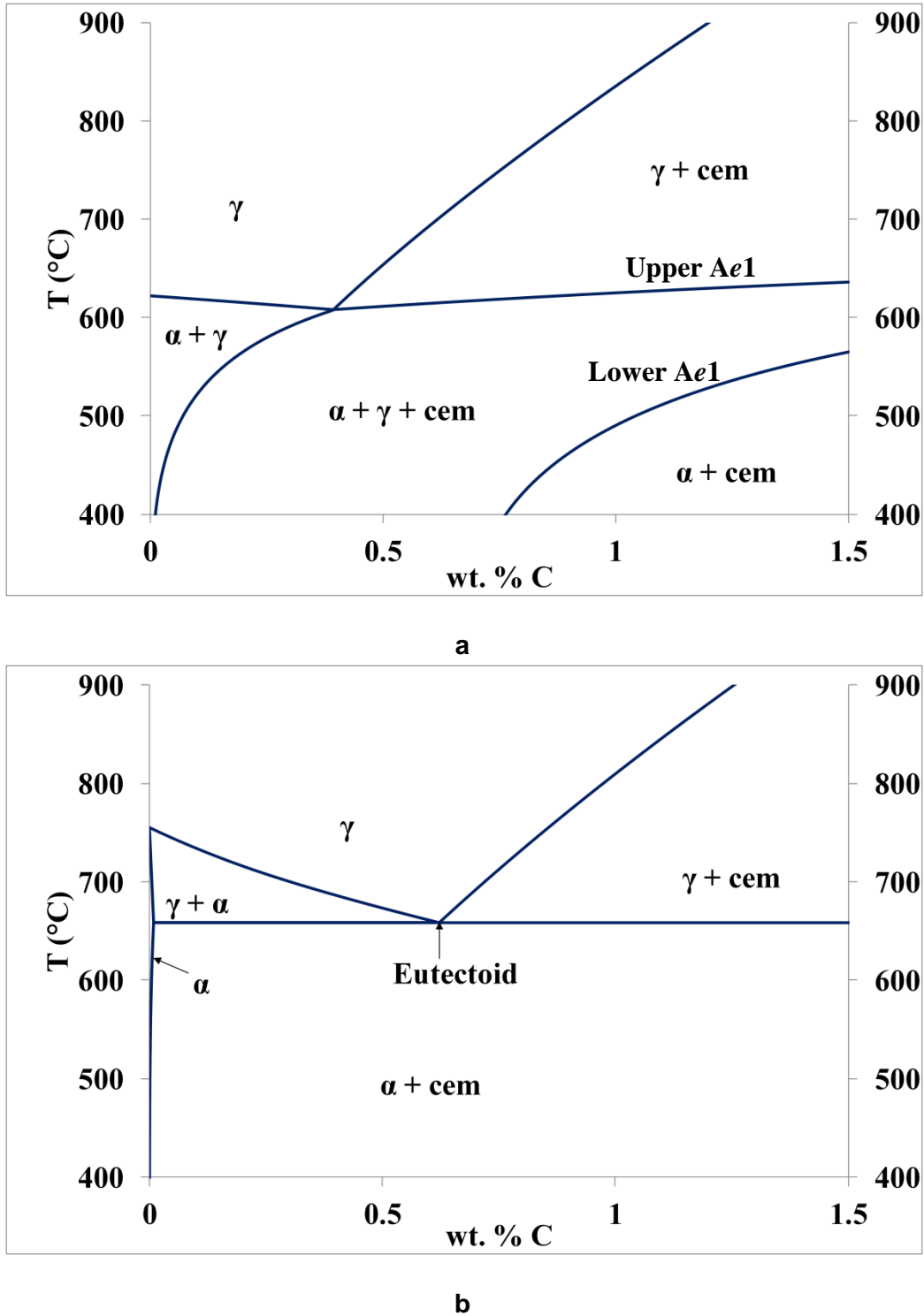
Figure 1.2: Section of the Fe-11.56Mn-C (wt. %) phase diagram. **(a)** Orthoequilibrium – full thermodynamic equilibrium. The three-phase field opens up from a point in the Fig. 1.1 to a (γ + α + cem) three-phase field. **(b)** Paraequilibrium – restricted thermodynamic equilibrium with partitioning of the interstitial element only. The paraequilibrium eutectoid point represents (γ + α + cem) three-phase equilibrium.

1.2 U-fraction

Figs. 1.1, 1.2a and b show phase diagram sections with the compositional variable expressed in carbon wt. %. Currently, a consistent and quantitatively accurate local measurement of carbon content is impossible by experimental limitations. It is therefore useful to employ a new variable: U-fraction, first defined by Kirkaldy in his initial paper on diffusion in multicomponent metallic systems.[2] [kirkaldy1957] Given $X_{Fe} + X_C + X_{Mn} = 1$, U-fraction of an element in the Fe-C-Mn alloy system is expressed as

$$U_i = \frac{X_i}{X_{Mn} + X_{Fe}} = \frac{X_i}{1 - X_C} \qquad (1.1)$$

where X represents the atomic fraction of the element specified by the subscript i (ex: $i=Fe, C, Mn$). From this point forward, unless specified otherwise, all compositional values (computed and experimentally acquired) will be discussed in terms of U-fraction values.

1.3 Ternary Kinetic Analysis

Bowman was the first to report proeutectoid ferrite inheriting the molybdenum content of the parent austenite. [bowman1946] Hultgren, in his detailed study of manganese and silicon steels, observed partitioning of the substitutional alloying elements in pearlite but not bainite [hultgren1947]. The prefix "ortho" (ex: orthoferrite, orthocementite) was introduced to describe transformation products formed with partitioning of the substitutional alloying element required by full equilibrium. The prefix "para" was introduced to describe transformation products (ex: paraferrite, paracementite) formed without partitioning of the substitutional alloying element.[3]

In the binary Fe-C system, following nucleation of ferrite or cementite, diffusion of carbon is considered to be the rate-determining step in the kinetics of austenite decomposition. An assumption is often made that the interphase boundary conditions for the resulting diffusion problem are tie-line compositions from stable or metastable equilibrium phase diagram.[4] This is known as the "local equilibrium" assumption and it leads to a conclusion that at any stage of diffusion-controlled transformation, an equilibrium condition between the parent and the product

---

[2] Experimentally, knowledge of carbon content is not necessary to compute U-fraction. When used in theoretical derivations, U-fraction reduces the number of variables and equations needed to represent a system. [kirkaldy1957]
[3] The term paraproducts (paracementite or paraferrite) are not always synonymous with paraequilibrium. Formation of paraproducts under orthoequilibrium conditions is discussed in the LE-NP section. See Table 1.1.
[4] During growth, conditions in the bulk alloy are different than those at the interface.

phases is maintained at the interphase interfaces (*local* equilibrium).[5] [zener1946, hillert1953, hillert1971]

Table 1.1: Thermodynamic models describing diffusional growth of ferrite into austenite and associated thermodynamic conditions in Fe-C-Mn alloys. Diffusion of carbon is required for all models. The "spike" is discussed in text.

Nomenclature	Interphase interface compositions	Diffusion of manganese	Interface thermodynamic criteria	Bulk thermodynamic criteria	Spike	Product
Local Equilibrium – Partitioning (LE-P)	Tie-line conditions at α/γ boundary	Yes	$\mu_C^\alpha = \mu_C^\gamma$ $\mu_{Mn}^\alpha = \mu_{Mn}^\gamma$	$\mu_C^\alpha > \mu_C^\gamma$ $\mu_{Mn}^\alpha > \mu_{Mn}^\gamma$	No	Orthoproduct (orthoferrite)
Local Equilibrium – No (negligible) Partitioning (LE-NP)	Tie-line conditions at α/γ boundary	No or negligible			Yes	Paraproduct (paraferrite)
Paraequilibrium (restricted local equilibrium)	$\frac{U_{Fe}}{U_{Mn}} = \frac{X_{Fe}}{X_{Mn}} =$ *constant in both phases across boundary*	No	$\mu_C^\alpha = \mu_C^\gamma$ $U_{Fe}^\alpha \mu_{Fe}^\alpha + U_{Mn}^\alpha \mu_{Mn}^\alpha = U_{Fe}^\gamma \mu_{Fe}^\gamma + U_{Mn}^\gamma \mu_{Mn}^\gamma$	$\mu_C^\alpha > \mu_C^\gamma$ $\mu_{Mn}^\alpha > \mu_{Mn}^\gamma$	No	Paraproduct (paraferrite)

In ternary alloys the difficulty of analyzing growth kinetics is compounded by the nature of the alloying elements (substitutional vs. interstitial) and their relative mobilities. The atomic mobility of these two solute elements differs greatly ($\frac{D_{Mn}^\gamma}{D_C^\gamma} \approx 10^{-6}$) in the temperature range of interest (585 °C-750 °C). Because of this 6 order of magnitude disparity, several decomposition schemas are kinetically feasible. The following sections demonstrate various growth modes of ferrite from austenite derived using kinetic limitations while assuming local equilibrium at the interphase interfaces for the Fe-C-Mn alloy. Similar reasoning yields permissible growth modes for cementite, which isn't explicitly developed here but is shown in the subsequent sections.

For an Fe-C-Mn alloy quenched into the ($\alpha + \gamma$) two-phase field from a one-phase austenite region the thermodynamic requirement for ferrite growth following the nucleation of ferrite is partitioning of carbon between austenite and ferrite. Partitioning of manganese is not always a thermodynamic requisite for ferrite growth. This results in two basic models describing

---

[5] The term "local equilibrium" describes equilibrium conditions at the interphase interfaces. The term "equilibrium" describes the global state of the system.

idealized (limiting) cases of diffusion-controlled growth of ferrite (and carbide) from austenite: orthoequilibrium (full local equilibrium) and paraequilibrium (*i.e.*, restricted local equilibrium, with respect to the substitutional alloying element as shown in Table 1.1). In all cases, local equilibrium for carbon at the moving interface and partitioning of carbon is always assumed. The differentiating aspect is the choice of the restrictions governing the behavior of the substitutional alloying element. [hillert1953, kirkaldy1958, coates1972, coates1973-1, coates1973-2]

1.3.1 Orthoequilibrium

Orthoequilibrium (OE) is a thermodynamic growth condition where equilibrium compositions exist at the γ/α interface for carbon and manganese. Under the assumption of OE, the ferrite and austenite interface compositions lie on the ends of an (α + γ) tie-line, which is not necessarily the equilibrium tie-line. Under these partitioning conditions, the slow diffusivity of manganese is the rate controlling step for growth of ferrite.[6]

It is thermodynamically possible to form a product phase with the same substitutional alloy content as the bulk (paraproduct) given OE conditions. This would require the growth of the product phase behind a "spike" of the substitutional alloying element in the parent phase at the interphase boundary. The conditions at the interface are now determined by the isoactivity of carbon whereby the product phase inherits manganese content (U_{Mn}) of the parent phase. This leads to a new local equilibrium tie-line that does not pass through the bulk composition. This is kinetically possible because there is a large disparity in diffusivities of carbon and manganese. Hillert referred to this condition as false paracondition or quasi-paraequilibrium. [hillert1953, hillert1998] Diffusion of carbon is assumed to be the rate-controlling step.

These scenarios divide an isothermal section of the Fe-C-Mn ternary diagram into two different growth regimes, both under OE conditions: Local Equilibrium – Partition and Local Equilibrium – No Partition. The boundary that divides the two regions is called "Zero Partition envelope". The isotherm in Fig. 1.3 illustrates the regions corresponding to the two growth modes for OE that are thermodynamically permissible as applied to the Fe-C-Mn alloy quenched into the (α + γ) two-phase field from a single-phase austenite region. The following gives a full thermodynamic description.

---

[6] The same growth restrictions can be reasoned for the γ/cem interface, especially in the case of pearlite because the two phases, cementite and ferrite, grow cooperatively.
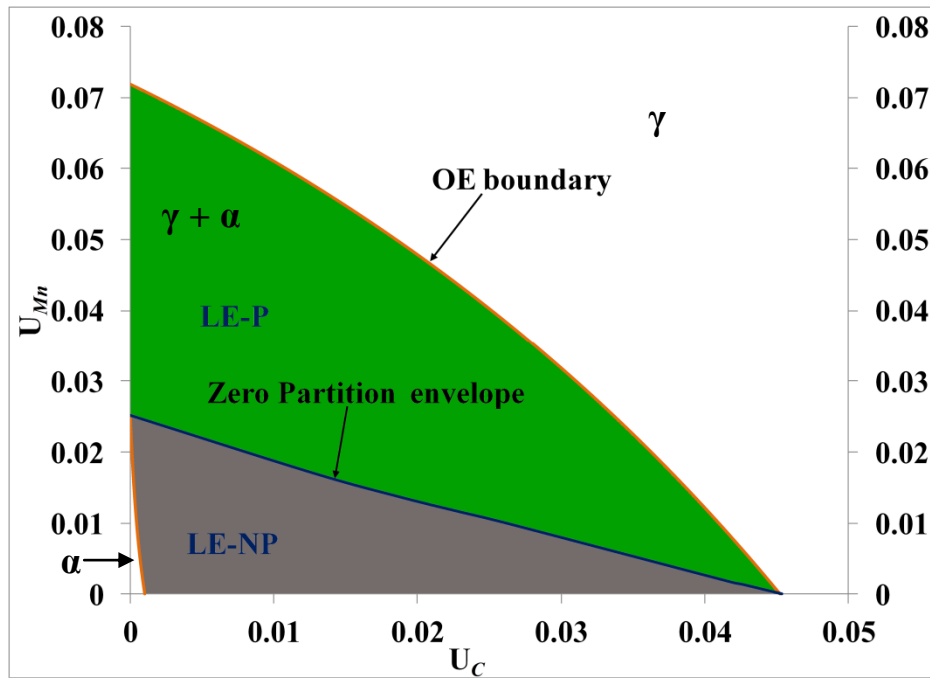
Figure 1.3: Isothemal section of Fe-C-Mn at 700 °C showing the (γ + α) two-phase field. Under OE, the region is divided into two growth modes LE-P (green) and LE-NP (gray). LE-P and LE-NP regions are divided by the "Zero Partition envelope".

1.3.1.1 Local Equilibrium – Partitioning (LE-P)

The LE-P region is characterized by slow manganese diffusion, and hence partitioning, during austenite decomposition. Local equilibrium conditions exist for both carbon and manganese at the γ/α interface (Fig. 1.4). The region of LE-P growth is highlighted in green in Fig. 1.3. For an alloy with bulk composition above the Zero Partition envelope, yellow circle in Fig. 1.4a, the equilibrium operative tie-line is represented by the light blue dashed line. Compositions at the interface are noted by the blue circle for the γ/(γ + α) and the orange circle at the α/(γ + α) and represent local equilibrium compositions for austenite and ferrite at the interphase interface, respectively. Concentration-penetration curves for manganese and carbon are shown in Figs. 1.4b and c. In this situation, for ferrite to grow, it is thermodynamically required for the manganese to partition away from the ferrite into the austenite. Similarly, carbon activity at the γ/α interface is different from carbon activity in the bulk, represented by the a_C^{bulk} line in Fig. 1.4a.

a

b

c
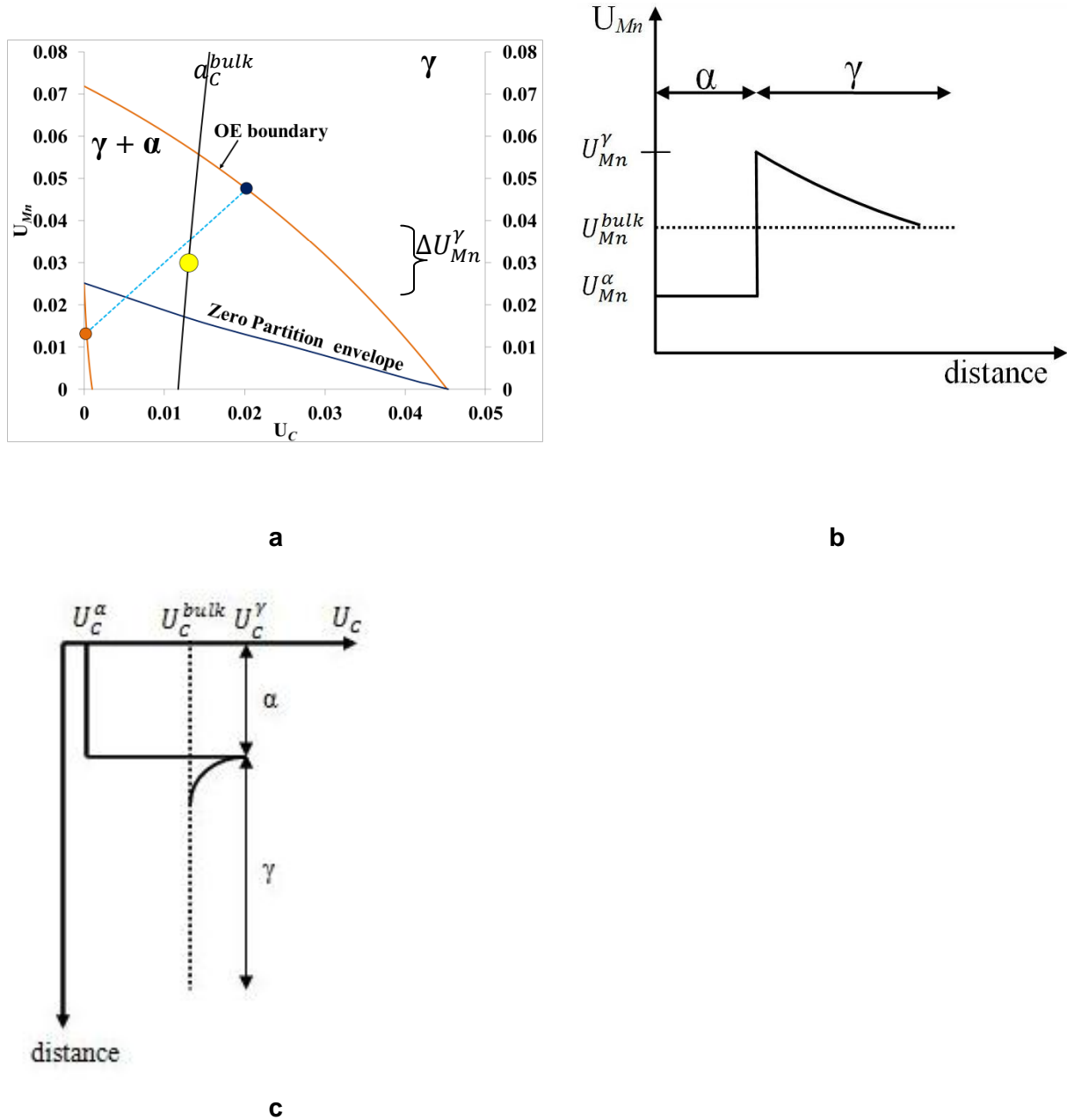
Figure 1.4: Isothemal section of Fe-C-Mn at 700 °C showing the (γ + α) a two-phase field. **(a)** Construction of the LE-P conditions at the γ/α interface. **(b)** Concentration-penetration profile for manganese. **(c)** Concentration-penetration profile for carbon.

However, diffusion of the substitutional alloying element away from the ferrite into the austenite is orders of magnitude slower than diffusion of carbon and, therefore, is the rate-controlling step. Consequently, growth of ferrite is proportional to the difference between the manganese content of the bulk alloy (U_{Mn}^{bulk}) and the manganese content of the growing ferrite (U_{Mn}^{α}), ΔU_{Mn}^{γ} in Fig.

1.4a. During the redistribution of the substitutional alloying element, there is sufficient time for carbon to react and maintain a uniform activity (isoactivity) in the austenite resulting in a concomitant and nearly instantaneous carbon activity readjustment (shifting the a_C^{bulk} to the right) in austenite during ferrite growth.

1.3.1.2 Local Equilibrium – No Partitioning (LE-NP)

LE-NP ferrite growth is a characterized by no partitioning of manganese. Compared to LE-P, growth is now governed by carbon diffusion, making it the rate-limiting step. However, local equilibrium conditions still exist for both carbon and manganese at the γ/α interface. The region of LE-NP growth is highlighted in gray in Fig. 1.3.

Figure 1.5a shows the precipitation of ferrite from austenite in an alloy where the bulk alloy composition, indicated by the yellow circle, is below the Zero Partition envelope. The activity of carbon in the austenite far from the interface is represented by the carbon isoactivity line a_C^{bulk} which passes through bulk alloy composition marked by the yellow circle. Manganese content of the bulk alloy is denoted by the horizontal line X_1. Under this construction, the ferrite in the α/(γ + α) interface inherits the bulk composition of the substitutional element content, orange circle at the end of the green tie-line in Fig. 1.5a. With formation of ferrite, the green component ray no longer represents local equilibrium conditions because the activity of carbon at the ends of the green tie-line is not the same. To satisfy the activity criteria required by local equilibrium, *viz.* $a_{C,Mn}^{\gamma} = a_{C,Mn}^{\alpha}$ at the γ/α interface, the operative tie-line becomes the dashed blue line. Given these conditions at the ferrite interphase interface, the conditions at the austenite interphase interface are obtained from the other end of the operative tie-line (blue circle). Note that the bulk alloy composition does not lie on this tie-line. Concentration-penetration curves for manganese and carbon are shown in Figs. 1.5b and c respectively. The activity of carbon in the austenite at the γ/α interface is described by the carbon isoactivity line $a_C^{critical}$ which passes through the point marked with the blue circle in Fig. 1.5a.
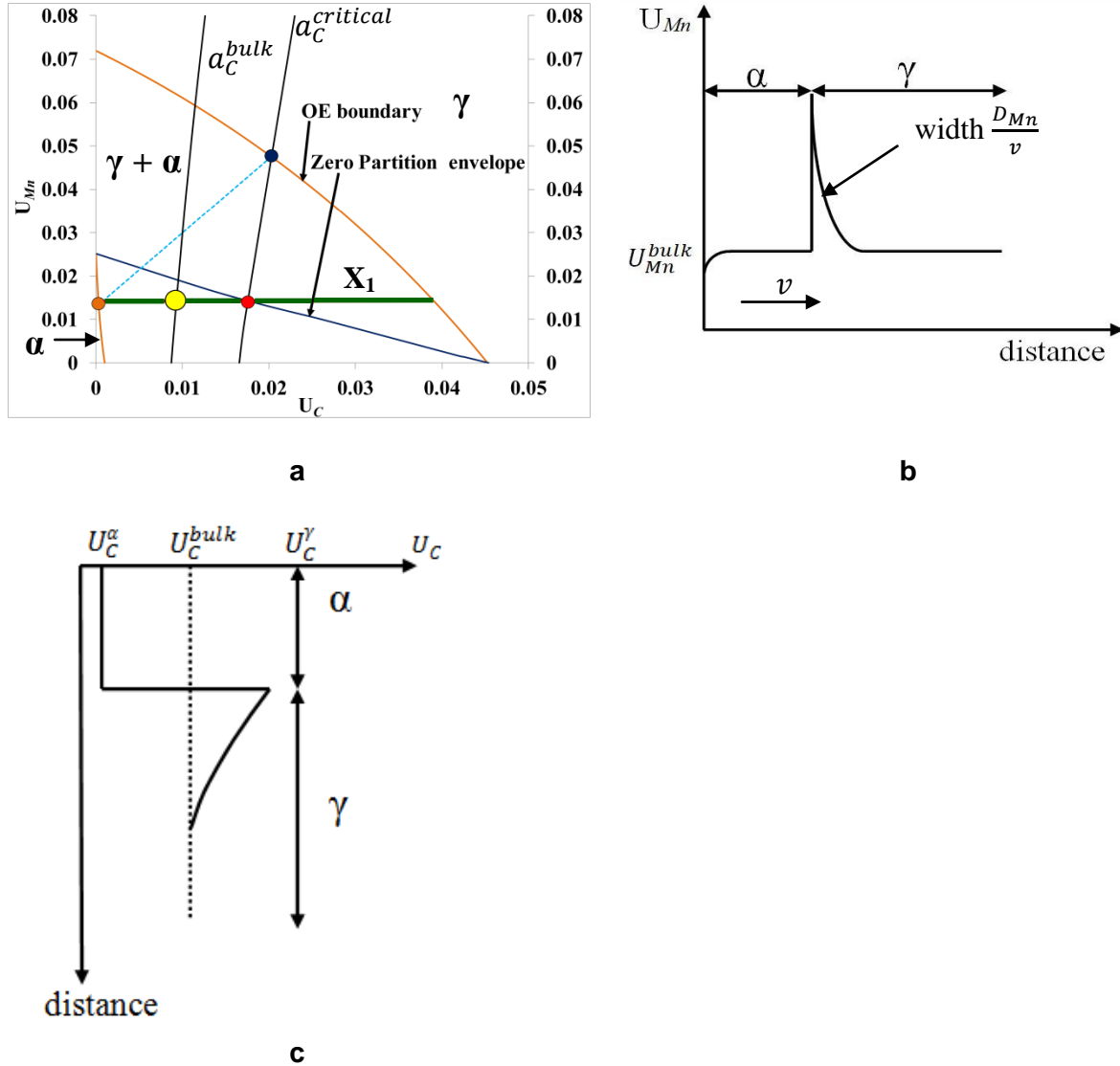
Figure 1.5: Isothermal section at 700 °C in the Fe-C-Mn showing the (γ + α) two-phase field. **(a)** Construction of the LE-NP conditions at the γ/α interface. **(b)** Concentration-penetration profile for manganese. **(c)** Concentration-penetration profile for carbon.

Ferrite growth requires carbon partitioning which in turn requires an activity gradient (driving force) for carbon to diffuse away from the γ/α interface into the austenite. For a carbon activity gradient to exist, carbon isoactivity in the bulk alloy must lie to the left of the point marked by the red circle, which lies on the critical carbon isoactivity line. The driving force for carbon diffusion, and subsequently the reaction, is the difference between the activity of carbon at the interface ($a_C^{critical}$) and that in the bulk austenite (a_C^{bulk}), Δa_c. The substitutional element is

assumed to play no role in the transformation except to accommodate all necessary structural changes.

The critical point (red circle) will adjust as bulk alloys with different compositions are examined, resulting in a line which represents the Zero Partition envelope. For alloy compositions below the Zero-Partition envelope it is thermodynamically *possible, but not necessary,* to form ferrite without partitioning of the substitutional alloying element.

The mathematical consequence of the local equilibrium treatment of LE-NP is the existence of a thin "spike" of the substitutional element in the austenite just ahead of the growing ferrite, depicted in Fig. 1.5b.[7] The width of the spike is approximated by $\frac{D_{Mn}}{v}$ where D_{Mn} is the diffusion of the substitutional alloying element in austenite and v is the velocity of the γ/α interface. The spike can be positive or negative. In most instances of Fe-C-Mn alloys the width of the spike is estimated to be less than atomic dimension of the atoms involved and has yet to be directly observed experimentally.

1.3.2 Paraequilibrium

Hultgren was the first to qualitatively extend the idea of local equilibrium at the interfaces in binary Fe-C to include a substitutional alloying element.[8] He postulated that paraproducts form under a *restricted* local equilibrium, where restricted means a constant ratio of iron to substitutional alloying element, at the interface which he termed "paraequilibrium" (PE). PE is characterized by the same *carbon activity* in the two phases at the interface and the same *content* of the substitutional alloying element with respect to iron, $\frac{U_{Mn}}{U_{Fe}} = constant$. The region of PE is highlighted in gray in Fig. 1.6. PE boundaries must necessarily fall inside the orthoequilibrium (LE-P) boundaries of the two-phase field. [hultgren1951, hillert1952] Compositions at the interface for ferrite and austenite under PE conditions can be obtained using PE tie-lines, horizontal orange lines in Fig. 1.6. The tie-lines are not horizontal, but nearly so, which is a consequence of the $\frac{U_{Mn}}{U_{Fe}} = constant$ restriction. For ferrite to grow, partitioning of

---

[7] In the literature Local Equilibrium-No Partitioning mode is sometimes called Local Equilibrium – Negligible Partitioning. This is so because the pile-up formation requires at least some (however negligible) amount of manganese partitioning

[8] Hultgren suggested the idea of local equilibrium at the interface for C during formation of pearlite in Fe-C alloys. [hultgren1920] Zener was the first to present a comprehensive analysis of local equilibrium for Fe-C. [zener1946]

manganese is not required. No spike of manganese ahead of the growing interphase boundary in the austenite is required. Diffusion of carbon is considered the rate-controlling step.
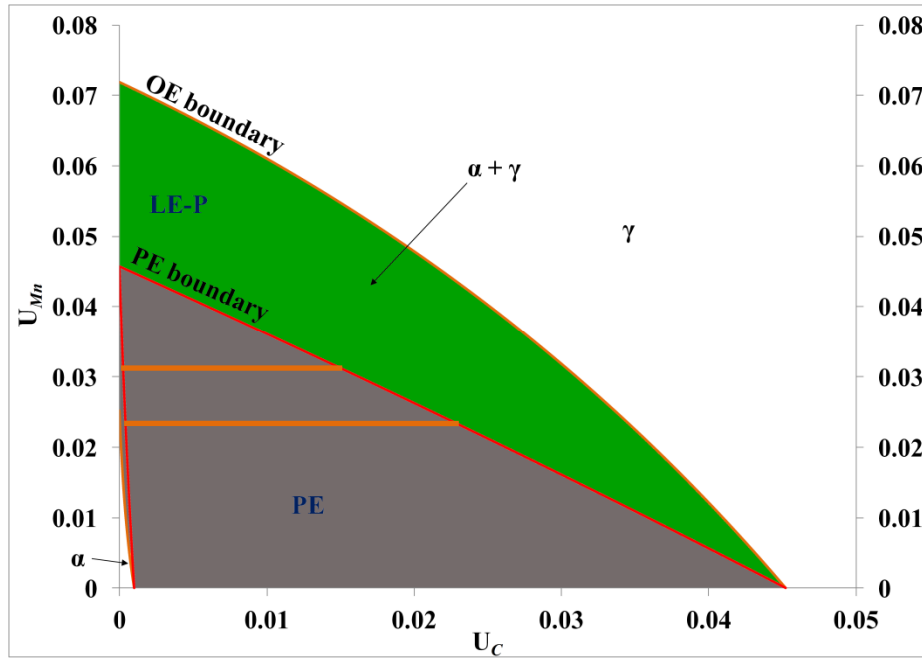
Figure 1.6: Isothermal section at 700 °C of the Fe-C-Mn showing the (γ + α) two-phase field. Red line outlines critical limit for formatiof ferrite under paraequilibrium conditions.

The isotherm in Fig. 1.7 shows the regions corresponding with various growth modes that are thermodynamically feasible for a Fe-C-Mn alloy quenched into the (γ + α) two-phase field from a single phase austenite region. In the region between the PE and OE boundaries, partitioning of manganese is thermodynamically necessary for ferrite to grow (LE-P regime). Between the PE and Zero Partition envelope boundaries the growth of ferrite can proceed without partitioning of manganese. Below the Zero Partition envelope, ferrite can grow under either PE or LE-NP conditions. Since the Zero Partition envelope segregates regions of the (γ + α) two-phase field based on the partitioning requirement, it is referred to as a partition/no partition boundary (P/NP boundary).
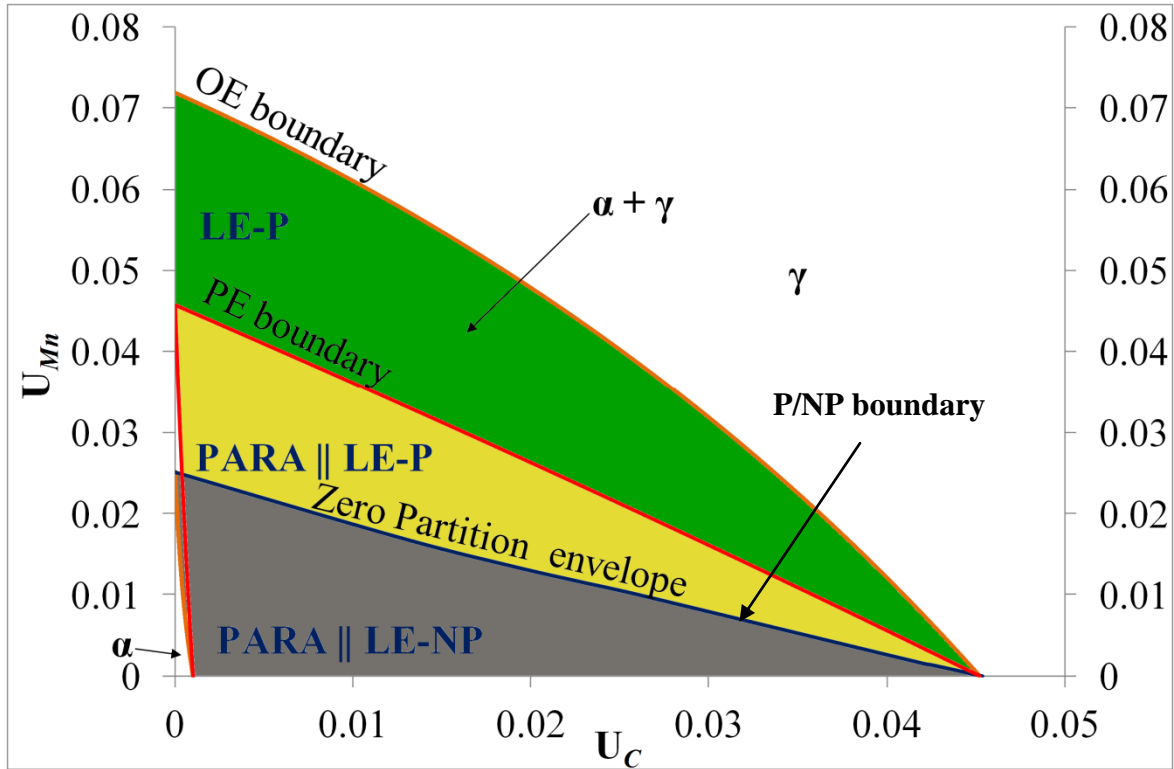
Figure 1.7: Isothemal section at 700 °C in the Fe-C-Mn summarizing thermodynamically permissible modes of growth for ferrite in the (γ + α) two-phase field.

1.4 Phase transformations

The reactions discussed in this section are all those occurring at a moving interface resulting in a two-phase lamellar product. The moving interface may be an interphase boundary (eutectoid decomposition), or it may be a matrix grain boundary (cellular decomposition).

1.4.1 Pearlite Reaction

The scope of this work requires a brief introduction to several pearlite associated reactions: pearlite growth, pearlite dissolution, and cementite coarsening. A mélange of alloy and temperature specific models for nucleation, growth kinetics, and product morphology of pearlite is readily available in the literature. Most are developed *post factum* and sometimes include phenomenological constants. A comprehensive introduction on various facets of the pearlite reaction can be found in the works by Ridley and Pandit. [ridley1984, pandit2011]

1.4.1.1 Pearlite Growth

      Pearlite growth results from cooling though the eutectoid whereby supersaturated austenite decomposes into ferrite and cementite. The reaction is described by Eqn. 1.2a.

$$\gamma \rightarrow cem + \alpha$$

                                                  (1.2a)

Pearlite consists of alternate lamellae of ferrite and cementite growing synchronously and cooperatively into the austenite phase. Pearlite mostly nucleates on austenite grain boundaries, as illustrated in Figs. 1.8a and b, and can be initiated by ferrite or cementite nucleation, subject to the composition of the bulk alloy. The nucleation rate of pearlite increases with the undercooling temperature. Interlamellar spacing decreases with lower temperature. If the requirement of synchronous and cooperative growth is not met, the pearlite is termed a "degenerate pearlite" or simply non-lamellar pearlite.

      As previously discussed, pearlite can be differentiated on the basis of partitioning behavior with the terms "orthopearlite" and "parapearlite" designating products formed under partitioning and no partitioning conditions respectively.[hultgren1947]

      Pearlite is usually assumed to grow with constant interlamellar spacing and growth rate, Figs. 1.8b and c. In 1962, Cahn and Hagel showed a pearlite nodule with divergent lamellae and decreasing growth rate, thus contradicting this conventional wisdom. Their results further subdivided the classification scheme of pearlite. Pearlite growing with constant interlamellar spacing and growth rate under conditions of LE-P was termed "constant orthopearlite". Pearlite growing with non-constant spacing or growth rate under conditions of LE-P was termed "divergent orthopearlite". [cahn1962]
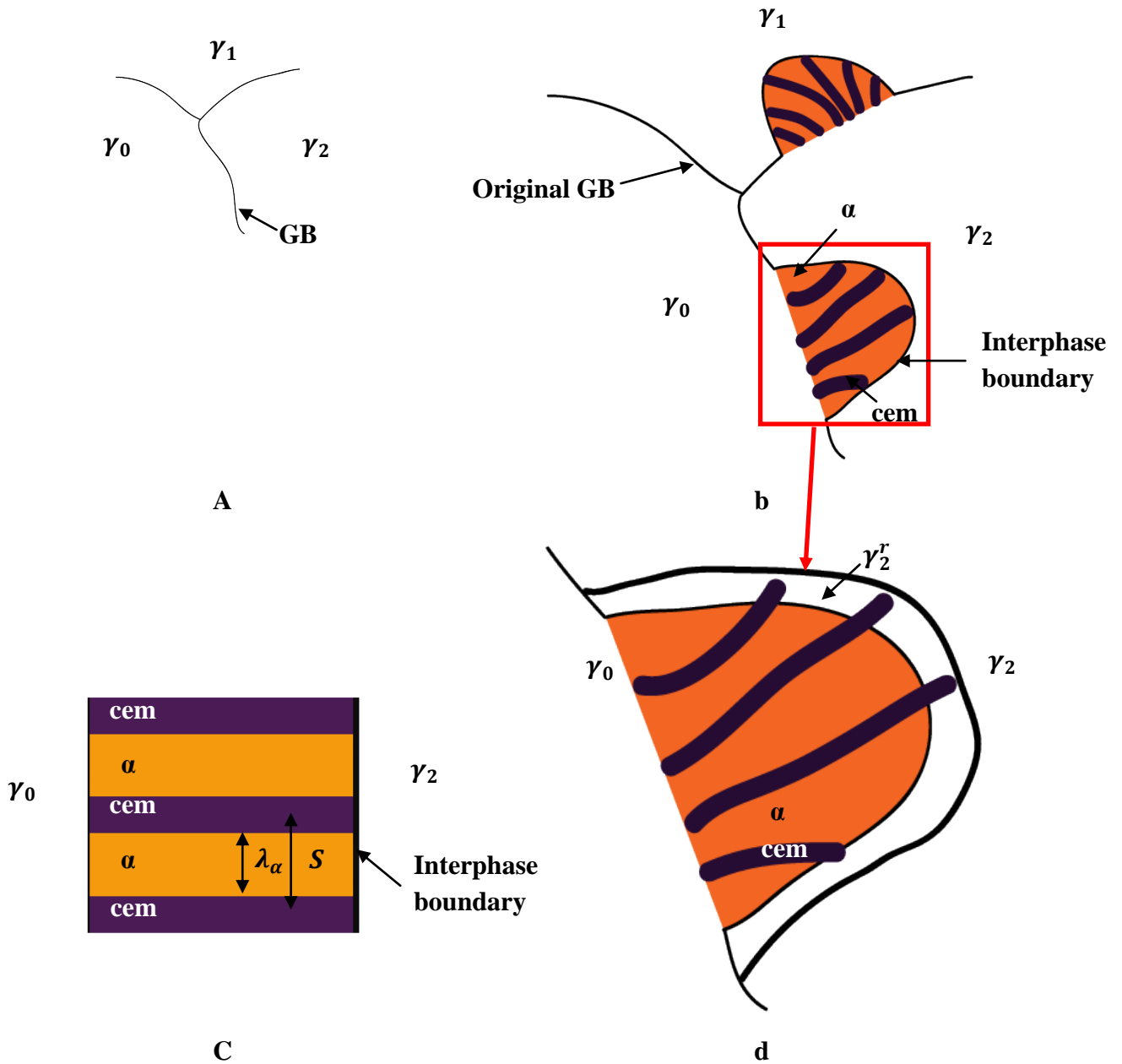
Figure 1.8: Schematic representations of various stages of divergent pearlite growth and dissolution **(a)** The grains of austenite, separated by grain boundaries (GB) prior to nucleation and growth of pearlite. Relative orientation relationship of the austenite grains is noted by the subscript. **(b)** Pearlite colonies. Pearlite consists of alternate lamellae of ferrite (α-orange) and cementite (cem-purple) growing synchronously and cooperatively into the austenite phase. **(c)** Lamellar two-phase microstructure (α + cem) in the austenite matrix. λ represents thickness of the constituent indicated by the subscript. S represents interlamellar spacing. **(d)** Dissolution of pearlite. The austenite grain into which pearlite previously grew is reclaiming the areas previously occupied by ferrite. This process is usually accompanied by coarsening of cementite.

1.4.1.2 Constant and Divergent Pearlite

A pearlite nodule with increasing interlamellar spacing and decreasing growth rate was first reported by Cahn and Hagel in Fe-1C-5Mn (wt. %) alloy isothermally heat treated at 680 °C. [cahn1962] Similar phenomena were later observed in high chromium and hypereutectoid silicon steels. [mannerkoski1964, fridberg1970] Cahn and Hagel reasoned that constant growth rate is not a requirement for the formation of pearlite in certain ternary alloys above the lower Ae1 temperature. If pearlite grows with higher or lower content of the alloying elements (carbon or manganese), austenite composition will change from the original bulk alloy composition until equilibrium is reached. This compositional variation of austenite was presumed to account for the non-constant interlamellar spacing and growth rate of pearlite. In the subsequent work Cahn and Hagel confirmed that it is possible to form similar non-constant pearlite both above and below the lower Ae1. [cahn1963] It was further concluded that carbon, the fast diffusing interstitial element, and not the manganese caused the observed phenomena.

Hillert provided a qualitative explanation for the observation using schematic phase diagrams coupled with the ideas of local equilibrium and isoactivity lines shown in Figs. 1.9a-h. Using these principles, Hillert provided several *possible* mechanisms for growth of pearlite. The reasoning for these constructions was to identify permissible thermodynamic *limits* with an attempt to predict morphology and chemistry of the product phases. Some of these models and predictions based on these models are now presented, however none of the outcomes prove applicable to our current work.[hillert1982]

Fig. 1.9a shows and an isotherm of Fe-C-Mn at 700 °C with metastable phase boundaries drawn as dashed lines. Using the concepts developed in the earlier sections, P/NP boundaries are added and shown in dash-dot-dot lines in Fig. 1.9b.

Consider an alloy with bulk composition indicated by the yellow circle in Fig. 1.9c. The composition falls within the (γ + α + cem) three-phase field and it is bounded by the extrapolated γ/(γ + α) and γ/(γ + cem) metastable phase boundaries. The composition lies above the P/NP boundaries (above the γ/α and to the left of γ/cem) for both ferrite and cementite and the pearlite is expected to form under partitioning conditions. At equilibrium, the compositions of the three phases are found from the corners of the three-phase field (tie-triangle). Since pearlite forms under partitioning conditions (LE-P) it is reasonable to expect that while the manganese partitioning is occurring, all carbon activity gradients in austenite in the vicinity of the interface

are removed (not at the interphase). As result, the conditions in the austenite in the vicinity of the γ/pearlite interface can be described by an isoactivity line for carbon in the austenite. This scenario is similar to the one described in Fig. 1.4a where carbon activity is adjusts immediately in response to the diffusion of manganese until full equilibrium is reached. At the earliest stages of transformation, after cooperative growth has been established, the isoactivity line for carbon in the austenite will be the one that passes through the bulk alloy composition (yellow circle); a_C^{bulk} in Figs. 1.9d and e. Fig. 1.9e correlates to the black rectangle in the Fig. 1.9d. The minimum permissible composition in austenite at the γ/α interphase is represented as the points of intersection of the carbon isoactivity line in the bulk alloy (a_C^{bulk}) and the extrapolated γ/(γ + α) boundary as shown in Fig. 1.9d and highlighted by the orange circle in Fig. 1.9e. As a consequence of the assumption of local equilibrium, the resulting tie-line from the ferrite phase boundary to the extrapolated γ/(γ + α) boundary represents the operative (γ + α) tie-line, shown in blue in Figs. 1.9d and e. Similarly, conditions in the austenite at the γ/cem interface are represented by the intersection of a_C^{bulk} and the extrapolated γ/(γ + cem) phase boundary, purple circle in Fig. 1.9e. Under assumptions of LE-P, carbon activity of cementite and austenite at the γ/cem interface must be equal and interphase interface compositions are, therefore, represented by the operative (γ + cem) tie-line, shown in blue in Figs. 1.9d and e. In both cases, the new operative tie-lines represent the lowest permissible compositional limits. For growth to occur carbon and manganese composition of each phase must be between composition at equilibrium and this limit.

If the resulting microstructure is pearlite the difference between the manganese content in austenite in front of the ferrite and that in front of the cementite (orange and purple circles respectively) growth front drives the lateral diffusion of manganese from ferrite to cementite, accomplishing the necessary partitioning. This difference in manganese content is a measure of the driving force for pearlite growth under these conditions.

The pearlite that forms will possess higher carbon content than the original bulk alloy and therefore long range volume diffusion of carbon from the austenite matrix will accompany growth. As the carbon content in the matrix falls, the carbon isoactivity line describing the conditions at the interface will shift further left to some intermediate value, a_C^{int} line in Fig. 1.9f, with an accompanying change at the interfacial conditions to satisfy local equilibrium. These interfacial conditions will trace the metastable γ/(γ + α) and γ/(γ + cem) phase boundaries in the

directions of the arrows, as shown in Fig. 1.9f, until the carbon activity reaches that which passes through the austenite corner of the three-phase field, a_C^{eq}, which represents equilibrium. The reaction then stops. Note that as the carbon activity decreases the interfacial manganese content in austenite in front of the ferrite and cementite continuously increases, but the difference between the two progressively decreases. This is shown in Fig 1.9f by the decreasing difference in manganese content of the light orange and light purple circles. Decrease in growth rate occurs because of its direct dependence on the manganese gradient. Hillert reasoned that these conditions are the reason for divergent pearlite.

Consider an alloy with bulk composition indicated by the yellow circle in Fig. 1.9g. The composition lies above the P/NP boundaries for both ferrite and cementite and the pearlite is expected to form under partitioning conditions. The bulk alloy composition falls on the same isoactivity line drawn in Fig. 1.9e but within the (α + cem) two-phase field. The operative tie-lines are the same as those in Figs. 1.9d and e. However, for the transformation in the two-phase field, equilibrium consists of ferrite and cementite only. There will be no austenite present at equilibrium. The pearlite forms with the same average alloy content (carbon and manganese) as the bulk alloy. No long range diffusion of carbon from the bulk to the growing pearlite is necessary. Therefore, shifting of the carbon isoactivity line describing the condition in the austenite at the interface does not occur. The driving force acting on the interface is proportional to $U_{Mn,\gamma}^{\gamma/\alpha} - U_{Mn,\gamma}^{\gamma/cem}$ and is constant. It is the same as the driving force at the earliest stages of formation for the bulk alloy content described in the three-phase field (Fig. 1.9e). The pearlite formed from the bulk alloy content shown in Fig. 1.9f is expected to grow with constant interlamellar spacing and growth rate.

Using the same strategy, Hillert divided the isotherm into several regions based on the bulk alloy composition. This is shown in the Fig. 1.9h. If the bulk alloy composition is located in the region highlighted by the orange triangle, constant orthopearlite is expected to grow behind the carbon-enriched zone. Hutchinson suggested that carbon-enriched zone ahead of the growing pearlite thermodynamically permits reduction in the lamellae size or what has been termed "convergent orthopearlite". This type of behavior has not been reported. [hutchinson2004] If the bulk alloy composition is located in the region highlighted by the blue triangle, constant orthopearlite is expected to grow behind the carbon-depleted zone. If the bulk alloy composition is located in the region highlighted by the green triangle, only divergent orthopearlite can form.

Using definitions of paraequilibrium and LE-NP the triangle formed by the intersection of ferrite and cementite P/NP boundaries with the U_C axis (gray region in Fig. 1.9h) is the region where formation of parapearlite is thermodynamically permissible.
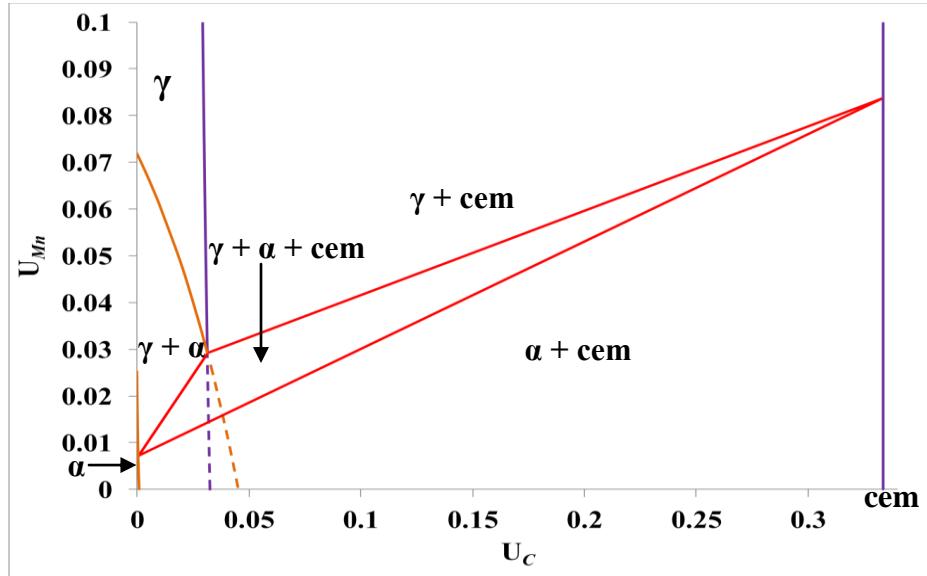
Figure. 1.9 (a) Isothermal section of the Fe-C-Mn system at 700 °C. Dashed lines are metastable extensions of the γ/(γ + cem) and γ/(γ + α) two-phase boundaries. The red lines bind the (γ + α + cem) three-phase tie-triangle.
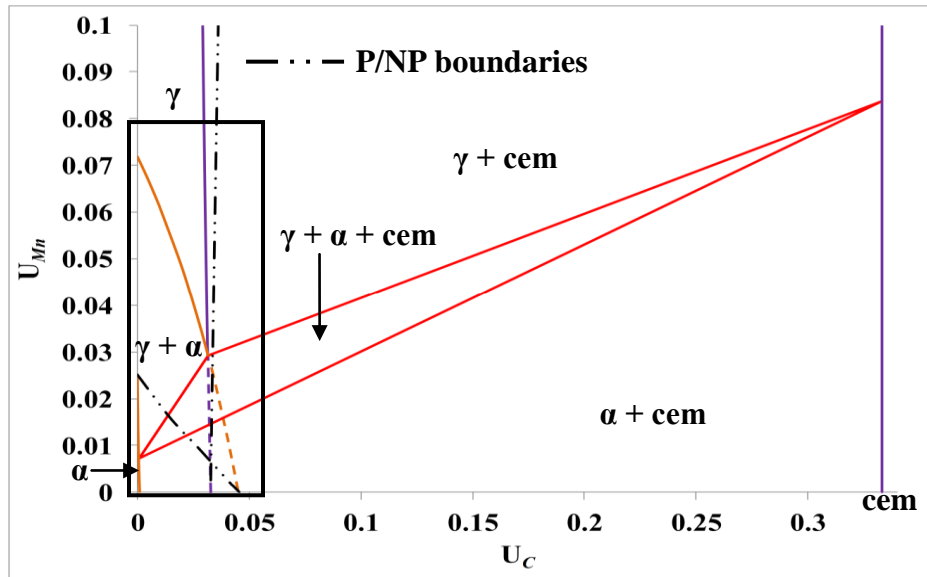
Figure. 1.9 (b) Same as **(a)** with P/NP boundaries drawn using dash-dot-dot lines. The black rectangle is discussed in the next figure.
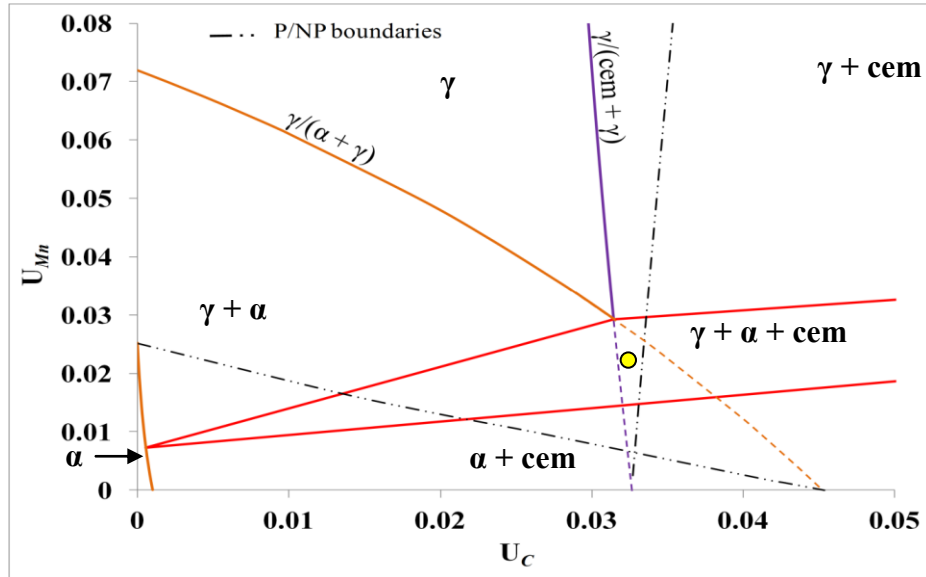
Figure. 1.9 (c) Magnified section of the isotherm correlated to black rectangle in **(b)** with an alloy with composition indicated by the yellow circle is selected. The alloy falls within the (γ + α + cem) equilibrium three-phase field and is bounded by the γ/(γ + cem) and γ/(γ + α) two-phase metastable boundaries The alloy composition lies above the P/NP boundaries for both ferrite and cementite.
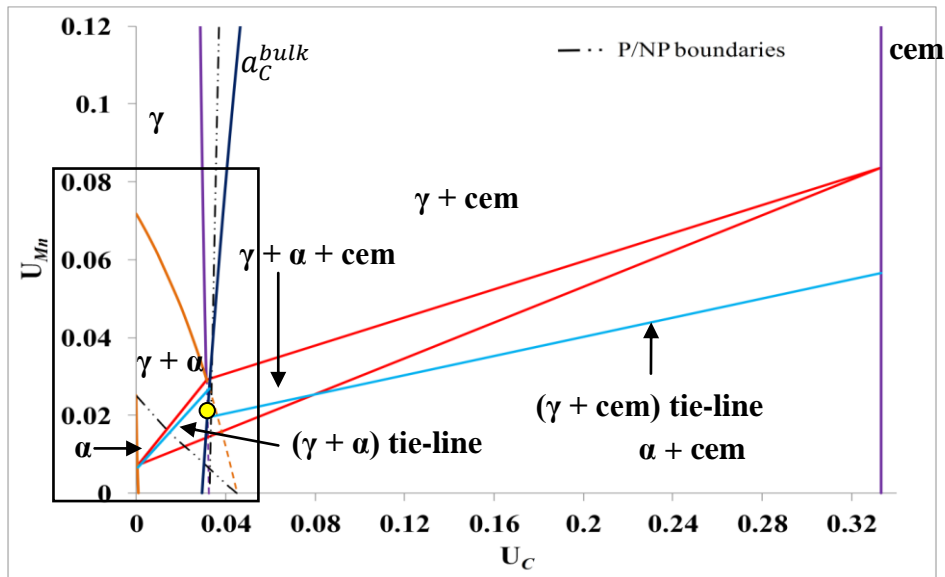
Figure. 1.9 (d) Same as **(b)** with the carbon isoactivity line passing through bulk alloy (shown in **(c)**) resulting in (γ + cem) and (γ + α) operative tie-lines shown in light blue. The black rectangle is discussed in the next figure.
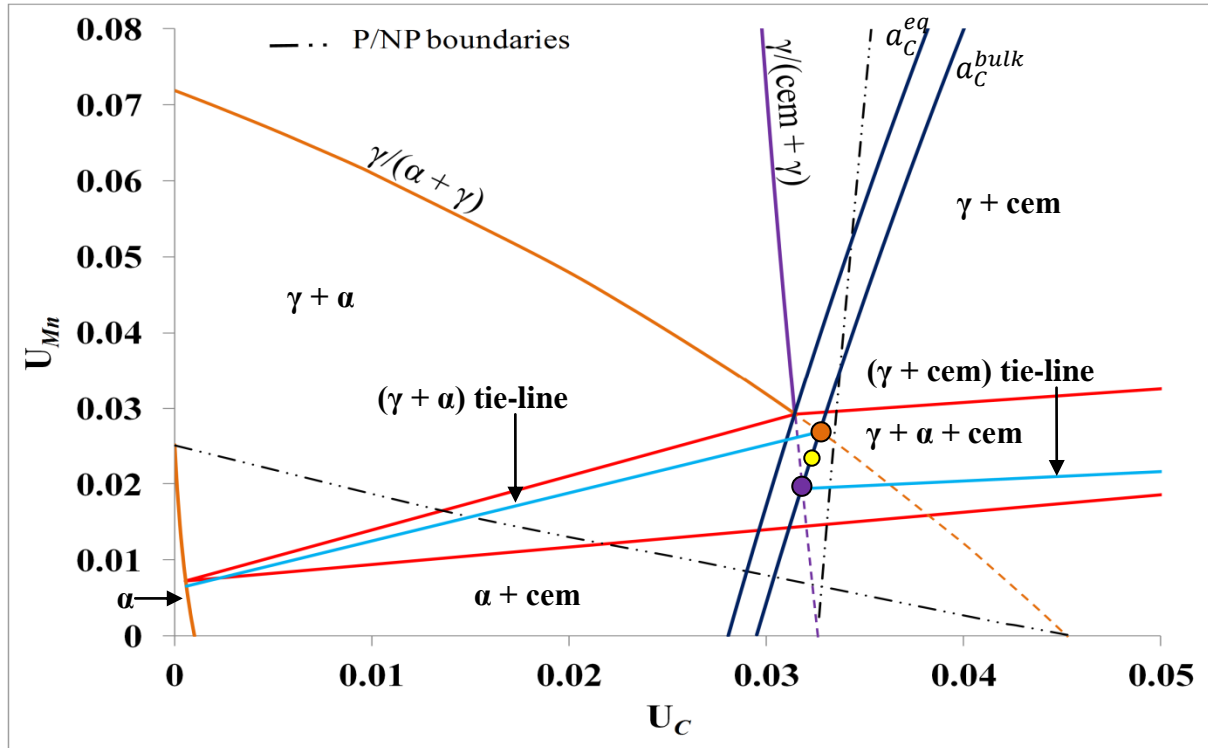
Figure. 1.9 (e) Magnified section of the diagram correlated to the black rectangle in **(d)**. Orange circle represents the composition in austenite immediately in front of the advancing ferrite. Purple circle, likewise, represents the composition of austenite ahead of the cementite.
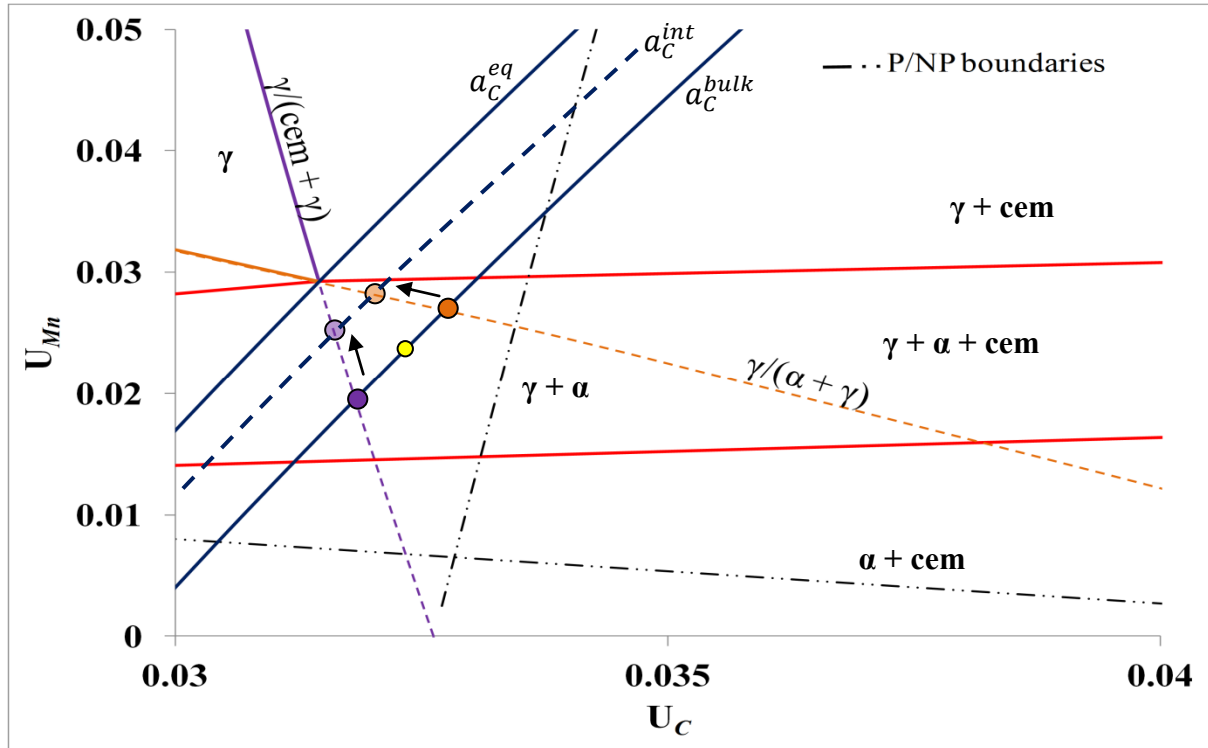
Figure. 1.9 (f) As the carbon content in the matrix falls, the carbon isoactivity line a_C^{bulk} describing the conditions at the interface will shift further left to some intermediate value shown by the a_C^{int} isoactivity line. There will be an accompanying compositional change for the interfacial conditions to satisfy local equilibrium. New interphase interface conditions are shown by light orange and light purple circles. These changes will trace the metastable phase boundaries in the directions of the arrows until carbon activity reaches the line a_C^{eq}. At that point the reaction stops. Note that as the carbon activity decreases the interfacial manganese content in the austenite in front of the ferrite and cementite continuously decreases but the difference between the two progressively decreases. Under these conditions pearlite is expected to grow with changing interlamellar spacing and decreasing growth rate.
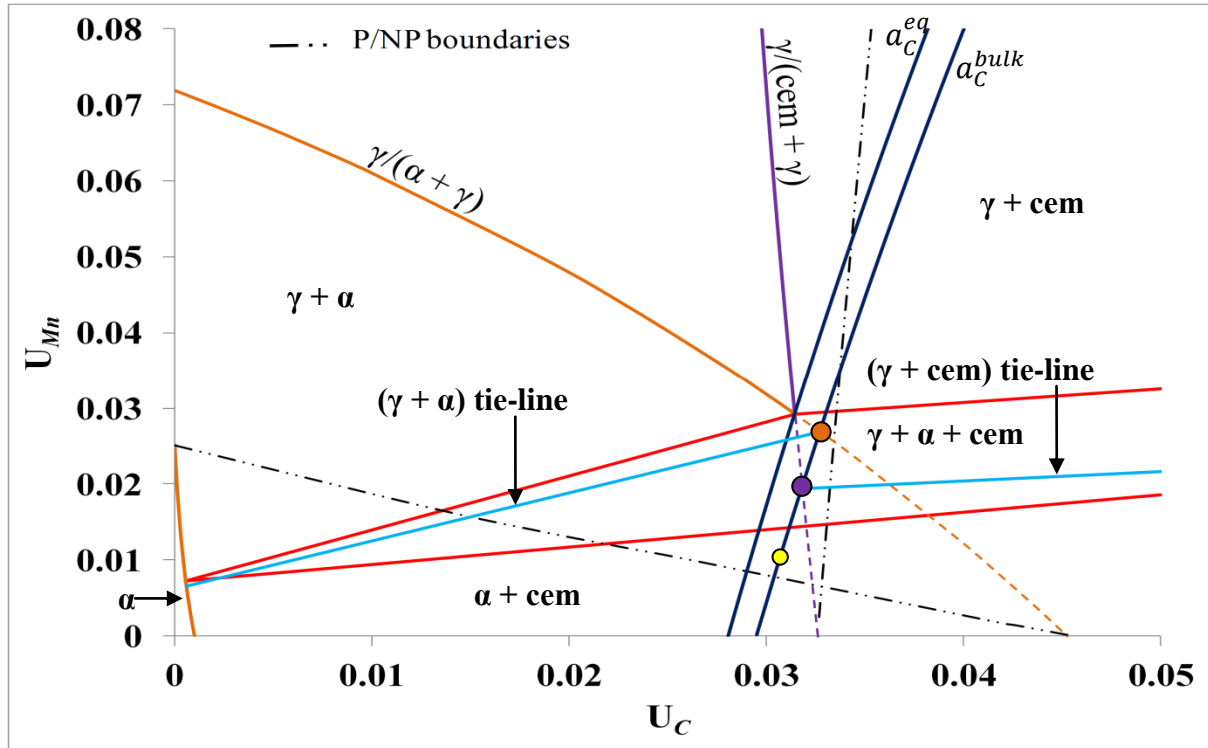
Figure. 1.9 (g) An alloy with composition indicated by the yellow circle is selected. The alloy falls within the (α + cem) two-phase field. The operative tie-lines are the same as those described in **(d)** and **(e)**, however, the pearlite will form with the average alloy content as the bulk. As a result, there will be no shift of the isoactivity line and consequently no change in the compositions at the interphase interface. Pearlite is expected to grow with constant interlamellar spacing and growth rate.
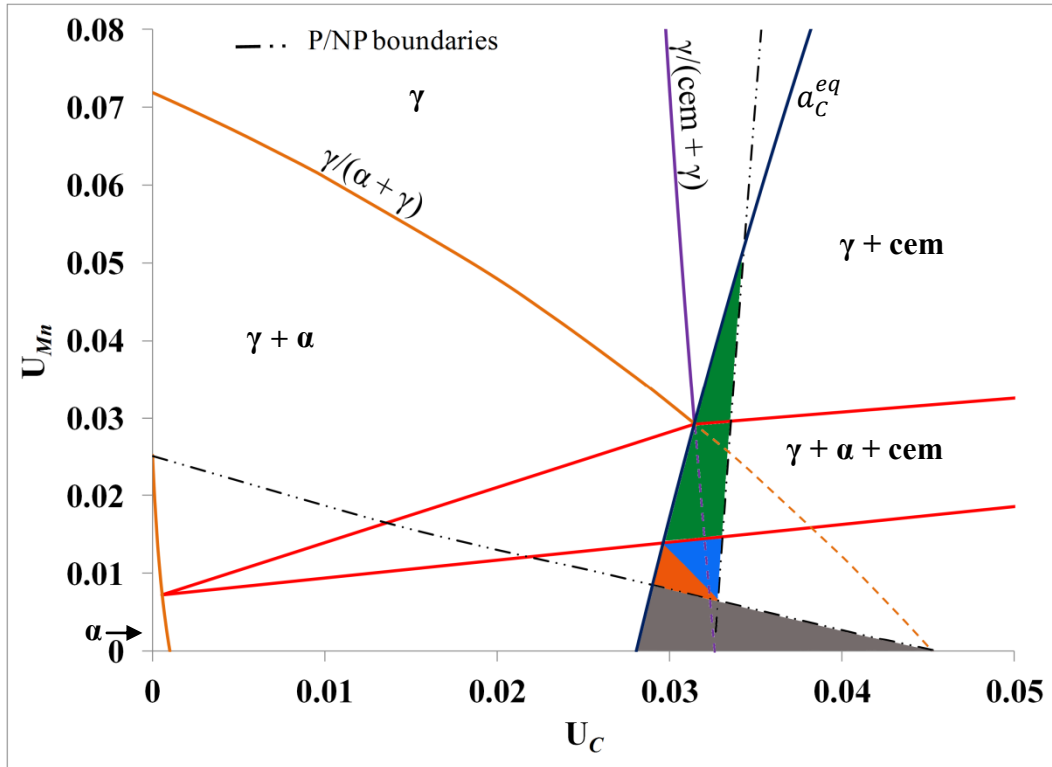
Figure. 1.9 (h) Isothermal section of Fe-C-Mn at 700 °C showing the regions of parapearlite (gray), constant orthopearlite growing behind a carbon-enriched zone (orange), constant orthopearlite growing behind a carbon-depleted zone (blue), divergent orthopearlite (green).
Figure 1.9: Captions associated with Figs. 1.9a-h are placed with respective figures.

In agreement with Cahn and Hagel, Hillert also concluded that the cause of the non-steady growth rate and divergent lamellae is the continuously changing carbon content of the austenite and the subsequent change in boundary conditions at the pearlite interface. [hillert1982, hutchinson2004]

1.4.1.3 Theory – formation of pearlite above upper Ae1

Hultgren and Edstrom reported grain boundary precipitation of cementite above the upper Ae1 in hypereutectoid steels containing as little as 0.2 (wt. %) Si within the ($\gamma + \alpha$) two-phase field. This is in clear disagreement with the Fe-C-Si phase diagram, i.e. equilibrium thermodynamics. The cementite precipitates *sometimes* have a porous appearance and the authors termed the structure 'porous cementite'.

Later, Fridberg and Hillert interpreted the formation of 'porous cementite' as a special kind of partitioned pearlite. [fridberg1970] It was suggested that the pores are, instead, ferrite

stabilized by the Si. Formation of pearlite at temperatures above the upper Ae1 was rationalized using schematic phase diagrams, isoactivity lines, and the assumption of local equilibrium conditions at the transformation interfaces. Hutchinson and Shiflet carried this idea to the Fe-C-Mn alloy and *experimentally* demonstrated that formation of pearlite is also possible above the upper Ae1. [hutchinson2004] The reasons for the formation of pearlite were again ascribed to local thermodynamic conditions at the interface.

Consider an alloy with bulk composition indicated by the yellow circle in the isopleths (Fig. 1.10a) and in the isotherm (Fig 1.10b). The composition lies above the P/NP boundaries for both ferrite and cementite and if pearlite forms it is expected to do so under partitioning conditions. Initially, proeutectoid cementite precipitation is expected and its growth is controlled by manganese diffusion. This is a very slow process and it is reasonable that carbon isoactivity is established early in time. Under the assumption of LE-P, thermodynamic conditions in the austenite at the γ/cem interface must lie on the γ/(γ + cem) phase boundary (or its extrapolation) and carbon activity in cementite and in austenite must be equal. Interphase boundary composition can then be represented as the intersection between the carbon isoactivity line passing through the bulk alloy and intersection with the metastable extension of the γ/(γ + cem) boundary, represented by the purple circle in Fig. 1.10b. The resulting tie-line from the cementite phase boundary to the metastable γ/(γ + cem) boundary represents the operative (γ + cem) tie-line, shown in blue in Figs. 1.10b. Compositions at the end of the operative tie-line represent local equilibrium conditions at the γ/cem interphase boundary. The intersection of the metastable γ/(γ + cem) and (γ + cem) operative tie-line represents the austenite composition at the γ/cem interface. This point now lies within the (γ + α) two-phase field and ferrite precipitation is now possible. Even though ferrite is a non-equilibrium phase at this temperature, austenite local composition conditions nearest to advancing cementite permit formation of ferrite. Evolution of the reaction has similar characteristics already described in Fig. 1.9f.

a

b
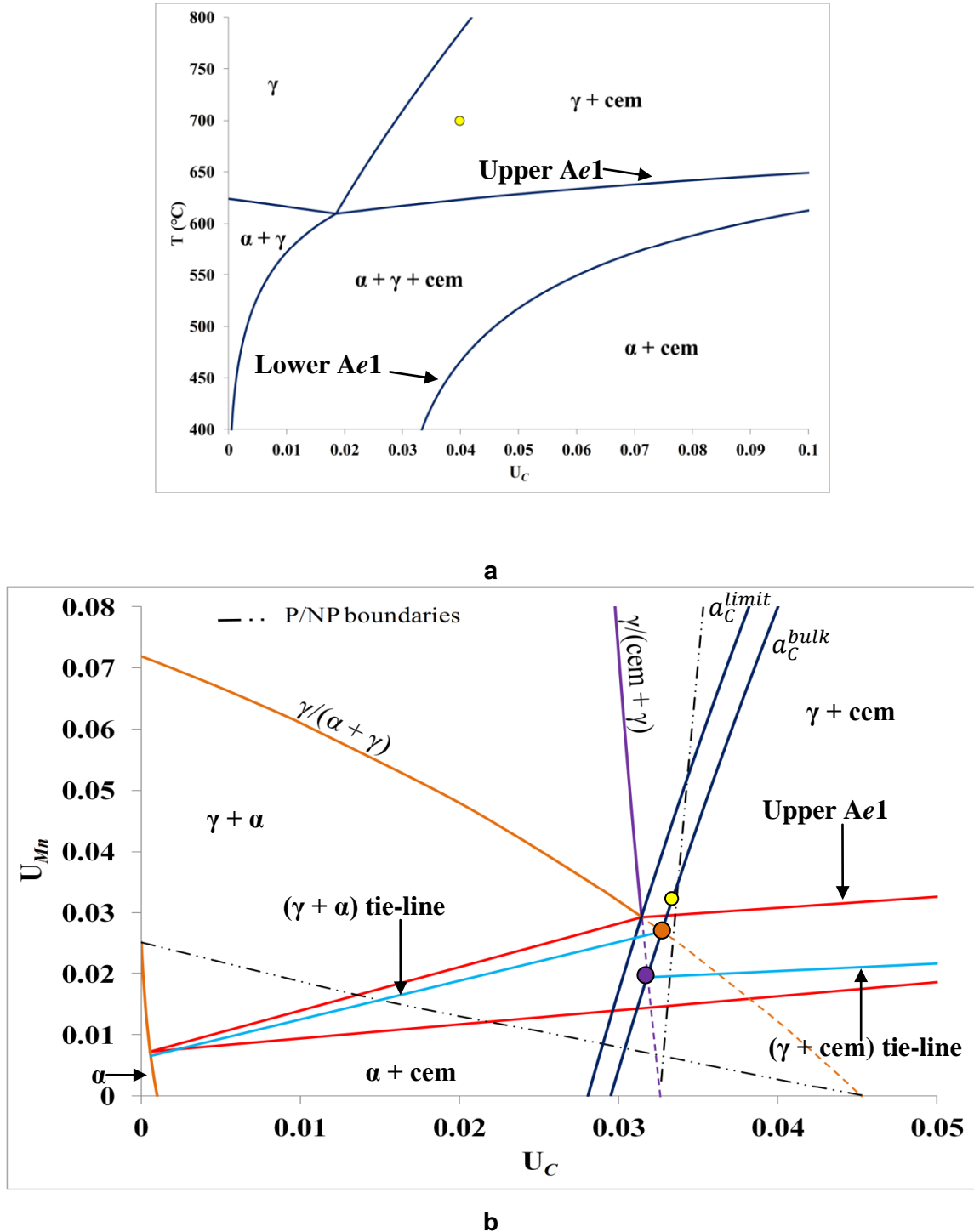
Figure 1.10: (a) Section of the Fe-C-11.56Mn (wt. %) phase diagram. The bulk alloy composition is marked by the yellow circle and lies above the upper Ae1. **(b)** Isothermal section of the Fe-C-Mn system at 700°C. The bulk alloy composition is marked by the yellow circle. Dashed lines are metastable extensions of the γ/(γ + cem) and γ/(γ + α) phase boundaries. The red lines form the three-phase tie-triangle. The bulk alloy composition falls within the (γ + cem) two-phase field. However, local equilibrium conditions show that formation of pearlite is thermodynamically permissible.

If the product phases are lamellar they are expected to be divergent. Formation of ferrite will cease to be thermodynamically viable when isoactivity of carbon reaches the activity indicated by the carbon isoactivity line a_C^{limit}. a_C^{limit} doesn't represent equilibrium and the reaction will continue by minimizing carbon activity (move left of the a_C^{limit})[9]. This further movement shifts the (γ + cem) tie-line onto the equilibrium γ/(γ + cem) phase boundary. The interphase boundary conditions will then be described by the thermodynamics of the (γ + cem) two-phase field. Knowing the alloy composition and the isothermal transformation temperature, it is always possible to compute the a_C^{limit}. Under local equilibrium assumptions the maximum temperature above the upper Ae1 where ferrite can form can be calculated. For the alloy used in this study (Fe-0.85C-11.56Mn wt. %) the approximate computed limit for the formation of ferrite above the Ae1 is 685 °C. [hutchsinson2004]

It must be noted that, as currently defined, the methodology used to justify formation of pearlite above the Ae1 provides little or no insight into the energetic pathway of the phase transformations, both equilibrium and non-equilibrium. Other than the end points, *i.e.*, equilibrium, this method is also not a good predictor of intermediate steps when experimental data is compared with the calculations. At best, it provides boundary conditions for the diffusion problem that assure 1) LE holds at the interface and 2) fluxes of all solutes are such that all yield the same growth rate. In turn, this provides thermodynamic limitations at the interphase interfaces for the system in question. This is not unexpected, as thermodynamics say nothing about kinetic path, only the end (equilibrium) state.

1.4.1.4 Ferrite Retrenchment

Above the upper Ae1, austenite and cementite are the two phases predicted by the phase diagram for the current alloy. It is observed that during the later stages of the phase transformations that ferrite formation and later dissolution leaves markedly different austenite characteristics when compared to austenite elsewhere. This intermediate (retrenched) austenite is identified as γ^r. To identify the areas of retrenchment, the variable γ^r is introduced, Eq. 1.2b.

$$\gamma \rightarrow \gamma + cem + \alpha \rightarrow \gamma + cem + \gamma^r \rightarrow \gamma + cem \qquad (1.2b)$$

---
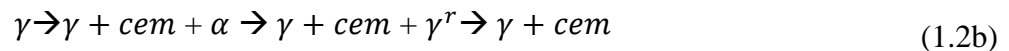
[9] This is shown in greater detail in Chapter 4.

1.4.1.5 Cementite Coarsening and Spherodization

After long times it is not uncommon to observe coarsening and spherodization of the cementite lamellae. This is represented by the equation 1.2c. As this reaction precedes the morphology changes but the total volume of the product phase (cementite) does not.

$$cem_{fine} \rightarrow cem_{coarse/spherodized}$$
(1.2c)
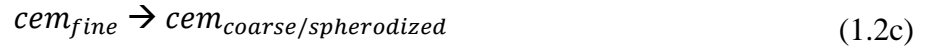
1.4.2 Discontinuous Growth (cellular reaction)

The scope of this work requires a brief introduction of discontinuous precipitation. A detailed assessment of nucleation, growth kinetics, and morphology models for this reaction can be found in the works by Gust *et al.* in [manna2001], [zieba2001], [williams1981], and [kaur1995]. These reviews are generally restricted to discontinuous reactions in binary substitutional systems where the diffusivities of both elements are of the same order of magnitude.

Relatively few DP studies are available on multi-component systems containing both substitutional and interstitial solutes. Kikuchi *et al*. first reported discontinuous precipitation in an alloy that contained both interstitial and substitutional solutes in a high chromium, high nickel austenitic stainless steel with 0.4 (wt. %) N. [kikuchi1982] Report shows cellular colonies had a decelerating growth rate with the eventual stoppage, even when a large portion of untransformed matrix remained. A qualitative explanation for the observed non-steady state growth features is attributed to the long range diffusion of the faster-diffusing element, nitrogen, from the untransformed matrix to the cells. It was found that the nitrogen content of the colony became higher at the expense of the nitrogen content in the untransformed matrix.

Generally accepted definitions of the discontinuous reaction are presented because discontinues precipitation in the Fe-11.56Mn-0.85C (wt. %) alloy is similar to one observed by Kikuchi *et al.* and has not been previously reported.

1.4.2.1 Discontinuous Precipitation

Discontinuous precipitation, also known as cellular reaction, is defined as

$$\gamma_0 \rightarrow cem + \gamma_0^d$$
(1.2d)

where cementite is a lamellar decomposition product. The new solute‑rich plates grow synchronously into one grain by advancing the grain boundary on which the precipitates nucleated. The grain between the plates, γ_0^d, is depleted of its supersaturation as shown in Figs. 1.11a and b. γ_0 and γ_0^d have the same orientation relationship which is indicated by the subscript orientation relationship of γ_0^d with respect to γ_2 is the same as the orientation relationship between γ_0 and γ_2.
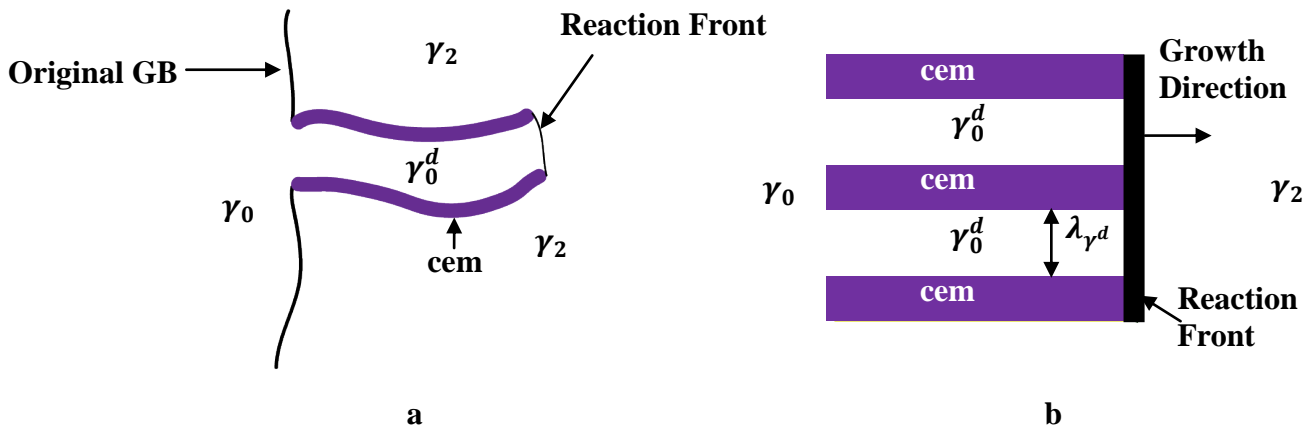
Figure 1.11: Schematic representation of **(a)** formation and growth of the cellular colony. The original grain boundary becomes the reaction front for manganese redistribution. **(b)** a lamellar two-phase microstructure (γ + cem) in the austenite matrix. λ represents thickness of the constituent indicated by the subscript.

Discontinuous precipitation solute redistribution is accomplished almost exclusively by diffusion along the advancing reaction front (original grain boundary), which is referred to in the literature as the cell boundary. The reaction front is a high‑angle boundary which serves as a short circuit diffusion conduit for transporting the solute from the parent phase to the solute‑rich precipitate. Typical morphology of the growing crystals (γ + cem) is lamellar, as depicted in Fig. 1.11b but rod‑type and globular shaped structures have also been reported. [nes1972, manna2001] Typically, the cellular colonies in binary substitutional systems are reported to grow with a constant rate and interlamellar spacing for a given undercooling and supersaturation.

1.5 Problem Statement

Theoretically, formation of ferrite above the Ae1 is supported by the notion of local equilibrium. Formation of pearlite is implicitly assumed. Ferrite is expected to eventually dissolve because it is not an equilibrium phase at these temperatures and bulk alloy composition.

This work is undertaken to gain a better insight into the initiation and progress of the metastable ferrite growth and the corrective mechanisms (dissolution of ferrite) utilized by the Fe-C-Mn during its evolution towards thermodynamic equilibrium. To address this problem, samples are heat treated in a systematic manner in various purposefully selected isothermal temperature-time regimes. Qualitative and quantitative observations are used to characterize various evolutionary stages. Quantitative observations are coupled with thermodynamic software packages to model and identify the reasons associated with the initiation and subsequent dissolution of ferrite. A primary objective is to critically test the utility of current theories associated with phase transformations in Fe-C-M alloys, where vastly different diffusivities permit formation non-equilibrium phases.

Chapter 2 – Experimental Procedure and Computational Techniques

2.1 Heat Treatments

The alloy used in this investigation is Fe-11.56Mn-0.85C (wt. %). Alloy composition was verified by an independent commercial company to ensure carbon content. Individual ingots sized approximately 15cm x 1cm x 1cm were cut from a larger rolled plate. Each ingot was encapsulated in a quartz tube under a partial pressure of argon and homogenized in a box furnace for 3 days at 1200 °C. The furnace was allowed to slow cool to room temperature. To avoid decarburized areas the ends of the ingot were cut off, yielding a 10cm x 1 cm x 1cm ingot. A slice from the middle section of the ingot was removed and quantitative energy dispersive (x‑ray) spectroscopy (EDS) was performed to verify alloy manganese and iron composition.

2.1.1 Isothermal Heat Treatments
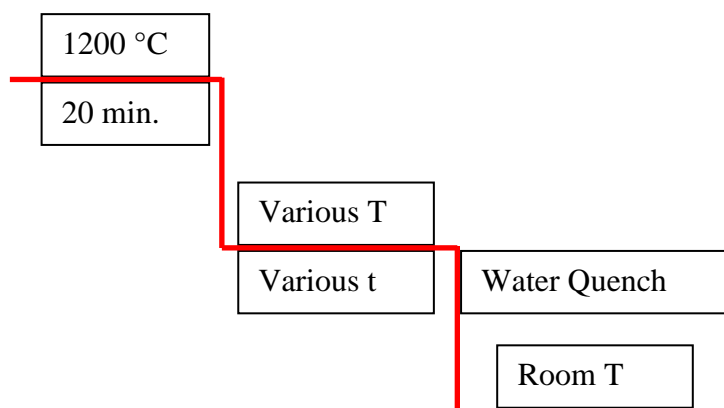
Figure 2.1: Isothermal heat treatment path.

Individual slices, ~3mm in thickness, were cut from the ingot and re-encapsulated prior to further heat treatment. Samples were austenitized at 1200 °C for 20 minutes followed by isothermal heat treatments in a tube furnace at temperatures 585, 600, 610, 620, 630, 640, 650, 660, 670, 680, 690, to 700 and 750 °C (±2 °C) for various times ranging from 1 hour up to 6 months as shown in Fig. 2.1. All samples were water quenched after final heat treatment. Temperature in the tube furnaces was monitored on weekly basis using a calibrated chromel-alumel (S type) thermocouple probe.

2.2 Metallography

Heat treated samples were mounted and polished using standard metallographic techniques. To eliminate decarburization effects, a sufficient amount of the material was removed from the top face of the sample by grinding. Also, no measurements were made close to the peripheral edges of the sample. The microstructural evolution was monitored using optical microscopy (OM), both black-and-white and color, and scanning electron microscopy (SEM) techniques. A 2% nital etch was used for black and white optical microscopy. Modified Klemm's tint (composition: 25ml H_2O, 12.5 $Na_2S_2O_3$, 1g $K_2S_2O_5$) was used for color microscopy.

Specimens for TEM preparation were first ground from heat treated material to a thickness of ~400 μm. Samples were further thinned (to approximately ~200 μm) using a solution of 14ml HF, 100ml of 27% H_2O_2 and 100ml of H_2O. [plichta1976] 3mm disks were mechanically punched from the foil. The samples were then dimpled and ion milled. Several studies indicate that the milling process has no detectable effect on the local phase chemistries or dislocation density. [barber1993, kitano1995, cairney2000]

Growth kinetics calculations require geometrical and spatial features of a pearlite colony or individual phases, *i.e.*, volume fraction of pearlite (Φ^p), volume fraction of cementite (Φ^{cem}), volume fraction of ferrite (Φ^α), and the length of the GB. These parameters are typically measured by a point counting techniques. [underwood1968] Active contours and k-clustering were introduced to the field of materials science to reduce the processing time of analysis as a substitute for point counting. [ontman2010] Since these techniques are new to metallurgy, the following sections develop each technique and demonstrate how results compare to the traditional point count method.

2.3 Active contours

Image segmentation (*e.g.*, extracting a phase of interest from the matrix), a process which is either done by manually outlining the microstructure or using a low level threshold-based edge detector such as Canny, is a typical intermediate step in the reconstruction of 3D models. [mangan1994, matsuoka1994] However, these segmentation techniques often require extensive supervision (user interaction) or a normalizing step (*e.g.*, histogram equalization) for datasets with variable contrast. As a result, if a dataset contains a large number of images, these techniques are impractical. Active Contouring (AC) is a segmentation approach developed in the

late 1980s for meteorology and has been applied in a number of fields including medicine and bioengineering. Although AC is an edge-based segmentation technique, it is less susceptible to contrast differences, making it ideal to use across datasets with varying contrast within regions of interest (ROI) without employing normalizing algorithms. More importantly, edge linking and spur removal (examples of these image outlining defects can be seen in Fig. 2.3d) procedures often associated with Canny edge detectors (or the similar Roberts and Sobel edge detectors), are not needed for AC.

2.3.1 Introduction to Active Contours

An active contour is a curve that evolves from a predefined initial position towards the boundaries of a desired object. Active contours can be divided into two general classes: geometric and parametric. Each class has its own implementation which makes its behavior unique. Both classes find use in a broad range of applications. [trucco1998] Following a brief introduction to AC types, metallurgical examples are presented illustrating their individual usefulness in segmenting microstructures.

2.3.2 Introduction to Parametric Active Contour (PAC)

PAC was first introduced by Kass *et. al.* for segmenting objects in images utilizing dynamic curves. [kass1987] This particular class of active contours is ideal to employ if boundary gaps are a problem because the contour can be constrained to be smooth, as shown in the next section. However, this constraint also makes this class of contours unsuitable if splitting or merging of the contour is required to isolate objects of interest. The behavior of the curve is constrained by minimization of the user-defined energy functional. The energy functional of a PAC usually consists of two defined energy terms: internal energy, E_{spline}, and external energy, $E_{external}$. [xu1998] E_{spline} is related to the line geometry and defines continuity and smoothness of the contour. $E_{external}$ is an image derived property, *e.g.*, an edge associated with a phase, a GB, or a color, and has local minima at features of interest. Conversely, $E_{external}$ may be used to drive the curve away from unwanted features by penalizing the functional near the undesirable feature. While not limited to, this work deals with closed contours only.

2.3.3 Background for Parametric Active Contours (PAC)

PAC is represented by a parameterized curve $C(s) = [x(s), y(s)]^T$, $s \in [0,1]$ where $x(s), y(s)$ describe normalized point coordinates on the image. $C(s)$ evolves in a fashion that minimizes the energy functional ($E_{spline} + E_{external}$):

$$E = \int_0^1 \left\{ \left(\frac{1}{2}\right) \left\{ \alpha [C'(s)]^2 + \beta [C''(s)]^2 \right\} + \gamma E_{external}[C(s)] \right\} ds \qquad (2.1)$$

where α, β and γ are weight coefficients that control the relative influence of individual terms and whose sum is set equal to one (*i.e.*, $\alpha + \beta + \gamma = 1$). C represents the active contour line and C' and C'' are the first (slope) and second (curvature) derivatives of $C(s)$ with respect to the arc-segment s and represent the continuity and smoothness of the contour, respectively. To minimize the energy functional (Eqn. 2.1), the contour evolves such that the following Euler equation is satisfied:

$$\alpha C'(s) - \beta C''(s) - \gamma \nabla E_{external} = 0 \qquad (2.2)$$

where ∇ is the gradient operator.

The external energy can be categorized as static or dynamic energy. The static energies, including edge-based static energies, are those that are calculated from the image and remain unchanged as the contour deforms, *e.g.*, gradient of the intensity. Dynamic energies are those that depend on the contour and change as the contour evolves. Recently, several variations of static $E_{external}$ were introduced to deal with difficulties associated with noise sensitivity, the need to initialize the contour near the boundary of the object (capture range), and poor convergence towards object's concavities (concavity convergence). In this dissertation a variation of the edge-based static $E_{external}$ called vector field convolution, introduced by Li and Acton, is used for its superior performance and flexibility. [li2007]

2.3.4 Introduction to Geometric Active Contour (GAC)

GAC, first introduced by Osher and Sethian for capturing moving fronts, is a contour that is represented as a zero level set of an implicit function, defined in a higher dimension. [osher1988] The key difference between the PAC and the GAC is GAC's ability to split and

merge during its evolution, automatically handling topological changes. This option makes GAC ideal for applications where multiple objects of interest are located in the same image, *e.g.*, outlining and extracting intragranular precipitates.

2.3.5 Background for Geometric Active Contours

A way to understand the basic inner workings of the GAC is to start with a closed contour and allow the points on the contour to evolve in the direction of the contour normal at some defined speed F. Similar to PAC, the curve and its evolution can be expressed using an explicit parametric form, but this method doesn't address the issue of splitting and merging. Instead, the implementation of GAC embeds the original interface in a higher dimensional scalar function that is defined over the entire image. The contour is now defined implicitly as a level set of this scalar function. Over the rest of the image space, this level set function is defined as a signed distance function from the zero level set. Specifically, given a closed curve C, the function is zero if the pixel lies on the curve itself, otherwise it is the signed minimum distance from the pixel to the curve. The evolution of the function is defined by a partial differential equation.

In traditional level set formulation, active contours are defined by the zero level set $C(t) = \{(x, y)\}\{\varphi(x, y, t) = 0\}$ of a level set function $\varphi(x, y, t)$. The idea is to track the positions of (x, y) at time t where $\varphi(x, y, t) = 0$ which correspond to the ROI boundary. To update the equation of the $\varphi(x, y, t)$ function, it can be differentiated with respect to time (and using the chain rule) as follows:

$$\frac{\partial \varphi}{\partial t} + \nabla \varphi(x, y, t) \cdot (x_t, y_t) = 0 \tag{2.3}$$

Where (x_t, y_t) is the velocity vector for point (x, y) on the GAC and if speed, F, is defined as

$$F = (x_t, y_t) \cdot \boldsymbol{n} \tag{2.4}$$

where $\boldsymbol{n}$ is a normal and defined as $\boldsymbol{n} = \frac{\nabla \varphi}{|\nabla \varphi|}$.

Combining Eqns. 2.3 and 2.4, a classical geometric update equation is obtained:

$$\varphi_t + F|\nabla \varphi| = 0 \tag{2.5}$$

By convention, points inside the contour are defined as negative and outside the contour as positive. Positions where $\varphi(x, y, t) = 0$ are stored. The speed function, F, is a user defined

function and can be related to the curvature of the contour, gradient magnitude or, as in the present application, image dependent property such as an edge.

During the implementation of the traditional level set method, it is numerically necessary to keep the evolving level set function close to a signed distance function. [gomez1992, peng1999, osher2003] This can be done using a technique known as re-initialization. A number of different techniques for re-initialization have been introduced because, as pointed out by Gomez and Faugeras, re-initializing the level set function can be problematic. [gomez1992] Since there is no systematic way to re-initialize a contour because of the nature of a computer image, this work follows the method proposed by Li *et al.* that eliminates the need for re-initialization. [li2005]

2.3.6 Performance and Applications of Active Contours

2.3.6.1 Parametric Active Contour (PAC)

One key advantage of PAC is its ability to handle artificial boundary gaps (missing pixels along the contour line), which can occur during the acquisition step of the process or due to noise, by constraining smoothness based on the application requirements. Additionally, incorporation of an external force reduces both noise sensitivity and the importance of precise initialization location which in practical terms increases the capture range (microstructural area available for the contour to access). The energy functional implemented in this paper has three terms (Eqn. 2.1) whose influence can be controlled by adjusting corresponding coefficients, *viz.* α, β and γ. Although, there is no systematic way of selecting coefficients, general guidelines are presented and tested to assist the user. Some exceptions to these guidelines occur when the ROI possesses points of high and low curvatures simultaneously, resulting in sharp concavities (or cusps), and since cases like this present conflicts with each other a compromise is needed. For example, if it is known *a priori* that a ROI has smooth edges but the acquired digital image of the ROI displays serrated edges (pixilated), which may be a result of limitations in acquisition hardware, it is best to choose coefficients to obtain a smooth curve to mitigate the serrations. Examples below will demonstrate the effect of coefficients on the resulting contours.

If the ROI exhibits low and gradually changing curvature, increasing α while keeping $\gamma > 0$, to keep the curve evolving towards the boundary, will produce the desired results. Similarly, if

the ROI contains points of high curvature and/or discontinuities, increasing β, the coefficient controlling the strength of C'', while keeping γ > 0 will allow PAC to successfully outline the ROI. The following four tables illustrate the adjustable parameters that determine segmentation quality. First, in Table 2.1, four synthetic shapes, representative of different phase morphologies, are generated to demonstrate the effects of α and β, while γ is held constant. The idealized drawings of typical metallurgical microstructure morphologies and optimized values for α, β and a fixed γ = 0.20 that best outline the phases are listed. Included in Table 2.1 are two statistical measurements concerning how well the PAC matches the original interphase boundary. The first measurement is the root-mean-squared error (RMSE) which is defined as: $\sqrt{\dfrac{1}{n}\sum_{i=1}^{n} y_i^2}$, where y is the minimum distance between the point on the contour and the contour of the actual noise-free boundary image. Values have most meaning when compared between each other, as is done in the Tables 2.1-2.4. A value of zero indicates a perfect match. Two dimensional cross-correlation, which measures statistical similarity of the two images, is measured between the original synthetic figure shown in Table 2.1 (the image is referred to as A in the following equation), and the final outlined area by the active contour (B in the equation) for each shape. The cross-correlation coefficient of images A and B is defined as:

$$ c = \frac{\sum_i \sum_j (A_{ij} - \overline{A})(B_{ij} - \overline{B})}{\sqrt{\left(\sum_i \sum_j \left(A_{ij} - \overline{A}\right)^2\right)\left(\sum_i \sum_j \left(B_{ij} - \overline{B}\right)^2\right)}} $$

where A_{ij} and B_{ij} represent the intensity value of each image at pixel coordinates i and j and $\overline{A} = mean(A)$ and $\overline{B} = mean(B)$. Values approaching 1 have a stronger correlation. Unless otherwise specified, active contours on all the images are initialized in the center of the image, with a beginning radius of R = 35 pixels (the initial contour placement and size is demonstrated for the square only) and the program allowed to run for 60 iterations. α and β values for smooth (corner-free) circular shapes are 0.24 and 0.56, while being approximately 0.1 and 0.6, respectively, for shapes with corners. These values are determined iteratively by varying both α and β to minimize the root mean squared error. This is in agreement with the proposed energy functional for PAC, discussed earlier. While the accuracy of the values presented is sufficient for further demonstration in this work, parameters can be adjusted to fit individual application requirements.

Table 2.1: Results of PAC for synthetic shapes. Value of γ is set at 0.2 while values for α and β are allowed to vary iteratively to minimize the root mean squared error. The active contour is initialized at the center of each image as a circle with radius $R = 35$ pixels illustrated for the square only. Each synthetic image is 100 x 100 pixels along an edge of the square frame. RMSE and correlation are defined in the text.
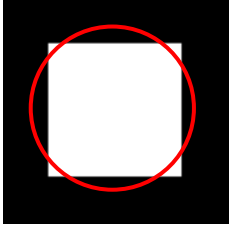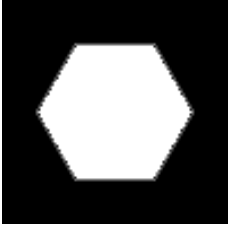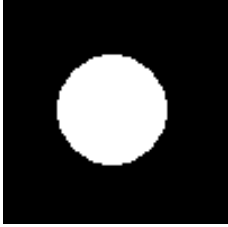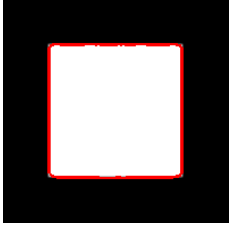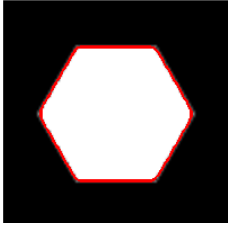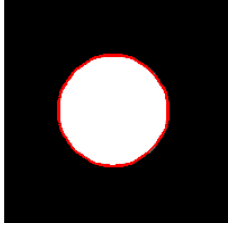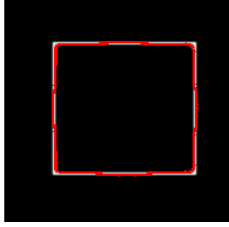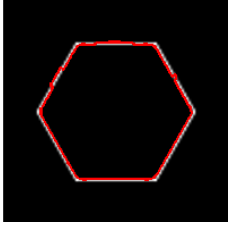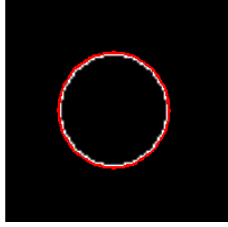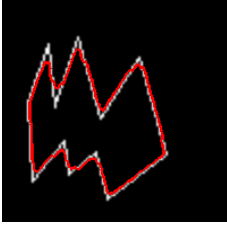
Shape	Square	Hexagon	Circle	Saw teeth
α	0.12	0.17	0.24	0.15
β	0.68	0.63	0.56	0.65
γ	0.20	0.20	0.20	0.20
Original Synthetic Shape				
Red PAC Outlines of Synthetic Shape				
Final Outlined Segmented Boundary				
Correlation	0.9618	0.9758	0.9906	0.9185
RMSE	0.378	0.469	0.241	0.653

Table 2.2 shows that for high quality images (noise free, as defined in a later section) the AC starting position is not critical to obtain good and consistent results (due to increased capture range discussed earlier). Here the active contour is initialized as a circle with a center at x, y and a radius R, where x and y are coordinates of the center of the image measured in pixels. As in Table 2.1, initial radius $R = 35$ pixels while x and y is varied by 10 pixels in the four major directions (up, down, left, right). Results are for the same square shaped figure and the same values for α, β, and γ shown in Table 2.1.

Table 2.2: Effect of changing starting position of PAC for the square shaped figure shown in Table 2.1.

Center of Initialization	$(x$-10, $y)$ [10 pixels left]	$(x$+10, $y)$ [10 pixels right]	$(x, y$+10) [10 pixels down]	$(x, y$-10) [10 pixels up]
Correlation	0.9740	0.9731	0.9734	0.9737
RMSE	0.421	0.369	0.411	0.398

An important consideration is the quality of image with respect to noise (corruption). Values for α, β are feature specific while γ depends on image properties such as noise. To demonstrate the effects of γ, various amounts of noise are added to the synthetic square-type image from Table 2.1 and the images are then again outlined (Table 2.3). Signal to noise ratio (SNR) can be estimated by SNR (dB) = $20\log_{10}[(I_{max}$-$I_{min})$/std(noise)]; where, I is the image intensity value and *std* is the standard deviation of the noise. Table 2.3 identifies the corruption, or noise, of the images based on this definition. Table 2.3 shows an example where the image is seriously corrupted, SNR of 5dB, and the outline of the AC is inaccurate. However, the result is still better than expected with typical edge detectors. In cases where the noise level is very high, the importance of initialization location does increase and it would be best to initialize the PAC as close as possible to the boundaries of the ROI. In Table 2.3 γ is fixed at 0.20, similar to the previous examples that exhibit clear contrast and little noise. Increasing the value of γ doesn't necessarily improve the quality of results for images severely degraded by noise, however, it may help with images having low to moderate amounts of noise as shown in Table 2.4 where a systematic improvement in correlation and root mean squared error occurs with increasing γ. Also, the improvement in results doesn't vary significantly after an adequate number of iterations is determined and executed.

Following the synthetic examples in Tables 2.1-2.4, the next table, Table 2.5, shows previously published microstructures. Applying PAC to micrographs from the literature illustrates the practical extension of the synthetic results. Presented shapes vary in geometry, curvature and size and it is shown how the inherent flexibility of PAC can be applied to accommodate all the changes by adjusting a set of parameters. Values for the coefficients α and β, optimized based on RMSE of the synthetic shapes, are also listed. The examples illustrate that PAC deals with noise reasonably well without significant pre-processing of the image, which isn't already built into the implementation of the PAC. The contour completely ignores the

martensite matrix while outlining the ferrite (columns 2 and 4). These are good examples where the martensite is treated as noise while the ferrite is the phase of interest.

Table 2.3: Effect of noise on PAC performance. The active contour is initialized at the center with radius R = 35 pixels. Square shape ROI is again employed with various noise levels specified in dB. γ = 0.2, α=0.12, β=0.68. Noise added is a Gaussian white noise with mean of 0 and variance set to match the indicated SNR. The noise was generated using Matlab's native *imnoise* command. Definition of the SNR is in the text.
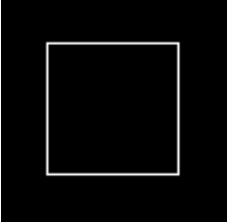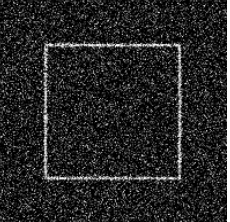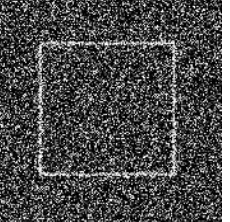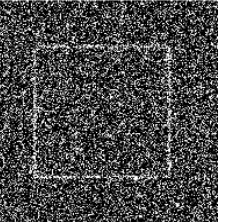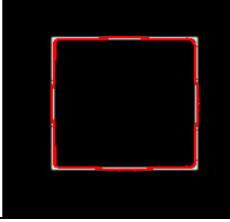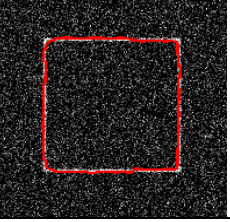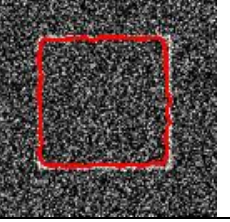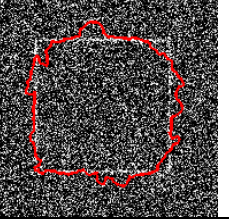
SNR	∞	20dB	10dB	5 dB
Corrupted Image (original)				
Outlined Image (boundaries segmented) 60 Iterations				
Correlation	0.9618	0.9690	0.9414	0.8973
RMSE	0.378	0.984	1.238	4.357

Table 2.4: PAC performance with varying γ. The active contour is initialized at the center with radius R = 35 pixels. SNR of the image is 10 dB. $α = β = \frac{1-γ}{2}$.
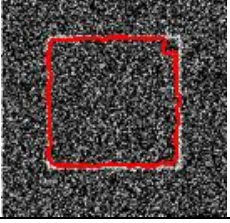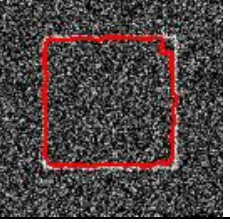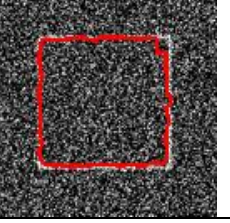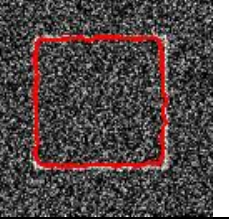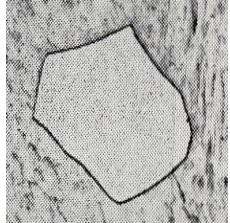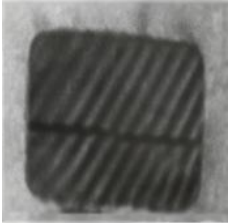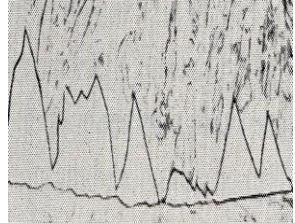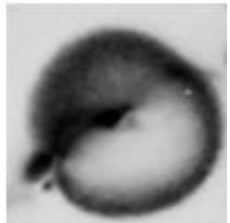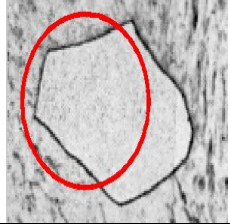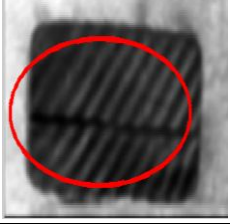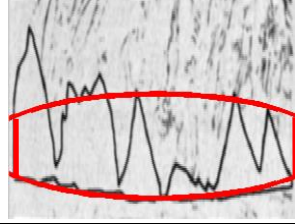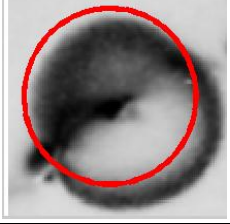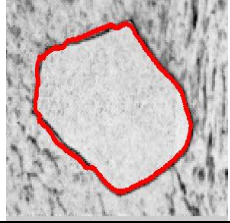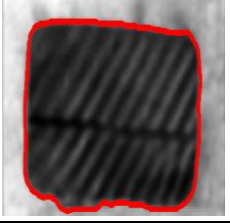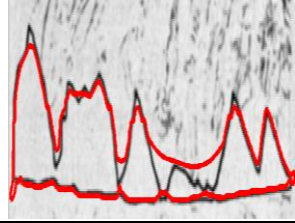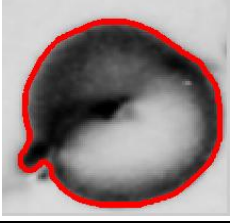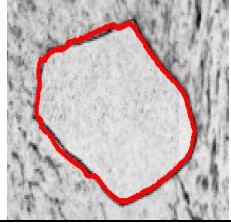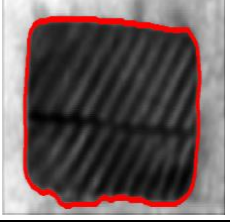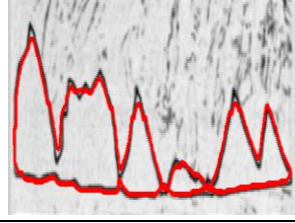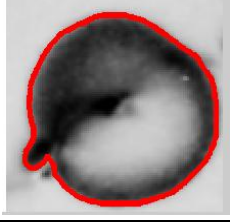
γ	0.05	0.10	0.15	0.20
Outlined Image boundaries (segmented)				
Correlation	0.9254	0.9281	0.9273	0.9414
RMSE	1.743	1.683	1.497	1.238

Table 2.5: Application of PAC on real microstructures. Images of microstructures and the outline obtained using PAC. Scales listed in row 1 apply to the image box edge length for each micrograph.

	Ferrite idiomorph Fe-0.2C (wt%) (from Fig. 5, p. 394, [aaronson1962]), 80μm	Cuboid precipitate (AlCuMg) (from Fig. 5, [schueller1992]), 0.05μm	Primary sawteeth Fe-0.8C (wt%) (from Fig. 63, p. 526, [aaronson1962]), 50μm	δ' particle Al$_3$Li (from Fig. 1a, [casada1992]), 0.1μm
α	0	0.1	0	0.6
β	0.8	0.7	0.8	0.2
γ	0.2	0.2	0.2	0.2
R, [x, y] Radius,[position]	40, [50, 50]	35, [70, 65]	35, [150, 70]	45, [55, 55]
Number of Iterations	50	50	50	50
Original Images of Microstructures				
Initial Contour Placement				
Iteration 15				
Final Outlined Microstructures (Iteration 45)				

Segmentation of objects with mixed curvatures can be problematic due to the conflict between the α and β terms of the energy functional. A compromise to satisfy the application

requirements is the suggested approach. For example, a martensite crystal contains points of high curvature and discontinuous cusps located on the plate ends as shown in Fig. 2.2a. Since user inspection indicated that sharp corners exist, setting $\alpha = 0.3$ and $\beta = 0.5$ favors the edges, thus allowing the PAC to exhibit sharp corners illustrated in Fig. 2.2c. To allow the energy functional to favor the plate's smooth edges, $\alpha = 0.5$ and $\beta = 0.3$ values are chosen with the resulting contour shown in Fig. 2.2d. Examination of the plate tips in Figs. 2.2c and 2.2d insets illustrate this difference.

a   b   c   d
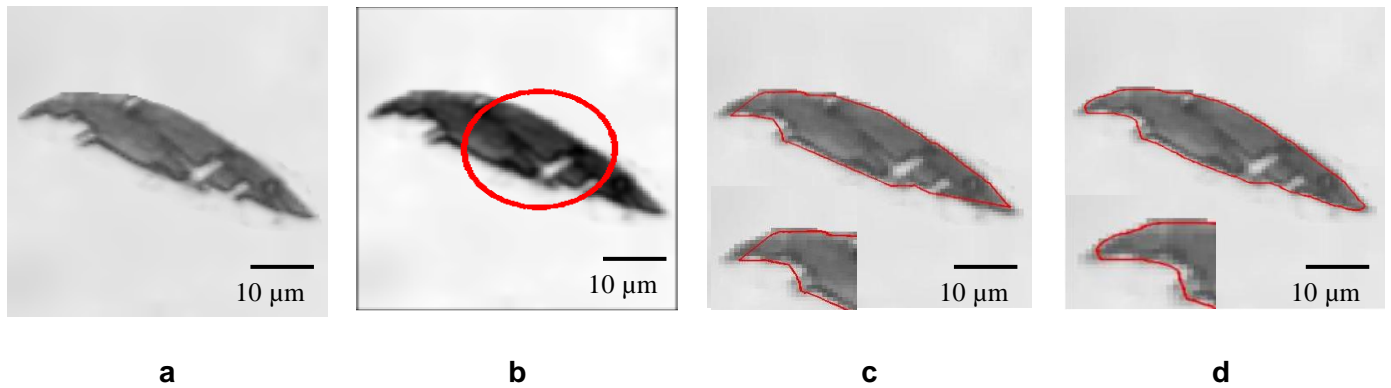
Figure 2.2: (a) Optical micrograph of a martensite plate in an Fe-29Ni-0.6C (wt. %) alloy, austenitized and quenched into chilled methanol. **(b)** Initial contour starting position. **(c)** Final contour using high curvature conditions ($\alpha = 0.30$, $\beta = 0.50$, $\gamma = 0.20$). **(d)** Final contour using low curvature conditions ($\alpha = 0.50$, $\beta = 0.30$, $\gamma = 0.20$. The contour lines are made thick for publication. In practice the line would be 1 pixel thick.

2.3.6.2 Geometric Active Contour (GAC)

Similarly to PAC, if the ROI possesses strong boundaries and the pixel intensity in the ROI varies significantly, as shown in Fig. 2.3a, GAC is likely to offer an advantage over traditional segmentation techniques. In Fig. 2.3b GAC is used and the final contour is continuous and closely follows the δ'/matrix boundary. Thresholding (Fig. 2.3c) and Canny edge detection (Fig. 2.3d), unable to deal with high pixel intensity variance located within the ROI, introduce errors that require additional processing to match the contour obtained using GAC. One common error with Canny edge detection on microstructures is the gaps and spurs along the final contour that must be corrected. Note, if the ROI is a single object with gap free boundaries, either class of contours can be used.

As way of comparison between GAC and PAC, the current implementation of GAC which is similar to that used in [li2005] has one image dependent variable (edge strength),

however, the performance measured in terms of correlation and RMSE for this application is similar to that of PAC shown in Table 2.1. On the other hand, by virtue of GAC's design experiments shown in Tables 2.3 and 2.4, where the starting position varies, would not readily be applicable to GAC.

| a | b | c | d |
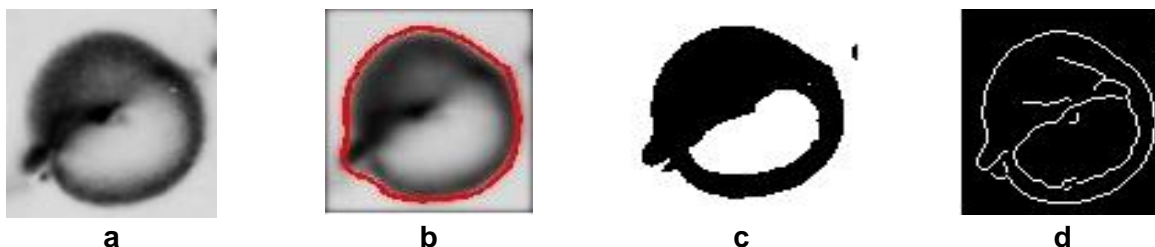
Figure 2.3: Al-3Li (wt. %) alloy heat treated at 300 ºC for 5 minutes. **(a)** Al$_3$Li δ' precipitate with variable contrast (TEM image) [cassada1992]. **(b)** Outline using GAC. **(c)** Result using thresholding. **(d)** Result using Canny edge detector. Note the boundary gaps and boundary spurs that must be repaired. Prior to segmentation a median filter followed by a 15x15 Gaussian filter with σ = 1 have been applied to eliminate impulse and high frequency noise components. Number of Iterations = 100. Length of each image box edge is approximately 100 nm for each frame.

The strength of GAC, however, lies in its ability to naturally handle topological changes, allowing the contour to split and merge and capture objects with strong edges. To evaluate and demonstrate the performance of GAC, the TEM dark-field image of an Al$_3$Li δ' precipitate field [wang1995], depicted in Fig. 2.4, is selected. Although mostly spherical, the δ' precipitates exhibit a range of contrast with the Al matrix. The clear and strong contrast of the micrograph makes it ideal for demonstrating the behavior of the GAC. The evolution of the GAC throughout this image is highlighted in the series of frames shown in Figs. 2.4a-d. So that the contour can outline particles that are clipped by the edge of the micrograph itself, the first step is to add a region with zero intensity (zero-pad) placed on the outside circumference (Fig. 2.4a). Fig. 2.4a also shows the positioning of the contour (red line) in a square pattern on the outside edge of the micrograph within the zero-padded zone. The update equation (Eqn. 2.5) will drive the line to collapse towards the center of the micrograph. As the contour moves toward the center it outlines each δ' particle, pinches off, and continues moving inwards. Two frames illustrating the AC progress and behavior as it contracts are shown in Figs. 2.4b and c. As the AC is driven towards the center of the micrograph the δ' particles outside the AC are now outlined. Along the circumference of the AC, the particles that are in contact with it are in various stages of being

circumvented, including several areas where δ' particles are almost completely surrounded and the AC lines nearly touching. When they touch the AC will pinch off (much like a dislocation gliding on a crystal plane and bypassing a non-shearable precipitate) and continue moving inwards. Once fully outlined (Fig. 2.4d) the resulting GAC is converted into a black and white image by standard means, shown in Fig. 2.4e and is now ready for further analysis or segmenting the δ' from the matrix.

Given the intensity distribution of the pixels (0 for the matrix and 255 for the white δ'), thresholding would be the traditional approach to segment the precipitate particles. For the purposes of this experiment, Otsu's method, which is based on minimization of inter-class variance of black and white pixels, is used to determine the threshold value. [otsu1979] The segmented particles obtained using thresholding with Otsu's technique are shown in Fig. 2.4f.

Table 2.6 shows the particle number and time to obtain these data using thresholding, manual evaluation and GAC. In terms of particle density, outcomes obtained using GAC are comparable to those of manual and threshold techniques. The Table does show that the particle count is fewer with GAC than obtained manually and a closer examination of Fig. 2.5 partly accounts for differences between results obtained using GAC and those obtained using other methods. In general, there are two cases which influence the final result. The first is GAC's inability to isolate edges of variable strengths (arrow A), and the second, GAC's failure to split when particles are in close proximity or overlapping (arrow B). Evaluation of the areas where GAC failed to split reveal the presence of lighter pixels that are smeared as shown on Fig. 2.5 area A (also inset). The smearing occurs because of the blurring step in the noise suppression step, thus reporting a similar area of coverage but under-stating the particle number. In other instances, the GAC outlined the particles, but because of weak edge strengths, the results for area coverage are again understated from the actual area presented in Fig. 2.5 area B.

Since information about the boundaries is incorporated in the implementation of the GAC, it is reasonable to expect outcomes that are of equal or higher quality than those obtained using thresholding. The advantage of GAC over thresholding operations is more apparent if image background and intensity distribution differs from one image to another in the dataset, as described in the previous section. Additionally, information obtained using GAC can be post processed to extract these data about the microstructures or used to reconstruct a 3D model if a series of images are concatenated.
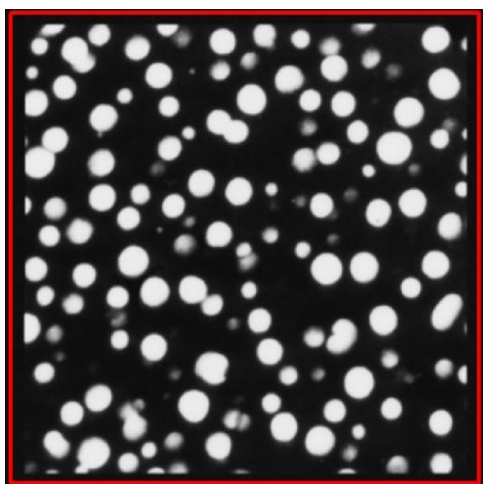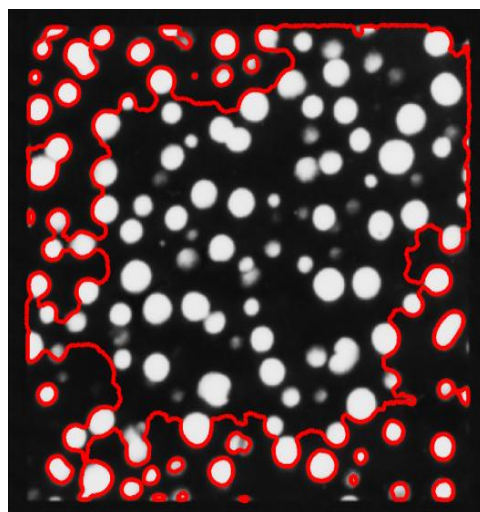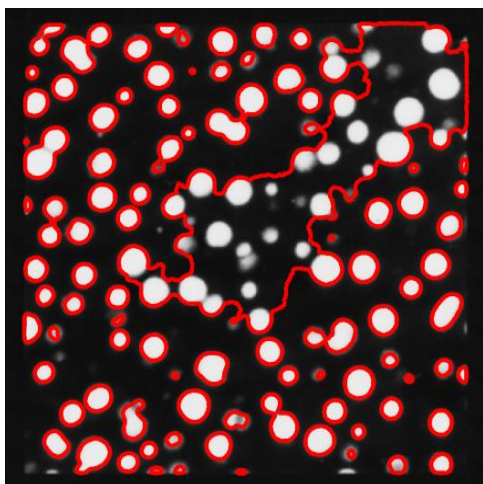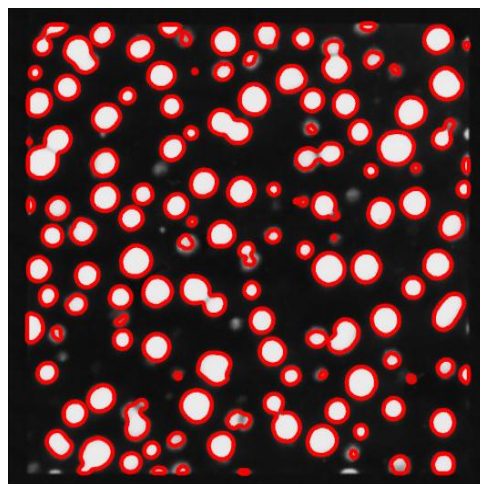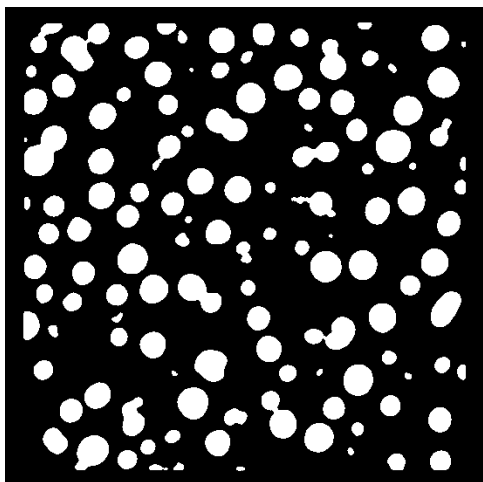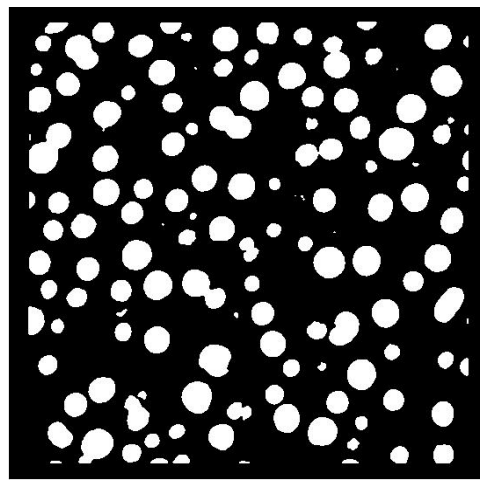
Figure 2.4: Al₃Li δ' precipitate field in Al-2.27Li (wt. %) alloy TEM dark-field micrograph. Progress of GAC across the Al₃Li δ' particle field **(a)** Initial contour within zero-padded zone. **(b)** Contour following 300 iterations. **(c)** Contour following 600 iterations. **(d)** Final contour. At this stage the δ' can be segmented from the matrix. **(e)** Resulting black and white image. In this image the matrix has a pixel intensity of 0 and the bright particles 255 as determined with Matlab software. Prior to segmentation a median filter followed by a 5x5 Gaussian filter with σ = 1 have been applied to eliminate high frequency noise components. GAC parameters: Number of Iterations = 1000. **(f)** Result obtained using thresholding of the δ' precipitate field using Otsu's Method. Solutionized at 550 °C and isothermally heat treated at 190 °C/10m followed by water quenching. Edge-to-edge width for each frame is 2 μm.
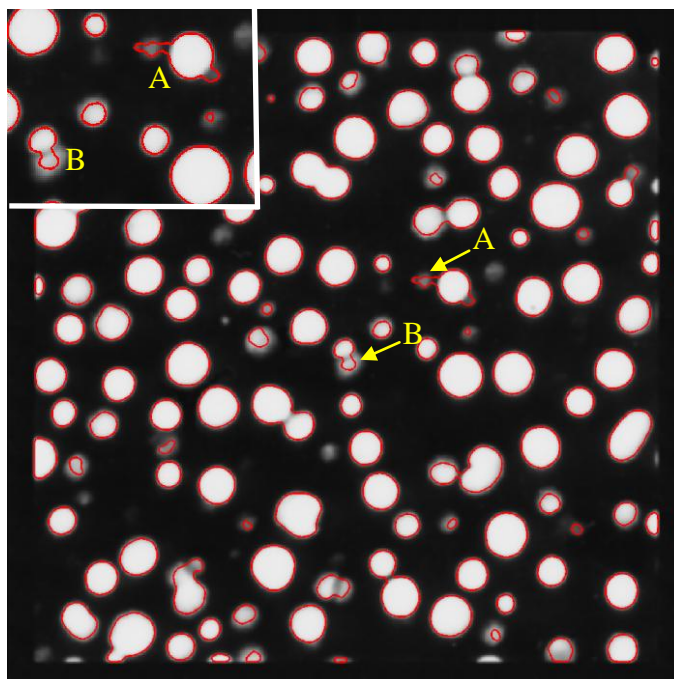
Figure 2.5: Area A and B are two typical errors (overstatement and understatement respectively) that occur when GAC is used.

Table 2.6: Results using various segmentation techniques.

	GAC	*Thresholding*	*Manual*
Number of δ' particles	123	133	136
δ' Area coverage (%)	24.25	24.57	25.74
Time (s)	748*	11*	>1800

*Time measured by MATLAB 7.4.0.287

2.3.6.3 Advanced Active Contour Applications

The examples, so far, demonstrate that GAC represents a solution if the objects of interest exhibit strong boundaries while having higher internal pixel variance or if multiple objects need to be outlined. PAC is employed anytime there is a break in the boundary of interest or if the

65

precise location of the initialization isn't known. The final microstructure illustrates a more sophisticated dataset, which employs GAC and PAC to operate in tandem to outline a multigrained ferrous microstructure with GB bainite (Fig. 2.6). The entire structure can be outlined and segmented without using additional post-processing.
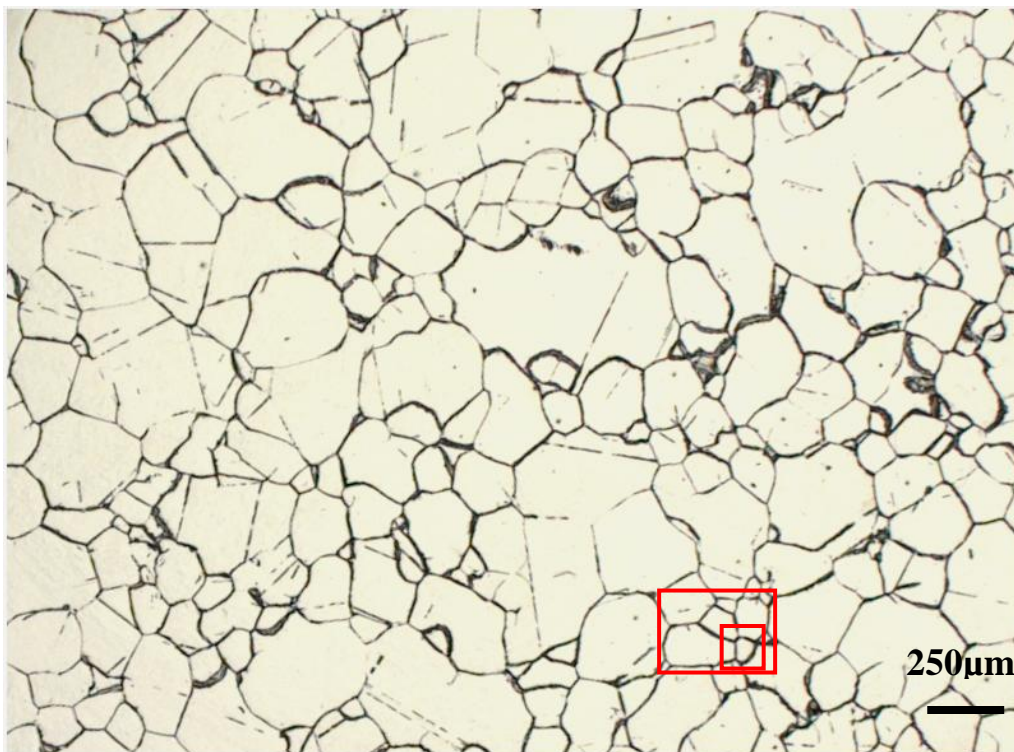
Figure 2.6: Optical image of Fe-0.24C-4Mo (wt. %) isothermally heat treated for 1 day at 560 °C, etched with 2% nital. The grain boundaries are covered with bainite (ferrite + Mo_2C), the matrix is martensite.[hackenberg]

If a user is presented with an image that contains a large number of grains, similar to Fig. 2.6, extracting the data about the microstructure may prove to be a daunting and a time consuming endeavor. Active contours can be used to reduce the time and enhance data quality obtained from the image while eliminating user interaction. To demonstrate the process used in isolating the microstructure from the matrix, first on a much reduced scale, the small square in Fig. 2.6 is selected and shown in Fig. 2.7. Initially, to outline the outer edges of the bainite/martensite boundary GAC is placed on the zero-padded image border (Fig. 2.7a, blue). The GAC will outline all the outside interphase boundaries once set in motion (Fig. 2.7b). Also, in Fig. 2.7b, the red circle is a PAC which will inflate and outline the interior interphase boundaries. PAC is used because it is less sensitive to its initialization location, as shown earlier

in Table 2 and discussed in [li2007]. This is demonstrated in Fig. 2.7b where PAC is initialized off-center. The strategy to select the interior of each grain can vary on the user and the type of microstructure. One approach is to automatically and systematically place a PAC along a grid where the spacing is some fraction of the average grain size. [xu2000, papandreou2007] An alternative approach employed here, because of the strong contrast between the matrix and GB bainite in Fig. 2.6, is choosing a location for initializing the PAC using crude thresholding to segregate the martensite matrix (white) and bainite (black) patches or regions. White patches are then sorted and evaluated for their geometrical center and size. Based on this information, the PAC is initialized at this calculated geometrical center with each PAC radius determined as

$r = \frac{1}{2}\sqrt{\frac{s}{\pi}}$ where r is the radius of the PAC and s is the size of the matrix patch in pixels. The

PAC inflates and fully outlines the interphase boundary between the martensite and bainite (red in Fig. 2.7c). The fully outlined GB bainite can now be segmented and is shown in Fig. 2.7d.

| a | b | c | d |
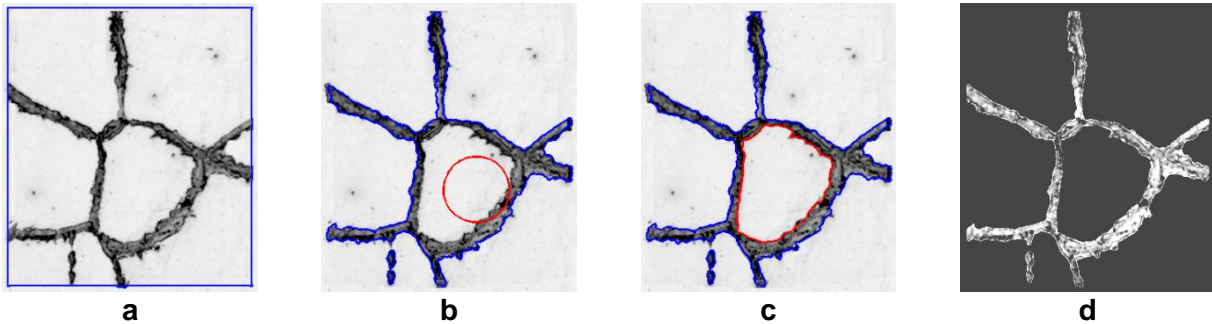
Figure 2.7: (a) GAC (blue) is placed on the zero-padded image border. **(b)** PAC (red) is used to outline the interior of the grain. PAC is initialized off-center to demonstrate PAC's reduced sensitivity to initialization location. **(c)** Completely outlined cell. **(d**) Boundaries of the microstructure are then segmented for further analysis. This correlates to the small square in the Fig. 2.6.

The larger rectangle in Fig. 2.6 contains a higher number of grains than used in Fig. 2.7 and is next selected to illustrate the inclusion of any number of PAC within the grain structures that will all run simultaneously with a GAC. Again, the GAC is initialized on the zero-padded circumference of the image (blue contour). When set in motion the GAC will outline all the exterior phase boundaries. Within each grain interior a PAC is placed according to the strategy noted above. The intermediate step is shown in Fig. 2.8b where the GAC is contracting and the four PACs are all inflating. Important when there is a range of grain sizes is that γ (Eqn. 2.1) is

selected to be higher than 0.2 so that the capture range for the PAC in the large grain (ca. center-left, Fig. 2.8) can be sufficiently wide-ranging (the PAC will move at an accelerated rate to accomplish this) to fully outline the boundary associated with this grain in the time allotted. Once finished (Fig. 2.8c) the segmented grain‑boundary bainite is separated from the martensite (Fig. 2.9). The strategy can be similarly employed for the entire microstructure shown in Fig. 2.6.

a   **b**   **c**
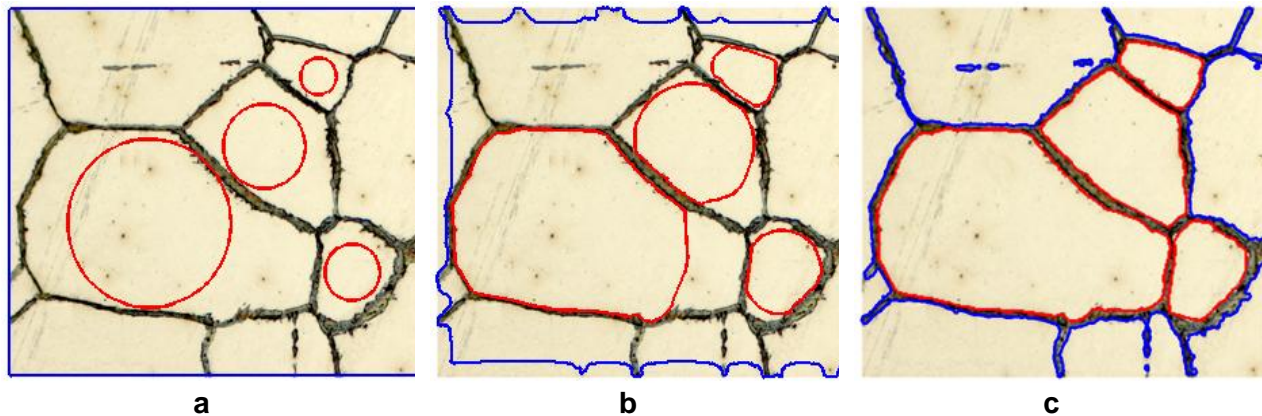
Figure 2.8: The grains selected correlate to the large rectangle in Fig. 2.6. **(a)** Initial placement of PAC (red) and GAC (blue). **(b)** An intemediate step illustrating the advancement of both types of active contours. **(c)** The final outlined micrstructure which can be segmented.
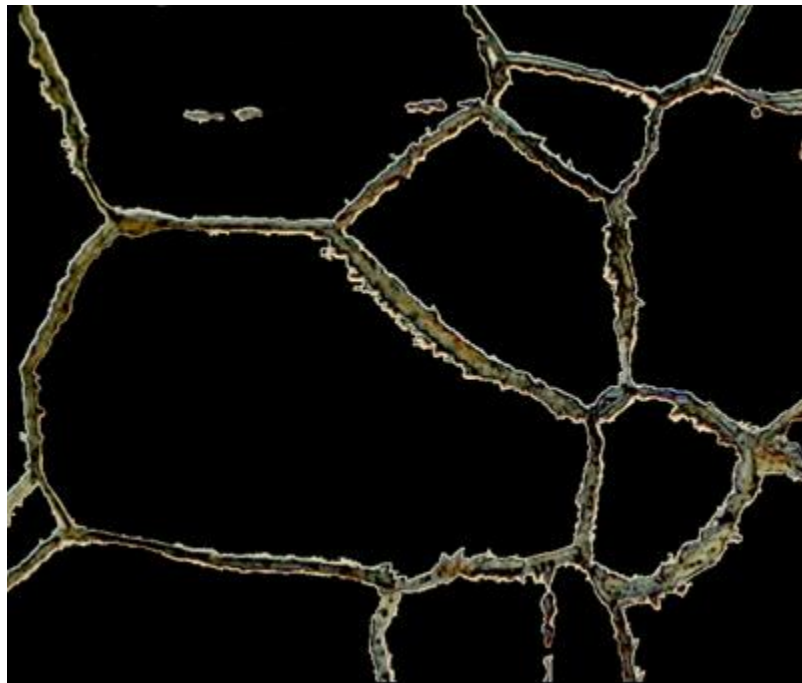
Figure 2.9: Final result of the segmentation shown in the Fig. 2.8 where all the GB bainite is segmented from the matrix. Note the detail of the serrated interphase boundary that the AC captured.

AC provides a consistent way of obtaining geometrical information (area, GB length, growth front) necessary to analyze pearlite. For example, Figs. 2.10b demonstrates how a GAC outlines what appears to be an intragranular pearlite colony (but unlikely) and pearlite growing along the GB. However if information regarding individual phases is sought (cem and α) additional tools are needed. K-clustering algorithm was introduced to the field of materials science to use in conjunction with AC to obtain all the information need to analyze the phase transformation of interest.
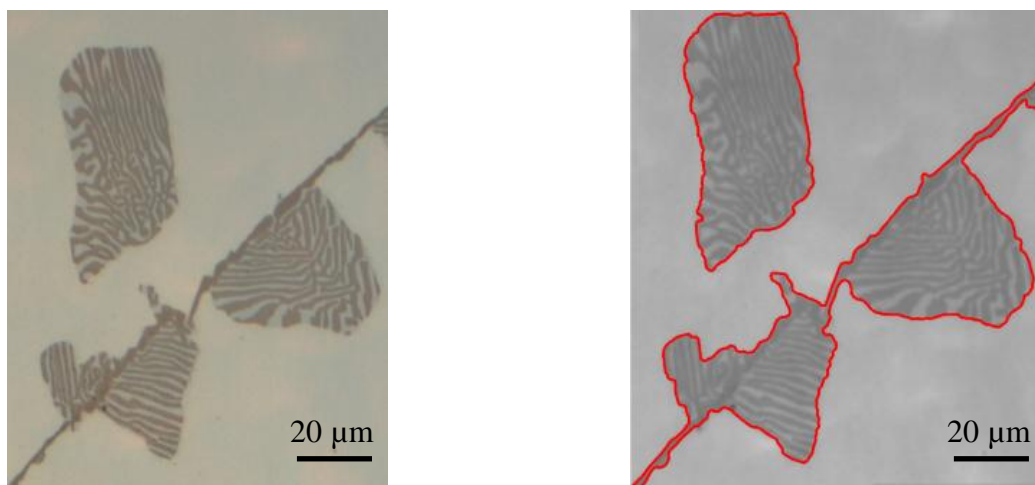
Figure 2.10: Optical image of pearlite colonies **(a)** As taken. **(b)** Outlined using GAC. Sample heat treated at 650 °C for 2 days. The sample is etched using 2% nital.

2.4 K-clustering

Cluster analysis is the task of assigning a set of objects into clusters so that objects in the same cluster are more similar than objects in another cluster. Cluster analysis relies on various algorithms to complete the task of partitioning the objects into different groups. These algorithms can be distinguished based on how the partitioning is accomplished. If the algorithm assigns the object to exactly one cluster it is termed a *strict partitioning clustering* algorithm. If the algorithm assigns an object to more than one cluster the algorithm is termed *overlapping clustering* or *multi-view clustering* algorithm. Furthermore, these algorithms are distinguished on the type of clustering being performed, *e.g.*, centroid‑based, distribution-based, density-based, etc. The rules for selection an appropriate algorithm depend on the application. For this work the goal is to separate various phases into different clusters for further analysis. The algorithm that

was is suited for this type of problem is the strict partitioning k-clustering (centroid-based) algorithm. [lloyd1982]

The k-clustering algorithm is defined as follows. Given a set of observations $(x_1, x_2, x_3, \ldots, x_n)$ where each observation is a d-dimensional real vector k-means algorithm partitions the n observations into k sets $(k \leq n)$ $S = \{S_1, S_2, S_3, \ldots, S_k\}$= minimize the inter-cluster sum of squares so that

$$\arg\min \sum_{i=1}^{k} \sum_{x_j \in S_i} \left\| x_j - \mu_i \right\|^2 \tag{2.6}$$

where μ_i is the mean of points in S_i.
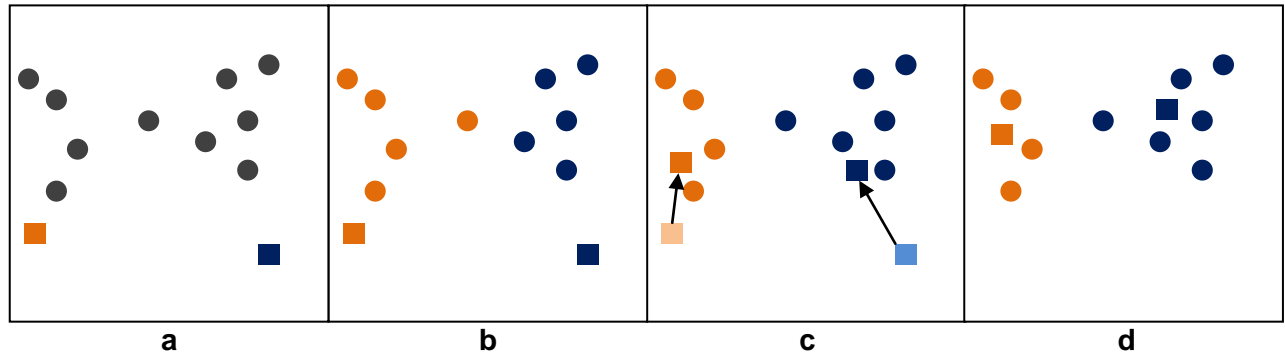
Figure 2.11: The evolution of the k-means algorithm. **(a)** A dataset indicated by black circles and two means (orange and blue squares). **(b)** Each observation in the dataset is assigned to a blue or orange cluster. **(c)** New mean values are computed. **(d)** Each observation is reclassified. The process ends when reclassification stops.

The algorithm is implemented as follows. Given a set observations $(x_1, x_2, x_3, \ldots, x_n)$, black circles in Fig. 2.11a, and k means $\mu_1 \ldots \mu_k$, indicated by the blue and orange squares, each observation is assigned to a cluster according to Eqn. 2.6 so that

$$S_i^{(t)} = \{x_p : \left\| x_p - \mu_i^{(t)} \right\| \leq \left\| x_p - \mu_j^{(t)} \right\| \forall\ 1 \leq j \leq k\} \tag{2.7}$$

where each x_p goes into exactly one $S_i^{(t)}$ as shown in Fig. 2.11b. The means $\mu_1 \ldots \mu_k$ are then updated so that

$$\mu_i^{(t+1)} = \frac{1}{S_i^{(t)}} \sum_{x_j \in S_i} x_j \tag{2.8}$$

This is illustrated in Fig. 2.11c where the previous means are indicated by the lighter blue and orange squares. The algorithm stops when the assignments (Eqn. 2.7) no longer change as shown in Fig. 2.11d.

For this work, the rule for determining the number (k) of sets, each with a unique mean value (μ_i), is twice the number of uniquely colored regions in the image. For example, image 2.12a shows cellular growth of cementite. There are two phases: cementite and austenite. However these phases result in three distinctly colored regions: cementite - white, austenite matrix - light gray, and manganese-depleted austenite - dark gray. The resulting number of sets is 6. Determination of the initial mean values for each set is a heuristic problem. All images obtained during this work are two dimensional matrices having $xDim$ rows and $yDim$ columns with integer pixel value range of [0 255] for black-and-white images and ([0 255], [0 255], [0 255]) for RGB color images. In this case μ_i represents a mean pixel intensity value for a set in question. The initial values for μ_i are determined by $\mu_i^{(initial)} = (1, 2, 3, \dots, k) \times V^{max}/k$, where V^{max} is the maximum pixel value of a $N \times 1$ vector obtained by reshaping the two dimensional image matrix into a one dimensional vector ($N = xDim \times yDim$). The largest pixel intensity value in image 2.12a is 177 and for $k = 6$, the initial $\mu = (29, 59, 88, 118, 148, 177)$. The algorithm evolves as described by the equations 2.7 and 2.8. Once the means are determined, the pixels in the original image are relabeled by assigning a value of 1 (white) to pixels above a given mean and 0 (black) to the pixels below. This process results in a total of six images. Three of those images are shown in the Figs. 2.12b-d. Fig. 2.12b shows an image that appears too white. This is so because $\mu = 56$ is too low (assigning 1 to too many pixels) to sufficiently differentiate between austenite and cementite regions. Fig. 2.12d, on the other hand, shows an image where portions of cementite are now black. This is a result of a mean value that is too high ($\mu = 117$) and too many pixels are being assigned a value of 0. Fig. 2.12c shows an image resulting from $\mu = 117$ and represents the best classifications of austenite and cementite. Visual examination of images 2.12b-c leads to an implementation of a filter based on the total number of objects in the image. Since cementite is white, the goal of the filter is to identify the mean that produces the least number of white objects. This eliminates all means but the one which results in an image shown in Fig. 2.12c. The image in Fig. 2.12c is easily analyzed to estimate the relative amount of cementite by counting the number of white pixels.
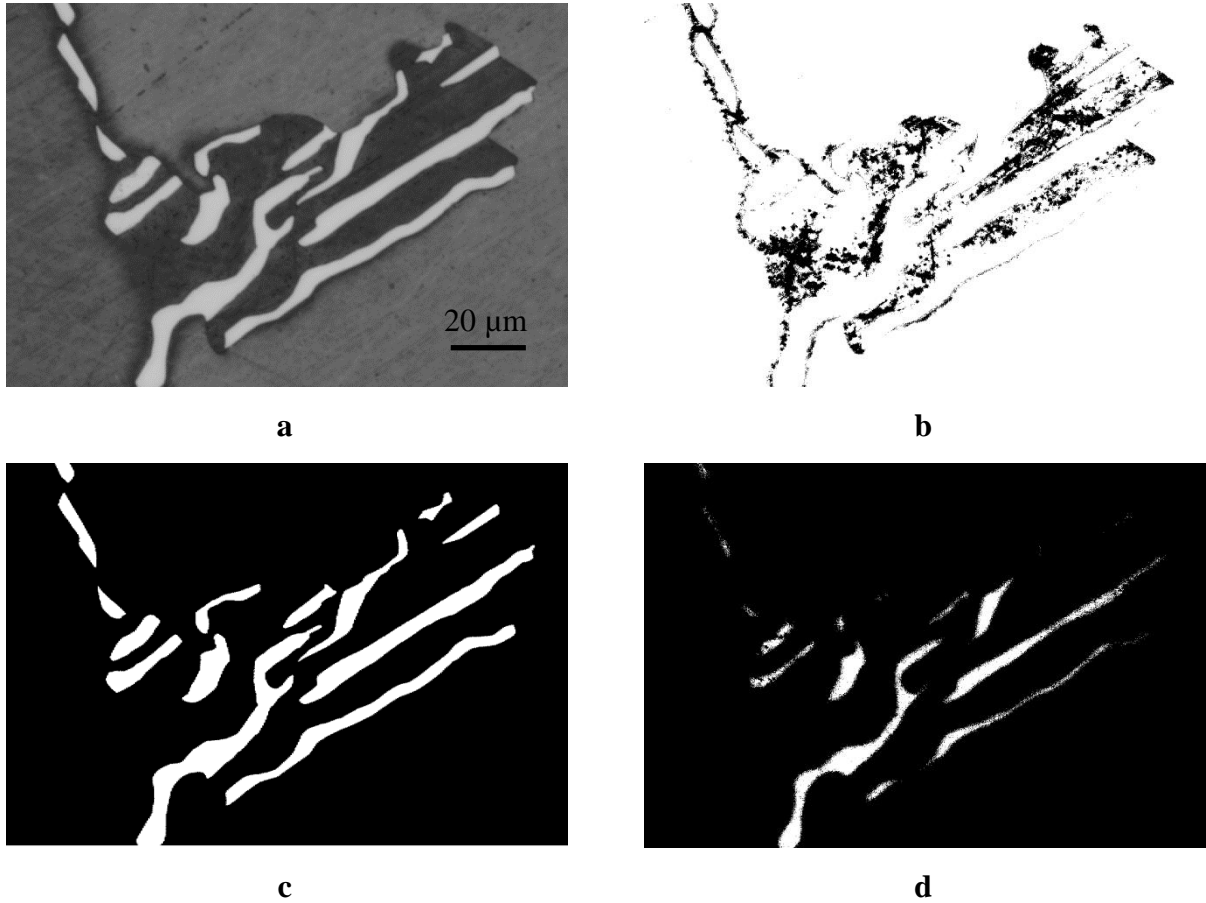
Figure 2.12: Results of k-clustering algorithm. **(a)** Original image. **(b)** $\mu = 56$ **(c)** $\mu = 117$. **(d)** $\mu = 174$. Alloy heat treated at 700 °C for 60 days. Note the difference between the initial (shown in text) and the final values of μ.

2.5 Growth Kinetics

The growth kinetics of the cellular transformation is measured using maximum nodule radius method (MNR) and the methodology introduced by Manna where an average colony size is multiplied by a stereological correction factor $\frac{\pi}{4}$. [manna2001]

The growth kinetics of the pearlite formed was measured using both the MNR method and a technique developed by Cahn and Hagel [cahn1963]. Cahn developed the technique to better account for time dependent transformations in divergent pearlite. Cahn was interested in the measurement of growth rates at the very late stages of transformation, long after hard

impingement had made it difficult to find the size of individual colonies. The technique evaluates the average growth rate, $\bar{G}$, as an instantaneous time rate of change of the volume fraction $\left(\frac{dx}{dt}\right)$, normalized by the instantaneous pearlite surface area, A_f, available for migration.

$$\bar{G} = \frac{1}{A_f} \cdot \left(\frac{dx}{dt}\right) \tag{2.9}$$

The quantities A_f (free pearlite transformation interface area/volume available for migration) and x (volume fraction of pearlite transformed) were measured using active contours and k-clustering algorithms, conforming to the requirements imposed by stereological statistical analysis. [underwood1968] The largest error comes from differentiation of x with respect to time. Cahn and Hagel evaluate $\left(\frac{dx}{dt}\right)$ from the following relationship:

$$\left(\frac{dx}{dt}\right) = \frac{(1-x)\ln\left(\frac{1}{1-x}\right)}{t} \cdot m \tag{2.10}$$

Where m is the instantaneous slope of the log $\ln(1/(1-x))$ vs. log (t) curve. They state that this technique requires almost no subjective judgment and provides an accurate average growth rate.

2.6 Quantatative EDS

In three dimensions, a colony of pearlite consists of a bicrystal of ferrite and cementite. In planar sections the phases appear as lamellae which grow with a common front into the austenite. To accurately measure chemical composition at a point with SEM-EDS it is important to measure lamellae that are perpendicular to the plane of polish to circumvent the influence of overlapping adjacent lamellae. Furthermore, the beam size must be small enough to ensure that the interaction volume associated with beam conditions acquires most, if not all, of the signal from the lamella of interest. Data on iron and manganese are acquired. As noted in (section 1.2), quantitative measurement of carbon content is not yet possible with the conventional EDS techniques, therefore, the variable, U_{Mn}, is used.

The manganese and iron standards along with, an as-quenched section of the alloy and the sample of interest were mounted together and loaded into the JEOL 6700F SEM. Accelerating voltage was set to 15kV. Current was measured using a Faraday's cup which was approximately 0.10 nA. Dead time was less than 20%. Total number of counts was larger than

73

10,000. When the feature of interest was located, the sample was titled -10 to +10 degrees in 1 degree increments and analyzed. The largest and smallest values of U_{Mn} for cementite and ferrite, respectively, were recorded. U_{Mn} values for austenite (depleted and retrenched) are reported as ranges.

Selected samples were also investigated using analytical TEM to confirm values obtained using SEM‑EDS. A standard, as-quenched, homogenous sample was analyzed using SEM-EDS. A TEM foil was made from the same material to obtain the k value (1.05 ± 0.01) and confirm that that was no preferential absorption or fluorescence effects over the ranges of foil thickness encountered. Relative foil thickness was determined using electron energy loss spectroscopy (EELS). A standard Cliff‑Lorimer ratio approach was used for quantification of the x‑ray spectra

$$U_{Mn} = k \frac{I_{K\alpha}^{Mn}}{I_{K\alpha}^{Mn} + I_{K\alpha}^{Fe}} \tag{2.11}$$

where I is the number of counts in the K_{α} peak of the spectra. Background subtraction for each collected x-ray spectra was carried out using the Spirit and TIA software packages for SEM‑EDS and TEM respectively. [cliff1975] All further quantifications steps were carried out manually using a spreadsheet.

2.8 Crystallography

Crystallographic studies were carried out with diffraction techniques using the FEI-Titan 80-300, Jeol 2000 FX TEMs and JSM840-EBSD. There are two phases that required crystallographic confirmation: ferrite phase, since it is a non-equilibrium phase, and the phase that replaced ferrite when equilibrium is approached, termed γ^r in the previous chapter. Each phase was analyzed using TEM selected area diffraction (SAD) technique. To confirm the ferrite phase, diffraction patterns were taken at three different zone axes on the same crystal and their angular relationships was recorded from the goniometer. Theoretical angles between the three zone axes were computed and compared to the experimentally obtained angles. Unless specified otherwise, crystallography and orientation relationship for the rest of the samples were studied using JSM840-EBSD, a technique more suitable due to the large number of samples and lengthy heat treatment times. The technique also provides the ability to view each measurement in the contexts of the microstructural location.

2.9 Calculations

Thermodynamic examinations were done using Thermo-Calc version S with TCS Steels/Fe-alloys database v. 6 and MatCalc with mc_sample_fe database v. 1.15 software packages coupled with the experimental observations made during the course of this study.

Chapter 3 – Results

This chapter presents data characterizing chemical, crystallographic, and morphological evolution. Results associated with all of the observed phase transformations are compiled into a time-temperature-transformation (TTT) diagram. Results used to build the TTT diagram are listed by temperature. Each temperature section starts with images representative of the phase transformations encountered during the course of the isothermal heat treatment. Tables showing computed equilibrium information and quantitative morphological and chemical information are shown next. Conditions and assumptions associated with the equilibrium calculations are listed in the opening section (last paragraph) of Chapter 4. Each temperature section is capped by a summary of the encountered phase transformations highlighting points needed for the discussion in Chapter 4.

3.1.1 Color Metallography

This (3.1.1) and the following sub‑section (3.1.2) validate color metallography as a tool for phase characterization employed to identify and quantify (ex: use of color metallography with k‑clustering to evaluate volume fraction of a phase) phase transformations encountered during the course of this work. Fig. 3.1a shows a typical pearlite colony, in a sample heat treated at 650 °C for 180 days. The sample is etched with 2% nital, which highlights ferrite (α) and boundaries (both grain and interphase). There is also a halo running along the perimeter of the pearlite colony. The image lacks contrast and that presents a considerable challenge for image processing techniques introduced in the previous chapter. Rectification of this matter requires user supervision and additional processing time, two factors these algorithms sought to eliminate. Application of the modified Klemm's tint accommodates image processing algorithms by introducing color metallography. Furthermore, use of color metallography permits visual identification of phases not possible with 2% nital.

Results of the modified Klemm's tint are shown in Fig. 3.1b. The following color scheme is observed while using Klemm's tint: austenite – various shades of brown (often indicative of the relative orientation relationship of the grains) and in one case dark blue, ferrite – various shades of blue and occasionally brown (but only when ferrite dissolution is observed), cementite

– white. There is, however, no known trend associated with the particular shade of color and the composition or orientation of the phase. The halo region is now brown (though a different shade of brown than the austenite matrix), indicating that it is austenite, and also appears mottled when compared to bulk austenite as shown in Fig. 3.1b. Note that modified Klemm's tint emphasizes scratches and pits more than 2% nital etch. Nonetheless, Klemm's tint provides sufficient contrast differential for image processing purposes and good starting points for additional studies (ex: SEM-EDS and SEM-EBSD).

Further characterization of the halo region shows that it has face-centered cubic (fcc) crystal structure with manganese content less than bulk austenite. Orientation relationship of the halo region is the same as the austenite grain into which pearlite colony grows. When compared to the samples heat treated at 650 °C for earlier times, volume fraction of ferrite decreases while the volume fraction of cementite remains approximately constant. It is concluded that the halo represents an area of ferrite retrenchment being reclaimed by the austenite. Consequently, the area is tentatively termed retrenched austenite and assigned the abbreviation γ^r.

A   **b**
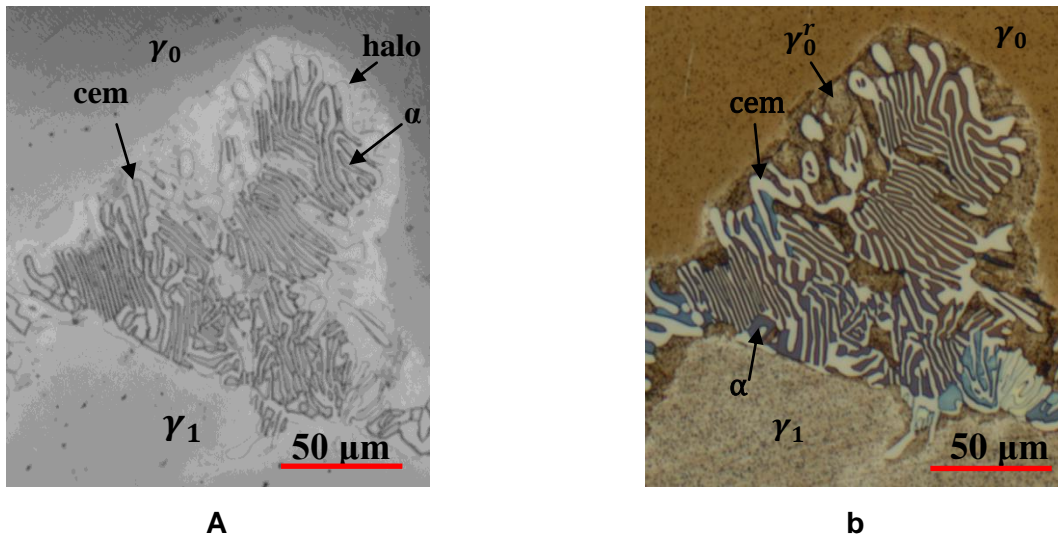
Figure 3.1: Optical images the same pearlite colony in a sample heat treated at 650 °C for 180 days. **(a)** Etched using 2% nital. Ferrite (α) appears as gray lamella, cementite (cem) is assumed to be between the ferrite plates within the colony. Note the halo region around the perimeter of the colony. **(b)** Tinted using modified Klemm's tint (composition in text). Cementite appears white, ferrite is various shades of blue, austenite (γ) and halo (γ^r) are of various shades of brown. The halo appears mottled when tinted using modified Klemm's tint. Phases have been verified using TEM SAD technique (see next section).

Another (inadvertently recognized) advantage of the modified Klemm's tint is its ability to discriminate between pearlite and cellular colonies. This attribute ruled out 2% nital etch as adequate for revealing and quantifying morphological progress of phase transformations. An example of the differences is shown in Figs. 3.2a and b. The upper limit (based on the concepts of local equilibrium) for ferrite formation in this alloy is approximately 685°C. Fig. 3.2a shows a sample heat treated at 690 °C for 14 days etched using 2% nital. Initially, the area between the two cementite lamellae was erroneously classified as ferrite. Fig. 3.2b shows the same area tinted using modified Klemm's tint. The product appears to have characteristics of a cellular colony. Further crystallographic and chemical investigations confirm characteristics of the cellular colony. Notice also the depleted austenite between the two cementite plates is a lighter shade of brown compared to the matrix.

a   **b**
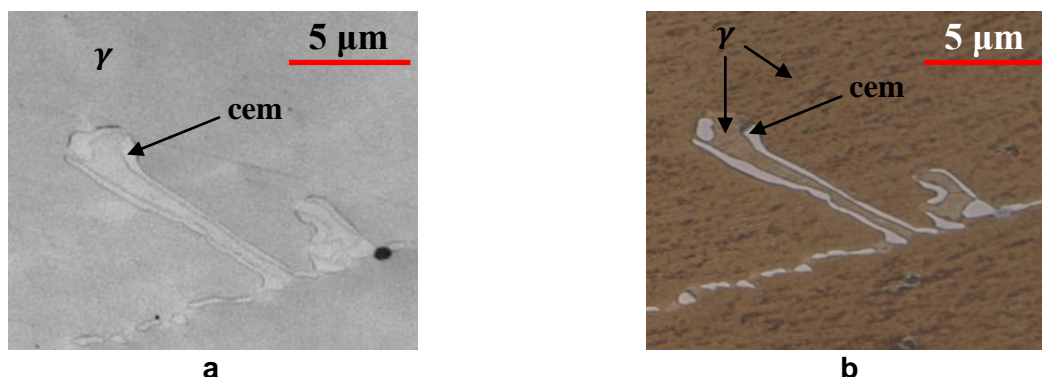
Figure 3.2: Optical images of a cellular colony. **(a)** Etched using 2% nital etch. **(b)** Tinted using modified Klemm's tint. Note the increased pitting associated with the Klemm's tint. Sample heat treated at 690 °C for 14 days.

3.1.2 Phase Confirmation

For the Fe-0.85C-11.56 (wt. %) alloy, ferrite is a non-equilibrium phase at temperatures above 623 °C. Formation of ferrite is verified crystallographically and chemically. Crystallographic results are shown in Figs 3.3-3.6 and Table 3.1 for a sample heat treated at 650 °C for 2 days. The experimentally obtained angles between the planes in the same ferrite crystal are in agreement with theoretically expected angles, confirming that the area under investigation has a body-centered cubic (bcc) crystal structure, Fig. 3.6 and Table 3.1.

a

b
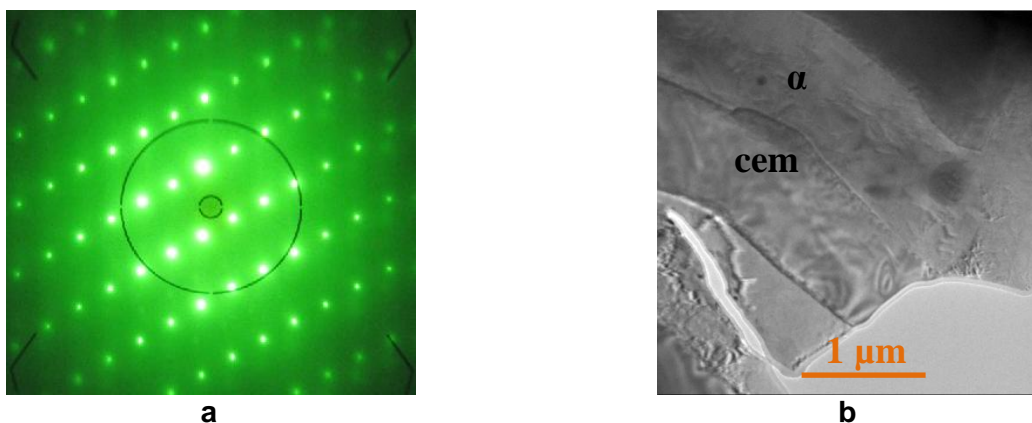
Figure 3.3: (a) <011> zone axis of presumed α-ferrite. **(b)** Brightfield image of the area where diffraction pattern is acquired. Fe-0.85C-11.56Mn (wt. %) alloy heated treated at 650 °C for 2 days.

a

b
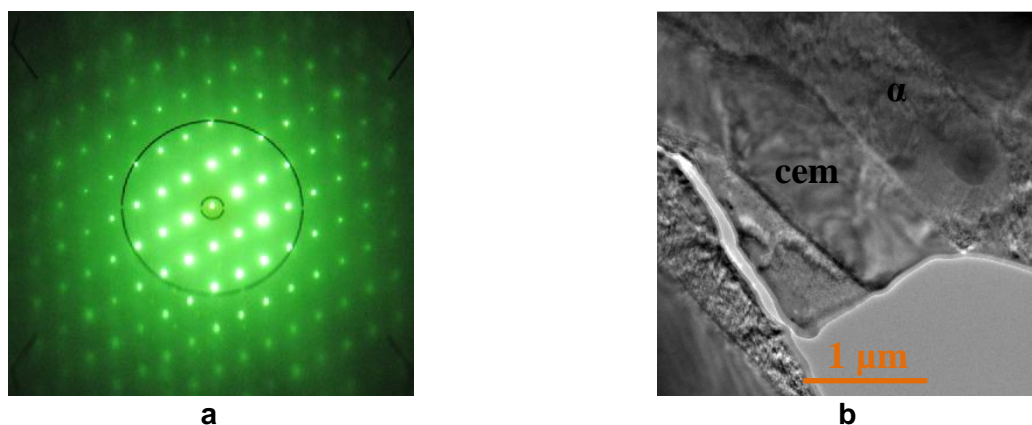
Figure 3.4: Same area as Fig. 3.3. **(a)** <$\bar{1}$33> zone axis of presumed α-ferrite. **(b)** Brightfield image of the area where diffraction pattern is acquired.

a

b
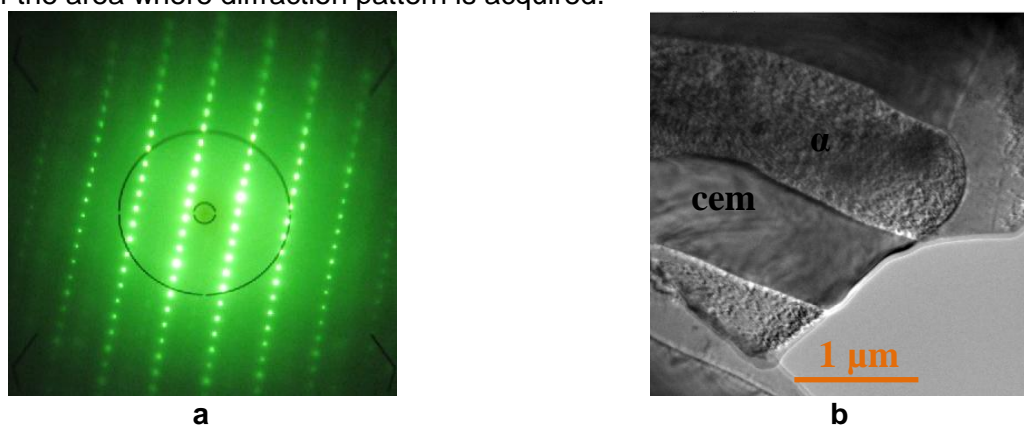
Figure 3.5: Same area as Fig. 3.3. **(a)** <$\bar{1}$31> zone axis of presumed α-ferrite. **(b)** Brightfield image of the area where diffraction pattern is acquired.
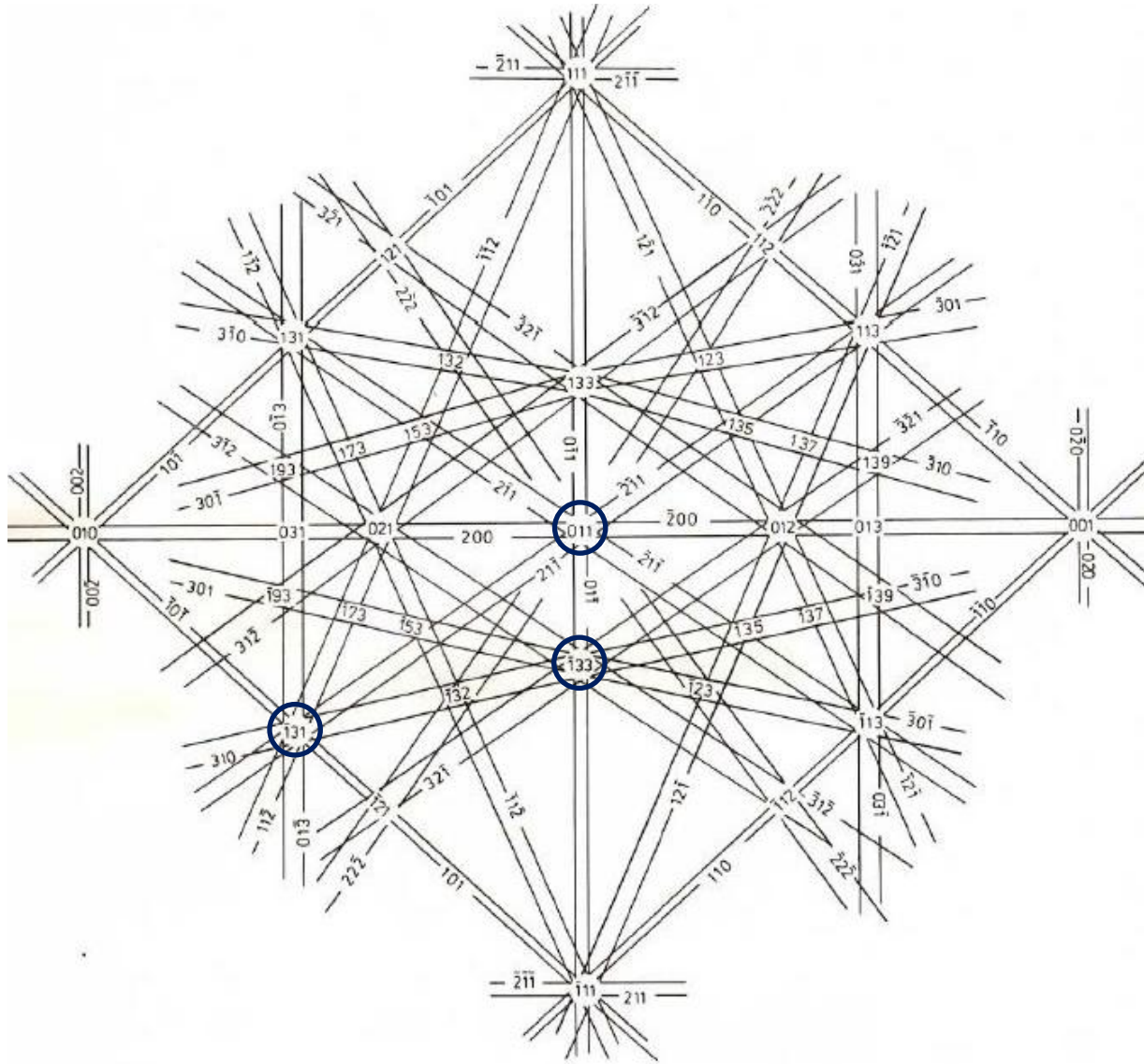
Figure 3.6: Schematic Kikuchi map for a BCC crystal centered at [011]. Experimentally observed planes, shown in Figs. 3.3-3.5, are circled.

Table 3.1: Computed vs. observed angles for the ferrite crystal (α) in Fe-0.85C-11.56Mn (wt. %) alloy heated treated at 650 °C for 2 days.

Planes	Computed Angle	Observed Angle	Difference
(-131) ∩ (011)	31.48	28.86	2.6
(-133) ∩ (-131)	25.94	22.22	3.7
(011) ∩ (-133)	13.26	10.56	2.7

Quantitative TEM-EDS for the same crystal gave $U_{Mn} \approx 0.02$, a result consistent with the $U-$ fraction expected for ferrite. Following the same procedure, it is determined that retrenched austenite (γ^r) has a fcc crystal structure, with angles shown in Table 3.2. U_{Mn} of retrenched austenite has less than bulk austenite but higher than ferrite. Table 3.3 summarizes

morphological and crystallographic characteristics of phases observed, providing a key for interpretation of image data in the following sections.

Table 3.2: Computed vs. observed angles for the retrenched austenite (γ^r) crystal in Fe-0.85C-11.56Mn (wt. %) alloy heated treated at 650 °C for 60 days.

Planes	Computed Angle	Observed Angle	Difference
111 ‖ 110	35.26	32.05	3.2
111 ‖ 321	22.20	21.87	0.33
110 ‖ 321	19.10	17.21	1.9

Table 3.3: Summary of crystal structure and morphological apperance for experimentally observed phases.

Phase	Austenite (γ)	Ferrite (α)	Cementite (cem)	Retrenched austenite (γ^r)	Manganese-depleted austenite (γ^d)
Appearance	Smooth	Smooth or Porous	Smooth	Mottled and Porous	Mottled or Pitted
Crystal Type	FCC	BCC	Orthorhombic	FCC	FCC

3.2 Experimental Data

A summary of all the heat treatments employed for the collected data is shown as a TTT diagram (Fig. 3.7). Quantitative information for each temperature-time range is listed in the respective tables of the temperature sections. Listing of a product on a TTT diagram but not in the corresponding time-temperature Table indicates presence of the product phase in negligible amounts. This is usually the case for early stages of grain boundary cementite precipitation and ferrite formation. The following abbreviation key is deemed helpful for the interpretation of the Table data.

Φ^{phase} – volume fraction of the phase indicated by the superscript.

$U_{element}^{phase}$ – Average (averaged over at least 10 data points) U-fraction of the element, indicated by the subscript, in the phase, indicated by the superscript. If the phase is a pearlite constituent (cementite or ferrite), this value represents the average U-fraction in the lamellae.

cem-type – cementite where the type is: **gb** – grain boundary, **p** – pearlitic cementite, **c** – cellular cementite, or **sph** – spherodized cementite.
α – ferrite.
γ-bulk – austenite prior to decomposition.
γ – austenite matrix depleted of carbon but well removed from any phase transformations.

γ^d – manganese-depleted austenite regions of cellular colonies. U-fraction for manganese-depleted austenite is reported as a range with high and low values.

γ^r – retrenched austenite in pearlite colonies. U-fraction for retrenched austenite is reported as a range with high and low values.

$\lambda_{phase}^{reaction}$– width of the phase indicated by the subscript. Reaction can be pearlite or cellular.

Nodule Size for both pearlite and cellular colonies:

MNR – Maximum Nodule Radius.

Gust: $(average\ nodule\ size) \times \frac{\pi}{4}$ and applies to cellular colonies only.
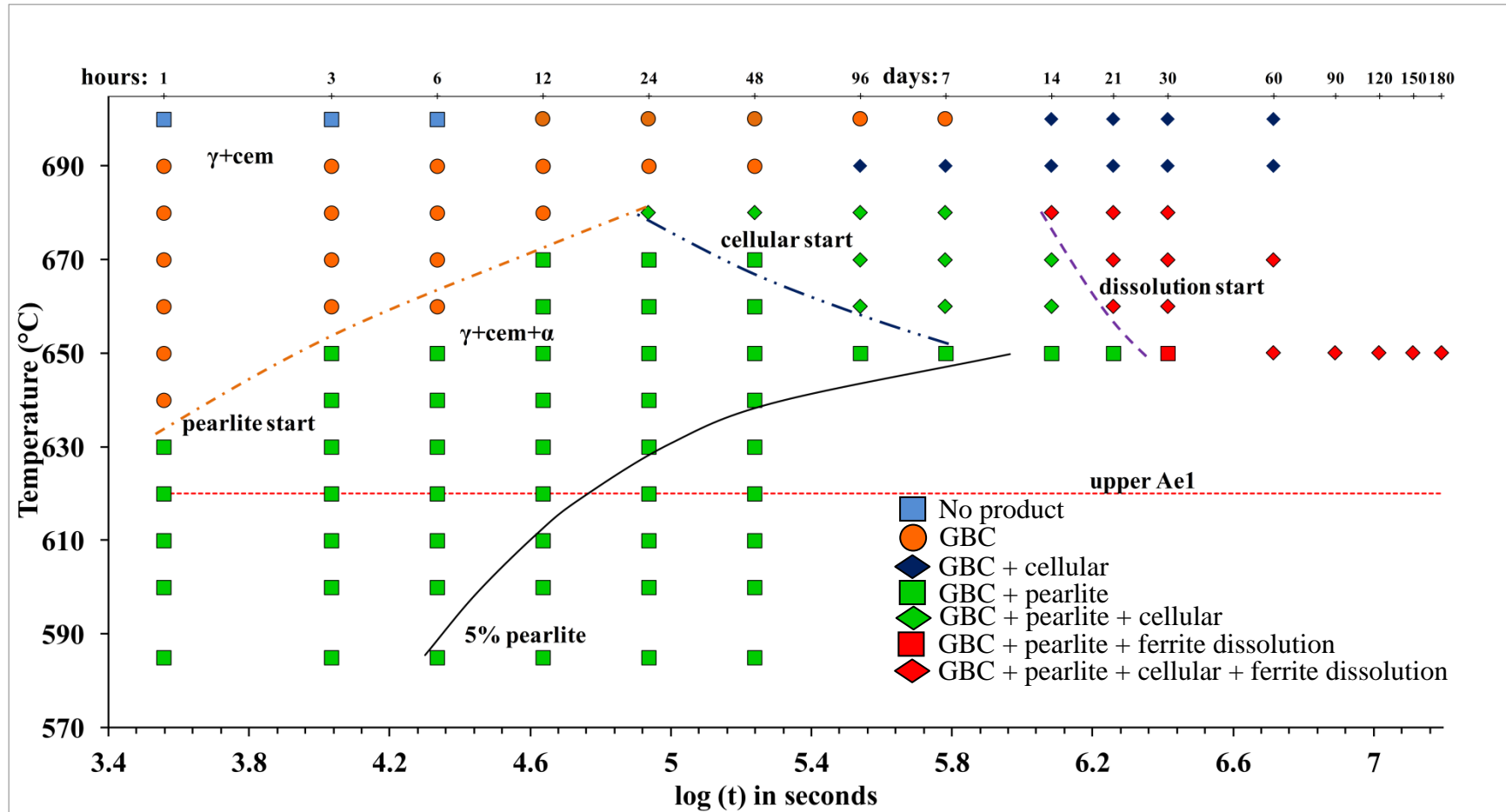
Figure 3.7: TTT Diagram for Fe-0.85C-11.56Mn (wt. %) alloy. Acm ~ 785 °C

3.2.1 750 °C

This temperature is selected so that the non-equilibrium pearlite region can be approached from above and may give some insight into pearlite systematics to come. The strategy is appropriate because higher temperatures imply smaller undercooling and small ΔG, which means less energy is available for various reaction paths.

Table 3.4: Predicted equilibrium volume fraction (Φ) and composition for cementite and austenite phases for the Fe-0.85C-11.56Mn (wt. %) alloy at 750 °C.

Φ^{cem}	U_{Mn}^{cem}	U_C^{cem}	Φ^{γ}	U_{Mn}^{γ}	U_C^{γ}
1.65×10^{-2}	2.72×10^{-1}	3.33×10^{-1}	9.83×10^{-1}	1.16×10^{-1}	3.52×10^{-2}

Comments

At this temperature, the assumption of local equilibrium at the interphase interface predicts no ferrite formation. Table 3.4 shows computed equilibrium volume fraction and manganese content cementite and austenite (γ) phases. No phase transformations are observed after 120 days of isothermal heat treatment.

3.2.2 700 °C

This temperature is selected as a continuation of the strategy to approach the non-equilibrium pearlite region from above to obtain any information that gives insight into pearlite systematics to come. Images in Fig. 3.8 illustrate typical morphology of cellular colonies observed at this temperature. Images on the left are optical micrographs of the microstructures with corresponding SEM image shown on the right.

Figure 3.8: Optical (**left**) and SEM images (**right**) illustrating typical microstructural evolution in the alloy at 700 °C. Phases marked with orange text are verified using EBSD.
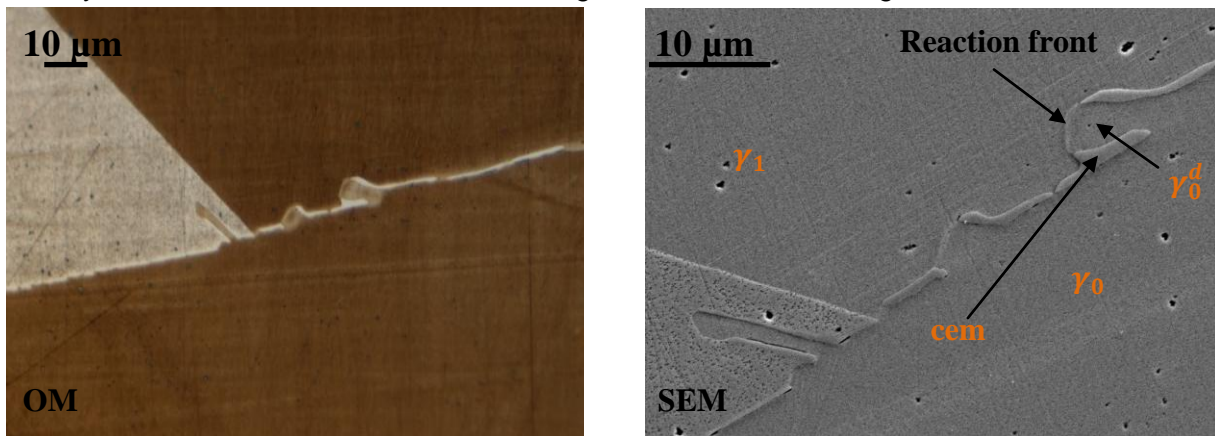
(a) Sample heat treated for 14 days.
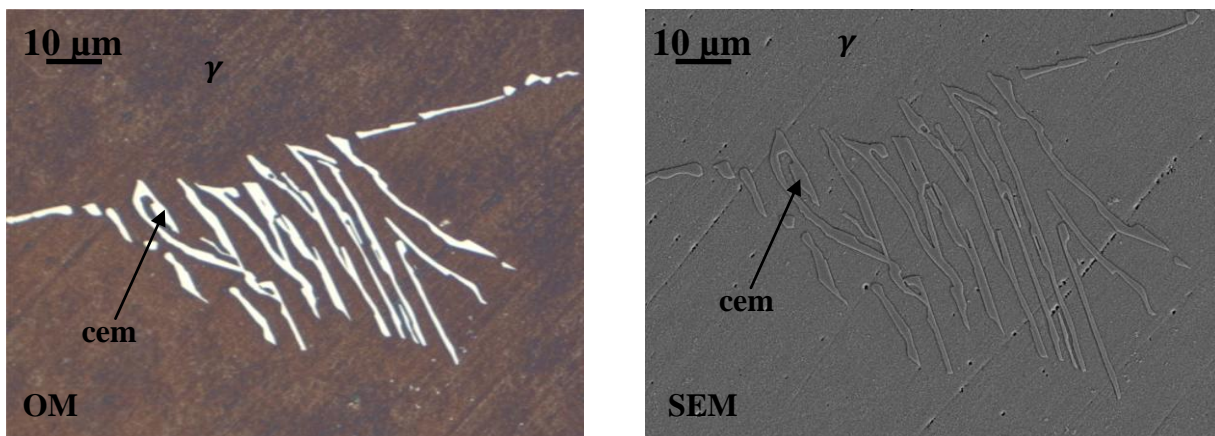
(b) Sample heat treated for 21 days.
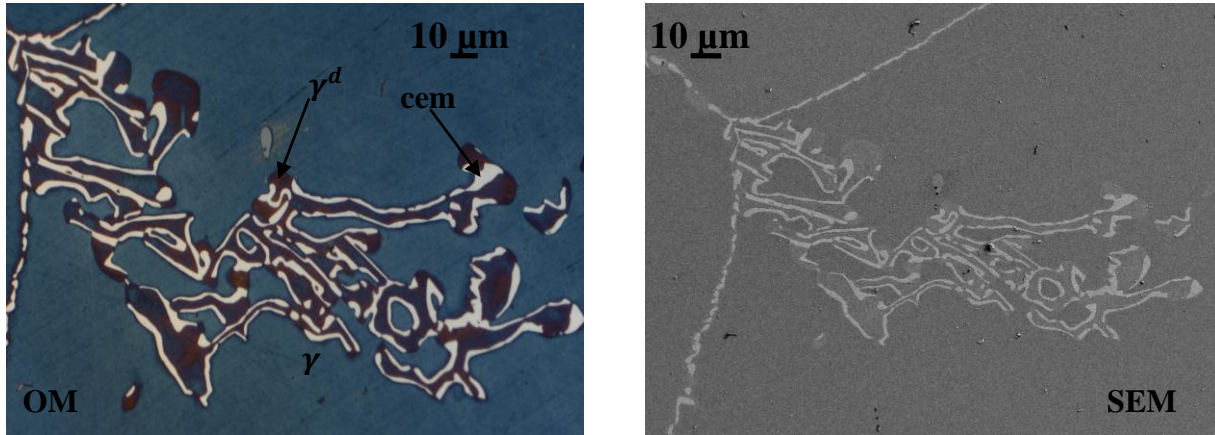
(c) Sample heat treated for 60 days.

Table 3.5a: Predicted equilibrium volume fraction and composition for cementite and austenite phases for the Fe-0.85C-11.56Mn (wt. %) alloy at 700 °C.

Φ^{cem}	U_{Mn}^{cem}	U_C^{cem}	Φ^{γ}	U_{Mn}^{γ}	U_C^{γ}
3.85×10^{-2}	2.85×10^{-1}	3.33×10^{-1}	9.62×10^{-1}	1.12×10^{-1}	2.90×10^{-2}

Table 3.5b: Experimental data for the alloy heat treated at 700°C. Nodule sizes are rounded to the nearest integer.

HT time (days)	Φ^{cem} $\times 10^{-2}$	Φ^{γ^d} $\times 10^{-2}$	$\lambda_{cem}^{cellular}$ (μm)	$\lambda_{\gamma^d}^{cellular}$ (μm)	Nodule Size	
					MNR (μm)	Gust (μm)
14	1.2	2.9	1.2	3.2	5.1	4.2
21	1.2	2.9	2.5	5.8	239	122
30	2.8	7.0	2.7	6.2	304	135
60	3.2	8.2	3.9	9.2	467	228

Table 3.5c: Summary of EDS and EBSD results for the alloy heat treated at 700°C. Blocks highlighted in blue have been confirmed using EBSD that they are the austenite component of the cellular colony. Blocks highlighted in gray indicate no experimentally observed information about the phase.

HT time (days)	U_{Mn}^{cem-gb} ± 0.01	U_{Mn}^{cem-c} ± 0.01	$U_{Mn}^{\gamma^d-low}$ ± 0.01	$U_{Mn}^{\gamma^d-high}$ ± 0.01	$U_{Mn}^{cem-sph}$ ± 0.01
14	0.21	0.21	0.09	0.10	
21	0.20	0.20	0.07	0.10	
30	0.21	0.20	0.05	0.10	0.21
60	0.21	0.21	0.06	0.10	0.22

Comments

Figs. 3.8a-c show images representative of the cellular colonies composed of cementite and manganese-depleted austenite (γ^d) observed during the progress of the phase transformation. Table 3.5a shows computed equilibrium volume fraction and manganese content of cementite and austenite phases. Tables 3.5b and c provide morphological and compositional characterization of the phase transformation over time, which is consistent with cellular decomposition, described in the previous chapter.

Grain boundary cementite and cellular decomposition are observed after 12 hours and 14 days, respectively. [10] The amount of grain boundary cementite prior to 14 days, presence of which is reflected on the TTT diagram in Fig. 3.7, is very small and is not listed in the Table 3.5b. Spherodized cementite initially appears after 30 days. Large cellular colonies are well developed, absent of impingement, but not numerous (at most 6 per sample). The number of small colonies, some as small as two cementite lamellae, is large. The appearance of the manganese-depleted austenite is smooth at times but mostly mottled. The width of cementite and the manganese-depleted austenite, as well as the size of the largest colony and the average colony size all increase during the course of the reaction (Table 3.5b).

U_{Mn}^{cem-c} and U_{Mn}^{cem-gb} remain approximately constant for the duration of the reaction. Both values are smaller than equilibrium predicted $U_{Mn}^{cem} = 0.285$. $U_{Mn}^{\gamma^d}$ ranges from 0.05 (low) to 0.10 (high), with lower values closer to the moving reaction front. Manganese distribution in the manganese-depleted austenite is consistent with the systematics of cellular decomposition which will be discussed in greater detail in Chapter 4 (Figs. 4.3 and Fig. 4.5).

---

[10] Note that the indicated start times are when the particular transformation is first observed. Given the large time gaps between sample heat treatments the initiation of the transformation lies between the reported time and the previous one.

3.2.3 690 °C

This temperature is the continuation of the strategy to approach the non-equilibrium pearlite region from above. Additionally this temperature evaluates prediction of pearlite formation based on the analysis by Hutchinson and Shiflet, which predicts pearlite in the vicinity of ~ 687 °C. [hutchinson2004] Images in Fig. 3.9 illustrate typical morphology of cellular colonies observed at this temperature. Figs 3.9 c, d and, e show examples of manganese-depleted austenite appearing smooth, pitted, and mottled.

Figure 3.9: OM and SEM images illustrating the microstructural evolution in the alloy at 690 °C. Phases marked with orange text and listed compositions shown in the images have been verified using EBSD and EDS respectively.
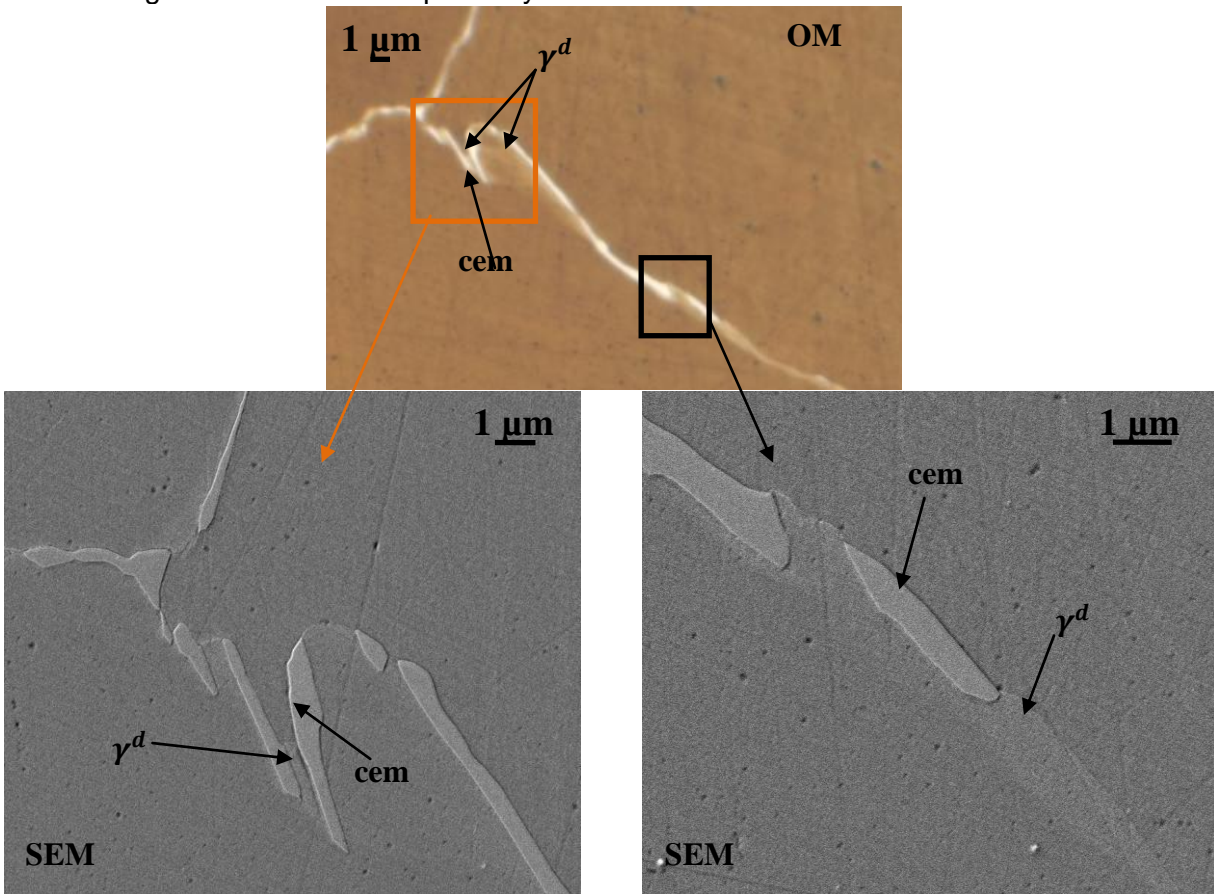
(a) Top – Optical image showing grain boundary cementite and cellular colony (orange rectangle), and manganese-depleted austenite (black rectangle) in a sample heat treated for 4 days. **Bottom left:** SEM image showing cellular colony. **Bottom right:** Grain boundary cementite.
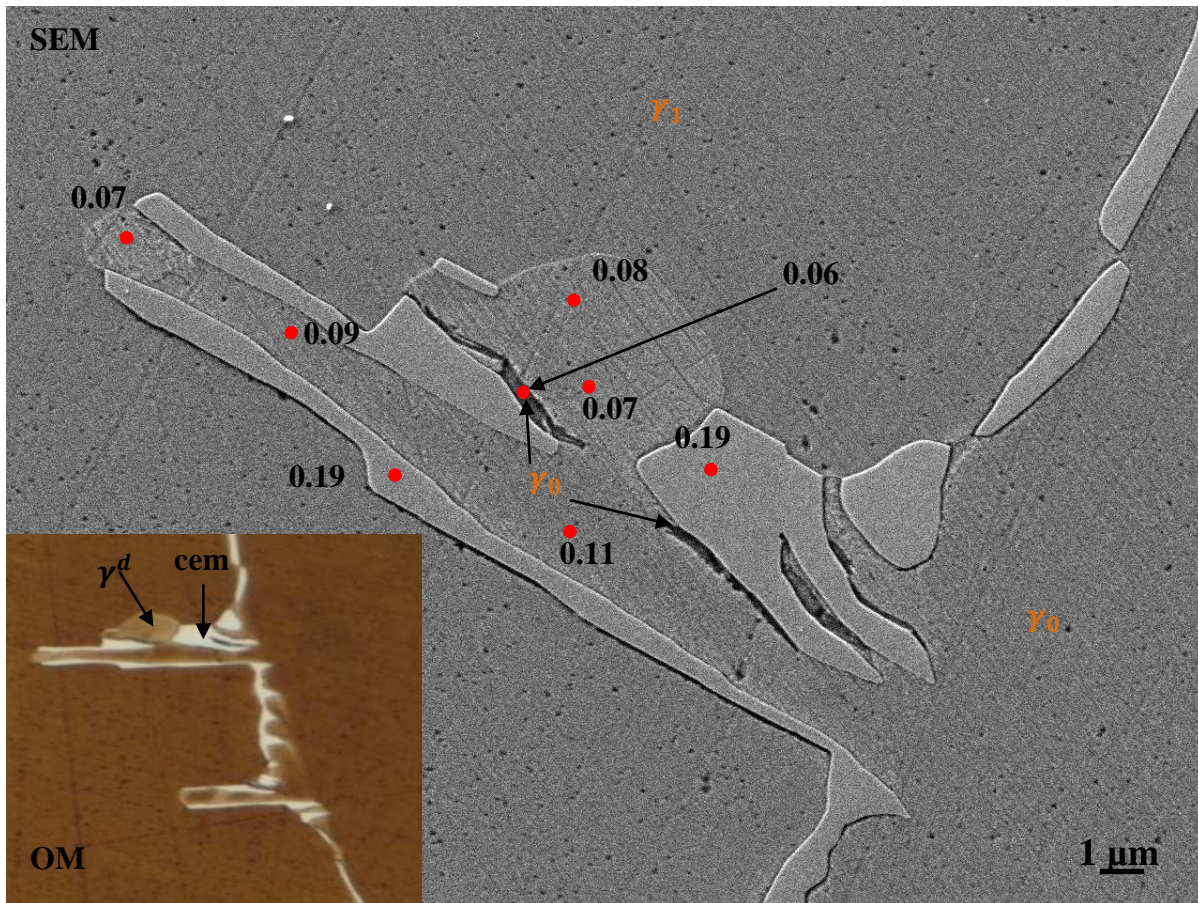
(b) SEM image with OM image insert showing a cellular colony for a sample heat treated for 4 days. Note the black areas adjacent to the cementite lamellae indicated by the arrows and observed using OM and SEM.
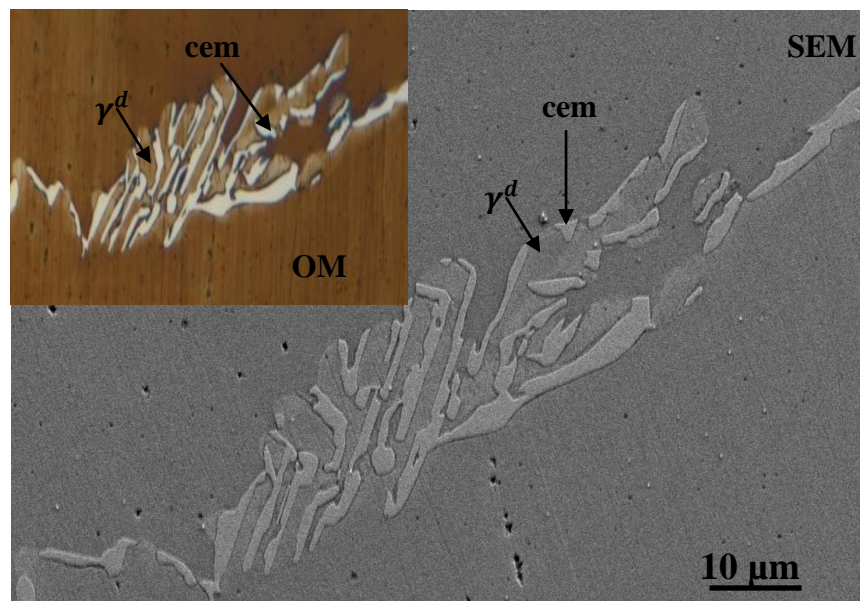
(c) SEM image with OM image insert showing a cellular colony for a sample heat treated for 7 days.
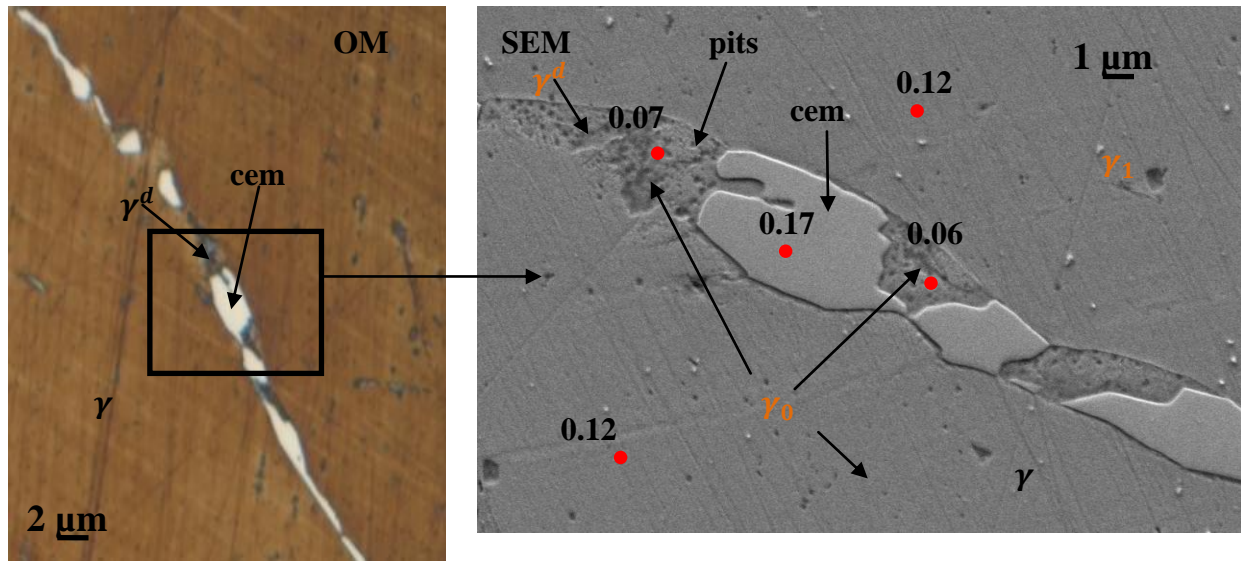
(d) Images of grain boundary cementite in a sample heat treated for 7 days. **Left:** OM with area enclosed by the black rectangle shown on the right. **Right:** Note the manganese content and pitted appearance of the manganese-depleted austenite adjacent to the cementite.
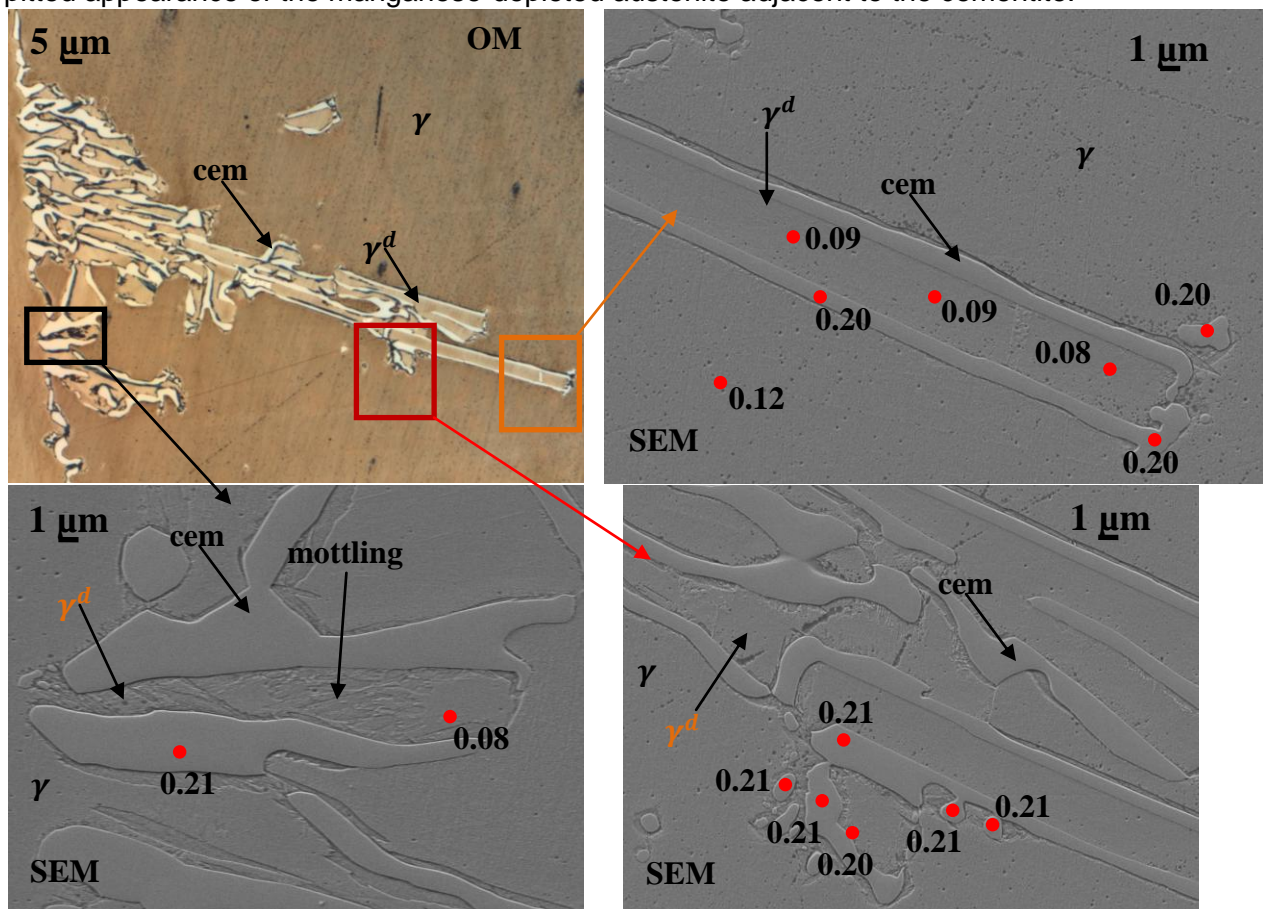
(e) Cellular colony in a sample heat treated for 60 days. **Top left:** Optical image of the colony. **Top right:** SEM image of the area selected by the orange rectangle. **Bottom left:** SEM image of the area selected by the black rectangle. Note the mottled appearance of the manganese-depleted austenite (unlike the pitted appearnce shown in **(d)**) **Bottom right:** SEM image of the

area selected by the red rectangle.

Table 3.6a: Computed equilibrium volume fraction and composition for cementite and austenite phases for the Fe-0.85C-11.56Mn (wt. %) alloy at 690 °C.

Φ^{cem}	U_{Mn}^{cem}	U_C^{cem}	Φ^{γ}	U_{Mn}^{γ}	U_C^{γ}
4.26×10^{-2}	2.88×10^{-1}	3.33×10^{-1}	9.57×10^{-1}	1.11×10^{-1}	2.78×10^{-2}

Table 3.6b: Experimental data for the alloy at 690°C. Nodule sizes are rounded to the nearest integer.

HT time (days)	Φ^{cem} $\times 10^{-2}$	Φ^{γ^d} $\times 10^{-2}$	$\lambda_{cem}^{cellular}$ (µm)	$\lambda_{\gamma^d}^{cellular}$ (µm)	Nodule Size	
					MNR (µm)	Gust (µm)
4	1.0	2.5	1.0	2.6	7.9	2.3
7	1.5	3.5	1.3	2.9	65	32
14	2.1	5.2	2.1	4.9	92	27
21	2.4	5.4	2.5	6.2	139	47
30	2.3	6.9	3.0	7.2	157	56
60	3.3	7.9	3.4	8.9	176	81

Table 3.6c: Summary of EDS and EBSD results for the alloy heat treated at 690°C. Blocks highlighted in blue have been confirmed using EBSD that they are austenite component of the cellular colony. Blocks highlighted in gray indicate no experimentally observed information about the phase.

HT time (days)	U_{Mn}^{cem-gb} ± 0.01	U_{Mn}^{cem-c} ± 0.01	$U_{Mn}^{\gamma^d-low}$ ± 0.01	$U_{Mn}^{\gamma^d-high}$ ± 0.01	$U_{Mn}^{cem-sph}$ ± 0.01
4	0.19	0.20	0.06	0.10	
7	0.17	0.20	0.06	0.10	
14	0.18	0.21	0.07	0.11	
60	0.19	0.21	0.07	0.11	0.21

Comments

Reaction characteristics and morphologies are similar to those observed at 700 °C. Figs. 3.9a-e show images representative of the colonies observed during the reaction progress. Table 3.6a provides computed equilibrium volume fraction and manganese content for austenite and cementite phases. Tables 3.6b and c provide morphological and analytical characterization of the phase transformation over time. Grain boundary cementite and cellular decomposition are observed after 1 hour and 4 days respectively, as shown on the TTT curve in Fig. 3.7. Large cellular colonies are well developed, absent of impingement, but again, not numerous (less than

4 per sample). The number of small colonies, some as small as two cementite lamellae, is significantly considerable. Spherodized cementite forms in a sample heat treated for 60 days. Manganese-depleted austenite usually has pitted appearance during the early stages of the decompositions near the grain boundary cementite as shown in Fig. 3.9d (right). Mottled appearance of manganese-depleted austenite, shown in Fig. 3.9e (bottom left), usually occurs far from the reaction front.

When compared to the samples heat treated at 700 °C for identical times, grain boundary precipitates are thicker but the number of well developed cellular colonies declines. The width of the cementite, width of manganese-depleted austenite, the size of the largest colony, and the average colony size all increase during the course of the isothermal heat treatment but all are smaller when compared to the samples heat treated at 700 °C for identical times.

During the course of the phase transformation manganese content of the cellular and the grain boundary cementite remains approximately constant while the total volume fraction of cementite is increasing. U_{Mn}^{cem-c} is approximately the same as the U_{Mn}^{cem-gb} but less than the equilibrium predicted amount. U_{Mn}^{cem-c} at 690 °C is also higher than U_{Mn}^{cem-c} at 700 °C. U_{Mn}^{gb-cem} at 690 °C is lower than at 700 °C. $U_{Mn}^{\gamma^d}$ ranges from 0.06 to 0.11 with lower values closer to the moving reaction front, similar to the pattern at 700 °C.

3.2.4 680 °C

      The analysis by Hutchinson and Shiflet predicts pearlite in the vicinity of ~ 687 °C. [hutchinson2004] Indeed, formation of pearlite is first observed just below this temperature, 680 °C. Cellular colonies independent of pearlite are also present. Images in Fig. 3.10 show pearlite only because characteristics of cellular colonies remain the same as those shown in Figs. 3.8 and 3.9.

Figure 3.10: SEM images illustrating pearlite colonies in an alloy heat treated for 1 day. Phases marked with orange text in the image have been verified using EBSD.

Table 3.7a: Computed equilibrium volume fraction and composition for cementite and austenite phases for the Fe-0.85C-11.56Mn (wt. %) alloy at 680 °C.

Φ^{cem}	U_{Mn}^{cem}	U_C^{cem}	Φ^{γ}	U_{Mn}^{γ}	U_C^{γ}
4.66×10^{-2}	2.90×10^{-1}	3.33×10^{-1}	9.53×10^{-1}	1.11×10^{-1}	2.66×10^{-2}

Table 3.7b-1: Experimental data for the alloy at 680°C. Blocks highlighted in gray indicate no experimentally observed information about the phase.

HT time (days)	$\Phi^{cem} \times 10^{-2}$	$\%^{cell}$	$\Phi^{\gamma^d} \times 10^{-2}$	$\Phi^{\gamma^r} \times 10^{-2}$	$\Phi^{\alpha} \times 10^{-3}$	$\lambda_{cem}^{cellular}$ (μm)	$\lambda_{\gamma^d}^{cellular}$ (μm)	$\lambda_{cem}^{pearlite}$ (μm)	$\lambda_{\alpha}^{pearlite}$ (μm)
1	1.1	92	2.6		3.2	0.7	1.8	0.42	0.32
2	1.2	98	2.8		4.2	0.8	1.9	0.50	0.27
4	1.9	85	3.6		7.8	1.7	3.8	0.82	0.31
7	1.7	88	3.5		6.5	1.8	4.2	1.22	0.59
14	2.7	89	5.4	0.2	7.2	2.3	5.2	0.92	0.46
21	3.2	88	6.9	0.9	7.5	2.8	6.9	0.84	0.39
30	3.4	95	7.5	1.6	6.9	3.2	7.4	0.85	0.45

Table 3.7b-2: Experimental data for the alloy at 680°C. Nodule sizes are rounded to the nearest integer.

HT time (days)	Nodule Size		Gust (μm)
	MNR (μm)		
	Cellular	Pearlite	
1	7	2.9	2.3
2	25	8.4	14
4	32	6.7	22
7	51	12	24
14	97	19	35
21	107	14	28
30	282	16	67

Table 3.7c: Summary of EDS and EBSD results for the alloy heat treated at 680°C. Blocks highlighted in blue have been confirmed using EBSD that they are ferrite or austenite component of the cellular colony. U_{Mn}^{α} and $U_{Mn}^{\gamma^r}$ are not reported because the regions were too small to resolve the interaction volume associated with the conventional SEM-EDS technique. Blocks highlighted in gray indicate no experimentally observed information about the phase.

HT Time (days)	U_{Mn}^{cem-gb} ±0.01	U_{Mn}^{cem-p} ±0.02	U_{Mn}^{α}	U_{Mn}^{cem-c} ±0.01	$U_{Mn}^{\gamma^d-low}$ ±0.01	$U_{Mn}^{\gamma^d-high}$ ±0.01	$U_{Mn}^{\gamma^r-low}$ ±0.01	$U_{Mn}^{\gamma^r-high}$ ±0.01
4	0.15	0.16	Not Reported	0.21	0.06	0.10		
14	0.16	0.15	Not	0.21	0.06	0.10		
30	0.15	0.18	Reported	0.21	0.07	0.11		

Comments

Grain boundary cementite and cellular decomposition resembling that seen at higher temperatures is observed after 1 hour and 1 day respectively. Ferrite precipitates in samples heat treated for longer than 1 day. Ferrite dissolution starts after 14 days. Colonies where dissolution occurs are small and usually devoid of any remaining ferrite. Limited volume fraction of ferrite (and subsequently retrenched austenite) coupled with small interlamellar spacing makes reliable chemical analysis unfeasible. Table 3.7a provides computed equilibrium volume fraction and manganese content of all phases. Tables 3.7b-1, 3.7b-2 and 3.7c provide morphological and compositional characterization of the phase transformation over time. There are now two types of lamellar cementite: cellular and pearlitic. Very few well developed cellular and pearlite colonies are observed. Spherodized cementite is not observed during the time of the reaction.

A distinguishing characteristic of pearlitic and cellular cementite is the width of the region between the cementite lamellae, Table 3.7b-1. Width of the depleted austenite, $\lambda_{\gamma^d}^{cellular}$, is almost 6-10 times that of ferrite and the subsequent austenite retrenchment zone. This is one of the two features, the other being variable U_{Mn}^{cem} of the cementite immediately adjacent to the austenite in question, used to qualitatively identify former pearlite colonies.

Cellular colony size (MNR and Gust) and lamellar width are lower when compared to the samples heat treated at 690 °C and 700 °C for similar times. For pearlite colonies, lamellar width, size of the largest colony and average colony size all increase with time at 680 °C. This is the first temperature where pearlite is observed so no other points of reference are available.

U_{Mn}^{cem-gb} at 680 °C is 0.15, continuing to trend down when compared to higher temperatures (0.19 at 690 °C, and 0.21 at 700 °C). U_{Mn}^{cem-p} ranges from 0.16 to 0.18. The U_{Mn}^{cem-p} in the earlier stages of the reaction is consistently higher than U_{Mn}^{cem-gb} but within the experimental margin of error. U_{Mn}^{cem-c} is higher than that of perlitic cementite (0.21) and remains approximately constant for the duration of the reaction. This difference in U_{Mn}^{cem} also helps distinguish cementite based on pearlitic or cellular origin confirming results based on the width of the region between the cementite lamellae. Both types of cementite had U_{Mn}^{cem} values lower than the equilibrium predicted value.

3.2.5 670 °C

At this temperature, both pearlite and cellular products are observed. Images in Fig. 3.11 show early stages of the development for pearlite and cellular colonies. Of particular interest are the areas adjacent to cementite, which in some cases transform into ferrite and in some cases remain austenite depleted of manganese (Fig. 3.11a).

Figure 3.11: OM and SEM images illustrating the microstructural evolution in the alloy at 670 °C. Compositions values shown in the images have been obtained using SEM-EBSD.
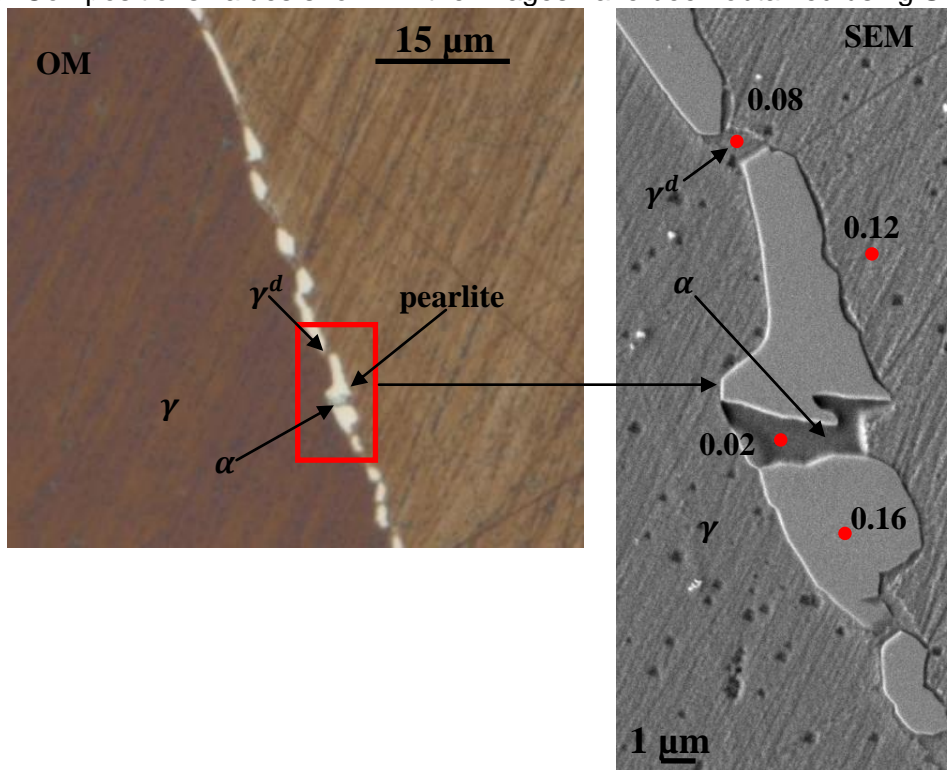
(a) Images of the grain boundary cementite, manganese‑depleted austenite, and pearlite in a sample heat treated for 4 days. **Left:** OM with the area enclosed in red rectangle is shown on the right. **Right:** SEM image of the area enclosed by the red rectangle. Note the manganese content difference in the manganese‑depleted austenite (γ^d) and ferrite (α).
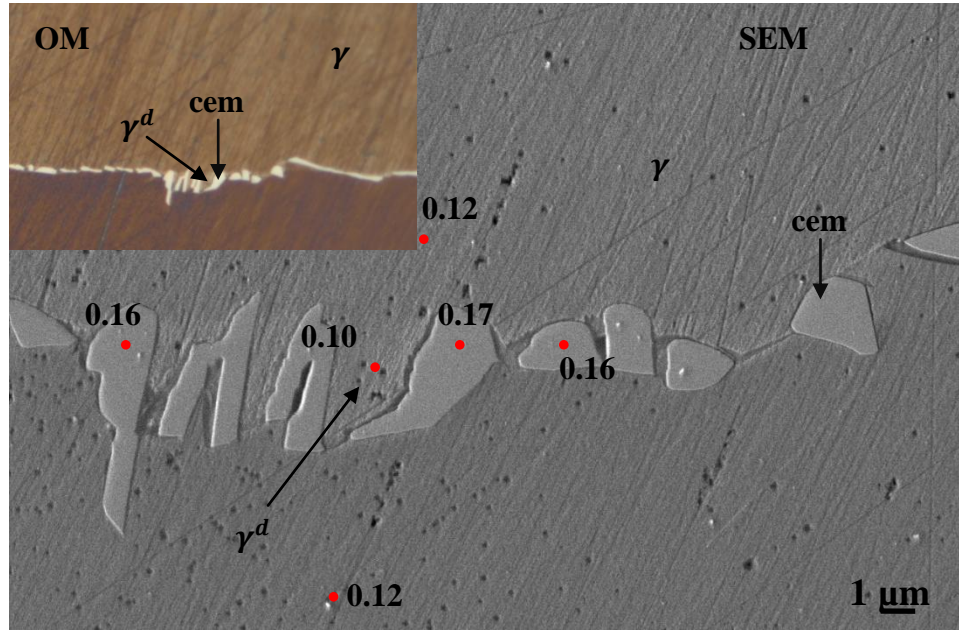
(b) SEM image of the grain boundary cementite with OM image insert in a sample heat treated for 4 days. SEM image shows grain boundary cementite with manganese-depleted austenite.

Table 3.8a: Computed equilibrium volume fraction and composition for cementite and austenite phases for the Fe-0.85C-11.56Mn (wt. %) alloy at 670 °C.

Φ^{cem}	U_{Mn}^{cem}	U_C^{cem}	Φ^{γ}	U_{Mn}^{γ}	U_C^{γ}
5.04×10^{-2}	2.94×10^{-1}	3.33×10^{-1}	9.50×10^{-1}	1.09×10^{-1}	2.54×10^{-2}

Table 3.8b-1: Experimental data for the alloy at 670°C. Blocks highlighted in gray indicate no experimentally observed information about the phase.

HT time (days)	Φ^{cem} $\times 10^{-2}$	$\%^{cell}$	Φ^{γ^d} $\times 10^{-2}$	Φ^{α} $\times 10^{-2}$	Φ^{γ^r} $\times 10^{-2}$	$\lambda_{cem}^{cellular}$ (μm)	$\lambda_{\gamma^d}^{cellular}$ (μm)	$\lambda_{cem}^{pearlite}$ (μm)	$\lambda_{\alpha}^{pearlite}$ (μm)
4	0.6	92	1.4	0.32		0.9	2.1	1.0	0.6
7	1.0	91	2.3	0.46		0.8	1.8	0.7	0.4
14	1.6	88	3.9	0.48		1.0	2.3	0.9	0.7
21	1.5	93	3.7	0.26	0.15	1.2	2.9	1.4	0.9
30	2.1	94	5.1		0.14	1.1	2.6	1.2	
60	2.3	92	5.4		0.23	1.4	3.4	1.4	

Table 3.8b-2: Experimental data for the alloy at 670°C. Nodule sizes are rounded to the nearest integer. Blocks highlighted in gray indicate no experimentally observed information about the phase.

HT time (days)	Nodule Size		Gust (μm)
	MNR (μm)		
	Cellular	Pearlite	
4	3	1.2	0.9
7	15	3.3	3.8
14	28	9.1	6.8
21	37	19	17
30	54	22	35
60	85		41

Table 3.8c: Summary of SEM-EDS and SEM-EBSD results for the alloy heat treated at 670°C. Ferrite and austenite component of cellular colonies (blocks highlighted in blue) have been confirmed using EBSD. Blocks highlighted in gray indicate no experimentally observed information about the phase.

HT time (days)	U_{Mn}^{cem-gb} ± 0.01	U_{Mn}^{cem-p} ±0.01	U_{Mn}^{α} ±0.01	U_{Mn}^{cem-c} ±0.01	$U_{Mn}^{\gamma^{d}-low}$ ±0.01	$U_{Mn}^{\gamma^{d}-high}$ ±0.01	$U_{Mn}^{\gamma^{r}-low}$ ±0.01	$U_{Mn}^{\gamma^{r}-high}$ ±0.01
4	0.16	0.16	0.02	0.20	0.07	0.09		
14	0.16	0.19	0.02	0.21	0.06	0.08		
30	0.17	0.24		0.21	0.06	0.11	0.09	0.10

Comments

Grain boundary cementite and pearlite are observed after 1 hour and 12 hours respectively. Cellular precipitation occurs after 4 days. Ferrite dissolution is first observed after 21 days. Ferrite dissolution, when it occurs, is first observed in smaller colonies with near complete dissolution of ferrite. In larger colonies dissolution of ferrite starts at the peripheries of the colonies. No ferrite is found in samples heat treated for 60 days. Table 3.8a provides computed equilibrium volume fraction and manganese content for cementite and austenite. Tables 3.8b-1, 3.8b-2 and 3.8c provide morphological and compositional characterization of the reaction. Grain boundaries are covered with both cellular and pearlite colonies. Very few well developed cellular and pearlite colonies are observed but the number of small colonies, some as small as two cementite lamellae, is significant. Spherodized cementite is not observed during the reaction.

Trends observed at 680 °C hold true for this temperature regime. For all colonies, cellular and pearlite, lamellar width, size of the largest colony and average colony size all increase over time. The size (MNR and Gust) of cellular colonies is smaller when compared to the samples heat treated at higher temperatures for similar times. The size of pearlite colonies (MNR) is larger when compared to the samples heat treated at higher temperatures for similar times, as expected. The width of the manganese-depleted austenite in cellular colonies is larger than the ferrite width in the pearlite colonies. For the duration of the reaction U_{Mn}^{cem-c} remains approximately 0.21 while U_{Mn}^{cem-p} ranges from 0.16 to 0.24 for pearlite and former pearlite colonies. U_{Mn}^{cem-gb} is 0.16, confirming a decreasing trend when compared to higher temperatures. Note that U_{Mn}^{cem-p} in the earlier stages of the reaction is, again, consistently higher than U_{Mn}^{cem-gb} but within margins of the experimental error.

3.2.6 660 °C

At this temperature, both pearlite and cellular products are observed. Images in Fig. 3.12 show development stages of pearlite and cellular colonies. Once again, of particular interest are the areas adjacent to cementite, which in some cases transform into ferrite and in some cases remain austenite, albeit depleted of manganese. Fig. 3.12 shows a colony that exhibits components of cellular and pearlite colonies simultaneously. This has never been reported previously. Fig. 3.12a bottom right (red rectangle) shows cementite lamellae joined by ferrite, forming a pearlite colony. There is also a grain boundary cementite with a sliver of ferrite, confirmed using EBSD, joining it with manganese-depleted austenite (orange rectangle).

Figure 3.12: SEM images illustrating the microstructural evolution in the alloy at 660 °C. Phases marked with orange text in the images have been verified using SEM-EBSD. Compositions are obtained using SEM-EDS.
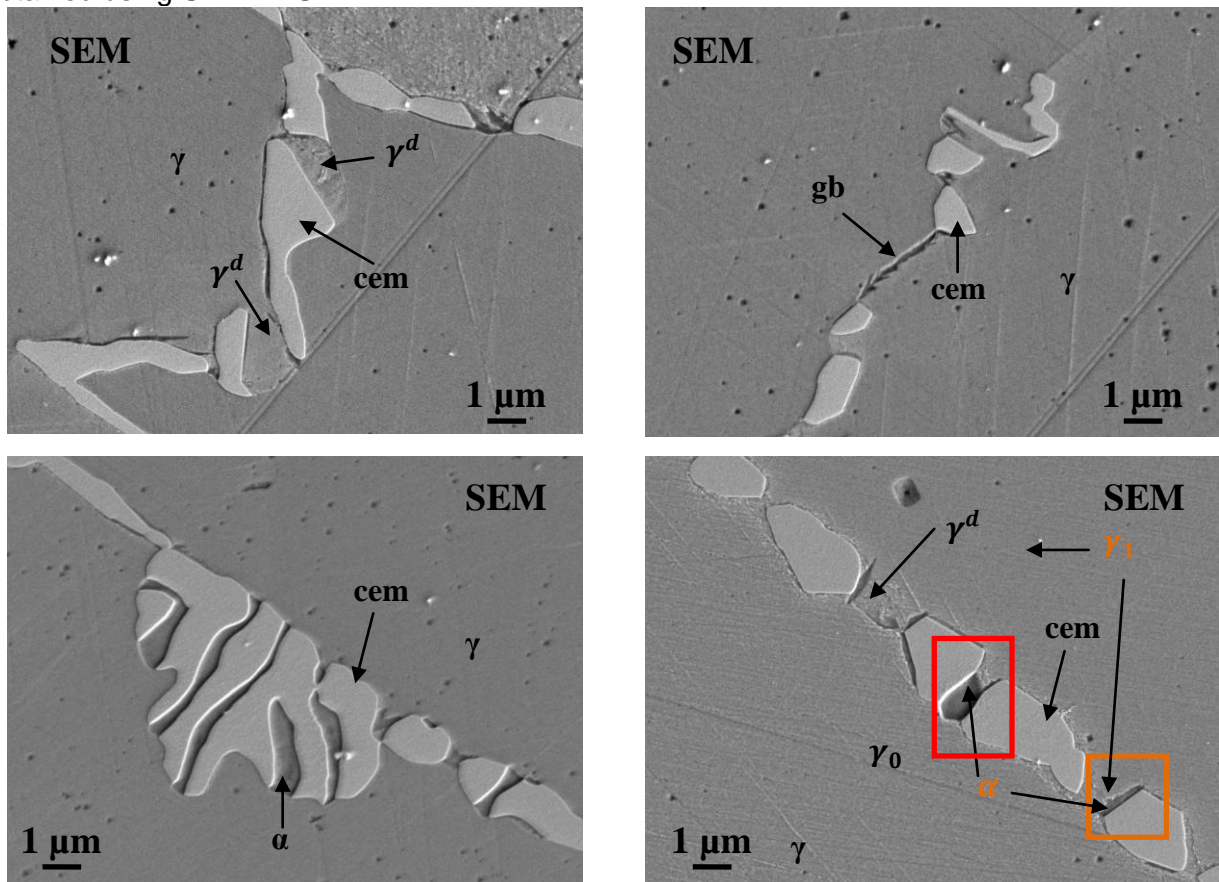
(a) Sample heat treated for 4 days. **Top left:** Grain boundary cementite with cellular colonies. **Top right:** Grain boundary cementite and a grain boundary separating the two. Note the black region running parallel to the grain boundary. The appearance is consistent with regions of manganese-depleted austenite adjacent to the cementite. **Bottom left:** Pearlite colony. Note that the average width of ferrite is smaller when compared to the width of the manganese-

depleted austenite in cellular colonies. **Bottom right:** Grain boundary with ferrite (indicated in the image) joining the two grain boundary cementite precipitates, red rectangle. A sliver of ferrite is also observed joining cementite and manganese-depleted austenite, orange rectangle.
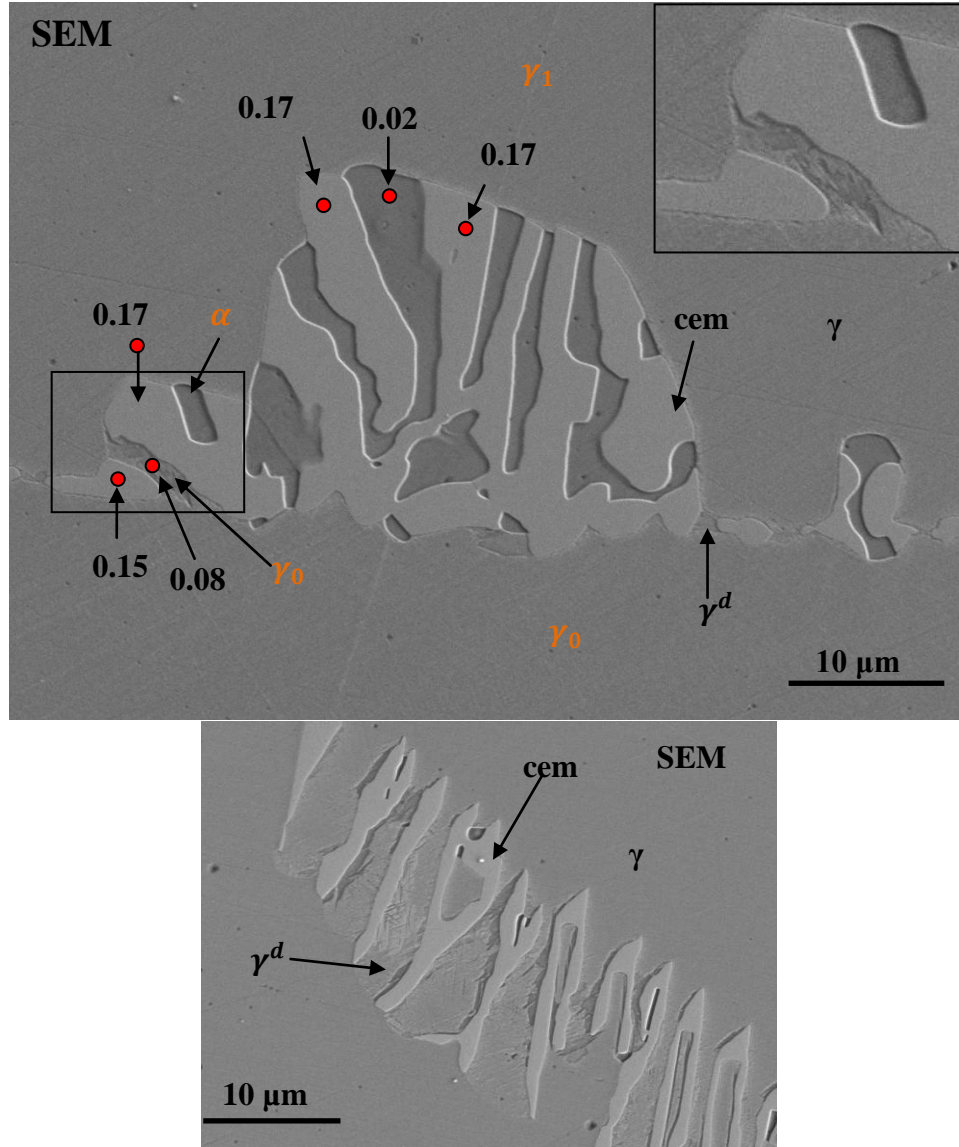
(b) Sample heat treated for 30 days. **Top:** A colony exhibiting both pearlite and cellular behavior. This colony will be analyzed in Chapter 4. **Bottom:** Portion of a cellular colony.

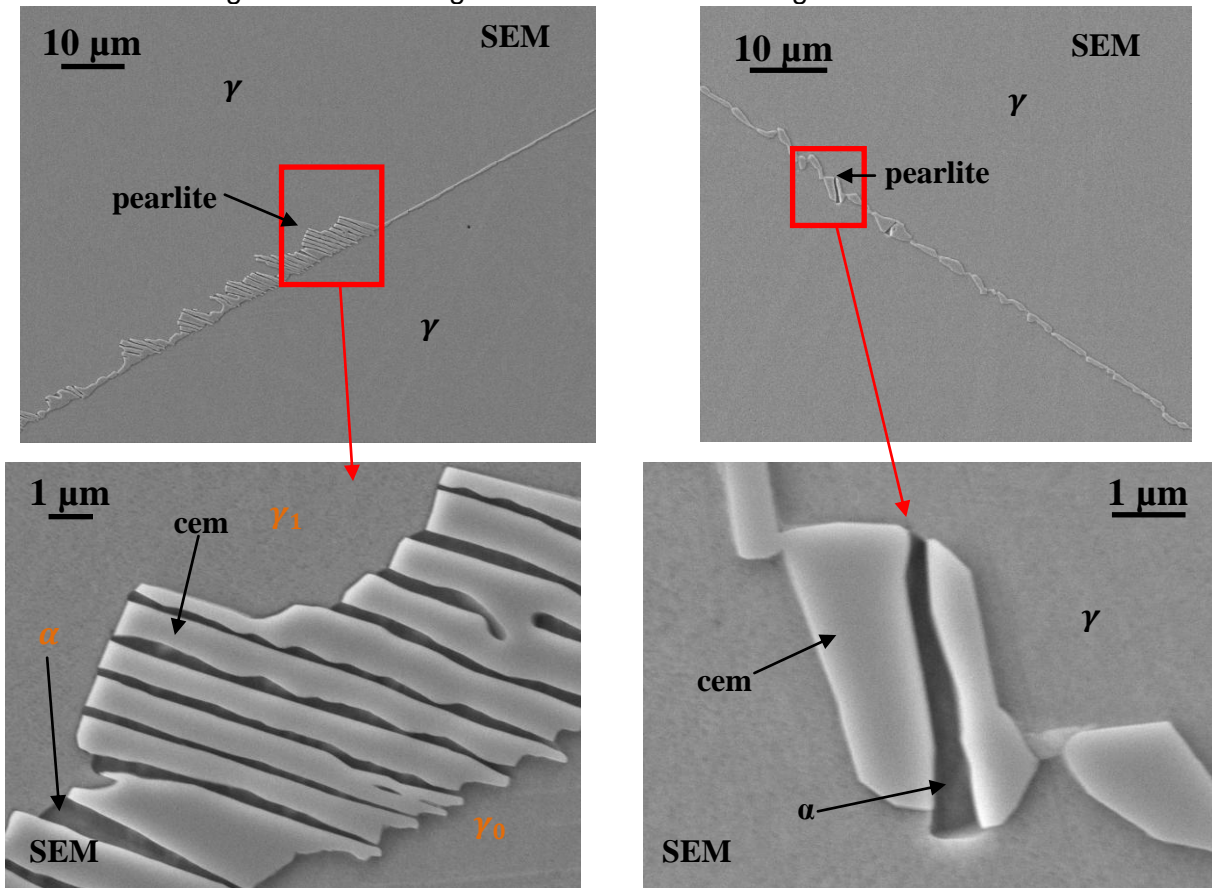**Table 3.9a:** Computed equilibrium volume fraction and composition for cementite and austenite phases for the Fe-0.85C-11.56Mn (wt. %) alloy at 660 °C.

Φ^{cem}	U_{Mn}^{cem}	U_C^{cem}	Φ^{γ}	U_{Mn}^{γ}	U_C^{γ}
5.43×10^{-2}	2.98×10^{-1}	3.33×10^{-1}	9.46×10^{-1}	1.09×10^{-1}	2.43×10^{-2}

Table 3.9b-1: Experimental data for the alloy at 660°C. Blocks highlighted in gray indicate no experimentally observed information about the phase.

HT time (days)	Φ^{cem} $\times 10^{-3}$	$\%^{cell}$	Φ^{α} $\times 10^{-3}$	Φ^{γ^r} $\times 10^{-3}$	Φ^{γ^d} $\times 10^{-3}$	$\lambda_{cem}^{cellular}$ (μm)	$\lambda_{\gamma^d}^{cellular}$ (μm)	$\lambda_{cem}^{pearlite}$ (μm)	$\lambda_{\alpha}^{pearlite}$ (μm)
0.5	1.7		0.9					0.7	0.4
1	3.9		2.1					0.9	0.6
2	4.8		3.1					0.8	0.5
4	6.2	27	4.2		4.4	0.8	2.2	1.5	0.8
7	8.5	16	5.4		3.2	0.9	1.7	1.6	1.1
14	11.5	18	4.9		4.9	1.3	2.9	1.3	0.8
21	29.6	23	8.6	1.2	11.5	1.8	2.2	1.4	0.9
30	34.4	20	7.2	5.3	17.3	1.6	3.9	1.8	1.1

Table 3.9b-2: Experimental data for the alloy at 660°C. Nodule sizes are rounded to the nearest integer.

HT time (days)	Nodule Size		Gust (μm)
	MNR (μm)		
	Cellular	Pearlite	
1	Not	3.8	Not
2	observed	4.1	Observed
4	2.0	7.9	0.4
7	16	5.1	3.2
14	25	17	10
21	31	16	7.4
30	48	9.2	7.2

Table 3.9c: Summary of SEM-EDS and SEM-EBSD results for the alloy heat treated at 660°C. Ferrite and austenite component of cellular colonies (blocks highlighted in blue) have been confirmed using EBSD. Blocks highlighted in gray indicate no experimentally observed information about the phase.

HT time (days)	U_{Mn}^{cem-gb} ± 0.01	U_{Mn}^{cem-p} ± 0.01	U_{Mn}^{α} ± 0.01	U_{Mn}^{cem-c} ± 0.01	$U_{Mn}^{\gamma^d-low}$ ± 0.01	$U_{Mn}^{\gamma^d-high}$ ± 0.01	$U_{Mn}^{\gamma^r-low}$ ± 0.01	$U_{Mn}^{\gamma^r-high}$ ± 0.01
4	0.13	0.14	0.02	0.22	0.08	0.10		
30	0.13	0.17	0.02	0.22	0.09	0.11	0.07	0.09

Comments

Grain boundary cementite and cellular decomposition, resembling that observed at higher temperatures, precipitates after 1 hour and 4 days respectively. Ferrite precipitates after 12 hours. Ferrite dissolution is first observed after 21 days. Table 3.9a provides computed equilibrium

volume fraction and manganese content of phases. Tables 3.9b-1, 3.9b-2, and 3.9c provide morphological and compositional characterization of the phase transformation over time. Very few well developed cellular colonies are observed. Many pearlite colonies are well developed, especially in the later stages of the transformation. Spherodized cementite is not observed during the reaction time. Ferrite dissolution, when it occurs, is first observed in smaller colonies with near complete dissolution of ferrite. At this temperature larger and well developed colonies do not exhibit dissolution within the experimental temperature-time regime, top Fig. 3.12b.

Trends observed at 670 °C hold true for this temperature. The size (MNR and Gust) of cellular colonies is smaller when compared to the samples heat treated at higher temperatures for similar times. The size of pearlite colonies (MNR) is larger when compared to the samples heat treated at higher temperatures for similar times. The width of the depleted austenite in cellular colonies is larger than the width of ferrite in the pearlitic colonies. For the duration of the reaction U_{Mn}^{cem-c} remains approximately 0.22 while U_{Mn}^{cem-p} ranges from 0.14 to 0.17. U_{Mn}^{cem-gb} remains 0.13, confirming a decreasing trend when compared to higher temperatures. U_{Mn}^{cem-p} in the earlier stages of the reaction is higher than U_{Mn}^{cem-gb} but it is within the experimental margin of error.

3.2.7 <u>650 °C</u>

This is the most extensively studied temperature in terms of chemistry and morphological data gathering and analysis. At this temperature, both pearlite and cellular products are observed. Images in Fig. 3.13 show development stages of pearlite (growth and dissolution) and cellular colonies. Grain boundary cementite allotriomorphs are spaced closer together than they are at higher temperatures.

Figure 3.13: Optical and SEM images illustrating microstructural evolution in the alloy at 650 °C. Phases indicated with orange text have been verified using SEM-EBSD.
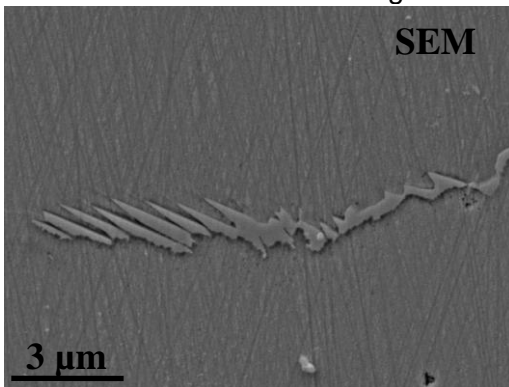
(a) Sample heat treated for 1 hour.
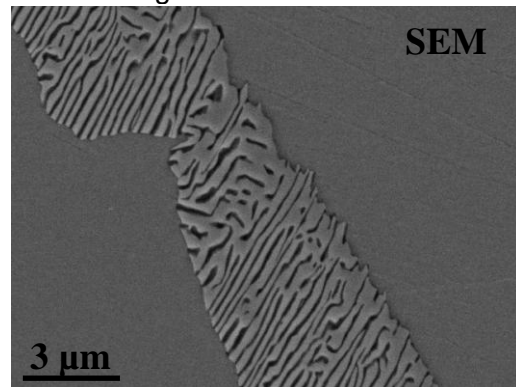
(b) Sample heat treated for 3 hours.
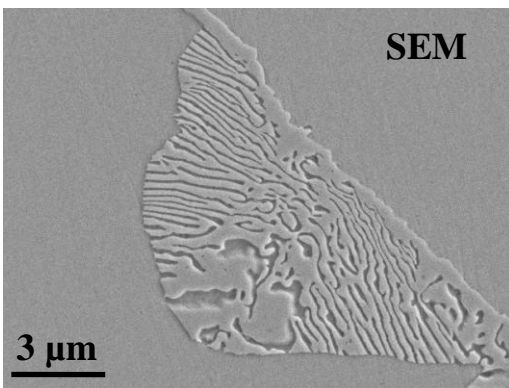
(c) Sample heat treated for 6 hours.
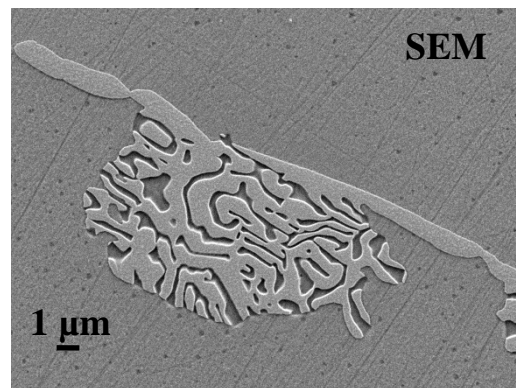
(d) Sample heat treated for 12 hours.
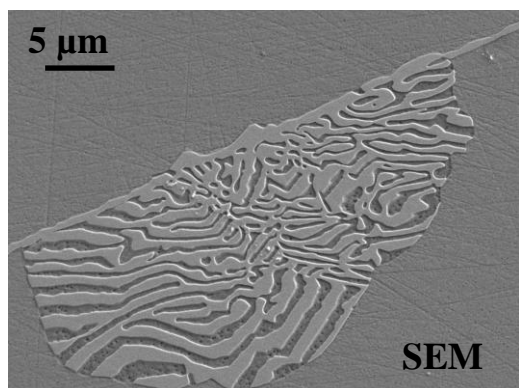
(e) Sample heat treated for 24 hours.
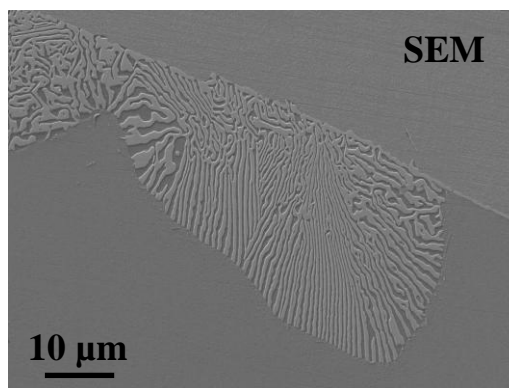
(f) Sample heat treated for 2 days.
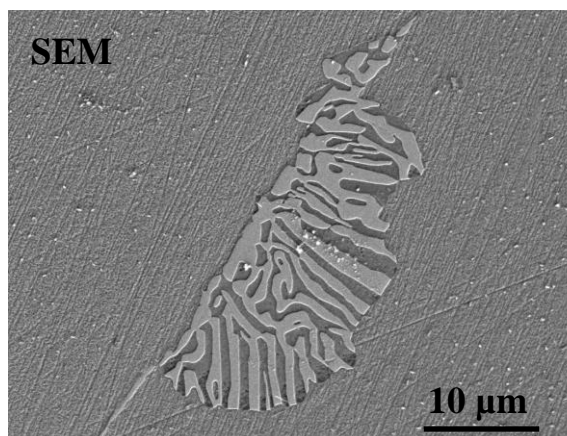
(g) Sample heat treated for 4 days.
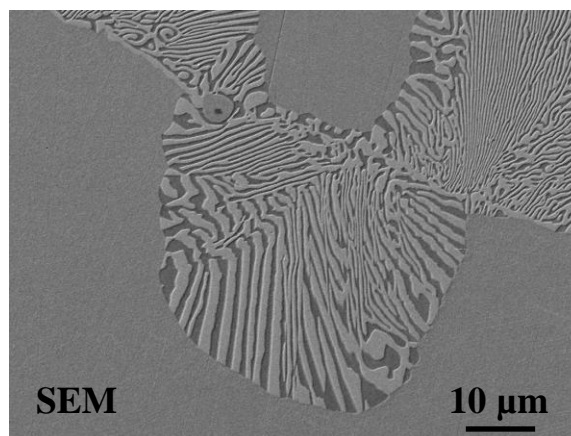
(h) Sample heat treated for 7 days.
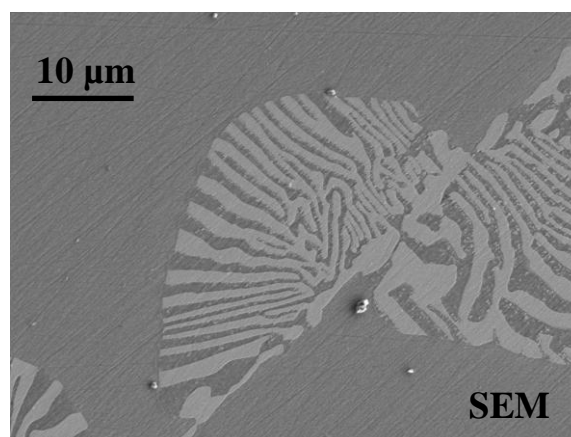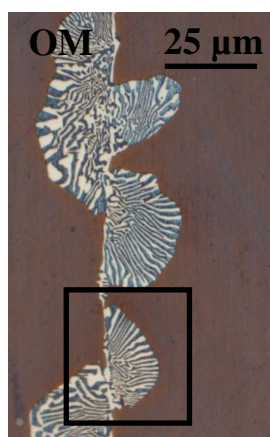
(i) Sample heat treated for 14 days. **Left:** OM image of a pearlite colony. Area enclosed in the black rectangle is shown on the right. **Right:** SEM image of the area enclosed by the black rectangle on the left.
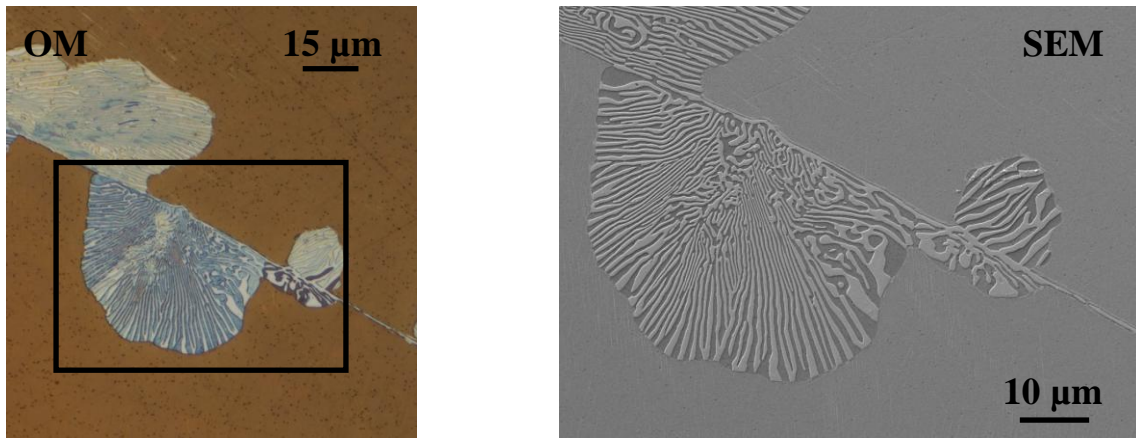
(j) Sample heat treated for 21 days. **Left:** OM image of a pearlite colony. Area enclosed in the black rectangle is shown on the right. **Right:** SEM image of the area enclosed by the black rectangle on the left.
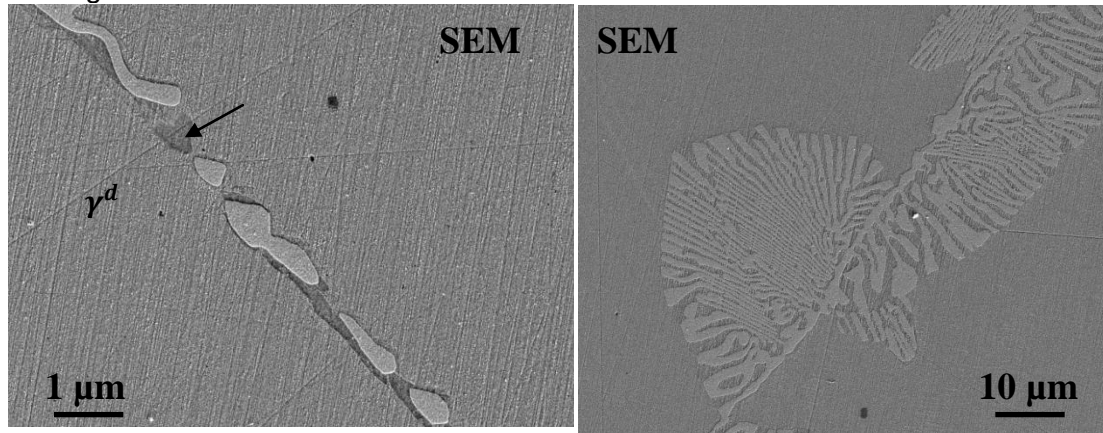
(k) Sample heat treated for 30 days. **Left:** SEM image of the grain boundary cementite. Note the manganese-depleted austenite regions adjacent to the cementite (black arrow). **Right:** SEM image of a pearlite colony.

20 μm
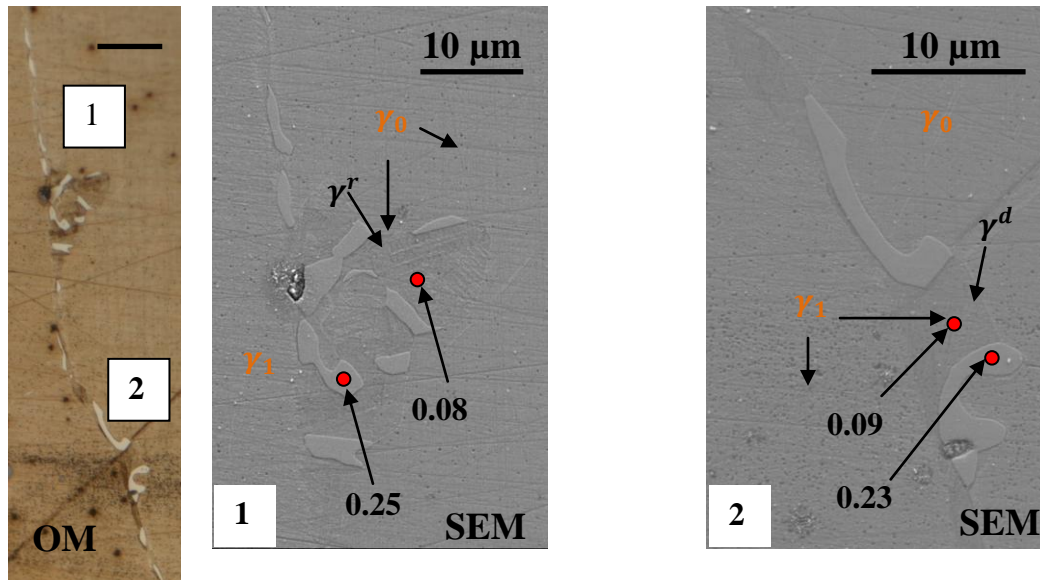
(l) Sample heat treated for 60 days. **(1)** Former pearlite colony. The ferrite has dissolved leaving behind retrenched austenite. **(2)** Cellular colony.
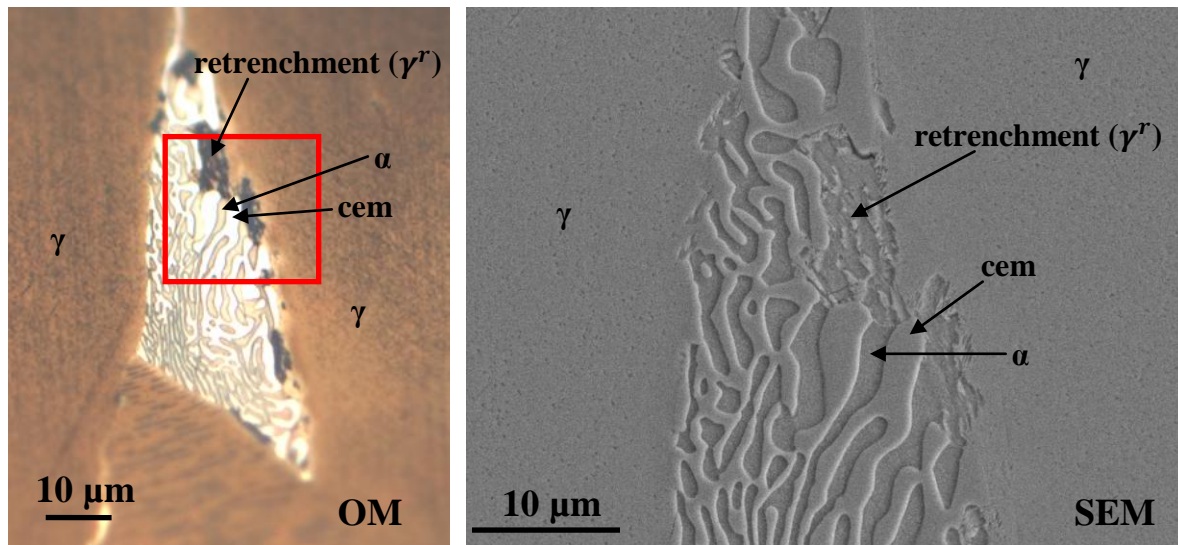
(m) Sample heat treated for 120 days. **Left:** OM image of a pearlite colony with retrenched austenite which marks dissolution of ferrite. Area enclosed in the red rectangle is shown on the right. **Right:** SEM image of the retrenched austenite inside the red rectangle shown on the left.
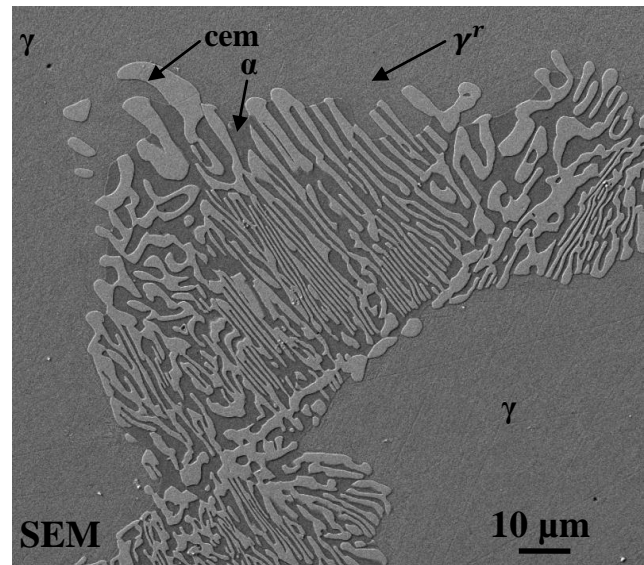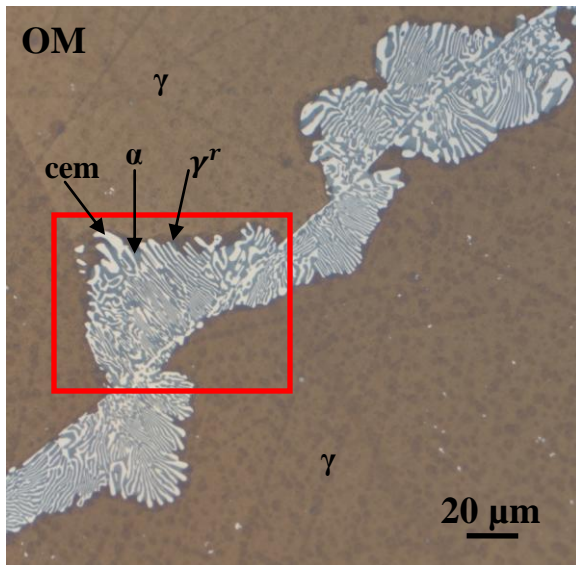
(n) Sample heat treated for 150 days. **Left:** OM image of a pearlite colony with the silhouette of the retrenched austenite. The colony enclosed by the red rectangle is shown on the right. **Right:** SEM image of the pearlite colony with retrenched austenite inside the red rectangle shown on the left.
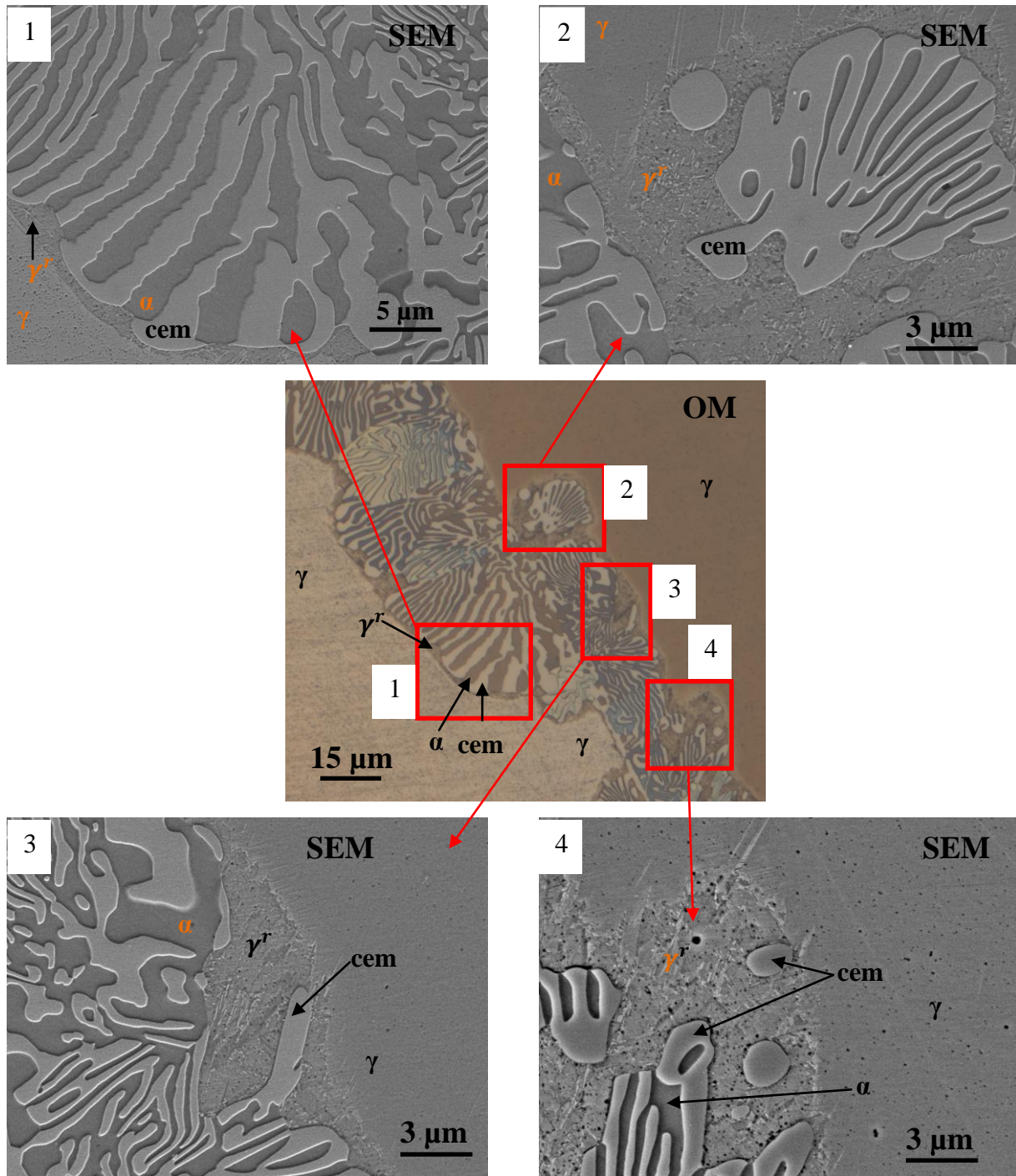
(o) Sample heat treated for 180 days. Areas enclosed in red rectangles are numbered and SEM images with corresponding numbers are shown.

Table 3.10a: Computed equilibrium volume fraction and composition for cementite and austenite for the Fe-0.85C-11.56Mn (wt. %) alloy at 650 °C.

Φ^{cem}	U_{Mn}^{cem}	U_C^{cem}	Φ^γ	U_{Mn}^γ	U_C^γ
5.81×10^{-2}	2.99×10^{-1}	3.33×10^{-1}	9.42×10^{-1}	1.08×10^{-1}	2.32×10^{-2}

Table 3.10b-1: Experimental data for the alloy at 650°C. Blocks highlighted in gray indicate no experimentally observed information about the phase.

HT time	Φ^{cem} 10^{-3}	$\%^{cell}$	Φ^α 10^{-3}	Φ^{γ^r} 10^{-3}	Φ^{γ^d} 10^{-3}	$\lambda_{cem}^{cellular}$ (µm)	$\lambda_{\gamma^d}^{cellular}$ (µm)	$\lambda_{cem}^{pearlite}$ (µm)	$\lambda_\alpha^{pearlite}$ (µm)
hours									
3	1.1		Negligible					0.6	0.1
6	2.2							0.6	0.1
12	3.6							0.7	0.3
Days									
1	5.4		4.3					0.9	0.3
2	7.8		6.9					1.2	0.4
4	11.9		9.4					1.2	0.5
7	20.2		16.8					1.3	0.6
14	25.7		22.2					1.4	0.7
21	25.1		28.9					1.5	0.8
30	27.8		24.2	1.6				1.5	0.8
60	28.2	15	24.6	1.8	1.0	2.2	5.3	1.3	0.9
90	27.3	15	23.4	2.4	1.0	2.2	5.4	1.4	0.7
120	28.6	14	22.9	3.0	1.0	2.4	5.8	1.5	1.1
150	27.3	5.1	17.2	6.4	3.3	2.4	5.7	1.6	1.2
180	37.1	4.9	21.3	11.6	4.1	2.6	5.9	1.9	1.2

Table 3.10b-2: Experimental data for the alloy at 650°C. Nodule sizes are rounded to the nearest integer. Blocks highlighted in gray indicate no experimentally observed information about the phase.

HT time	Nodule Size		Gust (µm)
	MNR (µm)		
	Cellular	Pearlite	
hours			
3		35	
6		31	
12		34	
days			
1		43	
2		51	
4		57	
7		43	
14		57	
21		38	
30		61	
60	10	50	7.2
90	12	61	8.8
120	16	47	11
150	8.1	38	5.6
180	24	37	13

Table 3.10c: Summary of SEM-EDS, SEM-EBSD, and TEM results for the alloy heat treated at 650°C. Ferrite and austenite component of cellular colonies have been confirmed using EBSD (blocks highlighted in blue) and TEM (blocks marked in green). Blocks highlighted in gray indicate no experimentally observed information about the phase.

HT time	U_{Mn}^{cem-gb} ±0.01	U_{Mn}^{cem-p} ±0.01	U_{Mn}^{α} ±0.01	U_{Mn}^{cem-c} ±0.01	$U_{Mn}^{\gamma d-low}$ ±0.01	$U_{Mn}^{\gamma d-high}$ ±0.01	$U_{Mn}^{\gamma r-low}$ ±0.01	$U_{Mn}^{\gamma r-high}$ ±0.01	U_{Mn}^{cems} ±0.01
hours									
3	0.13	0.14	0.02						
6	0.14	0.16	0.02						
12	0.13	0.16	0.02						
days									
1	0.13	0.17	0.02						
2	0.12	0.20	0.02						
4	0.13	0.22	0.02						
7	0.13	0.22	0.02						
14	0.12	0.23	0.02						
21	0.13	0.24	0.02						
30	0.12	0.25	0.02						
60	0.13	0.25	0.02	0.23	0.09	0.10	0.08	0.08	
90	0.12	0.26	0.02	0.23	0.09	0.09	0.09	0.10	
120	0.12	0.27	0.02	0.22	0.08	0.09	0.09	0.10	
150	0.13	0.29	0.02	0.23	0.08	0.10	0.08	0.09	
180	0.12	0.29	0.02	0.23	0.08	0.10	0.08	0.09	0.29

Comments

Grain boundary cementite appears after 1 hour and cellular decomposition, resembling that observed at higher temperatures, forms after 60 days. Ferrite precipitates after 1 hour. Ferrite dissolution is first observed after 60 days and, initially, mostly in smaller colonies. For smaller colonies, ferrite dissolution is marked by complete absence of ferrite in the colonies, Fig. 3.13l-1. For larger colonies, dissolution of ferrite is observed at later times and dissolution starts at the peripheries of pearlite colonies, Figs. 3.13m-o. Table 3.10a provides computed equilibrium volume fraction and manganese content of phases. Tables 3.10b-1, 3.10b-2, 3.10c provide morphological and compositional characterization of the phase transformation over time. Spherodized cementite is observed after 180 days of evolution.

Trends observed at 660 °C hold for this temperature regime. A small number of spherodized particles have near equilibrium manganese content. The size (MNR and Gust) of cellular colonies is smaller when compared to the samples heat treated at higher temperatures for similar times. The size of pearlite colonies (MNR) is larger when compared to the samples heat

treated at higher temperatures for similar times. The width of the manganese-depleted austenite in cellular colonies is larger than the width of ferrite in the pearlitic colonies for the duration of the experiment. U_{Mn}^{cem-c} remained approximately constant 0.23 while U_{Mn}^{cem-p} ranges from 0.12 to 0.29 for pearlite colonies. U_{Mn}^{cem-gb} is 0.12 confirming a decreasing trend when compared to higher temperatures. U_{Mn}^{cem-p} in the earlier stages of the reaction is higher than U_{Mn}^{cem-gb} but within the experimental margin of error.

At temperatures above 650 °C, where pearlite colonies are not very large, when dissolution of ferrite occur, the intermediate steps are hard to capture and analyze. In many cases, if dissolution of ferrite is observed it is based on the indirect evidence, *viz.*, manganese content of cementite, the width of the manganese-depleted austenite between two cementite lamellae, and the orientation relationship of the austenite grain between the cementite lamella similar to the former pearlite colony shown in Fig. 3.13 (letter) l. In large, well developed colonies ferrite dissolution begins at the periphery of the colony, as seen in the Figs. 3.13m-o, for samples heat treated longer than 60 days.

3.2.8 640 °C

For heat treatment times between 1 hour and 48 hours over the temperature range of 585 °C-640 °C only the pearlite product is observed. Heat treatment time intervals are too long to expose the sequential nature of the phase transformation reaction (ex: grain boundary cementite precipitation, which leads to pearlite or cellular austenite decomposition) observed at higher temperatures. Only the morphological evaluation is carried out at these temperature-time modes. Micrographs demonstrating pearlite growth are not shown.

Table 3.11a: Computed equilibrium volume fraction and composition for cementite and austenite phases for the Fe-0.85C-11.56Mn (wt. %) alloy at 640 °C.

Φ^{cem}	U_{Mn}^{cem}	U_C^{cem}	Φ^{γ}	U_{Mn}^{γ}	U_C^{γ}
6.17×10^{-2}	3.03×10^{-1}	3.33×10^{-1}	9.38×10^{-1}	1.07×10^{-1}	2.2×10^{-2}

Table 3.11b: Growth rate data for the alloy at 640°C.

HT time (hours)	$\lambda_{cem}^{pearlite}$ (nm)	$\lambda_{\alpha}^{pearlite}$ (nm)	$\Phi^{pearlite}$ $\times 10^{-2}$	A_f Free pearlite growth front area/volume (m^{-1})	$\dfrac{dx}{dt}$ (s^{-1})	$\overline{G} = \dfrac{1}{A_f} \cdot \dfrac{dx}{dt}$ (m/s)
1	150	100	0	0	5.40×10^{-11}	0
3	270	225	0.12	0.046	5.67×10^{-11}	1.27×10^{-9}
6	430	395	0.75	0.32	5.04×10^{-11}	1.58×10^{-10}
12	610	630	1.90	0.064	6.75×10^{-11}	1.06×10^{-9}
24	795	710	3.09	0.051	7.76×10^{-11}	1.51×10^{-9}
48	850	745	4.58	0.067	4.18×10^{-11}	6.26×10^{-10}

$\times 10^{-9}$
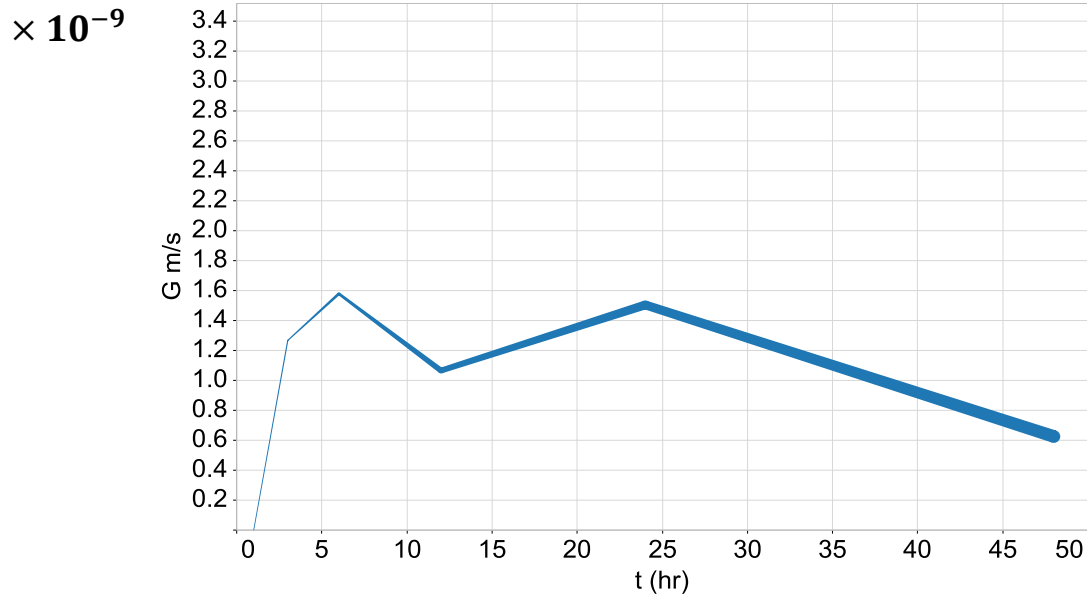
Figure 3.14: Growth rate of pearlite (m/s) over time (hr) at 640 °C. Thickness of the plot correlates with the volume fraction of the pearlite product (Table 3.11b).

3.2.9 <u>630 °C</u>

Table 3.12a: Computed equilibrium volume fraction and composition for cementite and austenite phases for the Fe-0.85C-11.56Mn (wt. %) alloy at 630 °C.

Φ^{cem}	U_{Mn}^{cem}	U_C^{cem}	Φ^{γ}	U_{Mn}^{γ}	U_C^{γ}
6.53×10^{-2}	3.06×10^{-1}	3.33×10^{-1}	9.35×10^{-1}	1.06×10^{-1}	2.10×10^{-2}

Table 3.12b: Growth rate data for the alloy at 630°C.

HT time (hours)	$\lambda_{cem}^{pearlite}$ (nm)	$\lambda_{\alpha}^{pearlite}$ (nm)	$\Phi^{pearlite}$ $\times 10^{-2}$	A_f Free pearlite growth front area/volume (m^{-1})	$\dfrac{dx}{dt}$ (s^{-1})	$\overline{G} = \dfrac{1}{A_f} \cdot \dfrac{dx}{dt}$ (m/s)
1	250	240	0.13	0.016	5.40×10^{-9}	3.35×10^{-9}
3	345	360	0.41	0.048	5.67×10^{-9}	1.18×10^{-9}
6	425	430	0.73	0.065	5.04×10^{-9}	7.77×10^{-10}
12	585	570	1.97	0.064	6.75×10^{-9}	1.06×10^{-9}
24	650	610	4.59	0.070	7.76×10^{-9}	1.16×10^{-9}
48	730	710	4.96	0.085	4.18×10^{-9}	4.90×10^{-10}
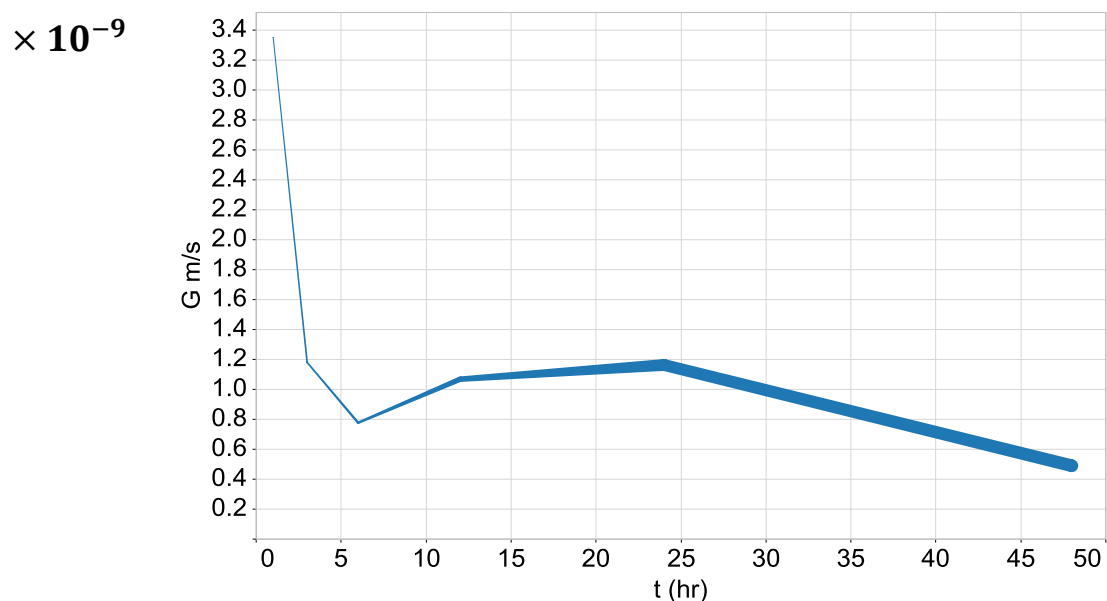
Figure 3.15: Growth rate of pearlite (m/s) over time (hr) at 630 °C. Thickness of the plot correlates with the volume fraction of the pearlite product (Table 3.12b).

3.2.10 <u>620 °C</u>

Table 3.13a: Computed equilibrium volume fraction and composition for cementite, ferrite, and austenite phases for the Fe-0.85C-11.56Mn (wt. %) alloy at 620 °C.

Φ^α	U^α_{Mn}	U^α_C	Φ^{cem}	U^{cem}_{Mn}	U^{cem}_C	Φ^γ	U^γ_{Mn}	U^γ_C
5.14×10^{-2}	2.07×10^{-2}	1.11×10^{-4}	7.26×10^{-2}	3.11×10^{-1}	3.33×10^{-1}	8.76×10^{-1}	1.06×10^{-1}	2.00×10^{-2}

Table 3.13b: Growth rate data for the alloy at 620°C.

HT time (hours)	$\lambda^{pearlite}_{cem}$ (nm)	$\lambda^{pearlite}_\alpha$ (nm)	$\Phi^{pearlite}$ $\times 10^{-2}$	A_f Free pearlite growth front area/volume (m^{-1})	$\dfrac{dx}{dt}$ (s^{-1})	$\overline{G} = \dfrac{1}{A_f} \cdot \dfrac{dx}{dt}$ (m/s)
1	100	120	0.11	0.027	4.49×10^{-9}	1.66×10^{-9}
3	175	190	0.73	0.061	9.90×10^{-9}	1.63×10^{-9}
6	220	260	2.16	0.089	1.45×10^{-8}	1.62×10^{-9}
12	320	345	4.64	0.10	1.54×10^{-8}	1.49×10^{-9}
24	480	460	6.23	0.11	1.02×10^{-8}	9.73×10^{-10}
48	525	520	8.38	0.10	6.82×10^{-9}	6.55×10^{-10}

$\times\,10^{-9}$
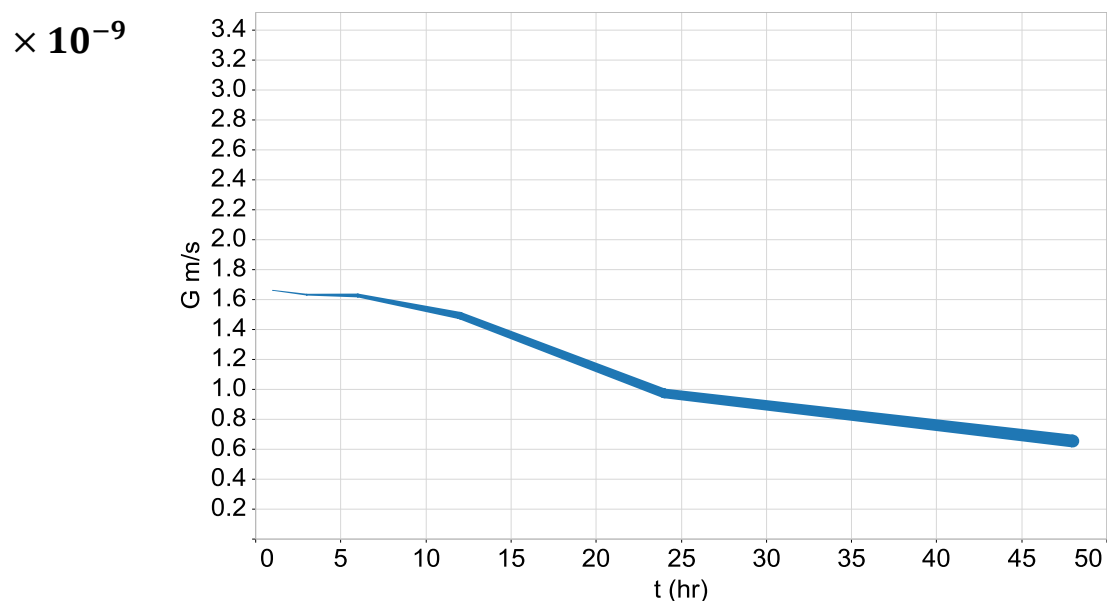
Figure 3.16: Growth rate of pearlite (m/s) over time (hr) at 620 °C. Thickness of the plot correlates with the volume fraction of the pearlite product (Table 3.13b).

3.2.11 <u>610 °C</u>

Table 3.14a: Computed equilibrium volume fraction and composition for cementite, ferrite, and austenite phases for the Fe-0.85C-11.56Mn (wt. %) alloy at 610 °C.

Φ^α	U_{Mn}^α	U_C^α	Φ^{cem}	U_{Mn}^{cem}	U_C^{cem}	Φ^γ	U_{Mn}^γ	U_C^γ
1.88 $\times 10^{-1}$	2.49 $\times 10^{-2}$	8.80 $\times 10^{-5}$	8.53 $\times 10^{-2}$	3.5 $\times 10^{-1}$	3.33 $\times 10^{-1}$	7.27 $\times 10^{-1}$	1.1 $\times 10^{-1}$	1.9 $\times 10^{-2}$

Table 3.14b: Growth rate data for the alloy at 610°C.

HT time (hours)	$\lambda_{cem}^{pearlite}$ (nm)	$\lambda_\alpha^{pearlite}$ (nm)	$\Phi^{pearlite}$ $\times 10^{-2}$	A_f Free pearlite growth front area/volume (m^{-1})	$\dfrac{dx}{dt}$ (s^{-1})	$\overline{G} = \dfrac{1}{A_f} \cdot \dfrac{dx}{dt}$ (m/s)
1	85	90	0.13	0.039	5.07×10^{-9}	1.30×10^{-9}
3	135	145	1.13	0.058	1.46×10^{-8}	2.52×10^{-9}
6	220	260	3.26	0.091	2.08×10^{-8}	2.29×10^{-9}
12	480	490	5.17	0.12	1.63×10^{-8}	1.35×10^{-9}
24	535	590	8.1	0.11	1.26×10^{-8}	1.11×10^{-9}
48	600	640	9.1	0.14	7.05×10^{-9}	5.07×10^{-10}

$\times \mathbf{10^{-9}}$
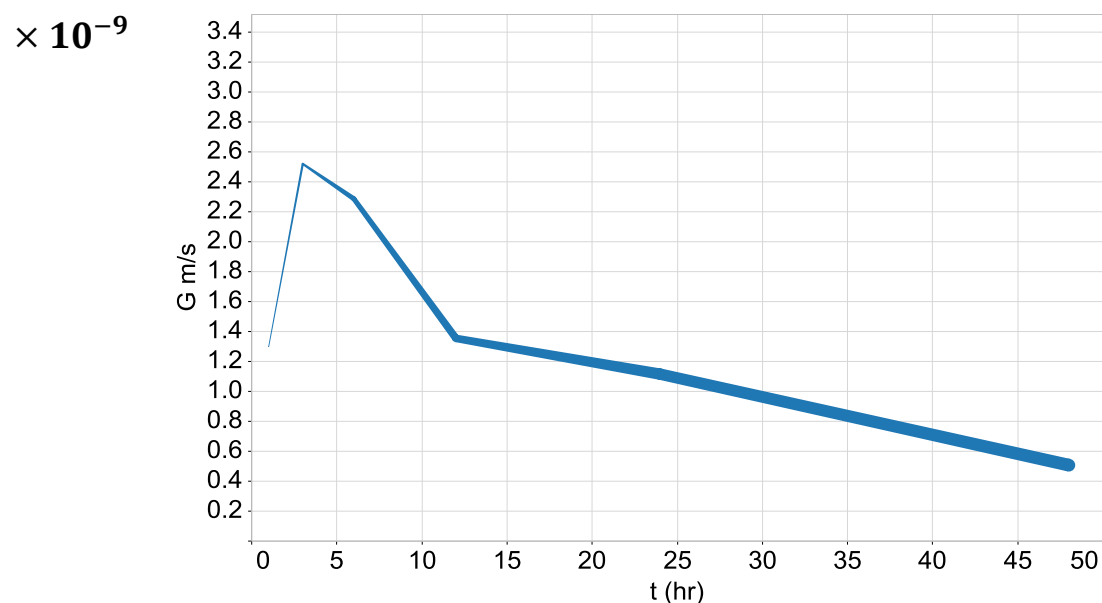
Figure 3.17: Growth rate of pearlite (m/s) over time (hr) at 610 °C. Thickness of the plot correlates with the volume fraction of the pearlite product (Table 3.14b).

3.2.12 <u>600 °C</u>

Table 3.15a: Computed equilibrium volume fraction and composition for cementite, ferrite, and austenite for the Fe-0.85C-11.56Mn (wt. %) alloy at 600 °C.

Φ^α	U^α_{Mn}	U^α_C	Φ^{cem}	U^{cem}_{Mn}	U^{cem}_C	Φ^γ	U^γ_{Mn}	U^γ_C
2.99 $\times 10^{-1}$	2.63 $\times 10^{-2}$	6.94 $\times 10^{-5}$	9.52 $\times 10^{-2}$	3.7 $\times 10^{-1}$	3.33 $\times 10^{-1}$	6.05 $\times 10^{-1}$	1.3 $\times 10^{-1}$	1.7 $\times 10^{-2}$

Table 3.15b: Growth rate data for the alloy at 600°C.

HT time (hours)	$\lambda^{pearlite}_{cem}$ (nm)	$\lambda^{pearlite}_\alpha$ (nm)	$\Phi^{pearlite}$ $\times 10^{-2}$	A_f Free pearlite growth front area/volume (m^{-1})	$\dfrac{dx}{dt}$ (s^{-1})	$\overline{G} = \dfrac{1}{A_f} \cdot \dfrac{dx}{dt}$ (m/s)
1	135	140	0.16	0.045	6.06×10^{-9}	1.34×10^{-9}
3	185	170	1.23	0.070	1.54×10^{-8}	2.20×10^{-9}
6	360	390	3.87	0.10	2.40×10^{-8}	2.39×10^{-9}
12	480	490	7.79	0.11	2.37×10^{-8}	2.22×10^{-9}
24	420	550	13.7	0.11	2.00×10^{-8}	1.78×10^{-9}
48	560	600	17.9	0.14	1.28×10^{-8}	9.08×10^{-10}

$\times 10^{-9}$
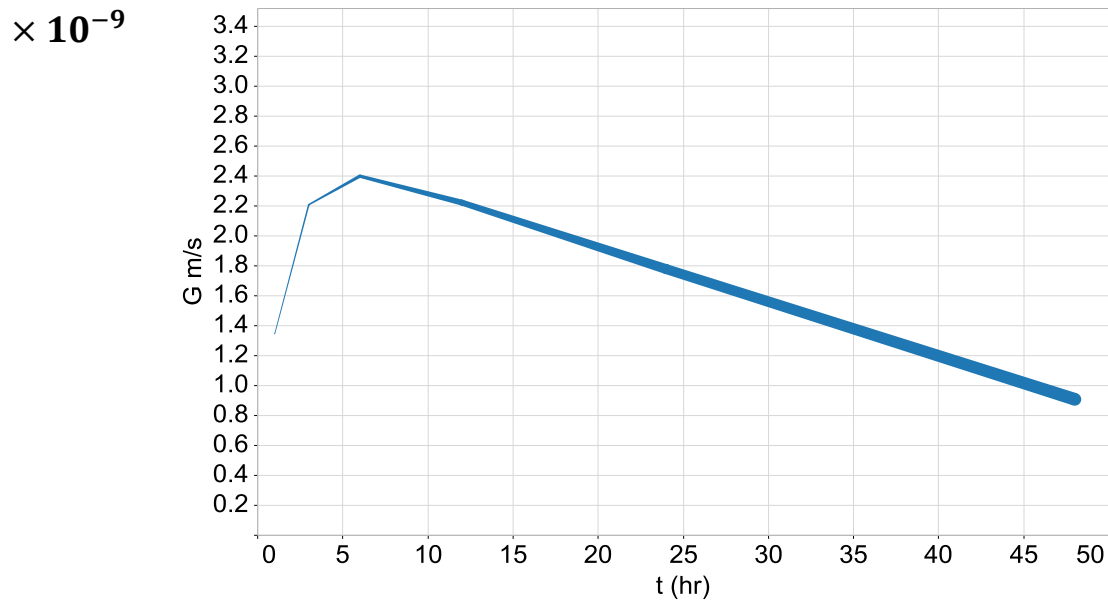
Figure 3.18: Growth rate of pearlite (m/s) over time (hr) at 600 °C. Thickness of the plot correlates with the volume fraction of the pearlite product (Table 3.15b).

3.2.13 585 °C

Table 3.16a: Computed equilibrium volume fraction and composition for cementite, ferrite, and austenite for the Fe-0.85C-11.56Mn (wt. %) alloy at 585°C.

Φ^α	U_{Mn}^α	U_C^α	Φ^{cem}	U_{Mn}^{cem}	U_C^{cem}	Φ^γ	U_{Mn}^γ	U_C^γ
4.33 $\times 10^{-1}$	2.82 $\times 10^{-2}$	4.00 $\times 10^{-5}$	1.06 $\times 10^{-1}$	4.1 $\times 10^{-1}$	3.33 $\times 10^{-1}$	4.6 $\times 10^{-1}$	1.4 $\times 10^{-1}$	1.54 $\times 10^{-2}$

Table 3.16b: Growth kinetics data for the alloy at 585°C.

HT time (hours)	$\lambda_{cem}^{pearlite}$ (nm)	$\lambda_\alpha^{pearlite}$ (nm)	$\Phi^{pearlite}$ $\times 10^{-2}$	A_f Free pearlite growth front area/volume (m^{-1})	$\dfrac{dx}{dt}$ (s^{-1})	$\overline{G} = \dfrac{1}{A_f} \cdot \dfrac{dx}{dt}$ (m/s)
1	110	140	0.18	0.052	6.64×10^{-9}	1.27×10^{-9}
3	150	175	1.53	0.084	1.87×10^{-9}	2.22×10^{-9}
6	200	220	5.63	0.12	3.36×10^{-9}	2.72×10^{-9}
12	250	270	9.88	0.13	2.88×10^{-9}	2.18×10^{-9}
24	310	345	14.82	0.11	2.10×10^{-9}	1.98×10^{-9}
48	350	425	23.36	0.13	1.57×10^{-9}	1.20×10^{-9}

119

$\times 10^{-9}$
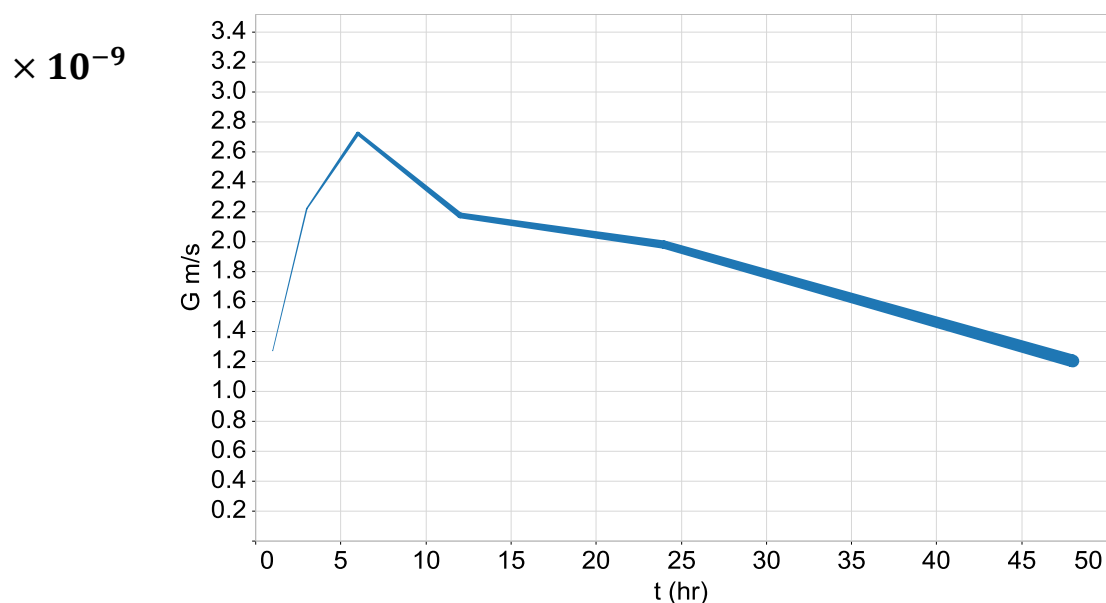
Figure 3.19: Growth rate of pearlite (m/s) over time (hr) at 585 °C. Thickness of the plot correlates with the volume fraction of the pearlite product (Table 3.16b).

3.3 General Trends

Tables 3.17a-c summarize general trends obtained from the data listed in the previous sections. These trends are consistent with literature reported trends for similar systems and phase transformation.

Table 3.17a: Matrix summarizing general trends for cellular reaction. Color scheme: green – increase, white – constant, orange – decrease.

Increasing Variable	U_{Mn}^{cem-c}	Φ^{cem}	Colony size	$\lambda_{cem}^{cellular}$	$\lambda_{\gamma^d}^{cellular}$
Time	Constant	Increases	Increases	Increases	Increases
Temperature	Decreases	Decreases	Decreases	Increases	Increases

Table 3.17b: Matrix summarizing general trends for pearlite reaction. Color scheme: green – increase, white – constant, orange – decrease.

Increasing Variable	U_{Mn}^{cem-p}	U_{Mn}^{α} pearlite	Φ^{cem}	Φ^{α}	Colony size	$\lambda_{cem}^{pearlite}$	$\lambda_{\alpha}^{pearlite}$
Time	Increases	Increases	Increases		Increases	Increases	Increases
Temperature	Increases	Constant	Decreases	Decreases	Decreases	Decreases	Decreases

Table 3.17c: General Trends for the entire sample.

Increasing Variable	U_{Mn}^{cem-gb}	Φ^{cem}
Time	Constant	Increases
Temperature	Increases	Decreases

Chapter 4 – Discussion

Transformation at the three selected temperatures (700, 660, 650 $^{\mathrm{o}}$C) begins by formation of grain boundary cementite in conjunction with manganese partitioning. This reaction alters the composition of austenite neighborhoods adjacent to cementite. This result arises from a large disparity between manganese volume diffusion and grain boundary diffusion in austenite. Therefore, the reaction paths involve austenite neighborhoods with chemistries and, consequently, thermodynamic properties different from the bulk alloy. These altered austenite regions are focused on in this chapter to develop the concept of neighborhood thermodynamics, which is employed to describe intermediate reactions during austenite decomposition towards equilibrium. The approach augments transformation pathway analysis by focusing on the reaction/microstructure type while remaining consistent with global thermodynamics. Utilizing this framework, the following sections account for ferrite growth and dissolution which is not clear when using global thermodynamics alone. Furthermore, this framework permits an evaluation of individual reactions (pearlite and cellular) to assess their thermodynamic feasibility independent of each other. The discussion makes extensive use of carbon activity, introduced in detail in the following section discussing 700 °C, with the key assumption being that carbon is able to essentially instantaneously redistribute itself in response to any manganese movement. Only the sections discussing 660 and 650 °C address the main objective of the dissertation: ferrite growth and dissolution. All calculations are for a pressure of 1atm, minimal decarburization, and software specified default reference phases. Thermo-Calc and MatCalc software packages, used extensively for all calculations in this work, employ subregular solution model for the Gibbs free energy of mixing. All references to free energy imply Gibbs free energy. Note that free energy sinks, *e.g.*, interfacial energies, curvature, are not included in the analysis.

4.1 700 °C

4.1.1 Predictions using interface local equilibrium model

Analysis begins at a temperature that is higher than where metastable ferrite can form (~687 °C). This temperature is selected so that the non-equilibrium pearlite region can be approached from above and may give some insight into pearlite systematics to come. This also allows application of our methodologies to a transformation initially thought to be simply the nucleation and growth of grain boundary cementite. Interestingly the transformation is more complicated and results in cementite cellular precipitation with an austenite component that, by itself, increases Gibbs free energy by partitioning too much manganese (excessively depleting of manganese). However, when coupled with high manganese containing cementite, the free energy decreases, as it must.

The bulk alloy composition at 700 °C (marked by the yellow circle in Figs. 4.1a-c) lies in the (γ + cem) two-phase field and above (to the right of) the P/NP boundary. This means that cementite can form with a chemistry that includes inheriting the bulk manganese content ($U_{Mn}^{\gamma} \approx$ 0.118). This value sets the lowest manganese content for any cementite that forms. Fig. 4.1b shows an enlargement of the boxed-in region in Fig. 4.1a with the calculated extrapolated $\gamma/(\gamma+\text{cem})$ and $\gamma/(\alpha+\gamma)$ boundaries added as dashed lines. Constructing a tie-line through the bulk alloy predicts an equilibrium amount of manganese in cementite for this temperature is $U_{Mn}^{cem} \approx$ 0.285, Fig. 4.1c purple circle, the highest manganese cementite content allowed. Of course, full equilibrium partitioning ($U_{Mn}^{cem} \approx 0.285$) or any partitioning between these two limits, *viz.*, 0.118 $\leq U_{Mn}^{cem} \leq 0.285$, will also reduce the free energy of the system.
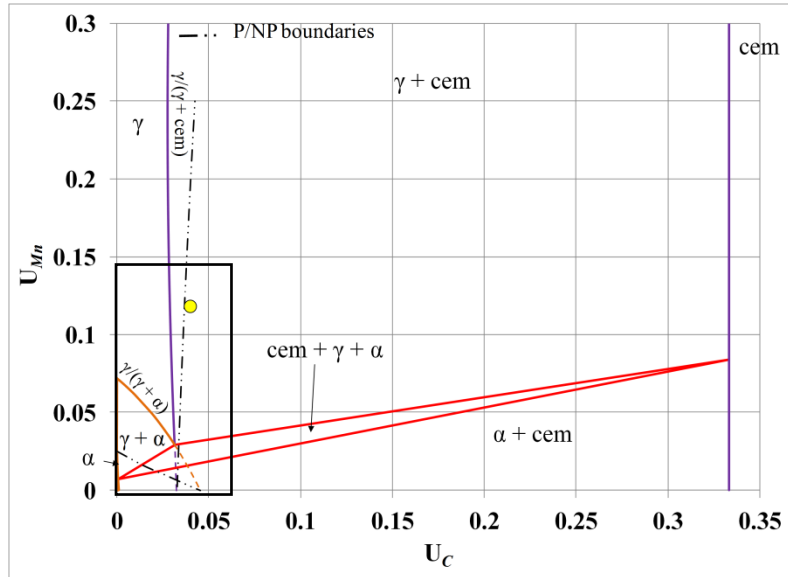
Figure 4.1a: 700 °C isotherm for Fe-C-Mn alloy. Yellow circle marks bulk alloy composition. Fig. 4.1b shows the area enclosed by the black rectangle.
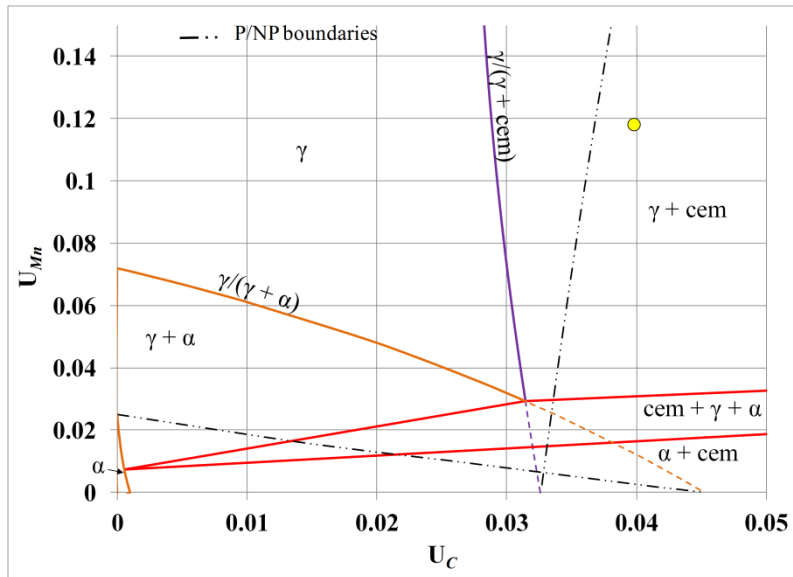
Figure 4.1b: Area highlighted by the rectangle in Fig. 4.1a.
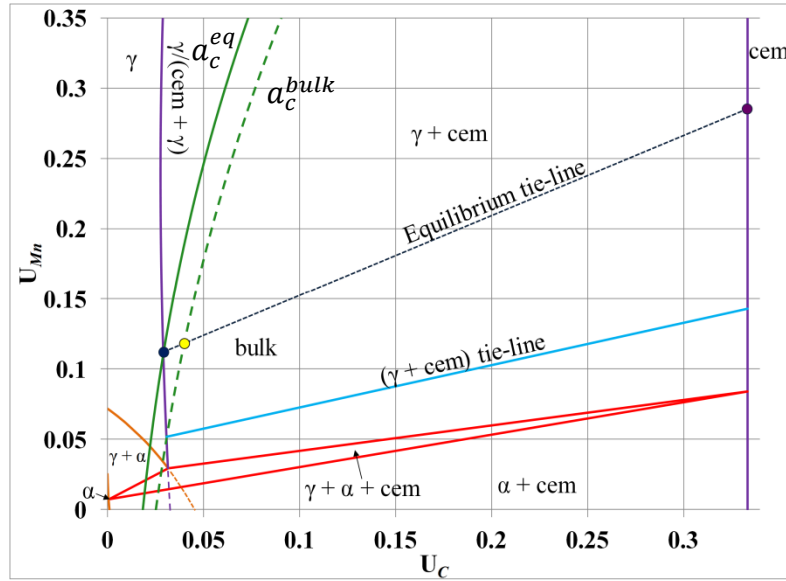
Figure 4.1c: 700 °C isotherm for Fe-C-Mn alloy. Yellow circle marks bulk alloy composition. Dashed and solid green lines represent bulk and equilibrium carbon isoactivity lines, respectively. Blue and purple circles represent austenite and cementite compositions at equilibrium (the end points of the equilibrium tie-line). LE-P model predicts $U_{Mn}^{cem} \approx 0.140$ and $U_{Mn}^{\gamma} \approx 0.050$ (cementite and austenite ends of the (γ + cem) tie-line) interphase interface compositions at the onset of the reaction. P/NP boundaries shown in Figs 4.1a and b are not shown.

Because of the large disparity in solute diffusivities, it is expected that the early phase transformations will not have compositions given by the equilibrium tie-line. An alternative is to then find a new tie-line reflecting the dominate role of carbon in effecting the transformation. Intersection of a carbon isoactivity line passing through the bulk alloy will allow a new non-equilibrium tie-line to be constructed. This is done using the dashed green a_c^{bulk} line in Fig. 4.1c, which intersects the γ/(γ + cem) phase boundary resulting in a composition of austenite at the γ/cem interface. From this intersection, a newly constructed tie-line (blue line), corresponding to $U_{Mn}^{\gamma} \approx 0.05$ at the interface (local equilibrium), predicts the manganese content in cementite at the γ/cem interface to be $U_{Mn}^{cem} \approx 0.140$ during the early stages of the transformation.[11]

4.1.2 Experimental Summary

Before utilizing the isotherm constructions above, a quick synopsis of experimental results for the current temperature is provided in graphical format from the extensive amount of data reported in Chapter 3. This will allow convenient access to the relevant results for

---

[11] Method proposed by Hutchinson and Shiflet in [hutchinson2004].

subsequent calculations and discussion. Once quenched from 1200 °C to 700 °C, the reaction sequence is grain boundary cementite precipitation, which occurs after 4 days, followed by cellular decomposition, which occurs between 7 and 14 days of heat treatment (the time gap between heat treatments). Cellular cementite and depleted-austenite widths, colony size, as well as, cementite and manganese-depleted volume fractions increase with heat treatment time, Figs. 4.2a-c. The combined (grain boundary and cellular) volume fraction of cementite reaches 0.032 (mole fraction of 0.037) or ~87% of equilibrium expected volume fraction, 0.039 (mole fraction 0.045), after 60 days, Table 3.5b.
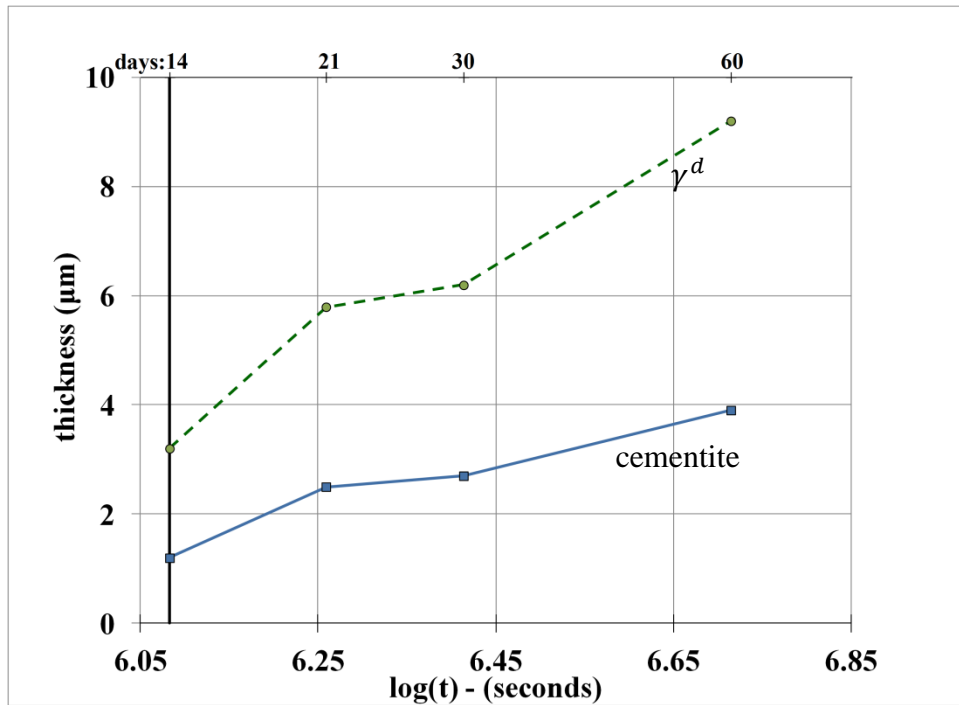
Figure 4.2a: Lamellar width of cementite (solid blue line) and manganese-depleted austenite (dashed green line). Vertical black line shows the estimated start of cellular transformation.
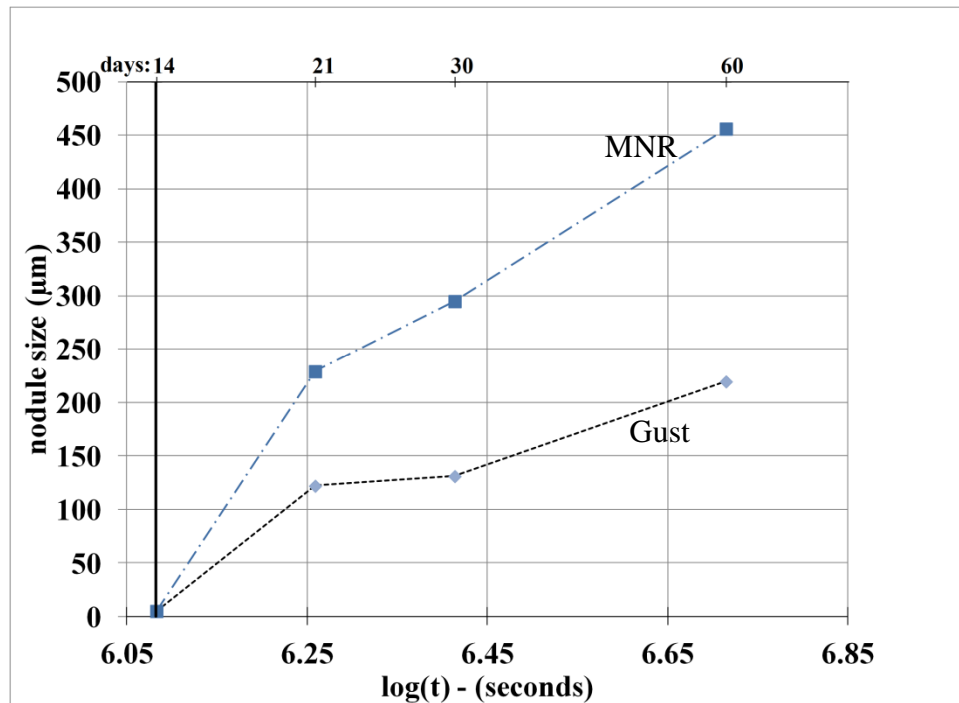
Figure 4.2b: Colony size using maximum nodule size (MNR, dash-dot blue line) and Gust (black dashed line) methods. Vertical black line shows the estimated start of cellular transformation.
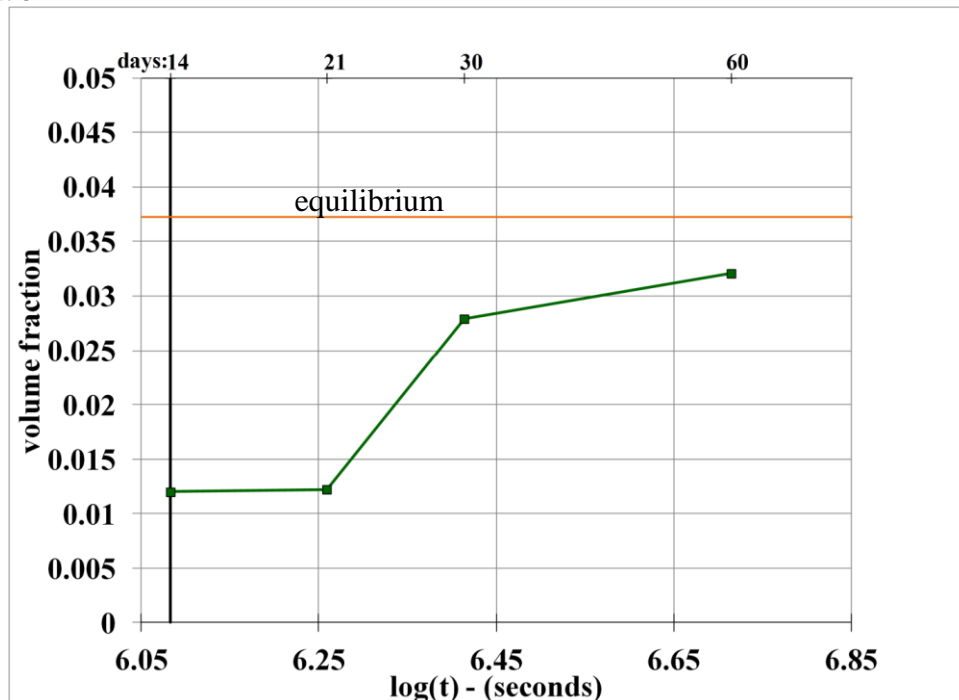
Figure 4.2c: The combined cementite volume fraction (green solid line) as a function of time. Orange line shows the equilibrium expected amount. Vertical black line shows the estimated start of cellular transformation.
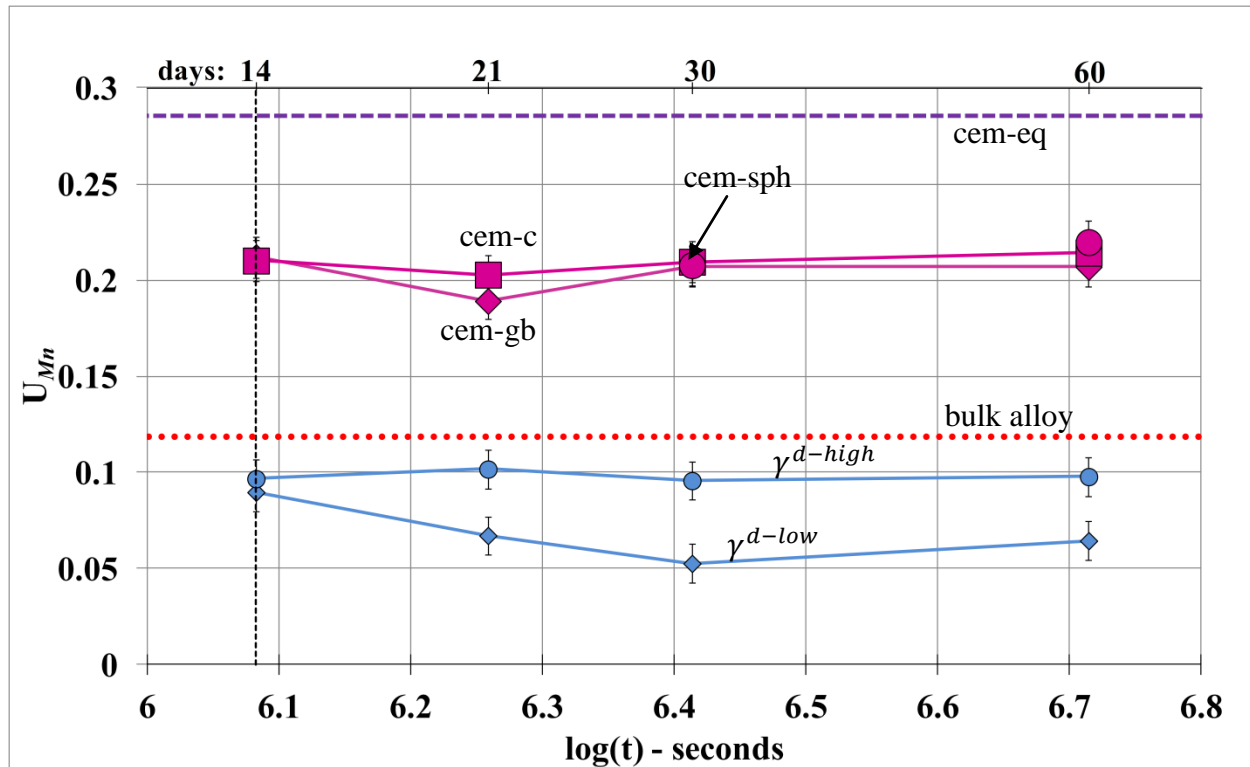
Figure 4.2d: Experimentally measured manganese content in cementite and austenite matrix. Dashed line (purple) is U_{Mn}^{cem} at equilibrium. $U_{Mn}^{\gamma-bulk}$ is shown with dotted red line. The purple squares refer to U_{Mn}^{cem-c}, rhombuses to U_{Mn}^{cem-gb}, the circles $U_{Mn}^{cem-sph}$. $U_{Mn}^{\gamma^{d}-high}$ (blue circles) and $U_{Mn}^{\gamma^{d}-low}$ (blue rhombuses) refer to the range of manganese content in the cellular colony's manganese-depleted austenite. Abbreviations are consistent with those used in the previous chapter. Dashed vertical black line shows the start of cellular transformation.

The manganese content in grain boundary cementite remains nearly constant for the duration of the reaction ($U_{Mn}^{cem-gb} \approx 0.20$, Fig. 4.2d). Manganese content in cellular cementite and spherodized cementite is equal to the manganese content in grain boundary cementite, which are all lower than the expected equilibrium manganese content of 0.285. A nearly constant manganese content of cementite between 0.5 and 2 months, in the three morphologies, is significant and reflects the manganese partitioning mechanism.

Grain boundary migration ahead of the cementite plates is concomitant with cellular colony growth. In all cellular colonies, the austenite region between two cementite lamellae behind the moving grain boundary has the following characteristics: 1) at every location the manganese content is lower than the manganese content of the bulk alloy and lower than the final

equilibrium austenite manganese content ($U_{Mn}^{\gamma-eq} \approx 0.112$); 2) the manganese content is highest at the midpoint between the cementite lamellae, shown schematically in Fig. 4.3 and experimentally in Fig. 4.5; 3) the manganese content increases when measured parallel to the cementite lamellae and away from the moving grain boundary (back in time, illustrated in Fig. 4.3). $U_{Mn}^{\gamma^{d-high}}$ represents data collected away from the growth front and at the austenite lamella midpoint. $U_{Mn}^{\gamma^{d-low}}$ represents data collected near the moving front and adjacent to a cementite lamellae. Consistent with the systematics of cellular transformations, the orientation relationship of the manganese-depleted austenite is the same as the grain the colony is not growing into.
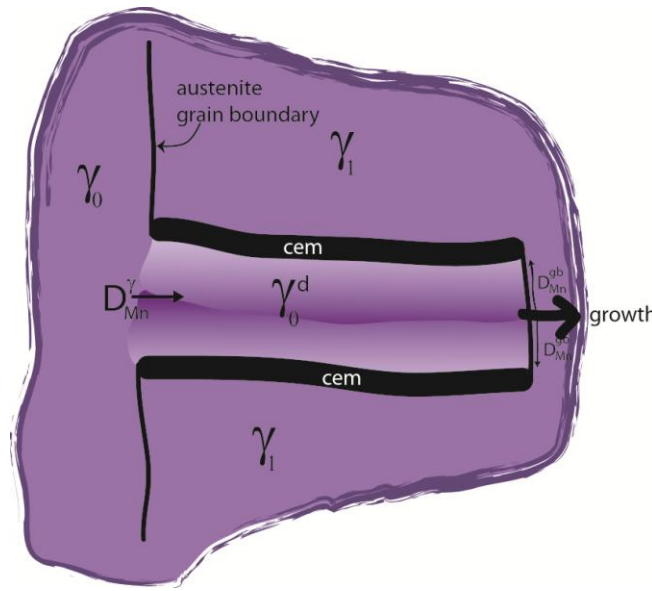
Figure 4.3: Schematic drawing highlighting the manganese distribution in the austenite cellular component. Color intensity of austenite represents relative amounts of manganese. Manganese content is higher at the midpoint between the cementite lamellae and away from the growth front towards the original grain boundary location. Non-uniform distribution of manganese in the manganese-depleted region is the result of slower manganese diffusion in austenite (D_{Mn}^{γ}) when compared to grain boundary diffusion (D_{Mn}^{gb}). Abbreviations are consistent with those used in the previous chapter.

4.1.3 Global Thermodynamics

The following discussion models the system's phase transformations using chemical and morphological experimental values taken over time. While cementite and austenite are the only two phases present during this reaction, for this discussion austenite is separated into two variations: 1) austenite matrix 2) manganese-depleted austenite (with greatest depletion labeled γ^{d-high} and the least depletion as γ^{d-low}). This is done to include all thermodynamically

important phases, **and** their relevant chemical variations, that are important to gain insight when the more local or 'neighborhood' considerations are discussed. In the sections discussing both 660 and 650 °C the number of phases and phase variants will be further expanded to account for the retrenched austenite, pearlitic cementite, and ferrite.
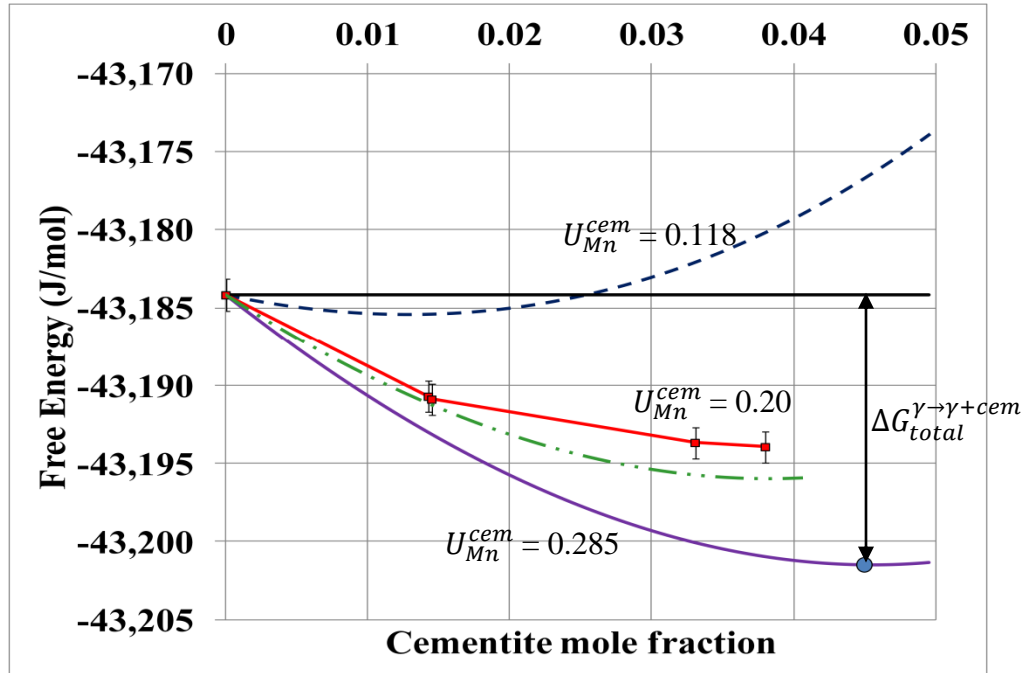
Figure 4.4a: Computed Gibbs free energy of the Fe-0.85C-11.56Mn (wt. %) system as a function of cementite mole fraction at 700 °C. **Black** solid line – energy of the system prior to austenite decomposition. **Blue** dashed line – the system contains cementite with U_{Mn}^{cem} = 0.118 (no manganese partitioning) and austenite matrix. **Purple** solid line – the system contains cementite with U_{Mn}^{cem} = 0.285 (equilibrium predicted value) and austenite matrix. Blue circle corresponds to final cementite mole fraction at equilibrium (0.045) **Green** dash-dot-dot line – the system contains cementite with U_{Mn}^{cem} = 0.20 (the experimentally measured value) and remaining austenite matrix. **Red** solid line – the experimentally observed system with U_{Mn}^{cem} = 0.20, the manganese-depleted austenite with $U_{Mn}^{\gamma^d}$= 0.09, and remaining austenite matrix. Table 3.5b lists volume fraction information for each phase.
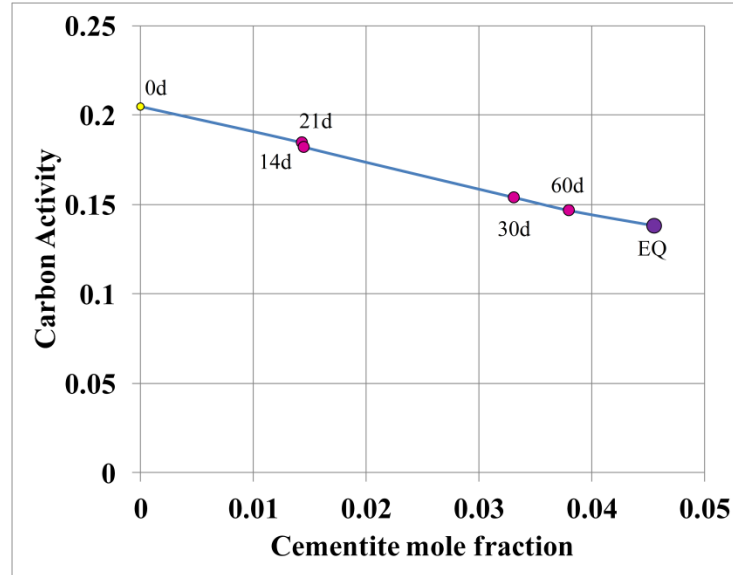
Figure 4.4b: Carbon activity in the austenite matrix as a function of experimentally observed cementite mole fraction for the alloy heat treated at 700 °C. Yellow circle represents the system prior to decomposition (dashed green line in Fig. 4.6b). Purple circle represents the system at equilibrium (solid green line in Fig. 4.6b). Magenta circles represent the system at the intermediate time steps.

To examine, thermodynamically, the effect of what seems to be an excessively manganese depleted austenite cellular component (no other example could be found in the literature where the lamellar depleted matrix plate component of the cell has a solute amount that is depleted below what will be the final matrix composition) Fig. 4.4 is constructed as follows. The solid black line in Fig. 4.4a shows computed Gibbs free energy of the current system at 700 °C prior to cementite formation. The purple solid line represents the Gibbs free energy change for the system where austenite and cementite approach equilibrium mole fraction quantity with cementite possessing the equilibrium manganese content, $U_{Mn}^{cem} = 0.285$. The total energy available, $\Delta G_{total}^{\gamma \to \gamma + cem}$, for transformation to austenite and 0.045 mole fraction of cementite (equilibrium) is ~17 J/mol, the difference between horizontal solid and the blue circle on the purple line. No other phase can have a negative change in Gibbs free energy below the purple line. At a minimum, the growing cementite must inherit the bulk alloy manganese content, where $U_{Mn}^{cem} = 0.118$. The dashed blue line in Fig. 4.4a plots Gibbs free energy as a function of cementite mole fraction (note that the abscissa is cementite mole fraction formed) associated with no partitioning (paracementite). From the plot, the initial decrease in Gibbs free energy permits growth of unpartitioned cementite thereby contradicting the *limitation* of $U_{Mn}^{cem} \approx 0.140$,

arising from calculation error by Hutchinson and Shiflet method.[12] One interesting feature is that with no partitioning of manganese the amount of cementite that can form is limited to 0.015, with any further growth resulting in an increase of Gibbs free energy. Consequently, partitioning of manganese into cementite must be concurrent with any additional growth of cementite. Since progress of any reaction requires only a sufficient reduction in Gibbs free energy, the region *between* the solid (horizontal) black and purple lines is the theoretically permissible manganese partitioning range, given the observed cementite mole fraction.

Computation of Gibbs free energy using our measured data results in the red line in Fig. 4.4a. The measured values are cementite with $U_{Mn}^{cem} = 0.20$, manganese-depleted austenite with $U_{Mn}^{\gamma^d} = 0.09$, and bulk austenite, $U_{Mn}^{\gamma^{bulk}} = 0.118$, with their respective experimentally determined mole fractions. Since the energy trend is increasingly negative, cellular decomposition with these experimental manganese contents and amounts is thermodynamically permissible. Overall, then, the cellular reaction accounts for ~57% of the energy reduction associated with a complete equilibrium phase transformation at this temperature. After 60 days at 700 °C, the maximum experimentally measured amount of cementite mole fraction is ~0.037.

What makes consideration necessary is that, with the formation of the equilibrium phase, cementite (albeit with less manganese than required by equilibrium), as noted, an excessively manganese-depleted austenite forms as part of the colony. Depleting the cellular austenite below the manganese content that exists at equilibrium ($U_{Mn}^{\gamma-eq} \approx 0.112$, equilibrium tie-line Fig. 4.1c) contributes a positive change in Gibbs free energy, which mitigates the negative free energy change associated with cementite formation, *i.e.*, $\Delta G^{cem} + \Delta G^{\gamma^d} < 0$. To expand this point, a further comparison can be visualized by considering Gibbs free energy for the same reaction and the same experimentally measured manganese content of $U_{Mn}^{cem} = 0.20$, but now rather than have a small volume of austenite supplying all the manganese (the manganese-depleted austenite lamella in cellular colony), all the manganese is supplied uniformly from the matrix by volume diffusion. Essentially, this microstructure would be widely-spaced cementite Widmanstatten plates growing into austenite. The green dash-dot-dot line represents this model in Fig. 4.4a. Here, the Gibbs free energy change is uniformly lower than the equivalent amount of cementite

---

[12] Reduction in Gibbs free energy associated with manganese partitioning (dashed blue vs. purple lines in Fig. 4.4a) thermodynamically permit growth of cementite with $U_{Mn}^{cem} \approx 0.140$ but it is not the thermodynamic limit, as predicted by Hutchinson and Shiflet. The cause of the error is incorrectly calculated P/NP boundary in [hutchinson2004].

that forms as a part of the experimentally determined cellular colony (red line) with its associated excessively manganese-depleted austenite lamella, i.e., $U_{Mn}^{\gamma\,eq} = 0.112$ *vs.* $U_{Mn}^{\gamma\,d} \approx 0.09$. The explanation, when comparing the red and green lines, is that for the actual microstructure the growing cementite receives nearly all of its manganese from short circuit diffusion (the grain boundary) and negligible amounts from volume diffusion (the green line example), and therefore, the energy cost by 'over' depleting the austenite lamella is more than compensated energetically by the additional manganese additions to the advancing cementite lattice. So, although, long range volume diffusion of manganese is energetically preferred—it is just not feasible at this low homologous temperature. However, this is yet another chemical imbalance that the system must fix before equilibrium can be attained. These imbalances only increase as the reaction temperature is lowered, as will be shown in later sections.

Another parameter indicative of the transformation progress is the activity of carbon (Fig. 4.4b). Because carbon is taken from the matrix and partitioned into M₃C, its activity decreases, and does so as the mole fraction of cementite increases. Since cementite is a stoichiometric compound with $X_C^{cem} = 0.25$ it is possible to compute carbon content that remains in the austenite matrix at each transformation stage when information about the cementite mole fraction is available at the same stage. Knowledge of carbon content in the remaining austenite matrix then permits computation of carbon activity, a_C^γ. For example, given the Fe-0.85C-11.56Mn (wt. %) alloy at 700 °C, equilibrium expected cementite mole fraction is ~0.0450 and, therefore, austenite mole fraction is ~0.955. Mole fraction of carbon in the alloy is 0.0383. Using a mass balance equation ($mole\ fraction\ of\ cementite\ \times\ X_C^{cem} + mole\ fraction\ of\ austenite\ \times\ X_C^\gamma$) = $X_C^{\gamma-bulk}$ or $(0.0455 \times 0.25 + 0.955 \times X_C^\gamma). = 0.0383$. The computed X_C^γ at equilibrium is 0.0281 which is the same as the equilibrium predicted carbon mole fraction in austenite, Fig. 4.1c. Using the computed X_C^γ as carbon content in the remaining austenite while keeping manganese content the same (so the composition of the remaining matrix is Fe-0.028C-0.114Mn at. % or Fe-0.60C-11.56Mn wt. %) yields a carbon activity for the remaining matrix ~0.134, which compares favorably with equilibrium expected carbon activity for the original alloy (Fe-0.85C-11.56Mn (wt. %)) ~0.138. The difference of ~3% is attributed to ignoring manganese partitioning, which is discussed shortly. Similar calculations, using experimentally mole fraction of carbon, yield carbon activity values for intermediate steps in Fig. 4.4b where after 60 days of

heat treatment, activity of carbon has not reached the expected equilibrium value, confirming the energy analysis shown in Fig. 4.4a.

It is critical to note that unlike free energy, change in carbon activity of a system is more sensitive to cementite formation, which consumes matrix carbon, than to partitioning manganese. This is illustrated in Table 4.1 where carbon activity is evaluated while changing manganese content and mole fraction of cementite. For a system where the cementite mole fraction is 0.01 and $U_{Mn}^{cem}= 0.20$, carbon activity is 0.189. Increasing manganese content of cementite by 43% to its equilibrium amount (partitioning) while maintaining cementite mole fraction increases carbon activity to 0.1897, a change of ~ 0.4%. On the other hand, increasing cementite mole fraction from 0.01 to 0.0143, a 43% increase, while maintaining $U_{Mn}^{cem}= 0.20$, changes carbon activity to 0.1824. This represents a change of approximately ~ 3.5% and it is ~8 times larger than the change in activity associated with manganese partitioning. This characteristic of carbon isoactivity demonstrates that to determine carbon activity in the system, a precise knowledge of manganese distribution in cementite, an experimentally challenging task, is not necessary. *More importantly, cementite is the only phase where the atomic percent of carbon (and only carbon) remains constant for the duration of reaction for all temperatures.* The linchpin of the strategy used to account for all observed phase transformations relies on the fact that quantitative information about cementite mole fraction provides all the necessary information to compute an approximate (as per Table 4.1) carbon activity in the remaining austenite. The advantages of this strategy will become more apparent in the sections discussing 660 and 650 °C temperatures.

Table 4.1: Computed carbon activity for various mole fraction and manganese content of cementite for a Fe-0.85C-11.56Mn (wt. %) alloy at 700°C. Values in the 2nd and 3rd rows are compared to the first row.

Mole fraction of cementite	U_{Mn}^{cem}	a_C	Δ Mole fraction of cementite	ΔU_{Mn}^{cem}	Δa_C
0.0100	0.200	0.189			
0.0100	0.285	0.190	0	~43%	~ (0.4%)
0.0143	0.200	0.182	~43%	0	~ (-3.5%)

4.1.4 Neighborhood Thermodynamics – Cellular Reaction

Cementite nucleates on austenite grain boundaries, most likely high angle (high energy) segments. The constant manganese content in cementite regardless of morphology: grain

boundary, lamellar, or spherodized, for the duration of the reaction indicates that bulk diffusion of manganese from austenite to cementite is minimal. If this were not so, then portions of cementite that formed 30 or 40 days earlier than more freshly formed cementite would be expected to contain manganese contents closer to equilibrium values, however, all cementite forms have similar compositions. It is reasonable then, that manganese redistribution from austenite to cementite is primarily by grain boundary diffusion (D_{Mn}^{gb} in Fig. 4.3). Further, the presence of manganese-depleted regions adjacent to the cementite precipitates and exclusively behind the moving grain boundary supports this notion. Because of the importance of manganese partitioning primarily by short circuit paths, a numerical estimate for D_{Mn}^{gb} is made using measured data from Chapter 3.

Within the framework of this project, grain boundary diffusivity is approximated using Petermann-Hornbogen (PH) model

$$D_{Mn}^{gb} \equiv s\delta\widetilde{D} = \frac{RT}{-8\Delta G^{cellular}}\lambda^2 v \qquad (4.1)$$

where $\widetilde{D}$ is the chemical diffusion coefficient, λ is the combined average width of cementite and the manganese-depleted zone, v is the velocity (MNR/time) of the moving reaction front, $\Delta G^{cellular}$ is the change in free energy associated with the cellular transformation (the difference between the red line and horizontal black line in Fig. 4.4a), and the term $s\delta$ corresponds to the effective cross-sectional area for grain boundary diffusion, δ, multiplied by the segregation factor, s, the affinity of an element to diffuse towards the grain boundary. [petermann1968]
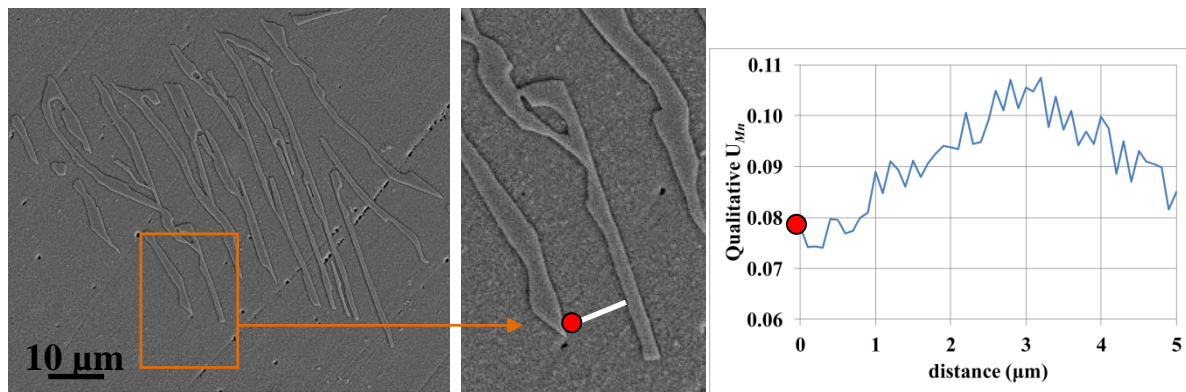
Figure 4.5: (Left) SEM image of a colony observed in a sample heat treated at 700 °C for 21 days (also shown in Chapter 3, Fig. 3.8d). **(Center)** Area corresponding to the orange on the left. White line shows the area of the line scan. **(Right)** EDS line scan of the line shown in the center image.

Results of the PH model have been shown to be consistent with those based on Cahn's model which balances solute atoms masses affected by diffusion along the reaction front and the motion of the reacting front into the supersaturated solution. [cahn1959, kaur1995] Cahn's solution predicts the concentration distribution across the manganese-depleted lamellae to exhibit a maximum in the center and minima at the edges, Fig. 4.3. While experimental results confirm this conclusion, Fig. 4.5, SEM techniques utilized in the experimental procedure associated with line scans are qualitatively correct with trends but not quantitative, which is necessary to employ Cahn's model. Therefore, the PH model is employed. The ancillary data used for the PH model (Eqn. 4.1) and calculated grain boundary diffusion are listed in the Table 4.1b. The average computed value for grain boundary diffusion in Table 4.2 is, then, $D_{gb}^{Mn} \approx 1.32 \times 10^{-18} \frac{m^2}{s}$. The average value calculation excludes D_{gb}^{Mn} for 14 days (highlighted in orange in Table 4.2) because the initial growth of cellular colonies can be sporadic unlike data obtained over longer heat treatment times. [zieba2002] Bulk manganese diffusion for this temperature is $D_{Mn}^{\gamma} = 5.20 \times 10^{-5} \times \exp\left(\frac{-282,000}{RT}\right) \approx 3.7 \times 10^{-20} \frac{m^2}{s}$. [fridberg1969] Using these diffusivities, the manganese-depleted austenite that lies almost entirely within the cellular colony and not the outside matrix is the result of the disparity between D_{Mn}^{γ} and D_{Mn}^{gb} ($\frac{D^{gb}}{D_{Mn}^{\gamma}} \approx 35$). These results are consistent with the assumption that grain boundary diffusion is the primary mechanism for manganese distribution. The analysis for the current temperature, therefore, assumes all manganese in cementite, greater than the bulk alloy content, partitions by means of grain boundaries. The consequence is manganese-depleted austenite located adjacent to the cementite, whether the cementite is a grain boundary allotriomorph or cellular formed plates. Both microstructures are intimately associated with a grain boundary. In the framework of the current analysis, manganese-depleted austenite regions are the thermodynamic neighborhoods which (as will be shown for 650 and 660 °C) exhibit thermodynamic properties different from those of the bulk alloy and are essential to consider apart from only the interphase interface and local equilibrium, which are normally done.

Table 4.2: Estimates of grain boundary diffusion computed using Eqn. 4.1 and experimental data at 700 °C. Value of D_{gb}^{Mn} is not counted in the average.

Time (d)	Time (s)	MNR (m) $\times 10^{-6}$ Table 3.5b	ΔG (J/mol) Fig. 4.4a	λ^{total} (m) $\times 10^{-6}$ Table 3.5b	v (m/s) $\times 10^{-12}$ MNR/time	D_{gb}^{Mn} (m²/s) $\times 10^{-20}$
14	1,209,600	5	-6.54	4.4	4.1	1.23
21	1,814,400	239	-6.73	8.3	131.7	136
30	2,592,000	304	-9.49	8.9	117.3	98.9
60	5,184,000	467	-9.77	13.1	90.1	160
Average						132

Overlaying the experimental neighborhood data onto the Fe-C-Mn 700 °C isotherm and examining thermodynamically permissible behavior associated with each neighborhood is the foundation of the neighborhood thermodynamics concept. Cementite is a stoichiometric compound, M_3C, with respect to carbon ($U_C \approx 0.333$ or $X_C = 0.25$). Although iron and manganese can have different ratios in the compound, it is assumed that carbon cannot. Furthermore, until the entire system reaches equilibrium cementite continues to grow removing carbon from the matrix and hence, lowering the carbon activity in austenite until equilibrium is attained. This is similar to the paraequilibrium mode described in Chapter 1 (Fig. 1.5) where the activity of bulk austenite (a_C^{bulk}) differs from the activity at the γ/α interphase interface ($a_C^{critical}$) permitting further growth of ferrite. Experimentally obtained manganese contents in cementite, and the transformation times when the content is measured, are plotted on the portion of the 700 °C isotherm that includes cementite line in Fig. 4.6a. Manganese levels rise only marginally, but do rise implying some D_{Mn}^{γ}, over the 60 days (similar to the plot in Fig. 4.2d). Experimentally obtained volume fraction of cementite (which provides information about the distribution of carbon in both phases) and its manganese content at any given time permit computation of carbon activity of the remaining austenite in the system. Since exact carbon content of the other phases is unknown, carbon activity (and carbon isoactivity lines) provides an alternative needed to map information onto the isotherm.
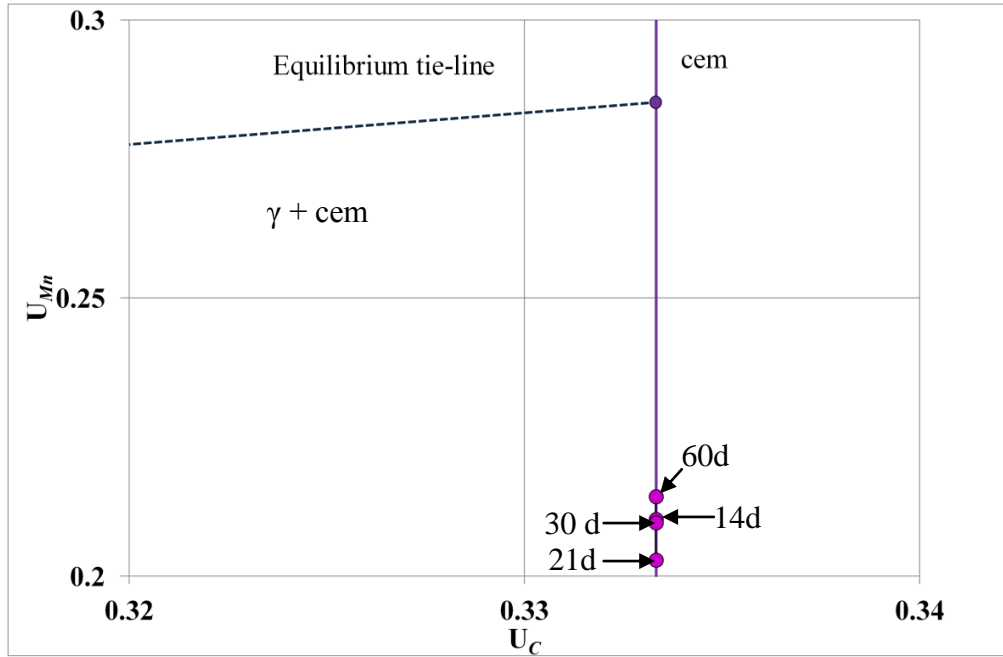
Figure 4.6a: Manganese content in cementite plotted on the Fe-Mn-C 700 °C isotherm.
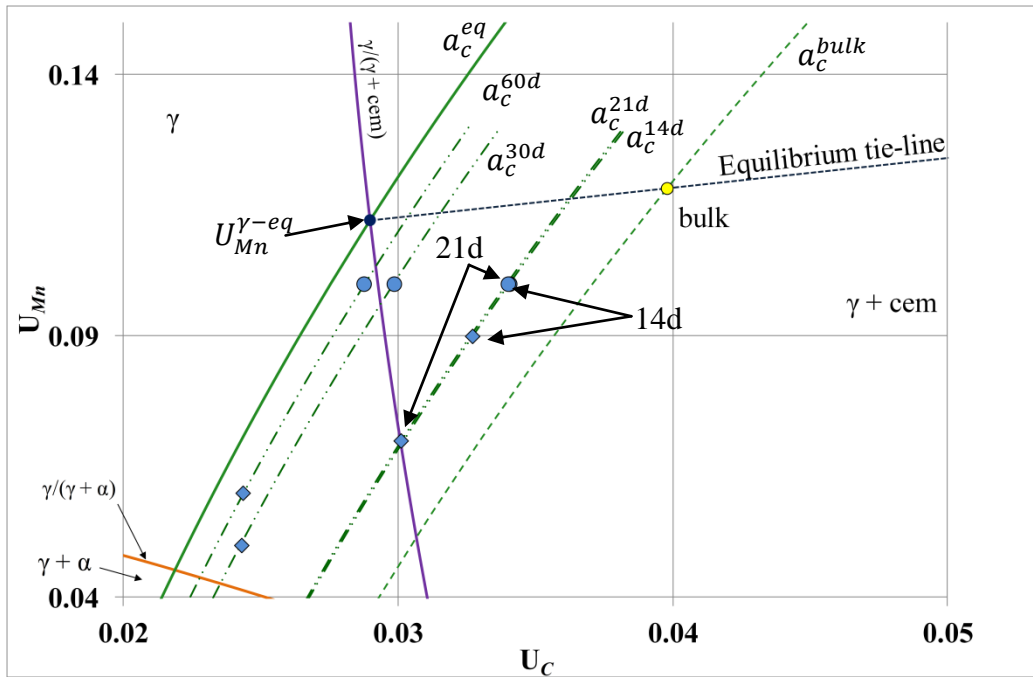
Figure 4.6b: Manganese content of the depleted regions mapped on the carbon isoactivity lines plotted on the Fe-Mn-C 700 °C isotherm. Yellow circle represents bulk alloy content. Blue circles indicate γ^{d-high} and rhombuses γ^{d-low}. P/NP boundaries shown in Figs 4.1a and b are not displayed.
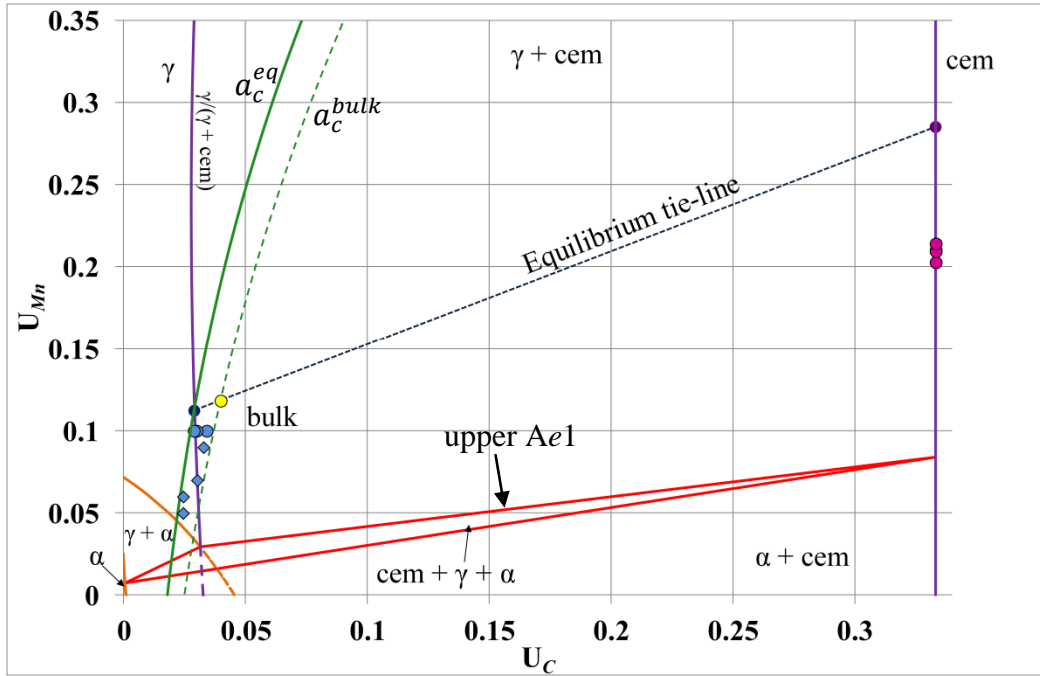
Figure 4.6c: Compilation of Figs. 4.6a and b with all of the data points plotted on the Fe-Mn-C 700 °C isotherm. P/NP boundaries shown in Figs 4.1a and b are not displayed.

Employing the carbon isoactivity concept says that at any given time $\mu_C^\gamma = \mu_C^{\gamma^{d-high}} = \mu_C^{\gamma^{d-low}}$ and $a_C^\gamma = a_C^{\gamma^{d-high}} = a_C^{\gamma^{d-low}}$, even if this assumption is extended from interfaces to austenite neighborhoods. This is a reasonable assumption since carbon diffuses many orders of magnitude faster than manganese ($\frac{D_C^\gamma}{D_{Mn}^{gb}} \approx 2.0 \times 10^5$). Fig. 4.6b shows evolution of carbon activity in the system over time where the dashed green line passing through the yellow circle (a_C^{bulk}) represents activity of the austenite prior to decomposition, and the solid green line passing though the dark blue circle (a_C^{eq}) represents the system at equilibrium (γ + cem). Green dash-dot-dot lines show computed carbon activities for intermediate periods where experimental data are gathered. All these values correlate to carbon activity values shown in Fig. 4.4b but now labeled to time, *i.e.*, a_C^{14d} is the carbon activity in austenite after 14 days. Since carbon activity in all austenite phases at any given time is the same, measured manganese contents for each austenite phase, at each time, must map on the corresponding isoactivity line. In Fig. 4.6b γ^{d-high}(blue circles), and γ^{d-low} (blue rhombuses) give the manganese range of cellular manganese-depleted austenite lamellae. Note that the γ^{d-low}, an area that would correspond to manganese-depleted austenite immediately adjacent to the cementite lamellae (Fig. 4.3, Fig. 4.5 red circle), is lower in

both manganese and carbon content when compared to γ^{d-high}. This result is not surprising due to depletion of both carbon and manganese immediately at the γ/cem interphase interface associated with growing cementite. All measurements and determinations of carbon activities remain range-bound between a_c^{bulk} and a_c^{eq}, as they should. Fig. 4.6c shows all the data measured and calculated for both phases and provides a more complete perspective.

Areas of manganese-depleted austenite are regions with alloy compositions, and thermodynamic properties, different from the bulk. As per Figs. 4.6b and c, these alloy compositions group into those that remain in the (γ + cem) two-phase field (14-day, 21-day, and 30-day γ^{d-high}, and 14-day γ^{d-low}) and those in the γ single-phase field (21-day, 30-day, and 60-day γ^{d-low}, and 60-day γ^{d-high}). All neighborhood chemistries that leave the (γ + cem) region, because of cementite growth (shift to the left on the U_C axis) and manganese partitioning (shift down on the U_{Mn} axis) into cementite, enter the (γ) single-phase field. Absence of neighborhoods in phase fields where formation of ferrite is possible (below the upper Ae1 line in Fig. 4.6c), therefore, explains the lack of ferrite at this temperature. Irrespective of the alloy compositions, manganese continuously diffuses from bulk austenite into the manganese-depleted austenite regions, with alloy composition climbing up the carbon isoactivity line. The rate of the climb is proportional to D_{Mn}^{γ}. When cementite reaches its equilibrium volume fraction and composition, these processes cease.

4.2 660 °C

4.2.1 Predictions using interface local equilibrium model

Transformation analysis at this temperature segues into examination the pearlite reaction, which for the current alloy comes into play at temperatures below 680 °C. The analysis builds on the methodology used to analyze the cellular reaction at 700 °C, while introducing additional complexity associated with pearlite (ferrite) growth and dissolution. Moreover, individual cementite-forming reactions (grain boundary, pearlitic and cellular) are evaluated on their thermodynamic ability as stand-alone reactions.

The method, previously described in Chapter 1 section 1.4.1.2 (Figs. 1.9a-e) to establish composition limits for any metastable phase is to employ an isoactivity line passing through the alloy chemistry. Intersection of this carbon isoactivity line with a phase boundary (or extrapolated portion thereof) represents the austenite endpoint of a new operative tie-line. The other tie-line endpoint represents the composition of either ferrite or cementite, depending on which phase boundary is intersected. If the alloy lies in the "must" partition portion of the isotherm, the area to the left and above the P/NP boundaries, then these values set allowable composition minima. However, in the 700 °C examples covered in the previous section, the alloy composition is in the NP region and, therefore, this technique doesn't apply (to set minima) because cementite growth without manganese partitioning is thermodynamically allowed. This is briefly mentioned in the section discussing 700 °C because at 700 °C the composition predicted by the (γ + cem) operative tie-line is thermodynamically permitted. It is only incorrect in a sense that it is not a true thermodynamic limit as shown by the decreasing Gibbs free energy of the dashed blue line in Fig. 4.4a, which represents growth of cementite with bulk alloy manganese content. At 660 °C, an incorrect conclusion regarding the region ("must" partition or P/NP) in which the bulk alloy composition is located can lead to erroneous and thermodynamically impossible results. For example, Figs. 4.7a and b show the Fe-C-Mn 660 °C isotherm with bulk alloy composition marked by the yellow circle. The alloy composition lies in the (γ + cem) two-phase field and above (to the right) of the P/NP boundary which means it is thermodynamically permitted for the growing cementite to inherit bulk alloy manganese content ($U_{Mn}^{\gamma} \approx 0.118$), that is, grow without partitioning manganese. Fig. 4.7b is an enlargement of the boxed-in region in Fig. 4.7a with the calculated extrapolated $\gamma/(\gamma + cem)$ and $\gamma/(\alpha + \gamma)$ boundaries added as dashed

lines. Intersection of the carbon isoactivity line a_c^{bulk} passing through the bulk alloy with the metastable extension of (γ + cem) phase boundary predicting $U_{Mn}^{cem} \approx 0.078$ and $U_{Mn}^{\gamma} \approx 0.025$ for cementite and austenite respectively at the γ/cem interface during the earlier stages of the transformation, Fig. 4.7c (γ + cem) blue tie-line. This operative tie-line requires rejection of manganese by cementite at the interface, which is not thermodynamically allowed. Similarly, the intersection of a_c^{bulk} with the metastable extension of γ/(γ + α) metastable phase boundary predicts $U_{Mn}^{\alpha} \approx 0.014$ and $U_{Mn}^{\gamma} \approx 0.062$ for ferrite and austenite respectively at the γ/α interface during the earlier stages of the transformation, Fig. 4.7c (γ + α) blue tie-line.
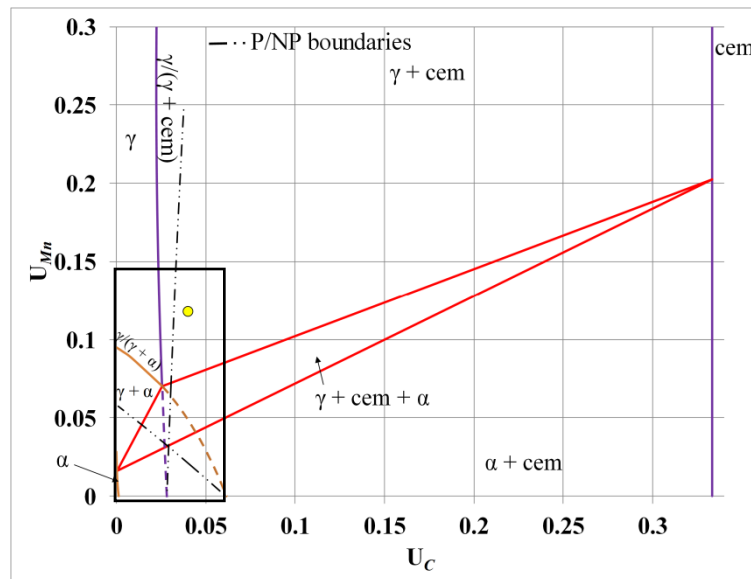
Figure 4.7a: 660 °C isotherm for Fe-C-Mn alloy. Yellow circle marks bulk alloy composition. Fig. 4.7b shows the area enclosed by the black rectangle.
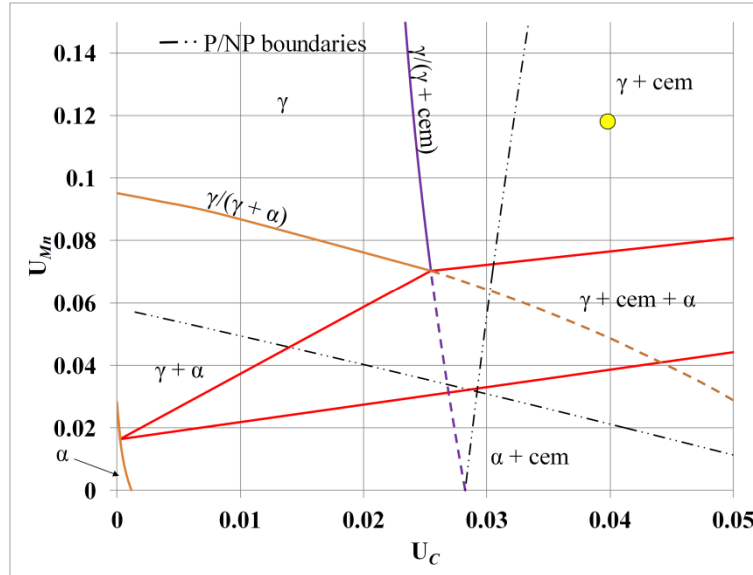
Figure 4.7b: Area enclosed by the rectangle in Fig. 4.7a Yellow circle marks bulk alloy composition which is to the right of the P/NP boundary. Dashed lines are metastable extensions of equilibrium phase boundaries.
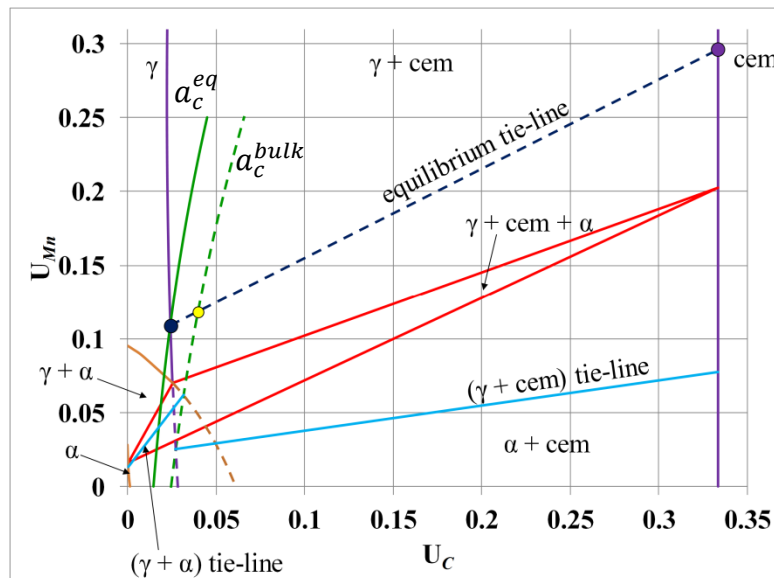
Figure 4.7c: 660 °C isotherm for Fe-C-Mn alloy. Yellow circle marks bulk alloy composition. Dashed and solid green lines represent bulk and equilibrium carbon isoactivity lines respectively. Blue and purple circles represent austenite and cementite compositions at equilibrium. LE-P model predicts $U_{Mn}^{cem} \approx 0.078$ and $U_{Mn}^{\gamma} \approx 0.025$ at the γ/cem (cementite and austenite ends of the (γ + cem) tie-line) and $U_{Mn}^{\alpha} \approx 0.014$ and $U_{Mn}^{\gamma} \approx 0.062$ at the α/γ (cementite and austenite ends of the (γ + α) tie-line) interphase interface compositions at the onset of the reaction. P/NP boundaries shown in Figs 4.7a and b are not displayed.

Table 4.3 shows computations of free energy for systems with compositions determined by

Hillert's restriction ($U_{Mn}^{cem-eq} \geq U_{Mn}^{cem} \geq U_{Mn}^{\gamma-bulk}$) and carbon isoactivity construction used by

Hutchinson and Shiflet, depicted in Fig. 4.7c. [hillert1998, hutchinson2004] The change in Gibbs free energy is calculated by subtracting computed Gibbs free energy of the system with various model-determined phase compositions from the computed Gibbs free energy of the system prior to decomposition. Results highlighted in red correspond to systems conforming to the $\Delta G < 0$ criterion. Results highlighted in green correspond to systems violating the $\Delta G < 0$ criterion. Results in the Table 4.3 show that use of carbon isoactivity lines for the construction of the (γ + cem) tie-line, at this temperature, violates the $\Delta G < 0$ criterion necessary for spontaneous reaction of a natural process at a constant temperature and pressure. Therefore, from this point forward, thermodynamic considerations exclude predictions and conclusions (ex: maximum permitted temperature for formation of metastable ferrite is ~685 °C) obtained using local (interphase interface) equilibrium model outlined by Shiflet and Hutchinson in [hutchinson2004] because of their incorrectly computed P/NP boundaries.

Table 4.3: Free energy calculations for the various models describing composition during growth. Numbers in green and red denote situations where ΔG < 0 and ΔG > 0 respectively. ΔG > 0 signifies thermodynamically impossible situations.

Cementite mole fraction $\times 10^{-3}$	U_{Mn}^{cem} $\times 10^{-2}$	Ferrite mole fraction $\times 10^{-3}$	U_{Mn}^{α} $\times 10^{-2}$	a_C	G^{sys} J/mol	ΔG J/mol
Bulk alloy, prior to decomposition						
0	0	0	0	0.2665	-40,307.4	
Assuming no ferrite formation and no manganese partitioning, Hillert [hillert1998], Kirkaldy[kirkaldy1958]						
1.0	11.8	0	0	0.2644	-40,307.9	**-0.5**
2.0	11.8	0	0	0.2244	-40,308.3	**-0.9**
3.0	11.8	0	0	0.2041	-40,308.8	**-1.4**
Carbon isoactivity lines, Hutchinson and Shiflet [Hutchinson2004]						
1.0	7.77	0	0	0.2643	-40,307.5	**-0.1**
1.0	7.77	1.0	1.35	0.2645	-40,307.1	**0.3**
1.0	7.77	2.0	1.35	0.2648	-40,306.7	**0.7**
2.0	7.77	1.0	1.35	0.2623	-40,307.2	**0.2**
50.0	7.77	10.0	1.35	0.1650	-40,291.4	**16.0**
Equilibrium predicted values						
6.40	29.8	0	0	0.1467	-40,344.8	**-37.4**

4.2.2 Experimental Summary

At 660 °C, decomposition of austenite occurs in several consecutive stages. The order of the reactions is cementite grain boundary precipitation (1 hour), formation of pearlite (12 hours), cellular growth (4 days), and dissolution of ferrite (21 days). Volume fraction of all (grain

boundary, cellular, and pearlite) cementite reaches 0.0344 (0.041 mole fraction) after 30 days, or ~63% of expected equilibrium volume fraction, 0.0543 (0.064 mole fraction). The width of the manganese-depleted austenite lamellae in cellular colonies is larger than the ferrite plate width in the pearlite colonies. This is one of the two main features (the other being cementite manganese content, U_{Mn}^{cem} which is $U_{Mn}^{cem-c} \approx 0.22$ and $U_{Mn}^{cem-p} \approx 0.14$ to 0.17) employed for classifying the two lamellar transformations, $i.e.$, pearlitic or cellular, if the dissolution of ferrite is suspected.

Manganese content in grain boundary cementite remains approximately constant for the duration of the reaction ($U_{Mn}^{cem-gb} \approx 0.13$) which is higher than $U_{Mn}^{bulk} \approx 0.118$. Pearlitic cementite has $U_{Mn}^{cem-p} \approx 0.14$ after 4 days and increases to $U_{Mn}^{cem-p} \approx 0.17$ after 30 days. Manganese content in cellular cementite is $U_{Mn}^{cem-c} \approx 0.22$ and remains constant for the duration of reaction (4-30 days). Analytical (SEM-EDS) data about manganese contents are available for only two times (4 days and 30 days) but the trends are consistent with those observed at higher temperatures as well as 650 °C. Morphological data (ex: volume fraction information, colony sizes, etc.) for times prior to 4 days and intermediate times between 4 and 30 days are reported in Table 3.9b-1. Presentation of experimental data in a separate graphical format, similar to Figs. 4.2a-d, is not done because the current temperature analysis does not make use of it.

4.2.3 Global Thermodynamics

The analysis of global thermodynamics begins by setting energy extrema and then computing energy at intermediate stages of the transformation using experimental data. Solid and dashed horizontal black lines in Fig. 4.8a depict Gibbs free energy of the system prior to decomposition and at equilibrium, respectively. The energy difference between these lines represents the total energy available, $\Delta G_{total}^{\gamma \rightarrow \gamma+cem}$, for any and all phase transformations at 660 °C and it is ~37.4 J/mol. Energy calculations at the intermediate transformation stages must not exceed either of these horizontal lines.

The energy range representing intermediate transformation stages can be computed by considering cementite growth with full equilibrium manganese partitioning at one extreme and no partitioning as the other extreme. The calculated behavior must lie between the horizontal solid and dashed black lines in Fig. 4.8a. Consider a hypothetical case where cementite grows as Widmanstatten plates into austenite. Plates with equilibrium manganese content when combined with our experimental cementite mole fraction measurements result in the largest change in

Gibbs free energy, plotted as the solid purple line in Fig. 4.8a. However, because the bulk alloy composition lies in the P/NP region of the 660 °C isotherm, cementite can also grow without partitioning manganese. The dashed blue line in Fig. 4.8a shows Gibbs free energy change associated with growing cementite ($U_{Mn}^{cem} = 0.118$) as a *function of the experimentally observed cementite mole fraction* for specified times. Although cementite can form without partitioning of manganese, this growth can't continue beyond a cementite mole fraction of 0.016 (corresponding to 21 days, black arrow), where any further growth would result in an increase of Gibbs free energy, as evidenced by the slightly positive slope of the dashed blue line in Fig. 4.8a for times beyond 21 days. The area between the dashed blue and purple lines represents the theoretically permissible Gibbs free energy range based on the $U_{Mn}^{cem-eq} \geq U_{Mn}^{cem} \geq U_{Mn}^{\gamma-bulk}$ composition criteria if cementite Widmanstatten plates grow into the austenite matrix. However, progress of any reaction requires only a sufficient reduction in Gibbs free energy, *given the observed cementite mole fraction* only the purple line sets the lowest attainable Gibbs free energy for the experimental system during the intermediate stages of the transformation. In other words, as long as the change in Gibbs free energy is negative it is possible for the austenite to continue to transform into new phases, such as the formation of ferrite provided the resulting Gibbs free energy level remains between the horizontal solid black and purple lines.

Given the energy extrema for the transformation as a function of the observed cementite mole fraction between 0 and 30 days, evaluation of energy consequences associated with actual microstructures is now possible. Using the data from Chapter 3, the full sequence of phase transformations are plotted in Fig. 4.8a. Individual microstructures (cellular and pearlite) will then be addressed separately following the current analysis to examine their contributions in reducing the free energy. At 660°C, growth of ferrite is observed after 12 hours and cellular cementite occurs after 4 days, again excessively manganese-depleted austenite. Ferrite dissolution, which results in austenite with manganese contents lower than equilibrium ($U_{Mn}^{\gamma-eq} \approx$ $0.11 > U_{Mn}^{\gamma r} \approx 0.08$), is observed after 21 days. Computation of Gibbs free energy matching the experimentally observed system is done for the same set of microstructures except that cementite lamellae for one set has a manganese composition $U_{Mn}^{cem-p} = 0.14$ (green dash-dot line in Fig. 4.8a) and the other set has cementite lamellae with $U_{Mn}^{cem-p} = 0.17$ (green dash-dot-dot line in Fig. 4.8a). Both sets include cellular cementite with $U_{Mn}^{cem-c} = 0.22$, manganese-depleted

austenite with $U_{Mn}^{\gamma^d} = 0.09$, pearlitic ferrite with $U_{Mn}^{\alpha} = 0.02$, and retrenched austenite $U_{Mn}^{\gamma^r} = 0.08$. Vertical bars in Fig. 4.8a indicate the start time of various reaction's microstructures used in calculation of the Gibbs free energy (read Fig. 4.8a caption). Table 3.9b-1 provides volume fraction information for the individual phases. Because the manganese content in pearlite cementite is over a small range, the Gibbs free energy of the system has a value located between the two (green dash-dot and dash-dot-dot) green lines in Fig. 4.8a, where the difference between the lines represents different manganese contents in pearlitic cementite.[13] This is possible because ferrite provides a more rapid diffusion path than austenite ($\frac{D_{Mn}^{\alpha}}{D_{Mn}^{\gamma}} \approx 377$). [friedberg1969]

Cementite growth and additional manganese partitioning into cementite lower the Gibbs free energy of the system from the green dash-dot line down towards the green dash-dot-dot line in Fig. 4.8a. As the Gibbs free energy of the total system is increasingly negative over time, although with a considerable way to go to reach equilibrium, well beyond the after 30 days of growth at this temperature, all phase transformations documented in the system are thermodynamically permissible. Specifically, growth of cementite for the duration of the reaction suggests that the negative change in Gibbs free energy associated with formation of cementite and manganese partitioning offsets the positive free energy contributions due to formation of excessively manganese-depleted austenite (retrenched and depleted) and ferrite, both are non-equilibrium at this temperature, *i.e.*, $\Delta G^{cem} + \Delta G^{\gamma^d} + \Delta G^{\gamma^r} + \Delta G^{\alpha} < 0$.

---

[13] Cementite in smaller pearlite colonies exhibit U_{Mn}^{cem-p} lower than cementite in larger pearlite colonies.
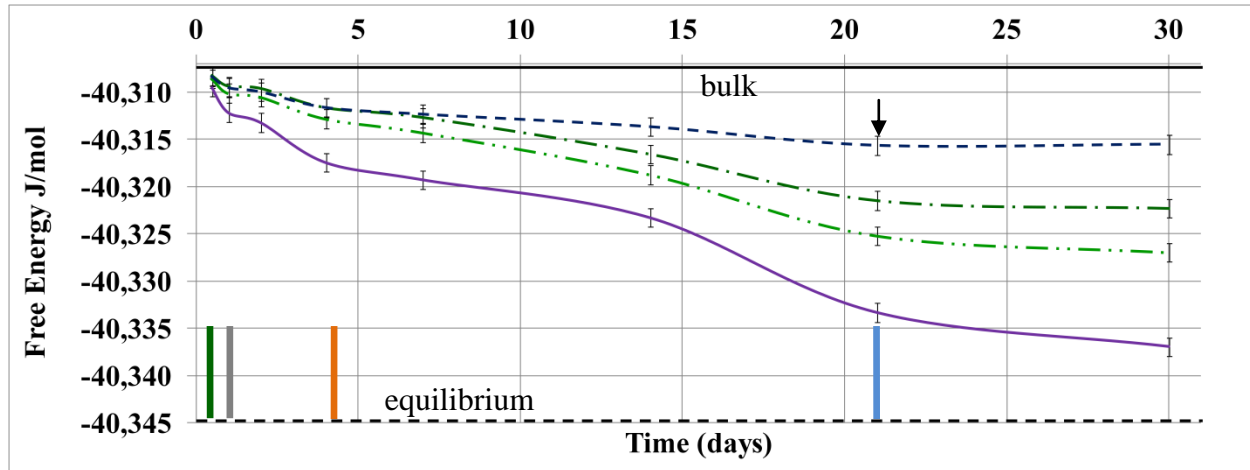
Figure 4.8a: Computed free energy of the system during isothermal transformation at 660 °C as a function of time. **Black solid** line – prior to decomposition. **Black dashed** line – at equilibrium. **Green dash-dot** line – the system comprised of grain boundary cementite (U_{Mn}^{cem-gb} = 0.13), pearlite (U_{Mn}^{cem-p} = 0.14, U_{Mn}^{α} = 0.02), retrenched austenite ($U_{Mn}^{\gamma^r}$ = 0.08), cellular cementite (U_{Mn}^{cem-c} = 0.22), manganese-depleted austenite ($U_{Mn}^{\gamma^d}$= 0.09), and remaining austenite. **Green dash-dot-dot** solid line – same as green dash-dot line but with U_{Mn}^{cem-p} = 0.17 Volume fraction information is listed in the previous chapter, Table 3.9b-1. **Blue** dashed line – the system comprised of cementite with U_{Mn}^{cem} = 0.118 (bulk alloy composition) and austenite. **Purple** solid line - the system comprised of cementite with U_{Mn}^{cem} = 0.299 (equilibrium predicted value) and austenite. The bars represent the initial observation of the experimentally observed reaction. All bars extend to 30 days. Green – grain boundary cementite precipitation. Gray – ferrite growth. Blue – ferrite dissolution. Orange – cellular growth.
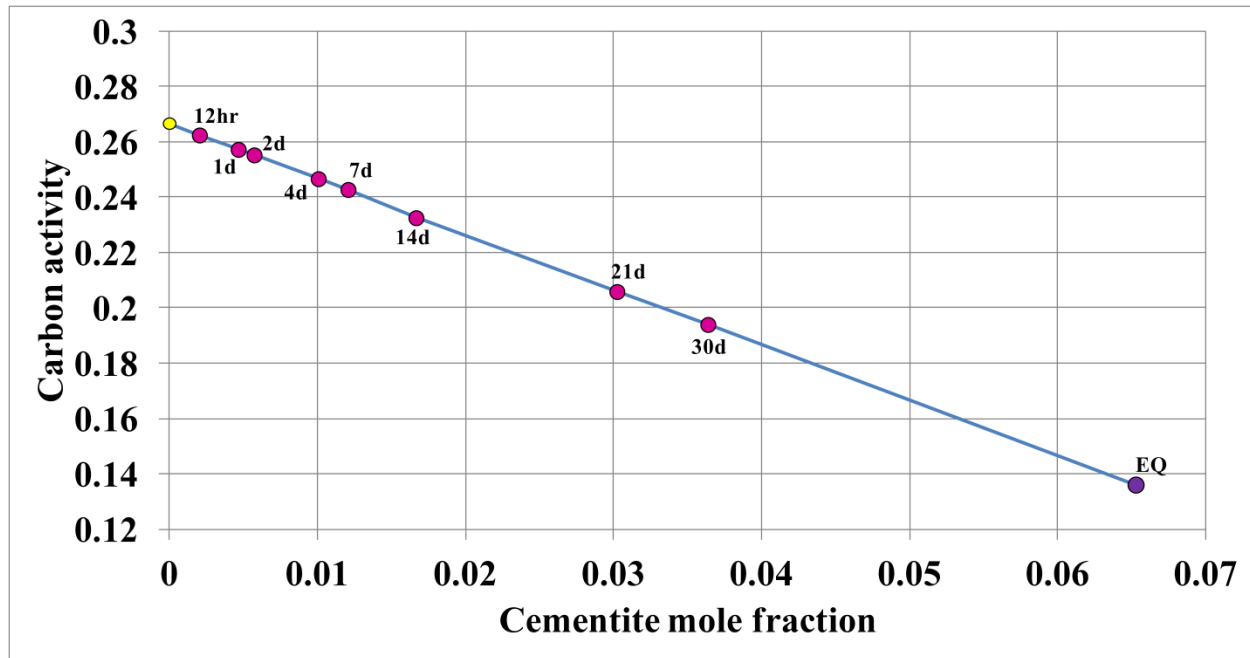
Figure 4.8b: Carbon activity in the austenite as a function of experimentally observed cementite mole fraction for the alloy heat treated at 660 °C. Yellow circle represents the system prior to decomposition (dashed green line in Fig. 4.9b). Purple circle represents the system at equilibrium (solid green line in Fig. 4.9b). Magenta circles represent the system at the experimentally determined mole fraction at the intermediate time steps (dash-dot lines in Fig. 4.9b).

Fig. 4.8b plots carbon activity in austenite as a function of the experimentally observed total cementite mole fraction specific times listed next to the data points. The method for computing of these values is the same as at 700 °C. Partitioning of carbon that is necessary for cementite growth reduces carbon activity in the austenite matrix. Activity of carbon shows a decreasing trend without reaching the equilibrium expect value after 30 days of heat treatment, in agreement with the energy analysis presented in Fig. 4.8a.

4.2.4 Neighborhood Thermodynamics

While global thermodynamics confirm permissibility of the experimentally observed results, the reasons for formation and dissolution of ferrite remain unclear. These conclusions are unsurprising because global thermodynamics, Fig. 4.8a, represents a cumulative state of the system at any stage of the transformation, obfuscating energy changes associated with concurrent austenite decomposition reactions. However, the system's cumulative state does provide critical information about carbon activity used in the scheme of neighborhood thermodynamics. The reasons for ferrite growth and dissolution emerge by mapping the experimental data, describing

composition of phases resulting from various reactions (*e.g.,* pearlite or cellular) onto the Fe-Mn-C 660 °C isotherm, as shown in Figs. 4.9a-c. The following discussion (sections 4.2.4.1, 4.2.4.2, and 4.2.4.3) uses the isotherm construction to explain thermodynamic reasons for ferrite growth (or lack thereof) and dissolution and it evaluates thermodynamic feasibility for individual reactions occurring independently. The latter helps explain experimentally observed pearlite growth.

Cementite is a line compound with $U_C \approx 0.333$ ($X_C = 0.25$). This value remains fixed for the duration of the reaction. Fig. 4.9a shows the cementite end of the (γ + cem) tie-line on the Fe-C-Mn 660 °C isotherm with manganese content of cellular and pearlitic cementite plotted on the line corresponding to $U_C \approx 0.333$. Manganese content in pearlitic increases over time but it remains nearly constant in cellular cementite.[14] However, as discussed with Table 4.1, if information about cementite mole fraction is available, precise knowledge of manganese distributions in any phase is not necessary to compute reasonably accurate carbon activity values in the remaining austenite. This is advantageous because manganese content in pearlite colonies varies, making the pursuit of precise distributions an experimentally impractical task. Nevertheless, the framework of neighborhood thermodynamics requires knowledge of manganese content in various phases to explain ferrite growth and dissolution. Fig. 4.9b shows the austenite end of the (γ + cem) tie-line on the Fe-C-Mn 660 °C isotherm with carbon isoactivity lines corresponding to the state of the system prior to decomposition (dashed green line passing through the bulk alloy, yellow circle), at equilibrium (solid green line), and at 4 and 30 days (dash-dot green lines).

---

[14] Note that manganese content of pearlitic cementite after 30 days, when ferrite dissolution occurs, is lower than manganese content of cellular cementite. While this is not important for the current discussion, this information provides a clue into the dominant stratagem of the transformation path, *i.e.*, the importance of cementite volume *vs.* cementite manganese content.
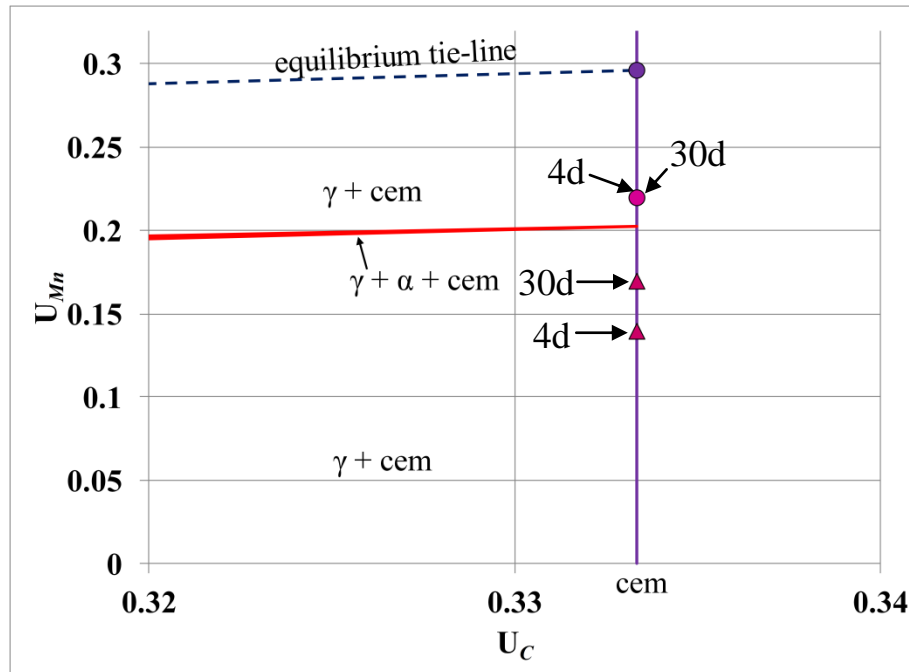
Figure 4.9a: Manganese content in cementite plotted on the Fe-Mn-C 660 °C isotherm. Magenta triangles and circles represent pearlitic and cellular cementite, respectively.
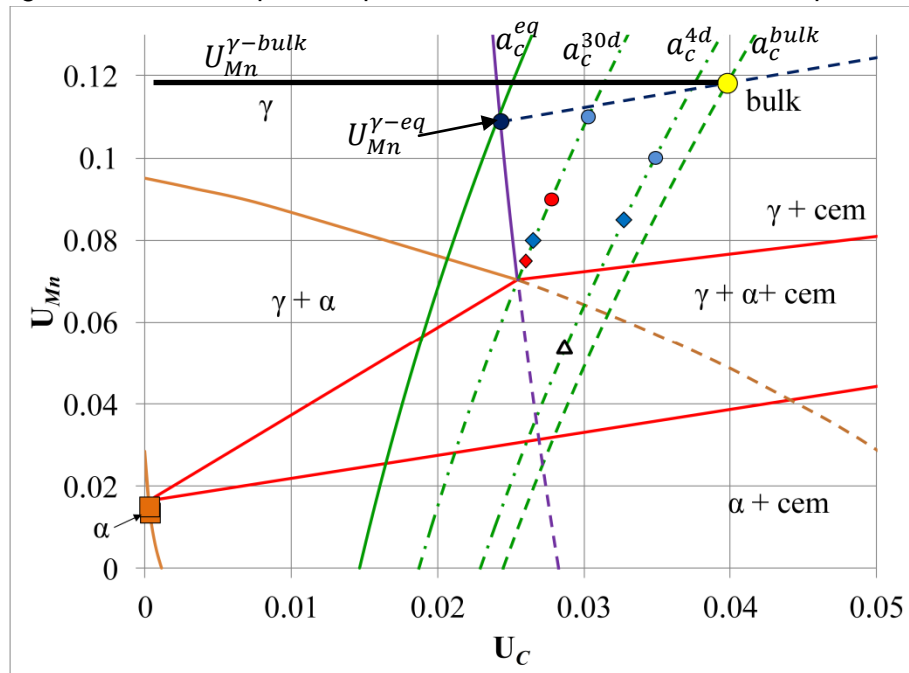
Figure 4.9b: Manganese content of the manganese-depleted austenite regions mapped on the carbon isoactivity lines plotted on the Fe-Mn-C 660 °C isotherm. Yellow circle represents bulk alloy content. Blue circles indicate γ^{d-high} and rhombuses γ^{d-low}. Red circle indicates γ^{r-high} and rhombus γ^{r-low}. Orange squares represent ferrite. Open black triangle is discussed with Fig. 4.11. P/NP boundaries shown in Figs. 4.7a and b are not shown.
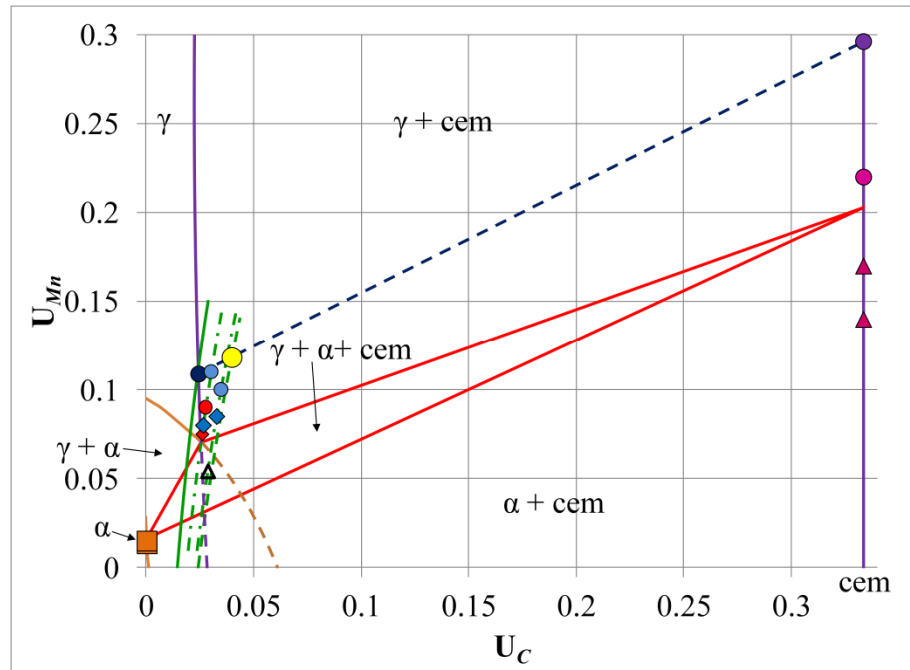
Figure 4.9c: Compilation of Figs. 4.9a and b with all of the data points plotted on the Fe-Mn-C 660 °C isotherm. P/NP boundaries shown in Figs 4.7a and b are not shown.
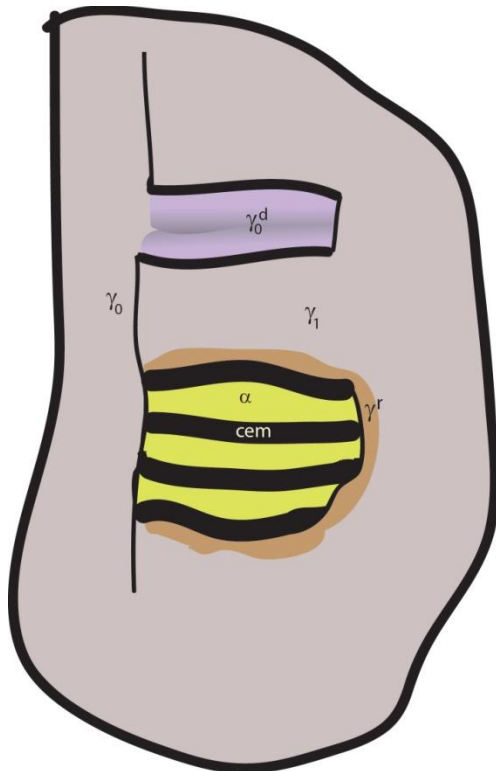
Figure 4.9d: A sketch of a pearlite and cellular colonies showing different forms of austenite. Chemical potential of carbon in all austenite forms is assumed to be equal.

Fig. 4.8b shows the numerical carbon activity values for each of these lines. Since carbon diffuses orders of magnitude faster than manganese, it is reasonable to assume that at any given time $\mu_C^\gamma = \mu_C^{\gamma^{d-high}} = \mu_C^{\gamma^{d-low}} = \mu_C^{\gamma^r}$ (Fig. 4.9d identifies austenite variant nomenclature) and therefore $a_C^\gamma = a_C^{high\,\gamma^d} = a_C^{low\,\gamma^d} = a_C^{\gamma^r}$ ($\mu_C^\gamma = \mu_C^{o\gamma} + RT\ln a_C^\gamma$) even if this assumption is extended from interphase interfaces to local neighborhoods ($\frac{D_C^\gamma}{D_{Mn}^{gb}} \approx 3.9 \times 10^5$ and $\frac{D_C^\gamma}{D_{Mn}^\gamma} \approx$ 1.4×10^7). Since carbon activity (which can be related to carbon chemical potential) in all austenitic forms at any given time is the same, measured manganese content of an austenite neighborhood must be synchronized with the corresponding isoactivity line for the time in question. Fig. 4.9b shows various austenite forms mapped on the corresponding carbon isoactivity lines, where the bulk alloy is shown with a yellow circle, γ^d- high with blue circles, γ^{d-low} with blue rhombuses, γ^{r-high} with a red circle, and γ^{r-low} with a red rhombus. Similar to the case presented for 700 °C, the value representing γ^{d-low} corresponds to the manganese-depleted austenite neighborhood immediately adjacent to cementite and it is lower in both manganese and carbon content when compared to γ^{d-high}. Fig. 4.9c shows both ends of the tie-line and data shown in Figs. 4.9a and b.

4.2.4.1 Neighborhood Thermodynamics - Cellular Reaction

Systematics of the cellular reaction at this temperature are similar to the one described at 700 °C, Fig. 4.3. Evaluation of this reaction is done first because it is similar to 700 °C and permits a qualitative evaluation of D_{Mn}^{gb}, which is needed to describe the pearlite reaction. Cellular growth occurs after 4 days (orange bar in Fig. 4.8a) of heat treatment at 660 °C, following the formation of pearlite (12 hours) and prior to dissolution of ferrite (21 days). Cellular colonies consist of cementite with average $U_{Mn}^{cem-c} \approx 0.22$ (overlapping magenta circles in Fig. 4.9a) and manganese-depleted austenite with $U_{Mn}^{\gamma^d}$ ranging from 0.08 to 0.11 (blue circles and rhombuses in Fig. 4.9b).
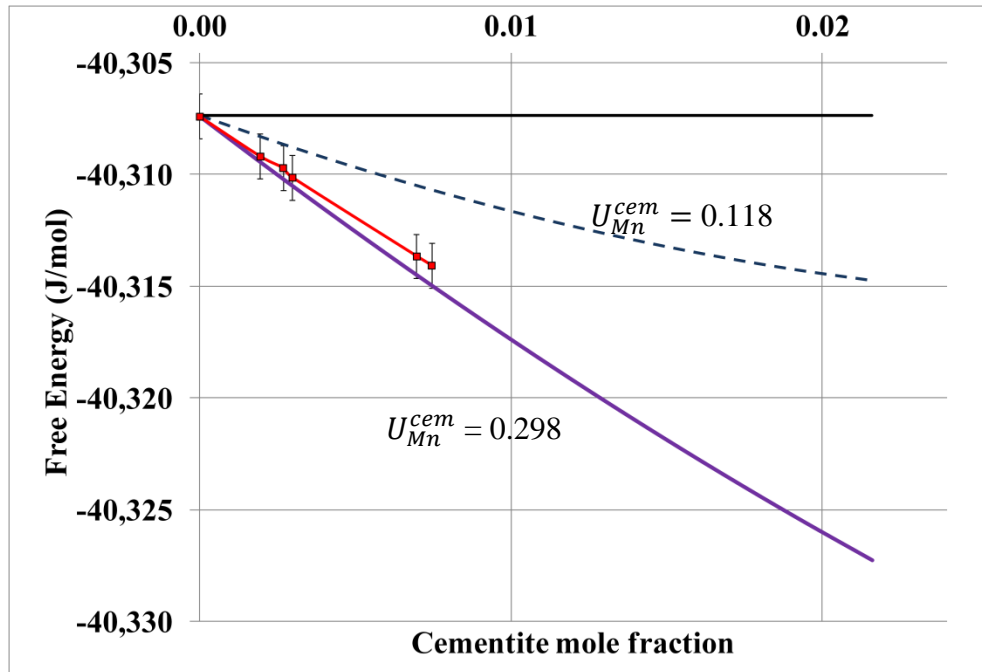
Figure 4.10: Free energy of the system as a function of mole fraction of cementite. As a stand-alone reaction, the free energy begins at the energy base line for the current alloy. **Black** solid line – the system prior to decomposition. **Blue** dashed line – the system comprised of cementite with U_{Mn}^{cem} = 0.118 and matrix austenite. **Purple** solid line - the system comprised of cementite with U_{Mn}^{cem} = 0.298 (equilibrium predicted value) and matrix austenite. **Red** solid line – the experimentally observed cellular system with U_{Mn}^{cem-c} = 0.22, $U_{Mn}^{\gamma^d}$ = 0.09, and matrix austenite.

Energy analysis of the cellular reaction considers two extrema based on the partitioning behavior of manganese. At a minimum, growing cementite must inherit the $U_{Mn}^{cem} \approx 0.118$, represented by the dashed blue line in Fig. 4.10. The purple solid line shows Gibbs free energy of the same two phase microstructure (cementite and austenite) with the cementite possessing the calculated equilibrium manganese content $U_{Mn}^{cem} = 0.298$. In both cases, the transformation consists of cementite Widmanstatten plates growing into the austenite matrix. Between these lines (dashed blue and solid purple) lies the theoretically permissible free energy range based on the $U_{Mn}^{cem-eq} \geq U_{Mn}^{cem} \geq U_{Mn}^{\gamma-bulk}$ criteria. The red line is the calculated Gibbs free energy of the system consisting of experimentally observed mole fraction of cellular cementite with measured manganese content $U_{Mn}^{cem-c} = 0.22$ and the colony's associated mole fraction of manganese-depleted austenite, *viz.*, $U_{Mn}^{\gamma^d} = 0.09$. The Gibbs free energy contribution of the excessively manganese-depleted austenite is positive, similar to the case discussed for 700 °C in Fig. 4.4a, but the net Gibbs free energy trend for the cellular reaction is negative and is within the

allowable energy range (solid black and purple lines in Fig. 4.10). Therefore, cellular decomposition with observed manganese contents is thermodynamically permissible, even as an independent reaction. Growth of cementite with $U_{Mn}^{cem-c} = 0.22$ (even with manganese-depleted austenite) reduces Gibbs free energy by up to 90% of the permissible reduction (purple line in Fig. 4.10). However, the observed cellular cementite represents no more than ~20% of the total cementite amount at any stage of the total transformation.

Manganese-depleted austenite with lower manganese contents is located closer to the moving grain boundary and adjacent to the cementite lamella. Manganese-depleted austenite with higher manganese content is located midway between two cementite lamellae. Experimentally observed $U_{Mn}^{\gamma^d}$ maps manganese-depleted austenite neighborhoods to the (γ + cem) two-phase field where ferrite formation is prohibited (Fig. 4.9b).

Using the Petermann-Hornbogen model outlined in the previous section and information depicted in Fig. 4.10 yields $D_{Mn}^{gb} \approx 3.06 \times 10^{-19} \frac{m^2}{s}$. Bulk manganese diffusion for this temperature is $D_{Mn}^{\gamma} = 5.20 \times 10^{-5} \times \exp\left(\frac{-282,000}{RT}\right) \approx 8.4 \times 10^{-21} \frac{m^2}{s}$.

4.2.4.2 Neighborhood Thermodynamics - Pearlite Reaction

Pearlite (ferrite) growth occurs after 12 hours (gray bar in Fig. 4.8a) of heat treatment and follows grain boundary cementite precipitation. Pearlitic cementite has $U_{Mn}^{cem-p} \approx 0.14$ after 4 days and increases to $U_{Mn}^{cem-p} \approx 0.17$ after 30 days (magenta triangles in Fig. 4.9a). Composition of ferrite is $U_{Mn}^{\alpha} \approx 0.02$ (orange squares in Fig. 4.9b). Manganese content in the grain boundary cementite remains approximately constant for the duration of the reaction ($U_{Mn}^{cem-gb} \approx 0.13$), which is higher than $U_{Mn}^{bulk} \approx 0.118$. Once again, the global thermodynamics approach, shown in Fig. 4.8a, offers limited insight into formation of ferrite but it provides information needed to compute carbon activity at any stage of the cumulative reaction. Evaluation of neighborhoods, while using carbon activity information, decouples the energy analysis of pearlite reaction from global thermodynamics, thus explaining ferrite growth and dissolution.

Grain boundary cementite precipitation is the prelude to ferrite growth. A higher driving force for cementite formation at 660 °C, when compared to 700 °C, results in a higher cementite nucleation rate leading to more closely spaced cementite allotriomorphs, Fig. 4.11a. For grain boundary cementite to attain the experimentally observed $U_{Mn}^{cem} \approx 0.13$ the austenite in the

immediate vicinity of cementite must supply the manganese, with the primary mechanism for manganese transport involving grain boundary diffusion (this is the reason for analyzing the cellular reaction first). Since $\frac{D_{Mn}^{gb}}{D_{Mn}^{\gamma}} \approx 58.8$, cementite depletes neighborhoods adjacent to it faster than manganese from the austenite matrix can replenish these areas. If two cementite grain boundary precipitates are spaced close to each other, **c1** and **c2** precipitates shown in Fig. 4.11a, the (former) austenite area between them, **a2** (now labeled α), has a larger depletion of manganese than the austenite area, **a1**, separating two cementite allotriomorphs spaced further apart, **c0** and **c1** in Fig. 4.11a. Pearlite reaction occurs when the conditions in the manganese-depleted austenite around the cementite allotriomorphs is sufficiently reduced so the region enters the (γ + α + cem) three-phase field.
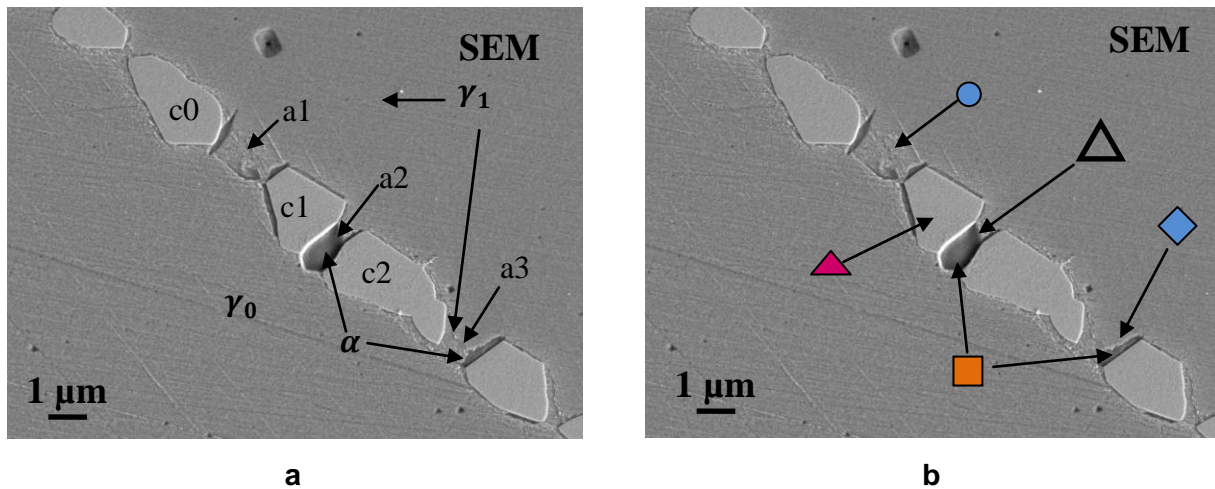
Figure 4.11: (a) SEM image showing cementite allotriomorphs and early development of a pearlite colony in a sample heat treated for 4 days at 660 °C. Discussion of **c0**, **c1**, and **c2** grain boundary precipitates and areas labeled **a1**, **a2**, and **a3** is in text. **(b)** Same as (a) with shapes correlating to shapes used in Figs 4.9a-c.

To demonstrate this point, consider the impact of the solute drain on the region **a2**, evaluated using a k-clustering algorithm previously discussed in Chapter 2 section 2.4.[15] Size of **c1** is 2496 pixels, size of **c2** is 4420 pixels, and the region between the two (**a2**), what is now ferrite, is 793 pixels. Pixel values correspond to area but represent volume. Since manganese from the

---

[15] The calculation does not provide a quantitative value because it ignores all stereological effects and assumes manganese in the grain boundary cementite comes evenly from manganese-depleted regions (rough regions adjacent to the cementite) on each side of the precipitate, Fig. 4.11a regions marked **a1**, **a2**, and **a3**.

manganese-depleted region is split evenly between the two cementite precipitates, **a2** region accounts for half of the manganese increase in both grain boundary cementite allotriomorphs when normalized with respect to the area, or ½ (**c1** + **c2**) = 3458 pixels. The cementite density at this temperature is 1.18 moles/(unit volume fraction) while ferrite density is 0.98 moles/(unit volume fraction). Using this information to set up a mass balance equation yields (volume of ferrite) × (molar density of ferrite) × ($U_{Mn}^{\gamma-bulk} - U_{Mn}^{\gamma^{d*}}$) = (volume of cementite) × (molar density of cementite) × ($U_{Mn}^{cem-gb} - U_{Mn}^{\gamma-bulk}$). The '*' here indicates former manganese-depleted region that transformed into ferrite. Substituting in the numerical values 793×0.98× ($0.118 - U_{Mn}^{\gamma^{d*}}$) = 3459×1.18× ($0.13 - 0.118$) results in $U_{Mn}^{\gamma^{d*}} = 0.055$[16]. This means that for grain boundary cementite to attain the experimentally observed $U_{Mn}^{cem-gb} \approx 0.13$ region **a2** must deplete to approximately $U_{Mn}^{\gamma^{d*}} \approx 0.054$. This neighborhood manganese value, if mapped on the corresponding (4 day) carbon isoactivity line, places manganese-depleted region into the (γ + α + cem) three-phase field where formation of ferrite is possible (unfilled black triangle in Fig. 4.9b).

As the total cementite mole fraction increases, carbon activity in the remaining austenite decreases, which corresponds to the carbon isoactivity lines shifting further left (Fig. 4.9b). An increase in the difference between the $U_{Mn}^{\gamma-bulk}$ line (solid heavy black line intersecting the yellow circle) and the upper Ae1 in Fig. 4.9b suggests that the amount of manganese depletion needed to produce conditions favorable to ferrite formation increases. This means that for new ferrite to form, cementite allotriomorphs must nucleate ever closer to minimize the area (such as **a2** in Fig. 4.11a) between them so that the necessary depletion can create conditions favorable to ferrite formation. It is reasonable to conclude that this outcome impedes ferrite formation.

To further demonstrate the effect of the initial cementite allotriomorph spacing on the manganese amount in the manganese-depleted regions adjacent to the cementite consider a mixed cellular-pearlite colony shown in Fig. 4.12a. The measured manganese content in the manganese-depleted austenite region (marked by the blue rhombus) in Fig. 4.12a is $U_{Mn}^{\gamma^{d}} \approx$

---

[16] The units for dimensional analysis are: $volume \times \frac{mole}{volume} \times \frac{Mn\ at.\%}{mole}$.

0.08.[17] Mapping this value on the carbon isoactivity line (blue rhombus on the 30 day carbon isoactivity line in Fig. 4.9b) places the alloy content in the manganese‑depleted region in to the (γ + cem) two-phase field where formation of ferrite is not possible. This implies that the extra width of the manganese-depleted austenite lamella has enough manganese so that the depletion associated with cementite growth doesn't place the manganese-depleted austenite region into the (γ + α + cem) three-phase field where thermodynamic conditions favor ferrite formation.
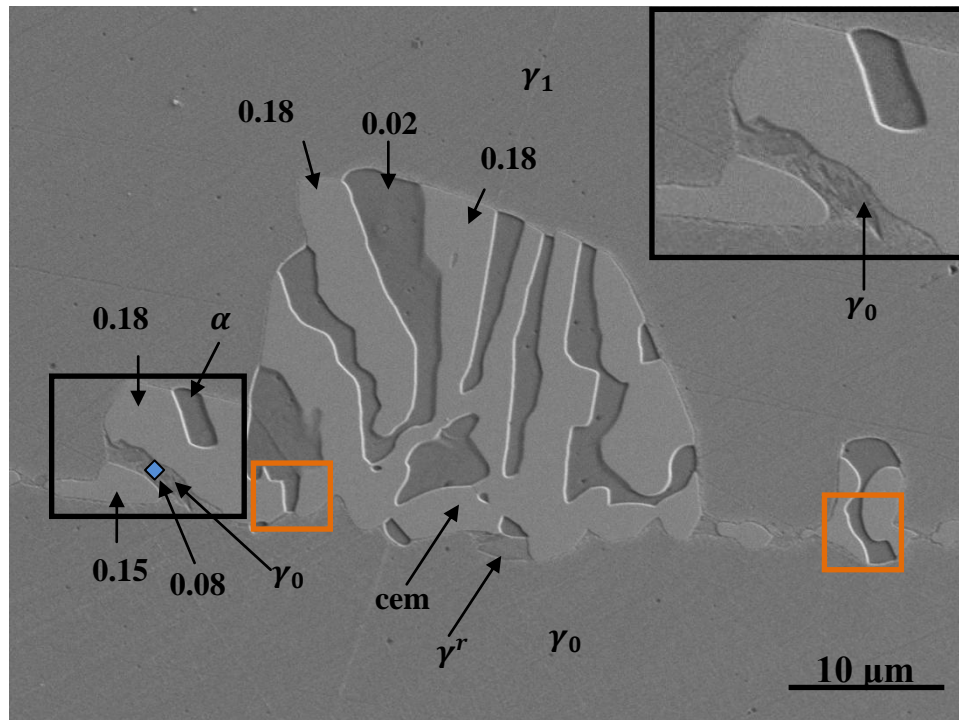
Figure 4.12a: A mixed cellular-pearlite (mostly pearlite) colony. Orange rectangles highlight areas demonstrating smaller ferrite width when compared to the width of the manganese-depleted austenite (black rectangle which is enlarged in the insert) in the early stages of colony growth. Sample heat treated at 660 °C for 30 days.

---

[17] Difference in manganese content in cementite on either side of the manganese‑depleted austenite precludes the possibility that the region is retrenched austenite, *i.e.*, ferrite region that later transformed to austenite. Additionally, relative orientation relationship of the manganese‑depleted region in question matches up with the grain opposite of the direction of the growth of the pearlite colony, a feature that correlates with initial depletion of manganese by grain boundary cementite or cellular decomposition and not the dissolution of ferrite.
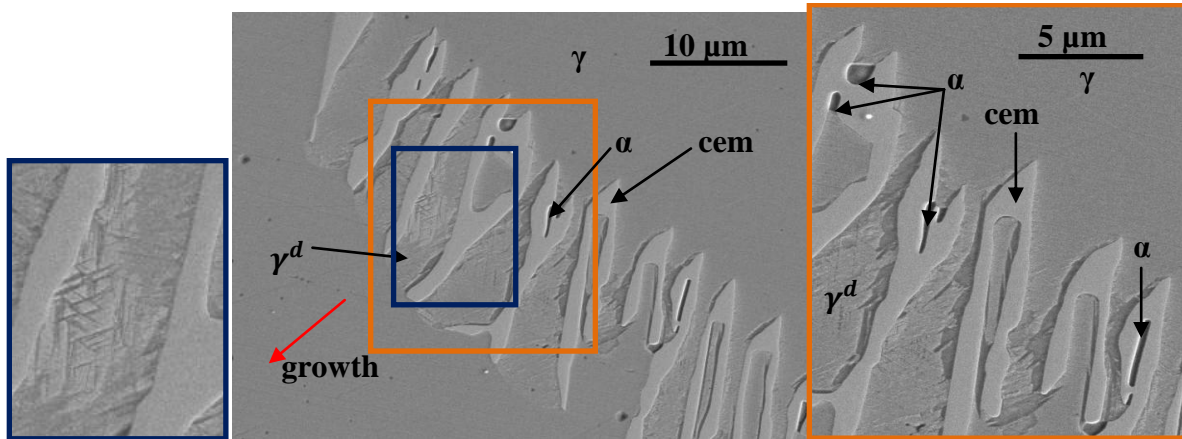
Figure 4.12b: A mixed cellular-pearlite (mostly cellular) colony. Orange rectangle highlights an area demonstrating smaller ferrite width when compared to the width of the manganese-depleted austenite in the early stages of colony growth. Sample heat treated at 660 °C for 30 days.

Fig. 4.12b presents yet another example of a mixed cellular-pearlite (mostly cellular) colony with allotriomorph spacing determining the subsequent austenite decomposition reaction. Here, the spacing between the cementite plates causes two different austenite decomposition reactions to run simultaneously in the same colony. Once again, in the early stages of the reaction ferrite width (which is indicative of the width of the manganese-depleted austenite region prior to transformation into ferrite) is smaller than manganese-depleted austenite component of the cellular colony. Note the mottling appearance of manganese-depleted austenite components of cellular colonies.

The next portion of the analysis evaluates the Gibbs free energy associated with ferrite growth and its relation with formation of equilibrium cementite. Global thermodynamics define the Gibbs free energy limits for the reaction and are set with the red and black lines in Fig. 4.13. The red line in Fig. 4.13 shows computed Gibbs free energy for the system as a function of cementite mole fraction with its equilibrium manganese content. The horizontal black line represents free energy of the system prior to austenite decomposition. The lowest point on the red line, marked by the circle, corresponds to a mole fraction of 0.064, which is the equilibrium mole fraction of cementite for the bulk alloy at this temperature. Additional growth of cementite increases Gibbs free energy of the system and, therefore, thermodynamically prohibited. The

energy associated with a phase transformation involving ferrite must fall in the range specified by the black and red lines in Fig. 4.13 with cementite mole fraction not exceeding 0.064.
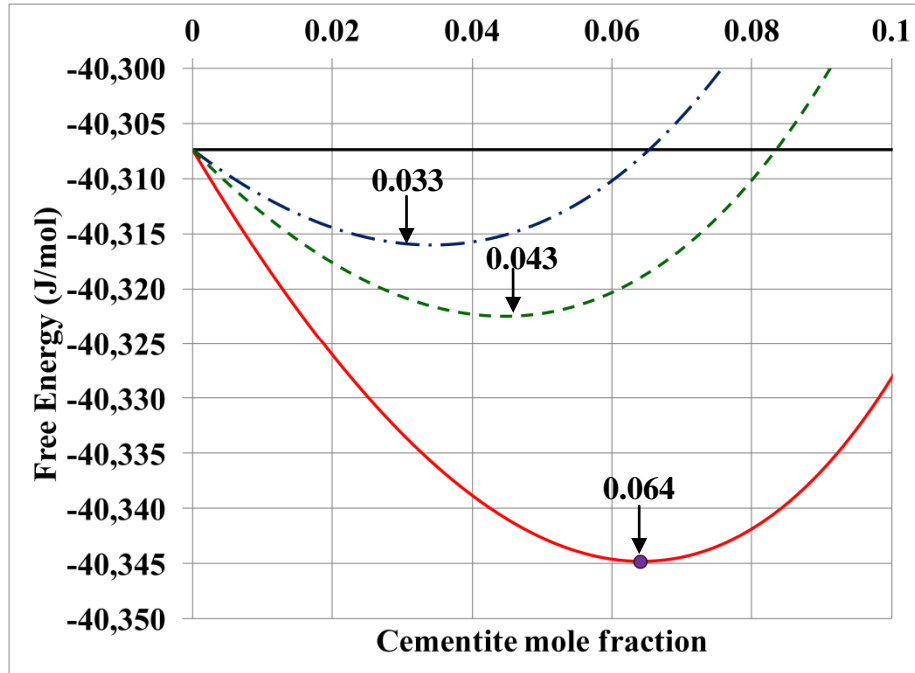
Figure 4.13: Computed free energy of the system at 660 °C as a function of cementite mole fraction. As a stand-alone reaction, the free energy begins at the energy base line for the current alloy. **Red** line corresponds to formation of cementite with equilibrium manganese content, U_{Mn}^{cem} = 0.298. The circle represents the minimum free energy and corresponds to equilibrium cementite mole fraction. **Horizontal black** line represents free energy of the system prior to decomposition. **The dash-dot blue** line represents the system where U_{Mn}^{cem} = 0.14, U_{Mn}^{α} = 0.02, and cementite to ferrite mole ratio (CFR) =2.5. **The dashed** green line represents the system where U_{Mn}^{cem} = 0.17, U_{Mn}^{α} = 0.02, and cementite to ferrite mole ratio (CFR) =2.

Modeling of pearlite requires accounting for two factors: manganese partitioning into cementite and relative amounts of cementite and ferrite mole fractions. After 4 days of heat treatment, the ratio of cementite to ferrite mole fraction (CFR) in a pearlite colony ~2.5 and $U_{Mn}^{cem-p} \approx 0.14$. The dash-dot blue line in Fig. 4.13 shows the system's Gibbs free energy with these characteristics (U_{Mn}^{α} = 0.02). The minimum occurs at cementite mole fraction of ~0.033.[18] This means that when the system reaches a cementite mole fraction of ~0.033, any further growth for the colony with these characteristics is no longer thermodynamically permissible. However, this calculation shows that growth of pearlite with experimentally observed

---

[18] Measured cementite mole fraction (grain boundary + pearlitic + and cellular) after 4 days is ~0.005.

characteristics is thermodynamically allowed, up to at least ~0.033. Similarly, CFR = 2 and $U_{Mn}^{cem-p} \approx 0.17$ describe the largest pearlite colony without ferrite dissolution after 30 days. The dashed green line in Fig. 4.13 shows the Gibbs free energy for a system with these characteristics ($U_{Mn}^{\alpha} = 0.02$). The minimum occurs at a cementite mole fraction of ~0.043, indicating cementite mole fraction where ferrite growth ceases. Measured cementite mole fraction (grain boundary, pearlitic, and cellular) after 30 days is ~0.041, also short of the ~0.064 needed to discontinue ferrite growth. However, the most significant conclusion of this analysis is that ferrite growth with experimentally observed characteristics describing pearlite colonies is thermodynamically permissible, up to at least cementite mole fraction of ~0.033, demonstrated by the decreasing Gibbs free energy shown by the dash-dot blue and green lines. This analysis also shows that pearlite growth, after nucleation of ferrite, is thermodynamically viable as a stand-alone reaction, explaining continued experimentally observed pearlite growth.

4.2.4.3 Neighborhood Thermodynamics - Ferrite Dissolution

Growth of pearlite (ferrite component) is concurrent with other cementite forming reactions in the system, *i.e.*, grain boundary precipitation and cellular reactions. As the total cementite mole fraction increases, carbon activity in the remaining austenite decreases, which corresponds to the carbon isoactivity lines shifting further left as shown in Fig. 4.14 where the experimental carbon activity data is plotted on the Fe-C-Mn isotherm at 660 °C. The difference between this construction and the one shown in Fig. 4.9b is how carbon isoactivity lines are drawn. In Fig. 4.9b carbon isoactivity lines are depicted as nearly straight lines. In Fig. 4.14 carbon isoactivity lines have "knees" with the lower end of the knee (orange dash-dot portion of the isoactivity line in Fig. 4.14) connecting the α and γ/(γ + α) metastable phase extension. The orange portions of the isoactivity lines represent the (γ + α) tie-lines and, therefore, characterize the maximum permitted carbon activity in ferrite during pearlite growth at each of the experimentally observed system states (which are described by the calculation of the carbon activity). Based on this construction, the lowest carbon activity attainable by ferrite corresponds to the equilibrium tie-line represented by the red (γ + α) edge of the (γ + α + cem) three-phase triangle. Since carbon content in ferrite is unknown, the actual carbon activity in ferrite is in the range between a specific orange line representing the current transformation stage and the (γ + α) edge of the (γ + α + cem) three-phase triangle.

Figure 4.14: Carbon activity at different transformation times plotted on the Fe-Mn-C 660 °C isotherm. Yellow circle represents bulk alloy content.

Consider a system comprised of the austenite matrix and cementite so that the carbon activity in the austenite matrix is ~0.25, Fig. 4.14 dash-dot carbon isoactivity line marked 0.25. This line describes the carbon activity in the austenite matrix after 4 days of transformation time. A decrease in carbon activity, caused by cementite growth, is represented by shifting the carbon isoactivity line to the left, for instance the isoactivity line marked 0.19 in Fig. 4.14 is for a 30 day heat treatment. This particular isoactivity line also coincides with the critical limit corresponding to the lowest carbon activity attainable by carbon in ferrite (activity through the γ vertex of the (γ + α + cem) three-phase triangle represented by the (γ + α) edge). At this point, the chemical potentials of carbon in the austenite matrix and ferrite would be equal, and there exists a metastable equilibrium between carbon in ferrite and austenite. However, the system continues forming cementite forms (cellular or grain boundary) other than pearlite resulting in a further decrease in carbon activity in the austenite matrix. The red dot-dash line (representing carbon

activity value of 0.17) in Fig. 4.14 shows a hypothetical isoactivity line resulting from further growth of cementite in the system before reaching equilibrium. This reduction in carbon activity in the austenite matrix creates a situation where carbon activity in ferrite is now higher than carbon activity in austenite, and therefore $\mu_C^{\gamma} < \mu_C^{\alpha}$. This difference in carbon activity (chemical potential) in ferrite and the austenite matrix produces thermodynamic conditions requiring dissolution of ferrite.

When carbon activity in the system reaches the γ vertex of the ($\gamma + \alpha + $ cem) three-phase triangle, austenite reclaims the ferrite portion of any pearlite colony, resulting in retrenched austenite,γ^r. It is reasonable to expect that during ferrite retrenchment, manganese from the austenite matrix diffuses into the retrenched austenite. Due to slow bulk manganese diffusion in austenite, the $U_{Mn}^{\gamma^r}$ (red circles in Fig. 4.9b) regions are higher than the manganese composition of the γ vertex of the ($\gamma + \alpha + $ cem) three-phase triangle manganese but still well below the $U_{Mn}^{\gamma-eq}$, dark blue circle in Fig. 4.9b. Detailed examination of the retrenched austenite as well additional verification of the thermodynamic reasons educing ferrite dissolution are discussed in the next section discussing 650 °C temperature where sparseness of chemistry data describing reaction phases is not an issue.

4.3 650 °C

4.3.1 Predictions using interface local equilibrium model

This temperature is selected for the most complete analysis as far as the extent of data collected over the longest heat treatment time. The analysis builds on the two higher temperatures and extends into covering ferrite dissolution. Once again, bulk alloy chemistry lies in the (γ + cem) two-phase field and to the right of the P/NP boundary. Accordingly, it is thermodynamically permitted for the growing cementite to inherit manganese content of the bulk alloy ($U_{Mn}^{cem} \approx 0.118$). Equilibrium amount of manganese in cementite at this temperature is $U_{Mn}^{cem} \approx 0.299$.

4.3.2 Experimental Summary

650 °C is most extensively studied temperature. With the exception of 1 hour, analytical data for this temperature are available for every heat treatment time reported in the TTT diagram, Fig. 3.7. At this temperature, decomposition of austenite occurs in several consecutive stages. The sequence of the reactions is cementite grain boundary precipitation (1 hour), pearlite formation (3 hours), cellular decomposition (60 days), and ferrite dissolution (60 days). It is worth noting that ferrite dissolution after 60 days is limited to small colonies and occurs sparingly. Widespread ferrite dissolution occurs after 180 days of heat treatment. Volume fraction of total cementite reaches ~0.037 (0.044 mole fraction) after 180 days, which is ~64% of the expected equilibrium volume fraction, 0.058 (0.069 mole fraction).

Manganese content in the grain boundary cementite remains approximately constant for the duration of the reaction ($U_{Mn}^{cem-gb} \approx 0.13$). Pearlitic cementite has $U_{Mn}^{cem-p} \approx 0.14$ after 3 hours and approaches $U_{Mn}^{cem-p} \approx 0.29$ after 180 days. Manganese content of cellular cementite is $U_{Mn}^{cem-c} \approx 0.23$ and remains approximately constant for the duration of the reaction.

4.3.3 Global Thermodynamics

The analysis of global thermodynamics at this temperature is similar to the one presented in the section discussing 660 °C. Solid and dashed horizontal black lines in Fig. 4.15a depict Gibbs free energy of a system prior to decomposition and at equilibrium respectively. The total energy available, $\Delta G_{total}^{\gamma \rightarrow \gamma+cem}$, for the transformation of the alloy at 650 °C is ~44.0 J/mol. To

verify the validity of the experimental results it is possible to narrow this permissible energy range by considering cementite growth with full equilibrium manganese partitioning at one extreme and no partitioning in the other.

Consider a hypothetical case where cementite grows as Widmanstatten plates into austenite. Plates with equilibrium manganese content ($U_{Mn}^{cem} = 0.299$) when combined with the experimental cementite mole fraction measurements result in the largest change in Gibbs free energy, plotted as the solid purple line Fig. 4.15a. Because the bulk alloy composition lies in the P/NP region of the 650 °C isotherm, cementite can also grow without manganese partitioning. The dashed blue line in Fig. 4.15a shows Gibbs free energy change associated with growing cementite ($U_{Mn}^{cem} = 0.118$) as a function of the experimentally observed cementite mole fraction for specified times. Although cementite can form without partitioning of manganese, the plotted results demonstrate this growth can't continue beyond a cementite mole fraction of 0.0340 (corresponding to 120 days, black arrow), where any further growth would result in an increase of Gibbs free energy, as evidenced by the positive slope of the dashed blue line in Fig. 4.15a after this point. The area between the dashed blue and purple lines represents the theoretically permissible Gibbs free energy range based on the $U_{Mn}^{cem-eq} \geq U_{Mn}^{cem} \geq U_{Mn}^{\gamma-bulk}$ composition criterion, if cementite Widmanstatten plates grow into the austenite matrix. However, given the observed cementite mole fraction, only the purple line sets the global limit that signifies the lowest attainable Gibbs free energy for the experimentally observed system. The horizontal solid black line represents the other energy extremum because progress of any reaction requires only a reduction in Gibbs free energy. Experimental results must fall within the energy level between the horizontal solid black and purple lines.

Now that the energy extrema for the transformation are set against the observed cementite mole fraction formed between 0 and 180 days, energy considerations associated with actual microstructures (which include non-equilibrium phases) are possible. At 650 °C, growth observations of ferrite and cellular cementite occur after 3 hours and 60 days respectively. Ferrite dissolution, which results in austenite with manganese contents lower than equilibrium ($U_{Mn}^{\gamma-eq} \approx 0.11 > U_{Mn}^{\gamma r} \approx 0.08$) is also observed after 60 days. Computation of Gibbs free energy matching the experimentally observed system is done for the same set of microstructures except that cementite lamellae for one set has manganese composition $U_{Mn}^{cem-p} = 0.14$ (green dash-dot line in

Fig. 4.15a) and the other set has cementite lamellae with $U_{Mn}^{cem-p} = 0.30$ (green dash-dot-dot line in Fig. 4.15a). Both sets include cellular cementite with $U_{Mn}^{cem-c} = 0.23$, manganese-depleted austenite with $U_{Mn}^{\gamma^d} = 0.09$, pearlitic ferrite with $U_{Mn}^{\alpha} = 0.02$, and retrenched austenite $U_{Mn}^{\gamma^r} = 0.08$. Vertical bars in Fig. 4.15a indicate the start time of various reaction's microstructures used in calculation of the Gibbs free energy. Table 3.10b-1 provides volume fraction information for the individual phases. Since the manganese content in pearlite cementite is over a range, the Gibbs free energy of the system has a value located between the two (dash-dot and dash-dot-dot) green lines in Fig. 4.15a, which represent different manganese contents in pearlitic cementite.[19] As the Gibbs free energy of the total system is increasingly negative over time, although still short of equilibrium value after 180 days of growth, all phase transformations observed in the system are thermodynamically permissible, *i.e.*, $\Delta G^{cem} + \Delta G^{\gamma^d} + \Delta G^{\gamma^r} + \Delta G^{\alpha} < 0$. Notice the hump in a system with $U_{Mn}^{cem-p} = 0.14$ (dashed-dot green line, black arrow) in Fig. 4.15a around 21 days (cementite mole fraction of 0.030). This temporary increase in Gibbs free energy is most like due to an error in measuring cementite volume fraction. Since the total amount of cementite in the system increases well after 21 days of heat treatment and pearlitic cementite in a sample heat treated for 21 days has $U_{Mn}^{cem-p} \approx 0.24$, Table 3.10c in Chapter 3, indicates that partitioning of manganese is continuously increasing from the $U_{Mn}^{cem-p} \approx 0.14$. This is possible because ferrite provides a more rapid diffusion path than austenite ($\frac{D_{Mn}^{\alpha}}{D_{Mn}^{\gamma}} \approx 530$). [frideberg1969] As pearlite colonies grow and manganese partitions into cementite the Gibbs free energy of the system moves from the green dash-dot line down towards the green dash-dot-dot line.

---

[19] Cementite in smaller pearlite colonies exhibit U_{Mn}^{cem-p} lower than cementite in larger pearlite colonies.
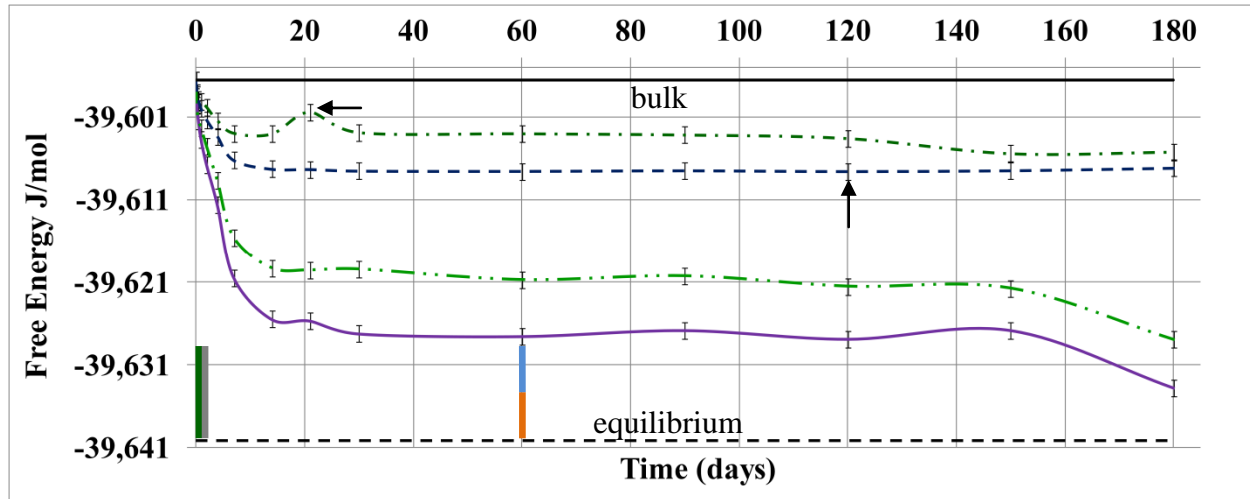
Figure 4.15a: Computed Gibbs free energy of the system during isothermal transformation at 650 °C as a function of time: **Black solid** line – prior to decomposition. **Black dashed** line – at equilibrium. **Green dash-dot** line – the system comprised of grain boundary cementite (U_{Mn}^{cem-gb} = 0.13), pearlite (U_{Mn}^{cem-p} = 0.14, U_{Mn}^{α} = 0.02), retrenched austenite ($U_{Mn}^{\gamma^r}$ = 0.08), cellular cementite (U_{Mn}^{cem-c} = 0.23), manganese-depleted austenite ($U_{Mn}^{\gamma^d}$= 0.09), and remaining austenite matrix. **Green dash-dot-dot** line – same as green-dash-dot but U_{Mn}^{cem-p} = 0.299. Volume fraction information is listed in the previous chapter, Table 3.10b-1. **Blue dashed** line – the system comprised of cementite with U_{Mn}^{cem} = 0.118 (bulk alloy composition) and austenite matrix. **Purple solid** line - the system comprised of cementite with U_{Mn}^{cem} = 0.299 (equilibrium predicted value) and austenite matrix. The bars represent the initial observation of the experimentally observed reaction. All bars extend to 180 days. Green – grain boundary cementite precipitation. Gray – ferrite growth. Blue – ferrite dissolution. Orange – cellular growth.
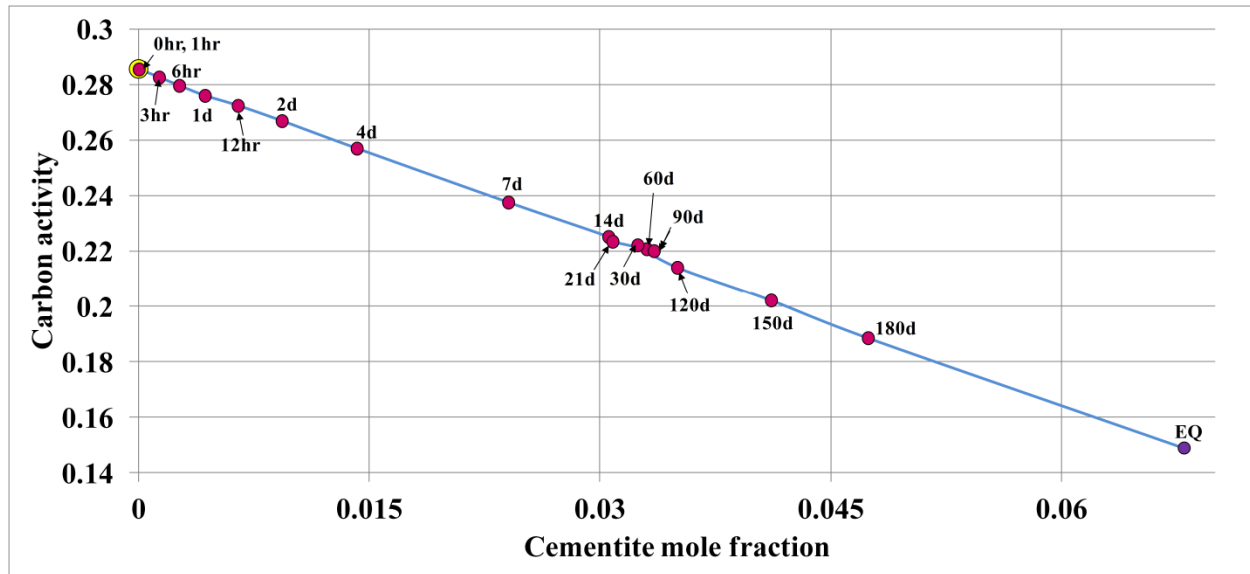
Figure 4.15b: Carbon activity in the austenite matrix as a function of experimentally observed cementite mole fraction for the alloy heat treated at 650 °C. Yellow circle (not visible) represents the system prior to decomposition (dashed green line in Fig. 4.16b). Purple circle represents the system at equilibrium (solid green line in Fig. 4.16b). Magenta circles represent the system at the intermediate time steps (dash-dot-dot lines in Fig. 4.16b).

The energy analysis in Fig. 4.15a (decreasing Gibbs free energy) is also strengthened by austenite carbon activity calculations shown in Fig. 4.15b. Determination of these values is the same as at 700 °C. Cementite growth, which necessarily consumes carbon, decreases carbon activity in the austenite matrix. Activity of carbon decreases over time, but even after 180 days of heat treatment does not reach the equilibrium value, in agreement with energy analysis shown in Fig. 4.15a.

4.3.4 Neighborhood Thermodynamics

Similar to the approach used in for 660 °C, global thermodynamics alone offers only limited insight concerning for the observed ferrite growth and dissolution. The analysis of ferrite formation and dissolution takes advantage of the ability to determine carbon activity in the system at each stage. Information about cementite mole fraction permits calculation of carbon activity in the austenite matrix because cementite remains a line compound, $U_C^{cem} = 0.333$ ($X_C = 0.25$). Table 4.1, section 4.1.3 (700 °C), shows cementite growth reduces carbon activity more than manganese partitioning. This is a useful result because manganese content in pearlitic cementite ranges from 0.14 to 0.29 with increasing time, shown in Fig. 4.16a where the triangles and circles represent manganese composition pearlitic and cellular cementite respectively. Note

168

that, while the manganese composition of cellular cementite at this temperature corresponds to the cementite end of the (γ + α +cem) three-phase triangle, it does so only at this temperature. Carbon isoactivity lines shown in Fig. 4.16b represent carbon activity values in the austenite matrix for the intermediate transformation time steps (also shown in Fig. 4.15b). Experimentally measured neighborhood manganese content in various austenite forms mapped on the resulting carbon isoactivity lines offers an approach for accounting for ferrite growth and its dissolution. The analysis of ferrite growth and its dissolution is similar to that employed for the cellular reaction, which provides D_{Mn}^{gb}. The following discussion sets $\mu_C^{\gamma} = \mu_C^{\gamma^{d-high}} = \mu_C^{\gamma^{d-low}} = \mu_C^{\gamma^r}$ and, therefore, $a_C^{\gamma} = a_C^{high\,\gamma^d} = a_C^{low\,\gamma^d} = a_C^{\gamma^r}$, which is based on the fact that carbon diffuses many orders of magnitude faster than manganese ($\frac{D_C^{\gamma}}{D_{Mn}^{gb}} \approx 7.2 \times 10^5$ and $\frac{D_C^{\gamma}}{D_{Mn}^{\gamma}} \approx 1.7 \times 10^7$) and, therefore, will remove all chemical potential gradients in the austenite phase.

Global thermodynamics reveal that the negative change in free energy resulting from the formation of cementite along with manganese partitioning (Fig. 4.15a) into cementite more than offset any positive free energy contribution due to growth of ferrite.
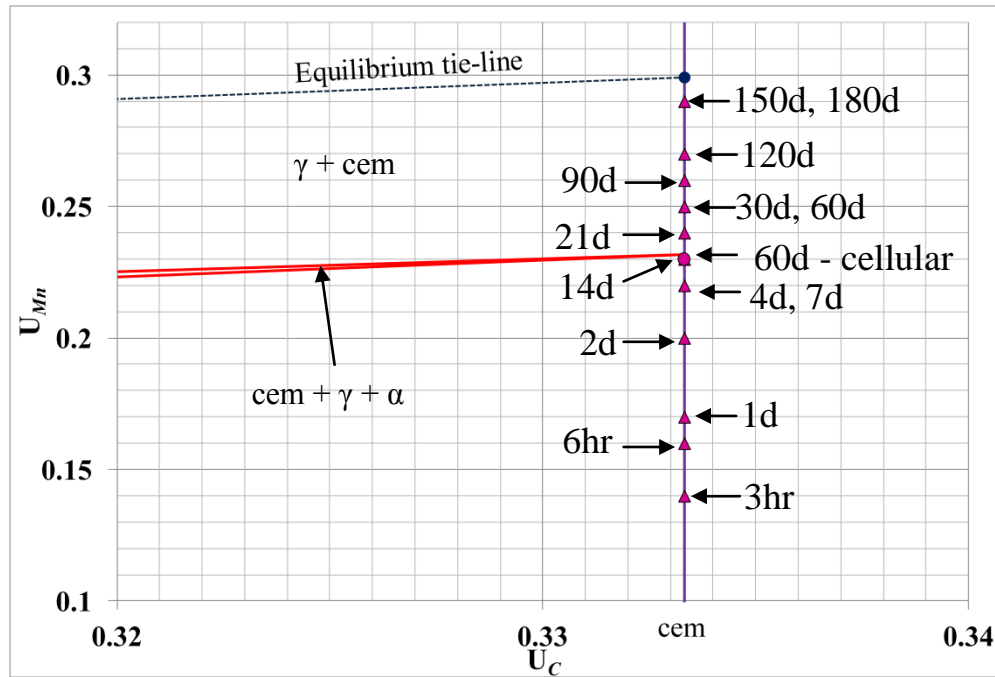
Figure 4.16a: Manganese content in cementite plotted on the Fe-Mn-C 650 °C isotherm. Magenta triangles and circles represent pearlitic and cellular cementite respectively.
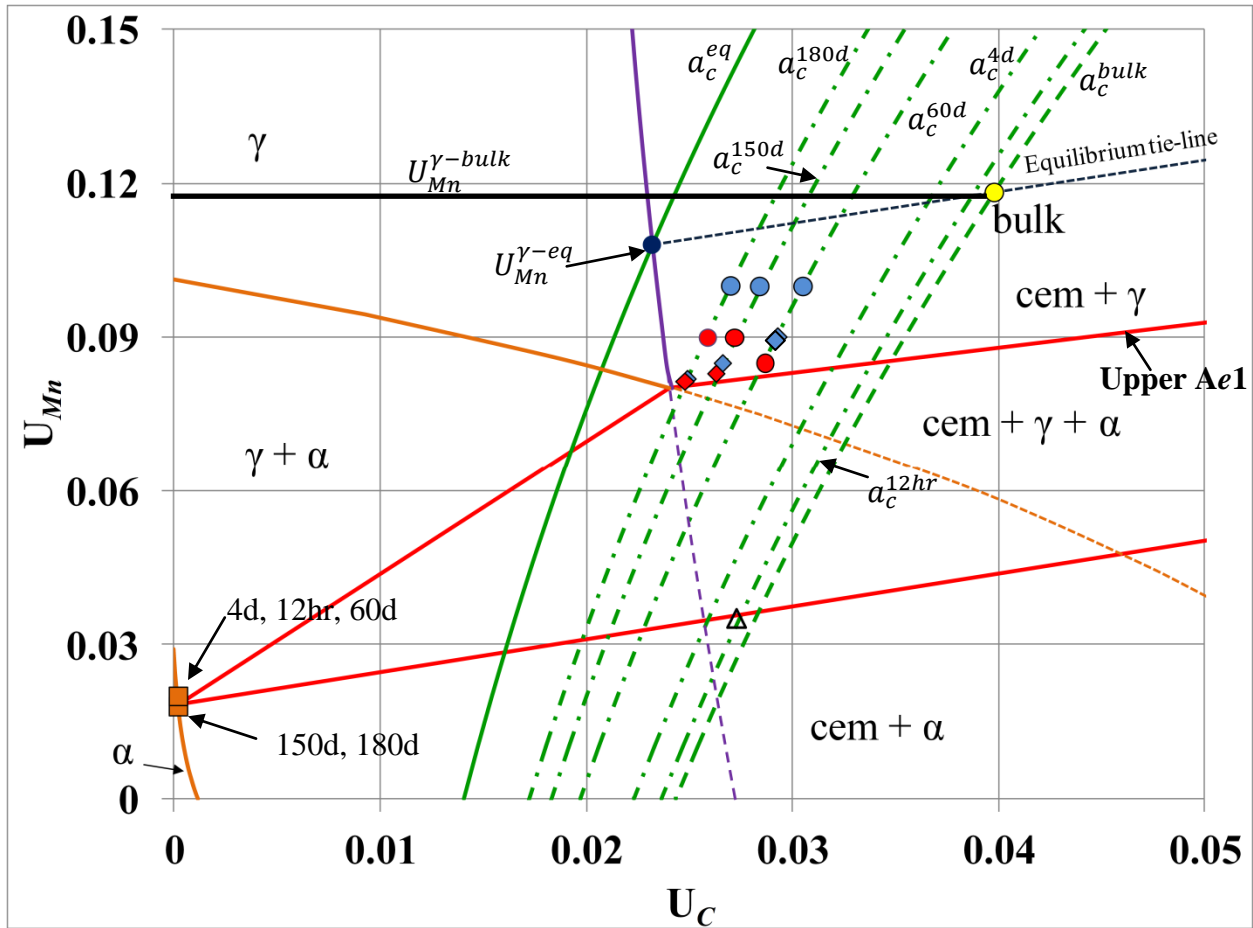
Figure 4.16b: Manganese content of the depleted austenite regions mapped on the carbon isoactivity lines plotted on the Fe-Mn-C 650 °C isotherm. Yellow circle represents bulk alloy content. Blue circles indicate γ^{d-high} and rhombuses γ^{d-low}. Red circles indicate γ^{r-high} and rhombuses γ^{r-low}. Orange squares represent ferrite. Black triangle is discussed with Fig. 4.18.
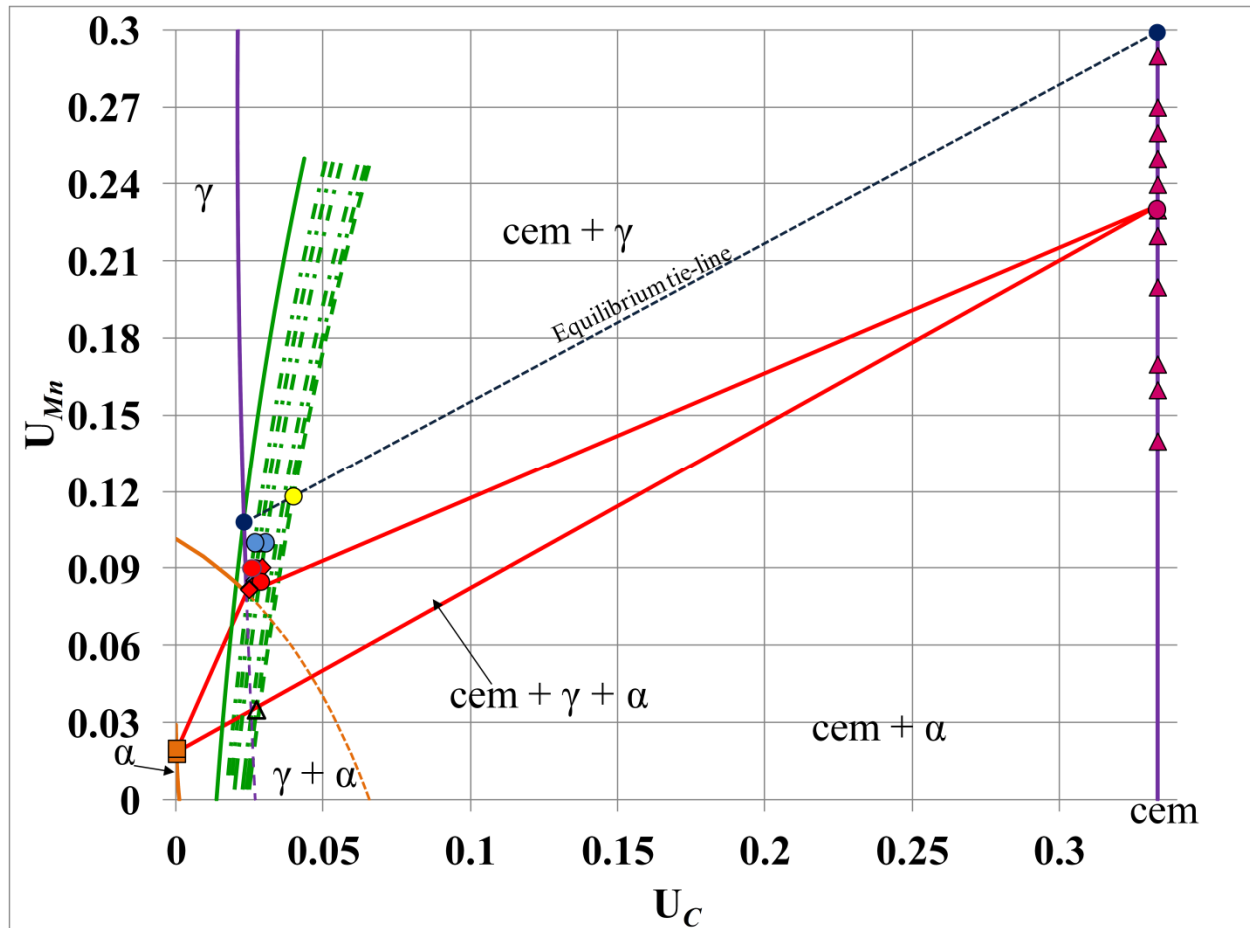
Figure 4.16c: Compilation of Figs. 4.16a and b with all of the data points plotted on the Fe-Mn-C 650 °C isotherm.

However, the bulk alloy composition (yellow circle in Fig. 4.16b) is in the (γ + cem) two-phase field where formation of ferrite is not expected. To account for ferrite growth it is necessary to consider local neighborhood conditions favorable to ferrite formation. The following discussion analyzes each reaction individually, assessing its thermodynamic viability as a stand-alone process. However, since carbon in the austenite matrix adjusts very quickly to any cementite growth or manganese partitioning, the discussion then considers the impact of carbon activity (a global variable) on the reaction mechanics.

4.3.4.1 Neighborhood Thermodynamics - Cellular Reaction

At this temperature, cellular precipitation is the last microstructure to occur, orange bar in Fig. 4.15a (same time as blue bar for ferrite dissolution). The analysis of this reaction is similar to those presented for 660 and 700 °C. At a minimum, growing cementite must inherit the U_{Mn}^{cem}

≈ 0.118, represented by the dashed blue line in Fig. 4.17. The purple solid line shows Gibbs free energy of the same two phase microstructure (cementite and austenite) with the cementite possessing the calculated equilibrium manganese content $U_{Mn}^{cem} = 0.299$. Similar to the 660 and 700 °C, in both cases, this microstructure can be envisioned as cementite Widmanstatten plates growing into the austenite matrix. The regions between these lines (dashed blue and solid purple) is the theoretically permissible free energy range for the current microstructure based on the $U_{Mn}^{cem-eq} \geq U_{Mn}^{cem} \geq U_{Mn}^{\gamma-bulk}$ criterion. The horizontal black and purple lines, however, provide the overall thermodynamically permissible energy range for any reaction.
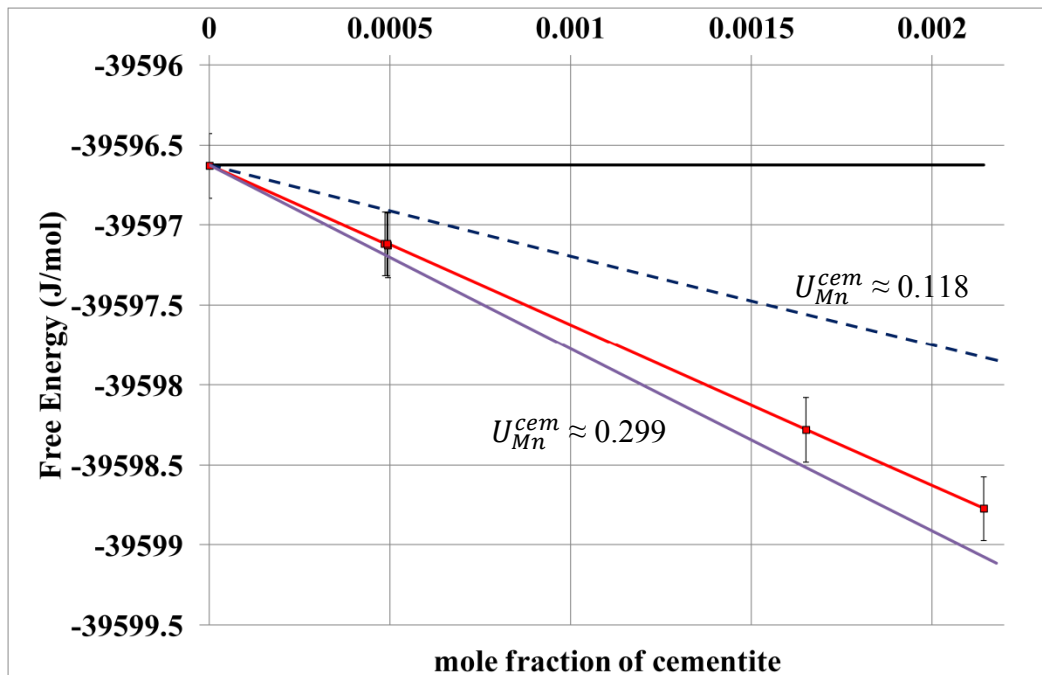
Figure: 4.17: Computed free energy for cellular reaction as a function of cementite mole fraction. As a stand-alone reaction, the free energy begins at the energy base line for the current alloy. **Black** solid line – prior to austenite decomposition. **Blue** dashed line – the system comprised of cementite with $U_{Mn}^{cem-c} = 0.118$ and austenite. **Purple** solid line - the system comprised of cementite with $U_{Mn}^{cem} = 0.299$ (equilibrium predicted value) and austenite. **Red** solid line –experimentally observed system with $U_{Mn}^{cem-c} = 0.23$ and $U_{Mn}^{\gamma^d} = 0.09$.

The red line shows calculated Gibbs free energy of the system consisting of our experimentally observed cellular cementite mole fraction with manganese content $U_{Mn}^{cem-c} = 0.23$ and the associated mole fraction of manganese-depleted austenite with $U_{Mn}^{\gamma^d} = 0.09$. The amount of cellular cementite in the whole system is no more than ~6% (Table 3.10b-1) at any given time,

when compared to the amount of cementite produced by grain boundary precipitation and pearlite growth. Once again, free energy contribution of the excessively manganese-depleted austenite is positive, similar to the case presented for 700 °C in Fig. 4.4a. However, the Gibbs free energy trend is negative and is within the allowable energy range specified by the, purple and blue dashed lines. This means that cellular decomposition with $U_{Mn}^{cem-c} \approx 0.23$ and manganese-depleted austenite is thermodynamically permissible, even as a stand-alone reaction. Using information in Fig. 4.17, Petermann‑Hornbogen model yields $D_{Mn}^{gb} \approx 1.34 \times 10^{-19} \frac{m^2}{s}$.

Bulk manganese diffusion in austenite at this temperature is $D_{Mn}^{\gamma} \approx 5.64 \times 10^{-21} \frac{m^2}{s}$.

A higher driving force for cementite formation at 650 °C, when compared to 700 °C and 660 °C, results in a higher cementite nucleation rate leading to more closely spaced cementite allotriomorphs. Cellular colonies necessitate larger spacing between cementite precipitates to accommodate the observed manganese content ($U_{Mn}^{cem} \approx 0.23$) without decomposition of manganese-depleted austenite neighborhoods into ferrite, as confirmed by the larger spacing of the manganese-depleted austenite cellular component when compared to ferrite spacing in pearlite colonies, Table 3.10b-1. Mapping manganese-contents of these areas ($U_{Mn}^{\gamma^d} \approx 0.09$) on the respective carbon activity lines places manganese-depleted austenite in the (γ + cem) two-phase field where formation of ferrite is prohibited, blue circles and blue diamonds in Figs. 4.16b and c.

4.3.4.2 Neighborhood Thermodynamics – Pearlite Reaction

As previously mentioned, grain boundary cementite is the first phase to precipitate. A higher driving force for cementite formation at 650 °C results in a higher cementite nucleation rate leading to more closely spaced cementite allotriomorphs. The manganese content of the allotriomorphs is also higher than the manganese content of the bulk alloy ($U_{Mn}^{cem-gb} \approx 0.13$, $U_{Mn}^{\gamma-bulk} \approx 0.118$). Grain boundary diffusion is the primary mechanism of manganese transport. For cementite to attain a manganese content in excess of the bulk content, it must deplete austenite adjacent to it utilizing the grain boundary. As cementite obtains manganese from the adjacent austenite, manganese from the matrix diffuses into the depleted austenite regions. However, since $\frac{D_{Mn}^{gb}}{D_{Mn}^{\gamma}} \approx 23.8$, cementite will deplete neighborhoods adjacent to it faster than

manganese from the bulk can replenish these areas. This manganese depletion of neighborhoods adjacent to cementite results in a composition and thermodynamic condition different from the bulk alloy. In some cases, a thermodynamic description of the neighborhood places it within the $(\gamma + \alpha + \text{cem})$ three-phase field, which results in ferrite nucleation and growth, forming a pearlite aggregate. Figs. 4.18 and related calculations show how manganese-depletion leads to creation of conditions favorable to ferrite growth.
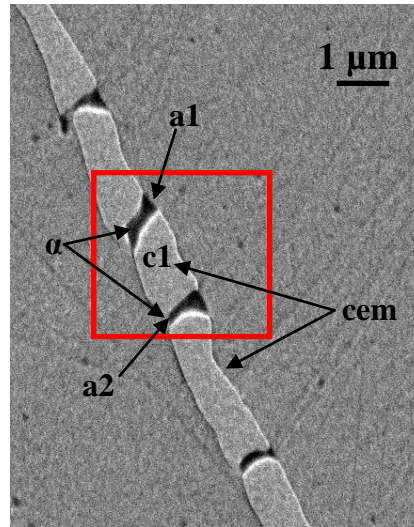
Figure 4.18: SEM image of a pearlite colony in the initial stage of development in a sample heat treated at 650 °C for 12 hours days.

Fig. 4.18 shows incipient stages of the pearlite colony development. The red rectangle encloses an area of particular interest. Using a k-clustering algorithm it is possible to compute the area (and thus volume) occupied by cementite and ferrites phases. Area of the cementite plate labeled **c1** is 3908 pixels. Area of the ferrite plate labeled **a1** is 690 pixels and **a2** is 674 pixels. Using the density of cementite (1.17 moles/unit volume) and ferrite density (0.98 moles/unit volume) it is possible to set up a mass balance equation to evaluate $U_{Mn}^{\gamma^{d*}}$ or the amount of manganese-depletion needed to produce $U_{Mn}^{cem-gb} = 0.13$. In this case, the region depleted by cementite (c1) is represented by the ½ (a1 + a2) = 682. Using $U_{Mn}^{cem-gb} = 0.13$, and $U_{Mn}^{cem-gb} = 0.02$ yields. $682 \times 0.98 \times (0.118 - U_{Mn}^{\gamma^{d*}}) = 3908 \times 1.18 \times (0.13 - 0.118)$ and results in $U_{Mn}^{\gamma^{d*}} = 0.035$[20]. Mapping this manganese value on the corresponding isoactivity line (12 hours), places it

---

[20] The units for dimensional analysis are: $volume \times \frac{mole}{volume} \times \frac{Mn\ at.\%}{mole}$.

into the (α + cem) two‑phase field, open black triangle in Fig. 4.16b, where ferrite formation is possible. This calculation demonstrates only an estimate of the depletion that occurs to support manganese partitioning associated with grain boundary cementite and it does not to provide a quantitative value because it ignores stereological effects. In all likelihood, transformation of the manganese-depleted austenite into ferrite occurs when the composition of the manganese-depleted region falls within the (γ + α + cem) three-phase field.

Due of the downward slope of the upper Ae1 with respect to lower carbon contents additional formation of ferrite is hindered by the decreasing carbon activity (this was briefly mentioned as one of three outcomes in section 4.2.4.3), which results in a shift of carbon isoactivity lines to the left, Fig. 4.16b. Because of the shifting carbon isoactivity lines the amount of manganese depletion needed to create neighborhood compositions that place a region into the (γ + α + cem) three-phase field increases.

Now that the mechanism by which thermodynamic conditions necessary for ferrite, and consequently pearlite, growth has been established it is necessary to evaluate changes in the Gibbs free energy associated with pearlite growth and its relationship with formation of equilibrium cementite. Global thermodynamics, once again, define Gibbs free energy limits for the reaction and are set with the red and black lines in Fig. 4.19. The red line in Fig. 4.19 shows computed Gibbs free energy for the system as a function of cementite mole fraction with an equilibrium manganese content. The horizontal black line represents free energy of the system prior to austenite decomposition. The lowest point on the red line, marked by the circle, corresponds to a mole fraction of 0.069, which is the equilibrium cementite mole fraction for the alloy at this temperature. Additional growth of cementite increases Gibbs free energy of the system and is, therefore, thermodynamically prohibited. The energy associated with a phase transformation involving ferrite must fall in the range specified by the black and red lines in Fig. 4.19 with cementite mole fraction not exceeding 0.069.
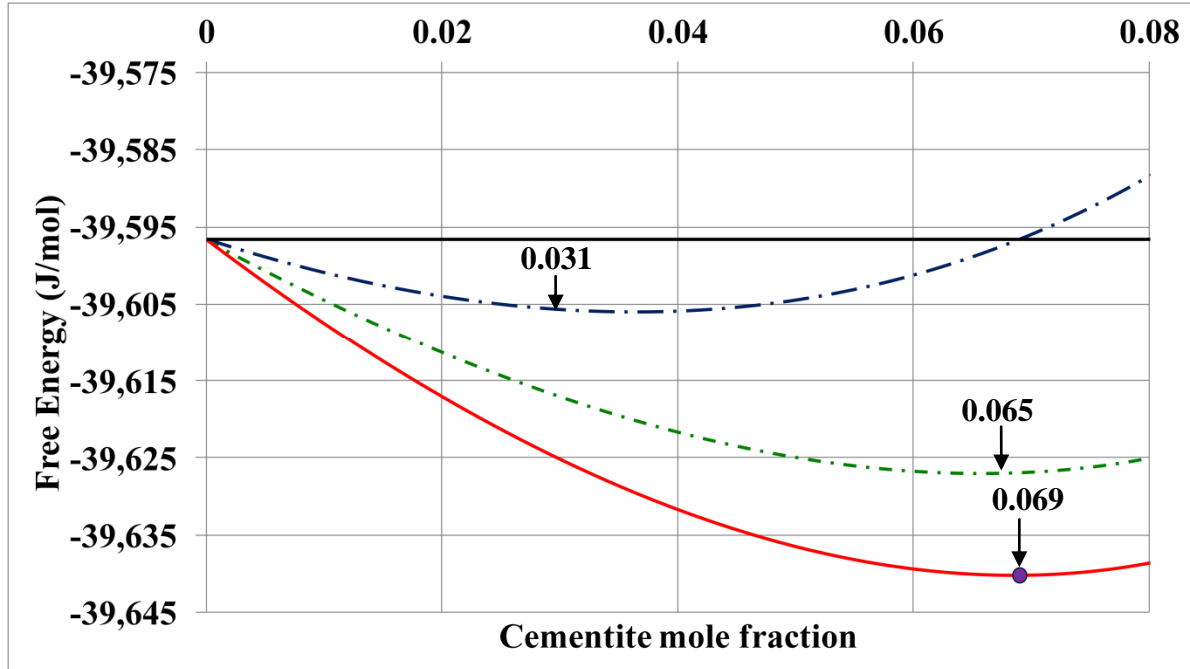
Figure 4.19: Computed free energy of the system at 650 °C as a function of cementite mole fraction. As a stand-alone reaction, the free energy begins at the energy base line for the current alloy. **Red** line corresponds to formation of cementite with equilibrium manganese content, U_{Mn}^{cem} = 0.298. The circle represents the minimum free energy and corresponds to equilibrium cementite mole fraction. **Horizontal black** line represents free energy of the system prior to decomposition. **The dash-dot blue** line represents the system where U_{Mn}^{cem} = 0.14, U_{Mn}^{α} = 0.02, and cementite to ferrite mole ratio (CFR) =1.54. **The dashed green** line represents the system where U_{Mn}^{cem} = 0.27, U_{Mn}^{α} = 0.02, and cementite to ferrite mole ratio (CFR) =1.05.

Modeling of pearlite requires accounting for two factors: manganese partitioning into cementite and sufficient depletion of the neighboring austenite making ferrite formation possible. After 12 hours of heat treatment, the ratio of pearlitic cementite to ferrite (CFR) mole fraction in a pearlite colony is ~1.54 and $U_{Mn}^{cem-p} \approx 0.14$. The dash-dot blue line in Fig. 4.19 shows the system's Gibbs free energy with these characteristics (U_{Mn}^{α} = 0.02). The minimum occurs at cementite mole fraction of ~0.031. This means that when the system reaches a cementite mole fraction of ~0.031, any further growth of ferrite in pearlite colony described by the CFR ≈ 1.54 and $U_{Mn}^{cem-p} \approx 0.14$ is no longer thermodynamically permissible. Measured cementite mole fraction (grain boundary, pearlitic, and cellular) after 12 hours is ~0.004, short of the estimated cementite mole fraction needed to stop further ferrite growth. Similarly, CFR ≈ 1.05 and $U_{Mn}^{cem-p} \approx 0.27$ describe the largest pearlite colony without ferrite dissolution after 120 days. The dash-dot green line in Fig. 4.19 shows the Gibbs free energy for a system with these characteristics (U_{Mn}^{α} = 0.02). The minimum occurs at cementite mole fraction of ~0.065, indicating cementite

mole fraction where ferrite growth ceases. Measured cementite mole fraction (grain boundary, pearlitic, and cellular) after 120 days is ~0.034, also short of the ~0.065 needed to discontinue ferrite growth. However, the most important outcome of this analysis is that ferrite growth with experimentally observed characteristics describing pearlite colonies is thermodynamically permissible, up to at least cementite mole fraction of ~0.031, demonstrated by the decreasing Gibbs free energy shown by the dash-dot blue and green lines. This analysis also shows that pearlite growth, after nucleation of ferrite, is thermodynamically viable as a stand-alone reaction.

4.3.4.3 Neighborhood Thermodynamics – Ferrite Dissolution

Similar to the observations at 660 °C, growth of pearlite (ferrite component) is concurrent with other cementite forming reactions in the system, *i.e.*, grain boundary precipitation and cellular reaction. As the total cementite mole fraction increases, a shift of carbon isoactivity lines to the left reflects a decrease in carbon activity in the remaining austenite matrix (Fig. 4.16b, 4.20). Ferrite dissolution is the direct consequence of the decrease in carbon activity associated with continued cementite formation. The following discussion describes thermodynamic reason that elicits ferrite dissolution, confirming the conclusion reached for the 660 ° C but utilizing the extensive analytical data available for the 650 °C temperature.

Fig. 4.20 shows a Fe-C-Mn isotherm at 650 °C (comparable to the one shown in Fig. 4.16b) with experimental carbon activity data plotted on the isotherm. Similar to the Fig. 4.14, the difference between this construction and the one shown in Fig. 4.16b is how carbon isoactivity lines are drawn. In Fig. 4.16b carbon isoactivity lines are depicted as nearly straight lines. In Fig. 4.20 carbon isoactivity lines have knees with the lower end of the knee (orange dash-dot portion of the isoactivity line in Fig. 4.20) connecting the α and $\gamma/(\gamma + \alpha)$ metastable phase extension. Again, the orange portions of the isoactivity lines represent the $(\gamma + \alpha)$ tie-lines and, therefore, characterize the maximum permitted carbon activity in ferrite during pearlite growth at each of the experimentally observed system states (which are described by the calculation of the carbon activity). Based on this construction, the lowest carbon activity attainable by ferrite corresponds to the equilibrium tie-line represented by the red $(\gamma + \alpha)$ edge of the $(\gamma + \alpha + cem)$ three-phase triangle. Since carbon content in ferrite is unknown, the actual carbon activity in ferrite is in the range between a specific orange line representing the current transformation stage and the $(\gamma + \alpha)$ edge of the $(\gamma + \alpha + cem)$ three-phase triangle.

Consider a system comprising of austenite matrix and cementite so that the carbon activity in the austenite matrix is ~0.28, Fig. 4.20 dash-dot carbon isoactivity line marked 0.28 This line describes the carbon activity in the austenite matrix after 6 hours of transformation time. Decrease in carbon activity caused by cementite growth is represented by shifting the carbon isoactivity line left, isoactivity line marked 0.22 in Fig. 4.20 (60 days). This leads to a reduction of the carbon activity range permitted in ferrite but it does not require dissolution. Experimentally, while dissolution occurs after 60 days it is limited to small colonies and occurs sparingly. A further decrease in carbon activity to a value of 0.18 represents a critical limit corresponding to the lowest carbon activity attainable by carbon in ferrite (activity through the γ corner of the (γ + α + cem) three-phase triangle). Incidentally, carbon activity in the austenite matrix after 180 days is ~0.18. At this point, the chemical potentials of carbon in the austenite matrix and ferrite are nearly equal, creating a metastable equilibrium between carbon in ferrite and austenite. However, the system continues forming cementite in reaction other than pearlite leading to a further decrease in carbon activity in austenite. The red dot-dash line (representing carbon activity value of 0.17) in Fig. 4.20 shows a hypothetical isoactivity line resulting from further growth of cementite in the system before reaching equilibrium. This reduction in carbon activity in the austenite matrix creates a situation where carbon activity in ferrite is now higher than carbon activity in austenite, and therefore $\mu_C^\gamma < \mu_C^\alpha$. This difference in carbon activity (chemical potential) in ferrite and the austenite matrix triggers dissolution of ferrite.
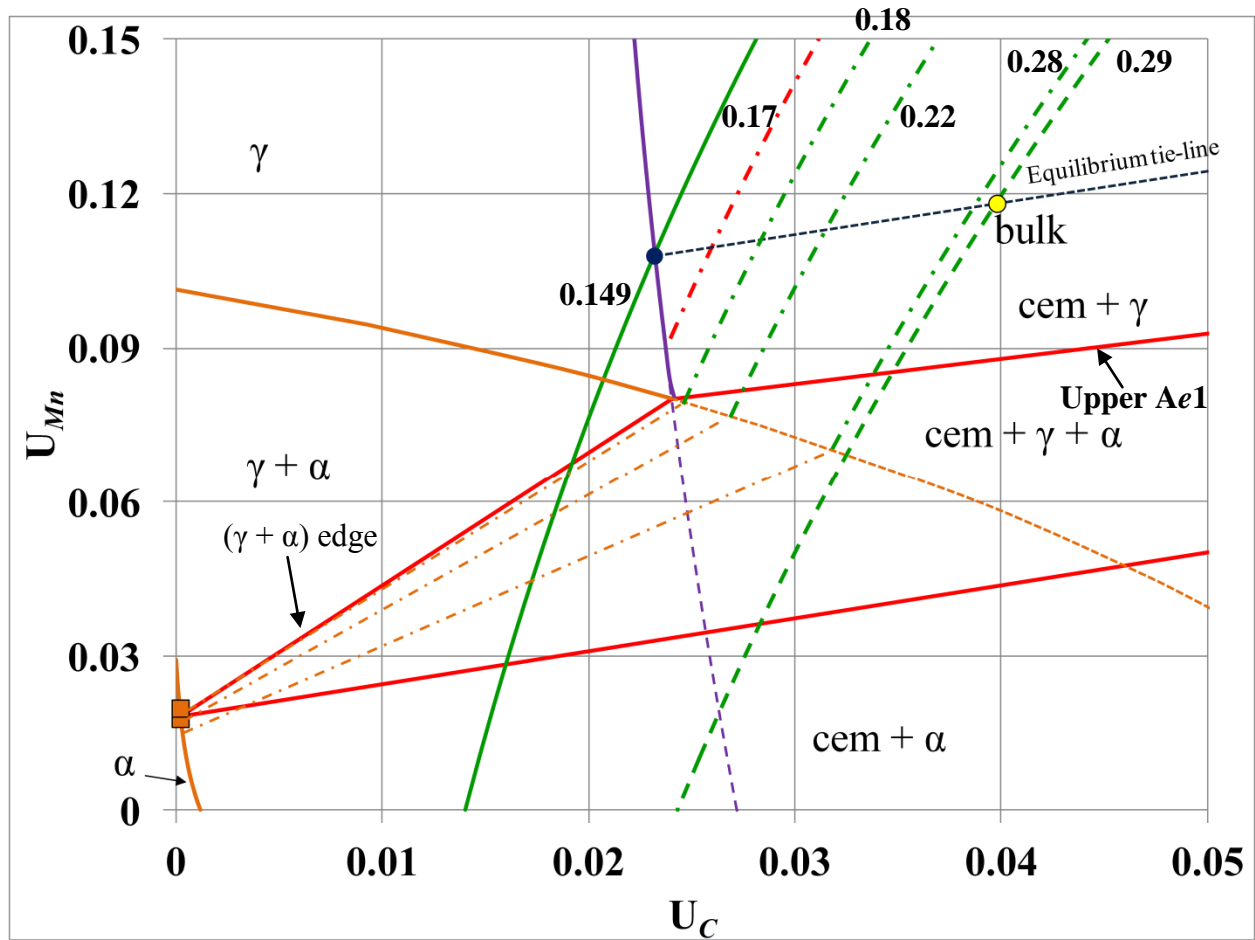
Figure 4.20: Carbon isoactivity lines that include the ferrite component (the "knee") plotted on the Fe-Mn-C 650 °C isotherm. Yellow circle represents bulk alloy content. Black unfilled squares depict evolution of pearlite aggregate with changing carbon activity in the system. Carbon isoactivity lines in this figure correspond to the carbon isoactivity lines in Fig. 4.16b. Red rhombus represents the terminating condition of the 0.17 carbon isoactivity line.

As noted, observation of ferrite dissolution after 60 days is isolated to small colonies and occurs sparingly but it is extensive after 180 days in all colony sizes, Fig. 4.21. This can be attributed to the higher interfacial energy (pearlite is divergent and therefore the plates are closer to one another when colony is small) as well as Gibbs free energy associated with smaller colonies (Fig. 4.19, blue dash-dot line). Carbon activity of the system after 180 days corresponds favorably to the value of carbon activity at the γ corner of the (γ + α + cem) three-phase triangle. This scenario is also identical to the case reported for 660 °C.
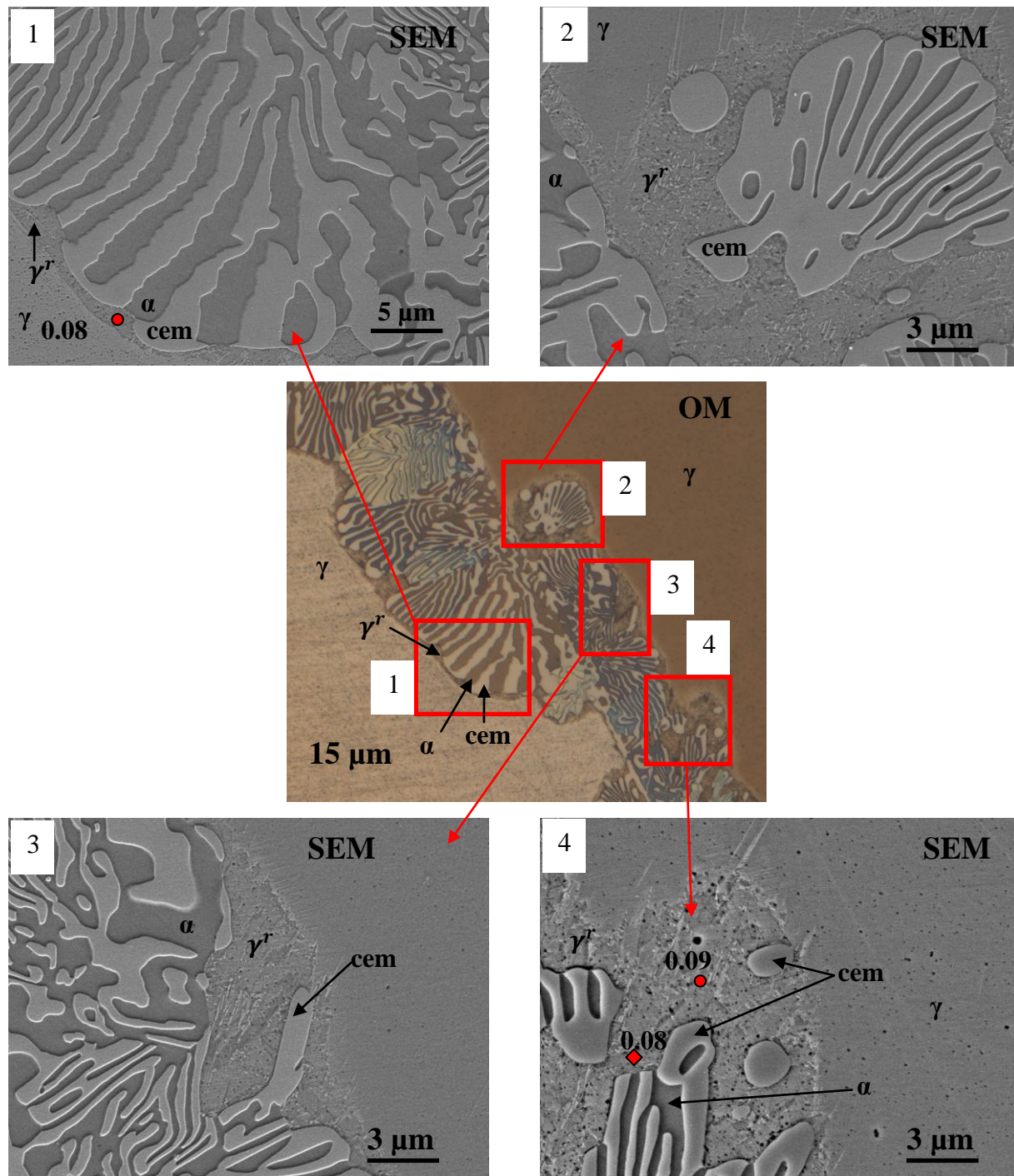
Figure 4.21 Optical and SEM images showing areas of retrenched austenite in a sample heat treated at 650 °C for 180 days. The shapes correspond to the shapes used in Fig. 4.16b.

When carbon activity in the system reaches the γ vertex of the $(\gamma + \alpha + \text{cem})$ three-phase triangle, austenite reclaims the ferrite portion of any pearlite colony, resulting in retrenched

austenite,γ^r. During ferrite retrenchment, manganese from the austenite matrix also diffuses into the retrenched austenite. Due to slow bulk manganese diffusion in austenite, the $U_{Mn}^{\gamma^r}$ (red circles in Fig. 4.16b) regions are higher than the manganese composition of the γ vertex of the (γ + α + cem) three-phase triangle manganese but still well below the $U_{Mn}^{\gamma-eq}$, dark blue circle in Fig. 4.16b. Red rhombuses correspond to areas of retrenched austenite closer to the pearlite aggregate (shown in frame 4 in Fig. 4.21). As expected $U_{Mn}^{\gamma^r}$ closer to the aggregate has lower manganese content but this value rises over time, as shown by the difference in high and low $U_{Mn}^{\gamma^r}$ values for different stages of the transformation in Fig. 4.16b.

Chapter 5 – Conclusions

This work explored kinetic and thermodynamic characteristics of austenite decomposition above the upper Ae1 in an Fe-0.85C-11.56Mn (wt. %) alloy. These characteristics included the transformation path (growth of cementite) and the chemical mechanism involved in formation and dissolution of the metastable ferrite. The analysis critically tested predictions made using the local equilibrium (LE) model. As suggested in Chapter 1, the LE model cannot predict the chemical mechanism used by the system during its transformation. Observation of a cellular reaction occurring concurrently with pearlite highlighted this drawback. At best, the LE model provided information about thermodynamically permissible phases and their respective compositions (LE model permits both pearlite and cellular). Furthermore, the LE model attributed a decrease in carbon activity to manganese partitioning, ignoring the effects of carbon consumption by cementite-forming reactions, which also acted to reduce carbon activity in the system. A comprehensive explanation of the experimental results required simultaneous thermodynamic evaluation of the intermediate transformation steps (global scale) and an examination of individual cementite-forming reaction paths (neighborhood scale). The former provided carbon activity values in all austenite forms at any given stage of the transformation. The latter described the atomic mechanism and the resulting composition of neighborhoods adjacent to the growing cementite. The combination of the two accounted for the thermodynamic conditions associated with ferrite growth (or lack thereof) and dissolution.

5.1 Transformation paths

The transformation paths employed by the system, in all considered temperature cases, utilized at least two of the three cementite-forming reactions: 1) grain boundary cementite precipitation; 2a) pearlite reaction; 2b) cellular reaction. In all cases, cementite mole fraction increased over time, suggesting that the system is not in a metastable equilibrium state, even during ferrite dissolution. After cementite grain boundary precipitation, the choice of the reaction qualitatively appeared to depend on the spacing between, and manganese content of, cementite allotriomorphs and plates. Other than formation of pearlite or cellular colonies, this also gave rise to unique situations where colonies exhibited both pearlitic (between the closely spaced

cementite allotriomorphs in the earlier stages of the reaction) and cellular characteristics (in the later stages of growth with wider spacing between cementite lamellae). Consistency of the experimental data (increased quantity of grain boundary cementite concomitant with a steady reduction of U_{Mn}^{cem-gb} with lower experimental temperatures) suggested some optimization principle, which connects the two. Furthermore, transformation paths taken by the system to attain equilibrium insinuated that initially cementite growth dominates the primary objective of the transformation as evidenced by pearlite growth with U_{Mn}^{cem-p} which is lower than U_{Mn}^{cem-c} and U_{Mn}^{cem-eq}.

Formation of ferrite, which is both carbon and manganese averse, increased manganese content of pearlitic cementite, but presented another obstacle in realization of equilibrium. In many cases, ferrite dissolution began when pearlitic cementite is short of equilibrium manganese content and $U_{Mn}^{cem-p} < U_{Mn}^{cem-c}$ and left behind retrenched austenite with manganese content below the equilibrium expected amount ($U_{Mn}^{\gamma^d} \leq U_{Mn}^{\gamma-eq}$). The subsequent corrective mechanism necessitates three additional steps: 1) complete ferrite dissolution; 2) bulk manganese diffusion from the austenite matrix into the newly formed retrenched austenite; 3) manganese diffusion from the austenite matrix into cementite. Similarly, cellular reaction resulted in cellular cementite with nearly constant manganese content and $U_{Mn}^{cem-c} < U_{Mn}^{cem-eq}$ and manganese-depleted austenite regions (with $U_{Mn}^{\gamma^d} \leq U_{Mn}^{\gamma-eq}$) between the cementite lamellae. Achievement of equilibrium, therefore, requires manganese partitioning from the austenite matrix into cementite and manganese diffusion into the manganese-depleted austenite of the cellular colonies.

5.2 Reactions

Reaction type used by the system as it advances towards equilibrium depended, in part, on the precipitation location and spacing of the grain boundary cementite. Grain boundary cementite had two temperature dependent variables: U_{Mn}^{cem-gb} and the number/spacing of cementite precipitates on the grain boundaries. Experimental temperature, which affected both variables, incidentally created conditions favorable to either result in cellular or pearlite reactions. Decreasing experimental temperature lowered the U_{Mn}^{cem-gb}, however $U_{Mn}^{cem-gb} > U_{Mn}^{\gamma-bulk}$ in all cases, but resulted in higher quantities of cementite precipitation on the grain boundaries. The opposite is true if the temperature was increased. To attain the necessary

manganese content, cementite allotriomorphs depleted adjacent austenite regions. The primary mechanism of manganese transport was grain boundary diffusion.

5.2.1 Cellular Reaction

In the case of the cellular reaction, manganese depletion of the austenite matrix, even to levels below $U_{Mn}^{\gamma-eq}$, kept the composition of the manganese-depleted austenite in the (γ + cem) two-phase field thus averting the conditions favorable to ferrite formation. Additionally, decreasing carbon activity in the system further inhibited the possibility of ferrite formation by increasing the necessary manganese depletion of the austenite neighborhood (difference between the manganese content of the bulk alloy and the upper Ae1 boundary evaluated on the same carbon isoactivity line.

5.2.2 Pearlite Reaction - Ferrite formation

Similar to the cellular reaction, pearlite reaction (defined by ferrite growth) started by precipitation of grain boundary cementite with austenite neighborhoods, adjacent to cementite allotriomorphs, depleted of manganese. For ferrite to form, grain boundary cementite must deplete a sufficient manganese amount from the adjacent austenite so that the intersection of the manganese content and the respective carbon isoactivity line placed the austenite neighborhood in the (γ + α + cem) three-phase field. However, a more common observation was when cementite allotriomorphs were spaced closer together, the manganese reservoir available to attain experimentally observed U_{Mn}^{cem-gb} was smaller and thus manganese depletion modified composition within the austenite neighborhood, so that it is within the (γ + α + cem) three-phase field, where ferrite growth is now permitted.

5.2.3 Ferrite dissolution

Decrease in carbon activity resulting from continued cementite growth created a condition where carbon activity in the austenite matrix was lower than carbon activity in ferrite, effectively triggering ferrite dissolution. The lowest carbon activity in ferrite had a value associated with a tie-line represented by the (γ + α) edge of the (γ + α + cem) three-phase field and this value was higher than the carbon activity associated with equilibrium. Dissolution commenced when *all* cementite-forming reactions reduced carbon activity in the system below

the carbon activity represented by the (γ + α) edge. Any further reduction in carbon activity is expected to only exacerbate the difference in chemical potential between carbon in ferrite and carbon in the retrenched austenite (chemical potential of carbon in the latter is the same as chemical potential in the austenite matrix) and this difference is expected to persist until ferrite is completely dissolved.

References

[aaronson1962]   Reprinted from publication Aaronson HI, "Decomposition of Austenite by Diffusional Processes", pp. 387-548, Interscience, New York, NY, 1962, with permission from TMS.

[barber1993]   Barber, D. J., *Ultramicroscopy*, **52**, pp 101-125, 193.

[bowman1946]   Bowman, F. E., *Trans. ASM*, **36**, p. 6, 1946.

[cahn1962]   Cahn, J. W. and Hagel, W. C., in <u>Decomposition of Austenite by Diffusional Processes</u>, pp. 131-192, Eds.: Zackay, V. F. and Aaronson, H. I., Interscience (1962).

[cahn1963]   Cahn, J. W. and Hagel, W. C., *Acta Met.*, **11**, 561, 1963.

[cassada1992]   Reprinted from publication Cassada, W.A., Shiflet, G.J. and Jesser, W.A., *Acta Met.*, **40** (1992) pp. 2101-2111, with permission from Elsevier.

[cairney2000]   Cairney, J. M., Smith, R. D. and Munroe, P. R., *Microsc. Microanal.*, **6**, pp. 452-462, 2000.

[cliff1975]   Cliff, G. and Lorimer, G. W., *J. Micros.*, **103**, 203, 1975.

[coates1972]   Coates, D. E., *Met. Trans. B.*, **3**, 5, pp. 1203-1212, 1972.

[coates1973-1]   Coates, D. E., *Met. Trans. B.*, **4**, 4, pp. 1077-1086, 1973.

[coates1973-2]   Coates, D. E., *Met. Trans. B.*, **4**, 10, pp. 2313-2325, 1973.

[friedberg1969]   Friedberg, J. and Hillert, M., *Acta Met.*, **18**, 1253, 1970

[gomez1992]   Gomez, J. and Faugeras, O., Reconciling distance functions and level sets. Technical report No: 3666, INRIA, 1992.

[hackenberg]   Hackenberg, R. E. and Shiflet, G. J, *Unpublished work*, University of Virginia.

[hillert1952]   Hillert, M*., Jernkont Ann.*,**136**, p. 25, 1952.

[hillert1953]   Hillert, M., Paraequilibrium. *Internal Report*, Swedish Institute of Metals, 1953.

[hillert1971]   Hillert, M., Nilsson K., and Torndahl L., *J. Iron Steel Inst.*, **20**, p. 949, 1971.

[hillert1982]   Hillert, M., in Solid-Solid Phase Transformations, pp. 789-806, Eds.:

References

Aaronson, H. I., Laughlin, D. E., Serkerka, R. F. and Wayman, C. M, 1982.

[hillert1998]   Hillert M., *Phase equilibria, phase diagrams and phase transformations and their thermodynamic basis*, Cambridge, Cambridge University Press, 1998.

[hultgren1947]   Hultgren, A., *Trans. ASM*, **39**, pp. 915-1005, 1947.

[hultgren1951]   Hultgren, A., *Jernkont Ann.*, **135**, p. 403, 1951 (in Swedish). *Kungl. Svenska Vetensk Akad Handl*, 4th Series, Bd 4, No. 3 (in English).

[hutchinson2004]   Hutchinson, C. R., Shiflet, G. J., *Scripta Mat.*, **50**, pp. 1-5, 2004.

[kass1987]   Kass, A. Witkin, A., and Terzopoulos, D., *Int'l J. Comp. Vis.*, **1**, pp. 321-331, 1987.

[kaur1995]   Kaur, I., Mishin, Y., Gust, W., <u>Fundamentals of grain and interphase boundary diffusion</u>, John Wiley & Sons Inc., New York, NY, 1995.

[kikuchi1982]   Kikuchi, M., Choi, S. and Tanaka, R., in <u>Solid-Solid Phase Transformations</u>, pp. 969-973, Eds.: Aaronson, H. I., Laughlin, D. E., Serkerka, R. F. and Wayman, C. M., TMS-AIME, Warrendale, PA, 1982.

[kirkaldy1957]   Kirkaldy, J. S., *Can. J. Phys.*, **35**, pp. 435-440, 1957.

[kirkaldy1958]   Kirkaldy, J. S., *Can. J. Phys.*, **36**, pp. 907-916, 1958.

[kitano1995]   Kitano, Y., Fukikawa, Y., Kamino, T., Yaguchi, T., and Saka, H., *J. Electron Microsc.*, **44**, pp. 410-413, 1995.

[li2005]   Li, C., Xu, C., Gui, C. and Fox, M. D., *proceedings of the IEEE Computer Society Conference on Computer Vision and Pattern Recognition (CVPR),* Level Set Evolution Without Re-initialization: A New Variational Formulation, 2005.

[li2007]   Li, B. and Acton, S. T., *IEEE Transactions on Image Processing*, **16**, No. 8, pp. 2096-2106, 2007.

[lloyd1982]   Lloyd, S., *Transactions on Information Theory* , **28** (2), pp. 129–137, 1982.

[mangan1994]   Mangan, MA and Shiflet, GJ. In: WC Johnson, JM Howe, DE Laughlin and WA Soffa, Editors, *Solid–Solid Phase Transformations Proceedings*, TMS (1994), pp. 547–552.

[manna2001]   Manna, I, Pabi, S. K., Gust, W., *Int. Mater. Rev.*, 46 (2), pp. 53-91, 2001.

References

[mannerkoski1964]   Mannerkoski, M., *Acta Polytech. Scand.*, 26, 1, 1964.

[matsuoka1994]   Matsuoka S, Mangan MA, Shiflet GJ. In: Johnson, JM Howe, DE Laughlin and WA Soffa, Editors, *Solid–Solid Phase Transformations Proceedings*, TMS (1994), pp. 521-526.

[nes1972]   Nes, E., *Acta Met.*, **20**, 4, pp. 499-506, 1972.

[ontman2010]   Ontman, A. Y. M. and Shiflet, Gary J., *Met. Trans. A.*, **41**, 9, pp. 2236-2247, 2010.

[ontman2012]   Ontman, A. Y. M. and Shiflet, Gary J., *J. Microsc.*, **246**, 1, pp. 20-32, 2012.

[osher1988]   Osher, S., Sethian, J. A., *J. Comp. Phys.*, **79**, pp. 12-49, 1988.

[osher2003]   Osher, S. and Fedkiw, R., *App. Mathematical Sciences,* **153**, 2003.

[otsu1979]   Otsu, *IEEE Trans. Sys., Man., Cyber.*, **9**, pp. 62–66, 1979.

[pandit2011]   Dissertation: *Theory of the Pearlite Transformation in Steels*, Ashwin Pandit, University of Cambridge, 2011.

[papandreou2007]   Papandreou, G. and Maragos, P., *IEEE Trans. on Image Processing*, **16**, no. 1, pp. 229-240, January 2007.

[peng1999]   Peng, D., Merriman, B., Osher, S., Zhao, H., and Kang, M., *J. Comp. Phys.*, **155**, pp. 410-438, 1999.

[plichta1976]   Plichta, M. R., Aaronson, H. I., Lang III, W. F., *Metallography*, **9**, pp. 455-457.

[ridley1984]   Ridley, N., *Met. Trans. A*, **15**, pp. 1019-1036, 1984.

[schueller1992]   Reprinted from publication R. D. Schueller, A. K. Sachdev, and F. E. Wawner, *Scripta Metall. Mater*. **27**, pp. 1289-1294 (1992), with permission from Elsevier.

[trucco1998]   E. Trucco, E., Verri, A., *Introductory Techniques for 3-D Computer Vision*, Prentice Hall, New Jersey, 1998, pp. 108-114.

[underwood1968]   Underwood, E. E., in Quantitative Microscopy, pp. 77-127, Eds.: DeHoff, R. T. and Rhines, F. N., McGraw-Hill, NY, 1968.

[wang1995]   Wang, Z.M. and Shiflet, G.J., P*hysica Status Solidi (a)*, **149**, pp. 105-122,

1995.

[xu1998]   Xu, C. and Prince, J. L., *IEEE Trans. Image Processing*, **7**, pp. 359-369, 1998.

[xu2000]   Xu, C., Pham, D. L., and Prince, J. L., "Image Segmentation Deformable Models," Handbook of Medical Imaging: Image Processing and Analysis, SPIE Press, 2000.

[williams1981]   Williams, D. B. and Butler, E. P., *International Metals Review*, 26, pp. 153-183 (31), 1981.

[zener1946]   Zener, C., *Trans A.I.M.E.*, 167, p. 550, 1946.

[zieba2001]   Zieba, P. and Gust, W., *Zeitschrift fur Metallkunde*, 92, 7, pp. 645-654, 2001.

[zieba2002]   Zieba, P. and Gust, W., *Interface Science*, 10, pp. 27-30, 2002.

[zhou1992]   Zhou, D. S. and Shiflet, G. J, *Unpublished work*, University of Virginia, 1992.